Physical and Chemical Properties of Molecular Gas in Star Forming Regions

Inaugural-Dissertation

zur
Erlangung des Doktorgrades
der Mathematisch-Naturwissenschaftlichen Fakultät
der Universität zu Köln

vorgelegt von

Martin Emprechtinger
aus Neuhofen im Innkreis

Köln 2008

Berichterstatter:	Prof. Dr. Jürgen Stutzki Prof. Dr. Thomas Michely

Tag der letzten mündlichen Prüfung: im Jänner 2009

Zusammenfassung

In dieser Dissertation untersuche ich die physikalischen und chemischen Eigenschaften von molekularem Gas in Sternentstehungsregionen. Dabei mache ich mir den neu entwickelten CONDOR Empfänger zu nutzen, welcher spektral hochaufgelöste Beobachtungen bei Frequenzen von ca. 1.4 THz ermöglicht. Daher sind viele der im Rahmen dieser Arbeit getätigten Beobachtungen entweder mit CONDOR durchgeführt worden, oder durch die Wissenschaft, welche durch einen Terahertz Empfänger ermöglicht wird, motiviert.

In der massiven Sternentstehungsregion NGC 2024 wurden sieben ^{12}CO und ^{13}CO Emissionslinien, darunter auch ^{12}CO J=13-12 (ν = 1.497 THz) Beobachtungen mit CONDOR, gemessen. Mit Hilfe dieser CO 13-12 Spektren ließ sich eine schmale Schicht von heißem (~ 300 K) und dichtem (~ 10^6 cm^{-3}) molekularen Gas, welche sich zwischen der HII Region und der Molekülwolke befindet, erstmals nachweisen. Zusätzlich weist die geringe Breite dieser CO Linie darauf hin, dass diese heiße Schicht durch UV-Strahlung und nicht durch Schocks geheizt wird. Auf der Basis von physikalischen Szenarien, wie dem sogenannten "Blister Model" und dem PDR Szenarium, konnte ich mit Hilfe von Strahlungstransportrechnungen ein Model von NGC 2024 erstellen. Dieses Model erklärt sowohl die räumlich Dichte- und Temperaturverteilung entlang des Sehstrahles, als auch die kinematische Struktur der Quelle. Die komplizierten Linienprofile der beobachteten ^{12}CO und ^{13}CO Linien, welche sowohl Emission von verschiedenen Geschwindigkeitskomponenten als auch Selbstabsorption durch Vordergrundmaterial beinhalten, können mit diesem Model erklärt werden. Darüber hinaus, werden auch die integrierten Intensitäten von fünf weiteren, nicht geschwindigkeitsaufgelöst beobachteten Linien (J_{up} = 14 bis J_{up} = 19) richtig wiedergegeben.

Die Untersuchung der chemischen Zusammensetzung von massearmen Protosternen ist durch eine mit CONDOR beobachtbare H_2D^+ Linie motiviert. Neben seiner kosmologischen Relevanz spielt Deuterium auch in der Chemie in frühen Phasen der Sternentstehung eine entscheidende Rolle, wo extrem hohe Häufigkeiten von deuterierten Molekülen nachgewiesen wurden. Ziel der im Rahmen dieser Arbeit durchgeführten Untersuchungen war es die Veränderung die chemischen Häufigkeiten während der Sternentstehung zu charakterisieren. Die chemische Zusammensetzung des Gases wird in erster Linie durch das Ausfrieren von CO auf Staubkörner sowie durch die Auswirkungen des Fehlens von CO auf die Gasphasenchemie bestimmt. Eine Konsequenz des Ausfrierens von CO unterhalb einer Temperatur von 20 K ist, dass, wie auch in dieser Arbeit gezeigt wird, N_2H^+ im Zentrum von prästellaren Kernen sehr häufig vorkommt. In Objekten, welche bereits einen Protostern beherbergen, befindet sich das Gas mit verminderter CO Häufigkeit in einer Schale um einen durch das Zentralobjekt bereits erwärmten Kern. Je weiter der Protostern entwickelt ist, d.h. je mehr dieser das ihn umgebende Material erwärmt, desto kleiner wird diese CO-arme Region. Eine verminderte Häufigkeit von CO führt jedoch nicht nur zu einer erhöhten

Konzentration von N_2H^+, sondern auch zu einem größeren Vorkommen von deuteriumhaltigen Molekülen, wie H_2D^+, N_2D^+ und NH_2D. In dieser Arbeit zeige ich, dass die Häufigkeit dieser deuterierten Moleküle, und vor allem das Häufigkeitsverhältnis von deuterierter zu nicht deuterierter Form, als Indikator für das Entwicklungsstadium eines jungen Protosterns verwendet werden kann. So stellte sich heraus, dass ein hohes N_2D^+/N_2H^+ Verhältnis anzeigt, dass in diesem Objekt der Kollaps, welcher zur Entstehung eines Sternes führt, eben erst begonnen hat. Im Zuge der weitern Entwicklung des Protosternes sinkt dieses Verhältnis. Von mir durchgeführte Beobachtungen von NH_2D und NH_3 führen zu einem ähnlichen Resultat für das NH_2D/NH_3 Verhältnis. Beim DCO^+/HCO^+ Verhältnis kann jedoch keine solche Erhöhung festgestellt werden. Der Wert dieses Verhältnisses bleibt während der gesamten Sternentstehung in der Größenordnung von einigen Prozent.

Diese neuerdings mit CONDOR spektral hochaufgelöst beobachtbaren Linien bieten völlig neue Möglichkeit die physikalischen Vorgänge im interstellaren Medium zu untersuchen. Die Beobachtungen von hochangeregtem CO erlauben erstmals das heiße, molekular Gas gezielt zu beobachten und dadurch die Dichte und die Temperatur desselben viel genauer als bisher festzulegen. Die Profile dieser CO Linien lassen auch Rückschlüsse auf den Heizmechanismus dieses Materials zu. H_2D^+ Beobachtungen gewähren dagegen einen Einblick in die Physik der extrem kalten Teile des ISM, in welchen die Standardtracer, wie CO, auf Staub ausgefroren sind. Neue Empfängern im Terahertzbereich ermöglichen also, wie ich im folgenden in dieser Arbeit zeigen werde, das ISM unter extremen physikalischen Bedingungen zu untersuchen, was bisher nur sehr schwer möglich war.

Abstract

In this thesis I study the physical and chemical properties of molecular gas in star forming regions. This work takes advantage of the newly developed CONDOR receiver, which allows spectrally resolved observations of emission lines at frequencies of about 1.4 THz. Thus the thesis contains observational data obtained with CONDOR as well as observations motivated by the science one can do with receivers at terahertz frequencies are largely included.

In the massive star forming region NGC 2024, seven emission lines of ^{12}CO and ^{13}CO have been observed, including ^{12}CO J=13-12 ($\nu = 1.497$ THz) observations with CONDOR. These high-J CO data reveal a thin layer of hot (~ 300 K) and dense ($\sim 10^6$ cm^{-3}) molecular gas, which has not been detected with any other tracer before. This newly discovered component is located at the interface between an HII region and the molecular cloud. Furthermore, the narrow line width indicates that this layer is heated by radiation rather than by shocks. On the background of well established physical scenarios, such as the ”Blister Model” and the PDR scenario, I developed a model of NGC 2024, using radiative transfer computations. This model explains both, the spatial distribution of density and temperature along the line of sight and the velocity structure of the source. The complex profiles of the observed ^{12}CO and ^{13}CO lines, which include emission by multiple velocity components as well as self-absorption by foreground material, are reproduced by this model remarkably well. Furthermore, the integrated intensities of five additional lines ($J_{\rm up} = 14$ to $J_{\rm up} = 19$) can also be explained.

My study of low mass protostars was motivated by the H_2D^+ line observable with CONDOR, and shows the variation of chemical abundances along the star forming process. Next to its cosmological importance, deuterium plays also a significant role in the chemistry in the early phases of star formation. In such objects extremely high abundances of deuterated molecules have been measured. These abundances are mainly determined by the freeze out of CO onto dust grains, and the implication of the lowered CO abundance on gas phase chemistry. A consequence of the freeze out of CO at temperatures below 20 K, is that N_2H^+ is very abundant in the inner parts of prestellar cores, except for some possible depletion of N_2H^+ itself in the coldest spots. In objects, which harbor already a protostar, the CO depleted zone forms a shell around the warm core. The more evolved such an embedded protostar is, i.e., the more it heats up the surrounding material, the smaller gets the CO depleted shell. The lack of CO in the gas phase leads not only to an enhanced abundance of N_2H^+, but also deuterium bearing molecules, such as H_2D^+, N_2D^+ and NH_2D, are formed in a significant amount. As I will show in this work, the abundance of these deuterated species, and especially the abundance ratio of the deuterated to the non-deuterated form of molecule can be used as a tracer for the evolutionary stage of young protostellar cores. A high N_2D^+/N_2H^+ ratio (> 0.15) indicates, that in such a core the collapse, which forms a star, has just begun. This ratio decreases as the protostar evolves further. I conducted follow up

observations of NH_2D and NH_3 in the same objects. These observations give a similar trend for the NH_2D/NH_3 ration. However, other ratios, e.g., DCO^+/HCO^+ do not show such an enhancement, and stay at a level of a few percent throughout the protostellar evolution. The differences in the deuterium fractionation during the stellar evolution help us to understand the physical and chemical processes taking place.

The lines, now observable at high spectral resolution with CONDOR, provide new possibilities to study the physical processes in the interstellar medium. The observations of highly excited CO enable us for the first time to investigate the hot, molecular gas in the ISM specifically. Therefore the temperature and density of this material can be determined with much higher accuracy than previously. In addition, the shapes of the high-J CO lines draw conclusions on the heating mechanisms of the gas. H_2D^+ observations give us insights into the physics of the extremely cold part of the ISM, where standard tracers, like CO, are frozen out onto dust grains. As I will show in this work, observation at THz frequencies allow us to study the ISM under extreme physical conditions, which have been very difficult to investigate so far.

Contents

1 Motivation **1**

2 Star formation **5**

2.1 Low mass (isolated) star formation 5

2.1.1 Cloud Collapse 5

2.1.2 Prestellar Cores 7

2.1.3 Protostellar cores 8

2.1.4 Time scales 10

2.2 Chemistry in pre- and protostellar cores 10

2.2.1 Important gas-phase reactions 11

2.2.2 Relevance of Dust grains 13

2.2.3 Deuterium Chemistry 15

2.2.4 Molecular abundances in pre- and protostellar cores 17

2.3 Massive star formation 20

2.3.1 The process of high mass star formation 20

2.3.2 Interaction with surrounding material 21

3 The importance of THz lines in star forming regions **23**

3.1 Atmospheric transmission 23

3.2 Important emission lines in the 1.3-1.5 THz window 24

3.2.1 High-J ^{12}CO lines 24

3.2.2 Para-H_2D^+ and Ortho-D_2H^+ ground state transition 27

3.2.3 [NII] Fine structure Line 30

4 A line-of-sight model of the high mass star forming region NGC 2024 **33**

4.1 Introduction 33

4.1.1 The complex structure of the molecular material in high-mass star-forming regions 33

4.1.2 NGC 2024 34

4.2 Observation, Data-reduction and Results 35
4.2.1 Observed Lines 35
4.2.2 Observed Spectra 39
4.3 Modeling 43
4.3.1 Radiative Transfer 43
4.3.2 The Model of NGC 2024 46
4.3.3 Escape Probability Code Results 47
4.3.4 Full Radiative Transfer Model 48
4.4 Chapter summary 56

5 Comparison of a pre- and a protostellar core in IC 5146 59

5.1 The cloud filament associated with IC 5146 and its eastern core . . 59
5.2 Observation 60
5.2.1 Ammonia 61
5.2.2 $H^{13}CO^+$ and DCO^+ 61
5.2.3 $C^{18}O$ 2-1 and N_2H^+ 1-0 61
5.2.4 Optical Extinction 62
5.3 Results 63
5.3.1 Maps 63
5.3.2 Spectra 66
5.3.3 Gas temperature 69
5.4 Abundance profiles of pre- and protostellar cores 69
5.4.1 The Core at Position 2 - A prestellar core? 70
5.4.2 The structure of the protostellar core 77
5.4.3 Comparison with other protostellar cores 81
5.5 Summary 81

6 Deuterium fractionation as evolutionary tracer in Class 0 protostars 83

6.1 Introduction 83

6.1.1 Evolutionary tracer based on continuum observations 83

6.1.2 Principle Ideas 85

6.1.3 Previous Studies of the N_2D^+/N_2H^+ Ratio in Star Forming Regions 87

6.2 Observations 89

6.2.1 Source sample 89

6.2.2 Observations 90

6.3 Results 94

6.3.1 N_2H^+ & N_2D^+ 94

6.3.2 $C^{18}O$ & HCO^+ 98

6.4 Correlating the Deuterium fractionation with other physical properties 98

6.4.1 Dust Temperature 99

6.4.2 CO Depletion Factor 100

6.4.3 Bolometric Luminosity 106

6.4.4 Kinematic of the Gas 108

6.5 Evolutionary Sequence of the Sample 111

6.6 Comparison with chemical- and radiative transfer model 112

6.6.1 Cloud structure 112

6.6.2 Chemical- and radiative transfer model 114

6.6.3 Comparison between models and observations 115

6.6.4 Chemical stratification within the core 117

6.6.5 Sensitivity of the Model 119

6.7 Deuterium fractionation of other molecules 120

6.7.1 Preliminary analyzed NH_2D and NH_3 observations 122

6.8 Chapter summary 126

7 Summary and Outlook 129

References 133

List of Figures 143

List of Tables 145

Publikationen 147

Danksagung 149

Erklärung 151

Lebenslauf 153

1 Motivation

Stars, stellar evolution and, as part of stellar evolution, star formation are crucial for the understanding of the present cosmos. The importance of stars can be illustrated by the following statements.

- Many bound structures in the universes, ranging from single stellar systems via galaxies to galaxy clusters can be traced by stars. In most of these structures stars contain also the bulk of the baryonic matter. In spiral galaxies, for example, $\sim 70\%$ of the baryonic mass is stored in stars, whereas the rest exists as gas. An exception are galaxy clusters, where intra cluster gas dominates the mass and stars contain only $\sim 5\%$ of the baryonic matter. Because stars contain most of the baryonic mass, these objects must be easily formed under the physical conditions present in space.
- Only hydrogen, helium and to a much smaller amount lithium, beryllium and possibly boron are primordial elements, i.e., only these four elements are formed during the Big Bang. Furthermore the lithium and especially the beryllium nuclei formed in the Big Bang are not stable, and therefore these elements partially decay again. Present day lithium and beryllium are formed by spallation reactions of heavier nuclei. Hence almost all heavy elements are created in stars either by nuclear burning or, in the case of elements heavier than iron, in supernova explosions via nuclear fusion. Thus the observed abundances of metals, i.e., elements heavier than helium, are directly linked to the star-formation-rate and the properties, especially the mass, of the formed stars throughout time.

Because of the importance of star formation in astronomy and cosmology, it has been studied elaborately throughout the last 50 years. It is generally accepted that stars form by a collapse of a cold and dense molecular cloud core. However, the exact physical mechanisms driving these collapses are very complex, and many phenomena, such as rotation, turbulence, magnetic fields, disk formation, outflows, fragmentation of the clouds, etc. must be considered in a complete model. The typical time scale for star-formation is $10^5 - 10^6$ years and the more massive a star, the shorter its formation time scale. This shorter time scales cause, that low-mass and high-mass stars form differently. Low mass stars (i.e., stars with masses ≤ 8 $M_\odot$) are formed following a classification scheme based on infrared and sub-mm continuum observations (see chapter 2). These classes reflect the dissipation of the cold protostellar envelope during star formation. Contrary to low mass stars, high mass stars evolve much faster and reach the main sequence, i.e., a stable state at which stars stay for most of their lifetime, long before the protostellar envelope has disappeared, and thus high mass stars form deeply embedded into molecular clouds. Protostars and newly formed stars influence also the physical conditions of their parental cloud. The injection of energy, first by outflows and later by radiation, may cause complex temperature and density structures of the remaining molecular cloud and might trigger the formation of further star. This is especially true for the sites of massive star formation.

Because of the above mentioned reasons, our understanding of star formation is still far from being complete and many observed phenomena are yet not or just partly understood. Due to the complexity of the entire formation process, each investigation can focus only on a few details and try to embed the results in the overall picture of star formation, we have today. The two questions I try to answer in this work, which are motivated by newly developed observing techniques (see below), are:

- **How does the complex structure of molecular clouds surrounding massive stars look like, and how does this structure agree with theoretical predictions?**
- **How do the chemical abundances, especially the abundances of deuterium bearing molecules, change during the early phases of low mass star formation?**

The tools, with which I studied these questions, are observations of molecular emission lines in the (sub)-millimeter wavelength regime. The most important molecule for such observations is CO, which was first detected in space by Wilson et al. (1970). CO is so important, because it is, besides H_2, the most abundant molecule in the ISM ($x(CO) \sim 10^{-4}$, where x(CO) is the abundance of CO relative to H_2). Because H_2 has no permanent dipole, i.e., its transitions are *forbidden*, and the energy of the upper state of the lowest transition is 521 K above the ground state, H_2 is hardly observable in the ISM. The Energy of the upper state of the CO ground state transition is only 5.5 K above the ground state, and therefore much easier to populate. Furthermore, the critical densities of low-J CO lines are quite low ($\sim 10^3$ cm^{-3}), and therefore CO emits radiation from most parts of the clouds, whereas many transitions of other molecules are excited only at densities lager than $\sim 10^5$ cm^{-3}. Thus CO lines are among the brightest emission lines in molecular clouds. Because of their brightness CO lines are also important for the energy balance of molecular clouds. Next to dust, CO is the most important coolant in such environments.

To address the second question I observed the deuterium bearing molecules N_2D^+ and NH_2D. Deuterium is a primordial element, which is destroyed by nuclear fusion in stars and brown dwarfs. Therefore its current abundance (which is of the order of 10^{-5}) gives some constraints on cosmological models. Despite the low elemental abundance of deuterium, the abundance of deuterated molecules can be quite high. In cold ($\sim$ 10 K), dense ($> 10^5$ cm^{-3}) regions their abundances can get even as high as the abundance of their protonated analogues, which means that they are 5 orders of magnitude more abundant than it is expected from the elemental D/H ratio. Chemical models (e.g., Millar et al. 2000, Roberts & Millar 2000, Walmsley et al. 2004 and Flower et al. 2004) have revealed that in cold and dense environments, in which CO is largely frozen out onto dust grains, the formation of H_2D^+, a key molecule in the deuterium chemistry, is highly favored (see chapter 2). This makes H_2D^+ to an ideal candidate to study the coldest parts of cloud cores. The predicted abundance of deuterated molecules depends strongly on the temperature and the degree of CO depletion, which therefore provide an interesting tool to investigate changes of the physical parameters during the formation of stars.

The connection between the two separated questions raised above is the newly developed $\underline{\text{CO}}$ $\underline{\text{N}}^+$ $\underline{\text{D}}$euterium $\underline{\text{O}}$bservation $\underline{\text{R}}$eceiver (CONDOR, Wieching 2006). A description of the emission lines observable with this receiver is given in chapter 3. CONDOR is a heterodyne receiver covering a frequency band from 1.2 THz and 1.5 THz, and it was designed to be used at the Atacama Pathfinder EXperiment (APEX) telescope and, as part of the German REceiver At Terahertz frequencies (GREAT), on the Stratospheric Observatory For Infrared Astronomy (SOFIA). The nominal bandwidth of the intermediate frequency (IF) is 1 GHz. The mixing element is a Hot Electron Bolometer (HEB), made of NbTiN. As Local Oscillator (LO) two commercially available systems, a Gunn-oscillator with subsequent frequency multipliers and a solid state multiplier chain are used. With this system double sideband (DSB) receiver temperatures of $\sim$ 1600 K were reached. First light observations with this receiver were conducted in November 2005 at APEX. During this observing campaign we also obtained many data used in this work (chapter 3 & 4).

Observations in the THz regime are hampered by the low atmospheric transmission at these frequencies and the high surface accuracy required for these observations. Even from the best sites for THz observations on earth an atmospheric transmission above 20% is hardly reached (see chapter 3). With telescopes with a surface accuracy of 20 μm, which is a typical value for modern sub-mm telescopes, a maximum beam efficiency of only 21% can be reached according to the Ruze-formula (Ruze 1966). This means that with present day telescopes about 80% of the signal gets absorbed by the atmosphere and another 80% of the remaining signal is scattered into the extended error-beam(s). Despite these difficulties a few detections from ground based telescopes of lines above 1 THz have been reported by Kawamura et al. (2002), Marrone et al. (2004) and Oberst et al. (2006). To overcome the low atmospheric transmission airborne (Kuiper Airborne Observatory (KAO), e.g., Stutzki & Guesten 1990)) and satellite borne (Infrared Satellite Observatory (ISO), van Dishoeck 2004 and references therein, COsmic Background Explorer (COBE), e.g., Fixsen et al. 1999) observations have been carried out. However, most of these observations have low frequency resolutions and line profiles cannot be determined (only at the KAO a heterodyne instrument was installed, e.g., Boreiko & Betz 1993).

Despite all challenges, it is worth to observe emission lines at THz frequencies with high spectral resolution, and many astronomically interesting phenomena, especially in star forming regions, greatly benefit from such data. For example, the paper of

Stutzki et al. (1991) and Sun et al. (2008) show the potential of THz lines for studying the clumpy structure of the interstellar medium. Therefore several new telescopes for THz observations, such as the Stratospheric observatory for Infrared Astronomy (SOFIA), the Stratospheric Terahertz Observatory (STO) and the Cornell Caltech Atacama Telescope (CCAT) will be built within the next few years.

In the following sections I will give a short overview of the most important processes in low- and high-mass star formation (chapter 2) and introduce the most important emission lines in the 1.4 THz atmospheric windows (chapter 3). In chapter 4 I will present a study of multi-line transitions of ^{12}CO and ^{13}CO in NGC 2024. The main difference between the chemical abundances of low-mass prestellar cores and protostars will be reveal by investigation presented in chapter 5, and finally the variation of the abundances of deuterated molecules with the evolutionary stage will be discussed in chapter 6. Parts of this thesis, namely the investigation of NGC 2024 (chapter 4) and the abundance study of deuterated molecules in Class 0 protostars (chapter 6), have already been published in *Astronomy & Astrophysics*.

2 Star formation

The way, how stars form, their internal structure and their late stellar evolution are determined by their mass. High mass stars ($M_* > 8\ M_\odot$) are bright, hot, short living objects which end in a Supernova, whereas low mass stars live much longer (several 10^9 years) and end up as planetary nebulae and finally as a white dwarfs. The mass distribution of newly formed stars is described by the initial mass function (IFM), which can be written as:

$$dN = \xi(M)dM, \quad \xi(M) \propto M^{-\alpha} \tag{2.1}$$

Observationally derived values of the power-law index α are between 2.2 and 3 (Kroupa 2002 and references therein). Using the classical value of $\alpha = 2.35$ (Salpeter 1955), and mass limits of $0.072\ M_\odot$, which is the lower limit to start nuclear fusion, and $100\ M_\odot$, which are the most massive stars detected so far, shows that 99.8% of all newly formed stars are low-mass and intermediate stars ($< 8\ M_\odot$). Even 87.7% of the total stellar mass is stored in stars with masses lower than $8\ M_\odot$.

However, taking the luminosity-mass-function

$$L \propto M^{3.5} \tag{2.2}$$

(Eddington 1926) into account one sees, that the overall luminosity is dominated by the massive OB stars.

2.1 Low mass (isolated) star formation

Low mass stars are formed by the collapse of a dense cloud core. During the formation process the entire molecular envelope disappears, either because it gets accreted onto the star, or dissipated by outflows, stellar winds and radiation pressure. In the following I will give a short summary of the theory of low-mass star formation (section 2.1.1) and of observed parameters of pre- and protostellar cores (section 2.1.2 & 2.1.3).

2.1.1 Cloud Collapse

Stability of a cloud

It is generally accepted that stars are formed by the collapse of a gravitationally unstable cloud. However, a gravitational collapse can only occur, if the gravitational force overcomes the internal pressure of the gas, i.e.,

$$\frac{\partial p}{\partial r} \leq -\frac{G\rho M(r)}{r^2} \tag{2.3}$$

is fulfilled. Jeans (1902) established a criterion (now named after him *Jeans criterion*), which gives the size of a gas cloud of a density ρ_0, which is required for the collapse. He considered an infinitely extended isothermal gas cloud with a constant density and added a small perturbation to it. Because the perturbation is small, the hydrodynamic equations (force equation, Poisson equation, equation of continuity) can be written as a set of linear differential equations, which have wave like solutions (i.e., $e^{-i(kx-\omega t)}$). However, for solutions with wavenumbers smaller than $\sqrt{\frac{4\pi G\rho_0}{a^2}}$ the frequency ω gets complex, and thus the initial perturbation increases exponentially with time, i.e., these perturbations are big enough to collapse. Converted into a mass inside a certain radius r, the *Jeans criterion* can be written as

$$M_J(r) \sim \frac{5 \cdot kT \cdot r}{\mu \cdot G} \tag{2.4}$$

Bonnor (1956) and Ebert (1955) calculated the density structure of a gravitationally bounded, isothermal gas cloud in equilibrium. In the outer parts of such a *Bonnor-Ebert-Sphere* the density falls of following a power-law ($\rho \propto r^{-\alpha}$, with $\alpha \sim 2$), whereas in the inner part the density stays constant. In the case of a pressure confined cloud another stability criterion can be established. The critical mass $M(r)_{crit.}$ given by

$$M(r)_{crit} = 1.18 \frac{a^4}{\sqrt{G^3 P_{ext}}}. \tag{2.5}$$

Above this mass no stable solution exists. This *Bonnor-Ebert-mass* corresponds to the *Jeans-mass*, because a cloud in hydrostatic equilibrium has exactly one Jeans-mass at each radius (Shu et al. 1987).

Collapse Models

In cases, where the total mass of the gas cloud is higher than the critical mass discussed above, the cloud starts to collapse. Two competing theories for the process of this collapse have been developed. The first one, called ”dynamical collapse” (e.g., Penston 1969, Larson 1969, see also the review by Larson 2003), starts from a supercritical ($M_{cloud}>M_{Jeans}$) gas cloud. The initial density distribution is unimportant for the later evolution, since a density gradient ($n \propto r^{-2}$) develops quickly, because the interior pressure of the gas rises during the collapse, whereas the boundary pressure does not (Bodenheimer & Sweigart 1968). The predicted density profile can therefore be described by a central plateau and a subsequent decline proportional to r^{-2}. The central plateau increases in density and decreases in radius with time. The collapse continues almost isothermally until the central density reaches $2 \cdot 10^{10}$ cm^{-3} and the core gets optically thick. At this point the gas gets adiabatic and therefore the collapse stops.

The second theory is the ”Inside-out collapse” (Shu 1977 & Shu et al. 1987), which starts from a critical Bonnor-Ebert-sphere ($M_{cloud}=M_{crit.}$). The collapse of such a cloud core is initiated by a small perturbation, which causes the most inner part to collapse, and progresses outwards with the speed of sound. For the outer regions the inside-out collapse model predicts an $n \propto r^{-2}$ density law, too, but inside the collapsing region the power law index decreases to -1.5. Hence, the density profiles of the ”dynamical collapse” and the ”inside-out collapse” look very similar. Like in the previous model, the collapse gets stopped as soon as the core gets optically thick.

Subsequent Evolution

Both models, the dynamical collapse model and the inside-out collapse model, predict a final mass of the protostar of $\sim 10^{-2}\ M_\odot$. The rest of the required mass, which is almost 100% of the mass of the Main Sequence (MS) star, has to be acquired by accretion of the remaining envelope. This accretion will occur mainly in a disk, because rotational flattening becomes important. Even a slowly rotating disk contains too much angular momentum (L) for direct infall onto the protostar. The main problem of disk accretion is, that angular momentum has to be carried outwards, which could be done by viscosity. However, since molecular viscosity is much too small for the required L-transport, some processes creating a higher effective viscosity are needed. Hydrodynamical turbulences, gravitational instabilities (Gammie 2001), magneto-rotational instabilities (Balbus & Hawley 1998), etc. have been discussed to cause the angular momentum transport, but no such process has been identified clearly so far.

When the protostar reaches a mass of 0.2 $M_\odot$ deuterium burning starts at the center, creating a local energy source, which prevents further contraction of the protostar with increasing mass. At the end of the accretion, a 1 $M_\odot$ protostar has a radius of $\sim 4R_\odot$. The protostar is obscured by the dust of the surrounding envelope during the entire accretion phase, and thus it becomes visible in the optical regime for the first time when accretion ceases to be important. In the Hertzsprung-Russel diagram it appears near the lower Hayashi track (Hayashi et al. 1962), which gives the effective temperature of a fully convective star of a certain mass and thus it maximum radius. Further contraction of the protostar occurs via quasi static Kelvin-Helmholtz-contraction, until the temperature and density, required to start nuclear fusion are reached.

2.1.2 Prestellar Cores

Prestellar or *starless* cores are the earliest stage of isolated low-mass star formation. These cloud cores, with densities $\sim 10^5$ cm^{-3}, do not show any sign of an embedded protostar. They contain masses of several $M_\odot$ (Evans 1999). The observed sizes of the cores depend on the tracers which are used. Myers et al. (1991) found, in sample of 16 dense cores, average full widths at half maximum (FWHM) of 0.15 pc (NH_3), 0.27 pc (CS 2-1) and 0.38 pc ($C^{18}O$ 1-0). The cores in this sample show typically an elongated shape with axial ratios of 0.5-0.6.

For the internal structure of prestellar cores, both models, dynamical collapse as well as inside-out collapse, predict a density profile of $n \propto r^{-2}$, with a flattened inner region. A detailed investigation of the density structure of Barnard 68, a very well known starless core, has been carried out by Alves et al. (2001). They used near-infrared observations at 1.25 μm, 1.65 μm, and 2.16 μm (J, H, and K-band, respectively) to determine the extinction of background starlight, and thus the column density of the core. The density structure of B 68 can be described very well as a pressure confined, self-gravitating isothermal sphere which is critically stable according to the Bonnor-Ebert criteria (Ebert 1955, Bonnor 1956). In physical unit this gives a radius of 12 500 AU, a total mass of 2.1 $M_\odot$ and an external pressure of $2.5 \cdot 10^{-12}$ Pa. These values are based on a distance of 125 pc and a temperature of 16 K.

The temperature profile of a prestellar core has been studied in L 1544 by Crapsi et al. (2007). They used interferometry data of the NH_3 (1,1) and (2,2) transition, observed with the VLA, to determine temperature at different projected radii. This investigation revealed a temperature profile of

$$T(r) = T_{out} - \frac{T_{out} - T_{in}}{1 + (r/r_{0,T})^{1.5}} \qquad (2.6)$$

with $T_{out} = 13.1$ K and $T_{in} = 6.5$ K. The outer parts of the prestellar core are heated by the surrounding radiation field, but close to the center, the radiation is weaker due to absorption, and thus this temperature dip occurs. Taking other heating mechanisms, such as direct cosmic-ray heating and heating by UV photons created following the cosmic ray ionization of H_2, into account damps this temperature dip, but it still remains (Evans et al. 2001)

2.1.3 Protostellar cores

Contrary to the *prestellar cores*, which do not contain any internal heating source, and whose temperature profiles are mainly dominated by the external radiation field and its extinction, *protostellar cores* do harbor internal energy sources. Depending on the evolutionary stage of the embedded protostar, this energy is gained either by adiabatic contraction, or by nuclear fusion (e.g., deuterium burning, see section 2.1.1). Since the mechanism of the energy production, as well as the properties, such as mass and radius, of the protostar core changes with time, the spectral energy distribution (SED) changes as well and can be used to determine the evolutionary stage of protostellar cores. The original classification scheme (introduced by Lada & Wilking (1984) and Lada (1987), interpreted by Shu et al. (1987)) is based on near infrared (NIR) observations in the star forming region ρ Oph. It divides the protostars into three classes (Class I-III) according to the spectral index between $\lambda = 2\mu m$ and $\lambda = 20\mu m$. Based on more recent observations at millimeter and submillimeter wavelengths André et al. (1993) proposed a fourth class (Class 0) of even younger protostars. In the following I will describe the four classes listed in the order of the star-formation.

Class 0:
The Class 0 objects are the youngest among the protostars and follow immediately the prestellar phase. Class 0 protostars are defined as objects with $M_\star/M_{env} < 1$ (André et al. 1993), i.e., the mass of the surrounding envelope exceeds the mass of the central object. Thus the differentiation between Class 0 and Class I is somewhat vague. At $M_\star = M_{env}$ the average dust temperature is about 30 K (André et al. 1993).

Looney et al. (2003) modeled the temperature and density profile of Class 0 source using interferometric continuum observations at $\lambda = 2.7\ mm$. Their model uses a self-consistent, luminosity conserving temperature profile and assumes an embedded point like protostar. The adopted density profile was a power-law. Independent from the other parameters (M_{cloud}, power-law index of the density profile), the temperature profile turns out to be $T \propto r^{-q}$ with $q \sim 0.4$ for $r > 200\ AU$. A power-law index of 0.4 is the model solution for an optical thin medium. At lower radii the temperature profile deviates significantly from this power-law, because the protostellar envelope gets optically thick. The best fit of the solution yields a density law of $n \propto r^{-p}$ and $p = 2$. This is very similar to the solution of the isothermal sphere and steeper than predicted by theoretical model ($p_{pre.} = 1.5$, e.g., Shu (1977)). For three out of six source $q = 1.5$ can be ruled out at the 95% confidence level.

Class I:
These are sources with an SED broader than the one of a blackbody, and the SED is rising longwards of $\lambda = 2\ \mu m$ (Lada 1987), but the mass of the central protostar exceeds already the mass of the surrounding envelope. In this phase of the stellar evolution a large fraction of the envelope has been accreted already onto the central star. Furthermore powerful protostellar outflows develop. However, the central object is still embedded in the environmental material and is only visible in the optical if one looks along the line of sight of the outflow.

Class II:
The SED of Class II objects is still broader than the blackbody SED, but it is flat or declining at $\lambda = 2\ \mu m$ (Lada 1987). Protostars at this evolutionary stage are commonly called T-Tauri stars. At this time the protostellar envelope has disappeared and accretion has stopped, but the protostar is still surrounded by a massive disk ($\sim 10^3\ M_\odot$), which causes the infrared excess of the SED of these objects. At optical wavelengths the SED is dominated by the light emitted from the central stellar object ($T_{eff} \sim 4000\ K$, see Mac Low & Klessen (2004) and references therein).

Class III:
The broadband spectrum of a Class III protostar can be described very well with a reddened blackbody (Lada 1987). At this stage the disk, which has dominated the IR-spectrum during the Class II phase, has depleted into a very thin disk of debris,

which can last until the main-sequence phase. Therefore the SED of such an object is dominated by the so called *pre-main-sequence star*, and thus very similar to a black-body SED with $T \sim 5000\ K$. At this stage the protostar contracts via Kelvin-Helmholtz contraction until it reaches stable conditions.

2.1.4 Time scales

A rough estimation of the time scale of star formation is the *free fall time*. This approximation assumes a gravitational collapse in the absence of any pressure or magnetic support of the cloud:

$$t_{ff} = \sqrt{\frac{3\pi}{32 \cdot G\rho}}. \tag{2.7}$$

This expression for the free fall time can be easily derived from the *third Kepler law* (Kepler 1618), assuming an orbit with an eccentricity $\epsilon = 1$. For an initial density of $10^5\ cm^{-3}$ the free fall time is $\sim 10^5$ years. This estimation is approximately correct for the early isothermal phases of the collapse, but later on, more complex models are required. Such models have been developed by several authors (e.g., Myers et al. (1998), André et al. (2000), Smith (1998)). These models calculate the continuum emission of the protostar, assuming a certain geometry (e.g., a star with a disk, surrounded by an envelope), and using radiative transfer codes. The main difference among the models is the different assumed temporary sequences of the mass accretion rate. Froebrich (2005) applied the model results to a large sample of Class 0 and Class I protostars. Although the final mass and the evolutionary stages predicted by the individual model agree fairly well the absolute age are very model dependent. For example, the predicted ages for the Class 0/I borderline objects vary from 10^4 years (model from André et al. (2000)) to a few times 10^5 years (model from Myers et al. (1998)).

2.2 Chemistry in pre- and protostellar cores

In this section I will give a short overview of the chemistry in star forming region, based on a review by Caselli (2005). Because most material in pre- and protostellar cores are highly shielded from radiation, chemical reaction induced by photons, such as photo-ionization and photo-dissociation, are not treated in the following. In the first part of this section I will discuss the principle mechanisms of chemistry in dark cloud cores, whereas in the second part their influence on the abundances in space is shown.

2.2.1 Important gas-phase reactions

Gas-phase reactions are, besides grain surface reactions, the only important reactions in interstellar chemistry. The rate coefficients are calculated by

$$k_{reac} = < \sigma v > \tag{2.8}$$

where σ is the reaction cross section and v the velocity of the reaction partners. Many reactions, even if they are exothermic, have noticeable activation energies, because often chemical bonds have to be broken up first. The rate coefficient of these reactions can be written as

$$k_{reac} = C(T) \cdot exp(-E_a/k_B T) \tag{2.9}$$

where, E_a is the activation energy, k_B the Boltzmann constant and C(T) a temperature dependent ”pre-exponential factor”. This formula is the so-called ”Arrhenius formula”. Typical E_a-values for neutral-neutral reactions are $10^3 - 10^4$ K. Hence these reactions are very slow, and thus negligible, under the conditions present in prestellar cores and protostellar envelopes. However, reactions including charged particles may be much faster and therefore determining the gas phase chemistry. Precise reaction rate for many astrochemically important reactions are listed in huge data bases, e.g., the UMIST database06 (Woodall et al. 2007), and the Ohio State Chemical Network[1].

Ion-neutral reactions

The importance of ion-neutral reactions for dark cloud chemistry has been shown by Herbst & Klemperer (1973). These reactions do not posses activation energies, because long range attraction forces between the reaction partners exist. The attraction is caused by the polarization of the neutral partner by the ionic one, and the potential can be written as

$$V(r) = -\frac{\alpha q^2}{2r^4} \tag{2.10}$$

where α is the polarizability of the neutral reaction partner, q is the electric charge of the ion (typically 1 e) and r is the distance between the reaction partners. From this potential one can derive the rate coefficient for such reactions quite easily

$$k_{reac} = 2\pi q \sqrt{\frac{\alpha}{\mu}}, \tag{2.11}$$

where μ is the reduced mass of the reaction partners. This so-called Langevin rate is typically of the order of 10^{-9} cm^{3}s^{-1}, i.e., the timescales for such reactions to reach equilibrium are a few decades, which is very short compared to the dynamical timescales of star formation (see section 2.1.4). Furthermore these rate coefficients are independent of the temperature. A special class of ion-neutral-reactions are charge transfer reactions, which are of the type

---

[1] www.physics.ohio-state.edu/ eric/research_files/osu_03_2008

$$A^+ + B \rightarrow A + B^+. \tag{2.12}$$

The rate coefficients of these reactions are approximately 10^{-9} cm^{3}s^{-1}, too.

Ionization

In space, molecules can be ionized by photons, cosmic radiation and shocks, but in the context of this section, the chemistry of cold, dense and quiescent gas, only ionization by cosmic rays is important. The rate of this process (ζ) is typically in the order of $10^{-17} s^{-1}$ (van der Tak & van Dishoeck 2000). The most important reaction is the ionization of H_2, because H_2 is the most abundant molecule. Most (96%) of these reaction form H_2^+

$$H_2 + c.r. \rightarrow H_2^+ + e^- + c.r. \tag{2.13}$$

whereas the rest of the ionization forms H^+ + H (Walmsley et al. 2004). Most H_2^+ react with H_2

$$H_2^+ + H_2 \rightarrow H_3^+ + H. \tag{2.14}$$

forming H_3^+, which does not react with H_2 anymore. Thus H_3^+ is one of the most abundant ions in cold cloud cores and an important key molecule in gas-phase chemistry.

Dissociative recombination

Dissociative recombination reactions are reactions of the type

$$AB^+ + e^- \rightarrow A + B. \tag{2.15}$$

The rate coefficient of such reactions can be determined by studying resonances in the scattering of electrons by molecules (Bardsley 1968a, Bardsley 1968b). The functional dependency on the temperature looks like

$$k_{reac.} = R_{300} \cdot (T/300)^{\beta} \tag{2.16}$$

where R_{300} is typically in the order of 10^{-7} cm^{3}s^{-1} and β about -0.5. Often dissociative recombinations can yield different products. For example, the recombination of H_3^+ forms either $H_2 + H$ or three hydrogen atoms. The fraction of recombination reactions, which will form the different products are called *branching ratios*.

2.2.2 Relevance of Dust grains

Freeze-out and Desorption of Molecules

At low temperatures (~ 10 K), many molecular species tend to freeze-out onto dust grains. This is due to the adsorption energies (E_D), which has to be overcome for desorption. The accretion rate of is calculated by

$$k_{acc.} = n_{Dust} < \sigma v > S \tag{2.17}$$

where n_{Dust} is the number density of dust grains, σ the cross section of the dust particles and S is the sticking factor, which is the probability of a molecule to stick on the grain. For typical cosmic values and a sticking factor of one $k_{acc.}$ is in the order of $10^{-17} \cdot \mathrm{n(H_2)}\ [\mathrm{s}^{-1}]$.

There are many different desorption mechanisms, which are described by Hasegawa & Herbst (1993) and, more recently, by Shen et al. (2004). The most important desorption mechanism is thermal evaporation, which is given by

$$k_{eva.} = \nu_0 \cdot exp(-E_D/T_d), \tag{2.18}$$

where ν_0 is the characteristic adsorbate vibrational frequency (~ $10^{12}\ s^{-1}$) and T_d is the dust temperature. Typical values of E_D are ~ 1100 K for CO and N_2 (Öberg et al. 2005) and ~ 5600 K for H_2O (Fraser et al. 2001). If only thermal evaporation is taken into account, the molecules deplete completely from the gas phase at a certain temperature of ~ 20 K and ~ 100 K for CO and H_2O, respectively (Fig. 2.1).

Other important desorption mechanisms are induced by cosmic rays, such as cosmic-ray grain heating, cosmic-ray spot heating and desorption by cosmic-ray induced UV-photons. All these mechanisms are independent of the temperature. As a result, even at very low temperature the abundance of molecules such as CO is not zero. The rates of cosmic ray induced desorption are $9.8 \cdot 10^{-15}\ s^{-1}$ and $1.4 \cdot 10^{-18}\ s^{-1}$ for CO and H_2O, respectively (Hasegawa & Herbst 1993). This means that even at a temperature of 10 K, 10% of the CO is still in gas-phase.

Looking at the numbers of the accretion rate of molecules, one can calculate that even at very low temperatures it takes, for a H_2 density of 10^5 cm^{-3}, a few times 10^5 years for CO to freeze out onto dust. For lower densities it takes even longer. Therefore in chemical models a time dependent treatment of the freeze-out and desorption processes is required.

Grain-surface-chemistry

Grain-surface-chemistry plays a crucial role in the formation of many molecular species, not at least the formation of H_2. Especially the large observed abundances of complex,

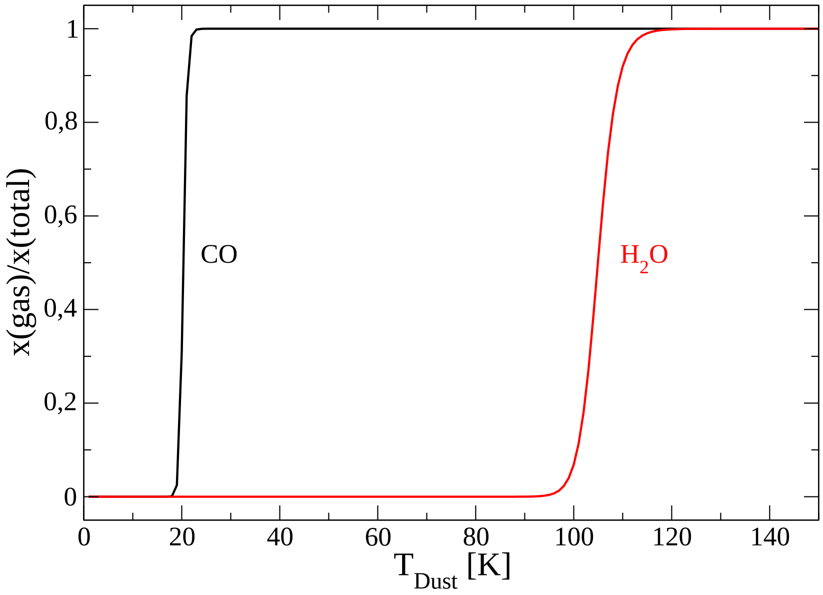

Fig. 2.1: *Relative gas-phase equilibrium abundance as function of* $\mathrm{T}_{\mathrm{Dust}}$ *for a molecule with* $E_D = 1100$ *K (CO, black) and* $E_D = 5600$ *K* (H_2O*, red). Only thermal evaporation is taken into account.*

hydrogen-rich species (e.g., Methanol) can be explained only by introducing grain-surface-chemistry. In principle, there are two mechanisms for the surface-chemistry, based on the strength of the binding energy of the reactants on dust.

Species, which are only weakly bound by van der Waals forces (*physisorbed* species, binding energy = 100 – 2000 K), can move quickly across the grain surface, overcoming the energetic barriers by quantum tunneling or thermal hoping. For light species, such as hydrogen, the crossing time scales are << 1 s. If such species meet another reactant on the surface, the chemical reaction occurs. Chemistry based on diffusion is called *Langmuir – Hinshelwood* chemistry. The most important class of reactions in Langmuir-Hinshelwood chemistry are hydrogenation reactions. Typical examples are the formation of H_2O from oxygen, and H_2CO and CH_3OH from CO.

Strongly bound *chemisorbed* species (binding energy ~ 10000 K) cannot move that easily. Thus chemical reactions of such species can only occur, if the other reactant lands nearby the chemisorbed species. Thus the reaction involving chemisorbed species (so-called *Eley – Rideal* chemistry) is only effective if the surface coverage is high.

In many cases the products of grain-surface-reactions stay on the dust grains, and are therefore not easily observable. An increase of the gas-phase abundances of these species thus requires an effective desorption mechanism, which typically occurs when the temperature rises. The methanol abundance, for example, is still very low at 10 K, although most of the CO is frozen out onto dust (Tafalla et al. 2002), and thus formation of CH_3OH is in principle possible. But as soon as the temperature rises CH_3OH evaporates and it gets very abundant in the gas-phase.

2.2.3 Deuterium Chemistry

The chemistry of pre- and protostellar cores can be explained by applying the reaction mechanisms described in the previous two subsections to cold (10 K) and dense ($> 10^5 cm^{-3}$) molecular clouds. In such an environment most molecules, including CO, are frozen out onto dust grains, and only hydrogen, deuterium and some nitrogen bearing species are left. Especially the deuterium bearing species become very abundant, due to the preferred formation of H_2D^+ under these conditions (see below). In some cases, the deuterated species get as abundant as their non-deuterated counterparts, which means, that the ratio of deuterated to protonated species exceeds the elemental D/H ratio by 5 orders of magnitude. Chemical models, which explain the increased abundance of deuterated molecules, have been calculated by e.g., Millar et al. (2000), Roberts & Millar (2000), Walmsley et al. (2004) and Flower et al. (2004).

All models show, that H_2D^+ and higher deuterated isotopologues are the key to understand deuterium chemistry. H_2D^+ is formed by the reaction

$$H_3^+ + HD \rightarrow H_2D^+ + H_2, \tag{2.19}$$

higher deuterated isotopologues are formed by subsequent reactions with HD. This reaction is exothermic with $\Delta E = 230$ K, and thus, the backwards reaction is very slow at low temperatures. Hence, H_2D^+ is only destroyed by either dissociative recombination

$$H_2D^+ + e^- \rightarrow products, \tag{2.20}$$

or by reactions with other molecules

$$H_2D^+ + X \rightarrow XD^+ + H_2 \ \ or \ \ XH^+ + HD, \tag{2.21}$$

where X are molecules like CO and N_2. Therefore depletion of CO (since it is the most abundant molecule next to H_2) is very crucial to the deuterium fractionation. In Fig. 2.2 the results of a simple, static chemical model are shown. One sees, that H_2D^+ is abundant ($x(H_2D^+) \sim 10^{-9}$) at temperatures lower than $\sim$ 20 K. But, as soon as CO desorbs from grains the H_2D^+ abundance drops by a factor of 100.

Because H_2D^+ consists of two hydrogen atoms it exists in an ortho form (parallel spin of the H atoms) and a para form (anti-parallel spin). The energy difference between the p-H_2D^+ ground state and the o-H_2D^+ ground state is 86.4 K (see the energy diagram in section 3), but at low temperatures the o/p ratio of H_2D^+ deviates significantly from thermal equilibrium. As shown first by Pagani et al. (1992) and later by Flower et al.

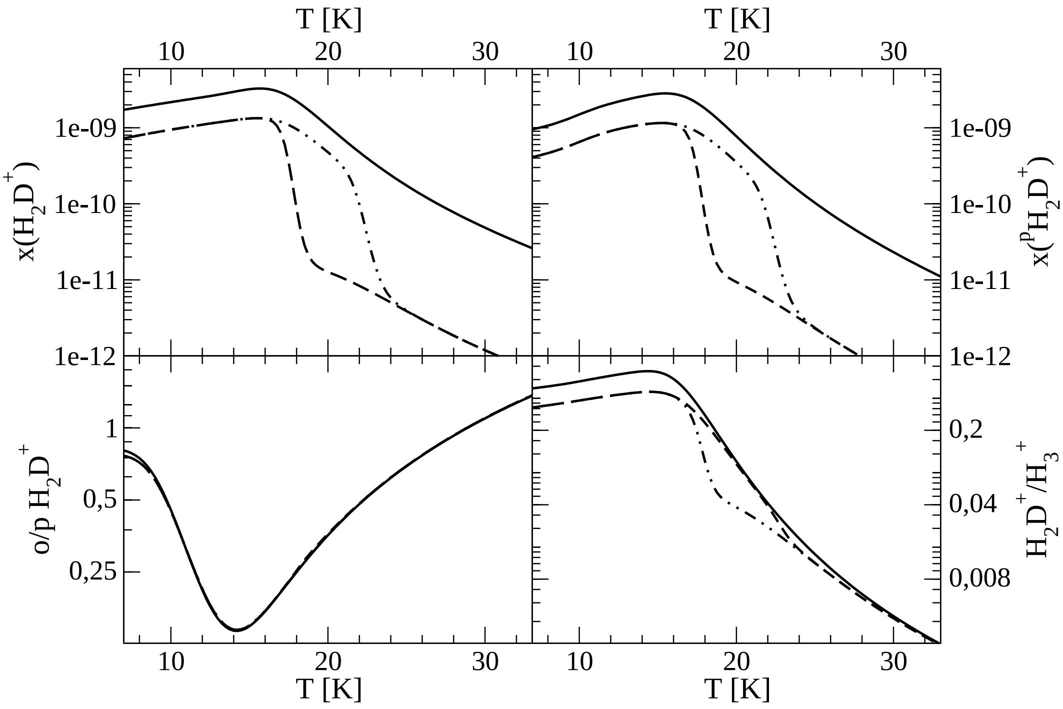

Fig. 2.2: *The overall H_2D^+ abundance, the para H_2D^+ abundance, the ortho-/para- ratio of H_2D^+ and the H_2D^+/H_3^+ ratio are plotted as functions of temperature for four different chemical models. The H_2 density is $10^6\mathrm{cm}^{-3}$ in all cases, and chemical equilibrium was reached. The solid line shows a model were CO is assumed to be completely frozen out onto dust. The dashed and dashed-dotted lines represent models in which CO depletion was computed following Hasegawa & Herbst (1993) assuming adsorption energies of 960 K (CO on CO-ice) and 1210 K (CO on water-ice), respectively.*

(2006b) the actual H_2D^+ ortho/para ratio depends on the o/p ratio of H_2, which is quite unknown, at low temperatures. Assuming that the minimum of the o/p ratio of H_2 is 10^{-3}, Pagani et al. (1992) derived an o/p ratio of H_2D^+ of 10 at a temperature of ~ 10 K (in thermal equilibrium the o/p ratio of H_2D^+ would be $5 \cdot 10^{-4}$). However, since any attempt to measure the o/p ratio of H_2D^+ in space has failed so far, this value is still under debate and model prediction ranges from 0.1 (Flower et al. 2006b) to 10.

As mentioned above, the abundance of H_2D^+ and higher deuterated versions are the key to understand the high abundance of deuterated molecules in general. This can be seen by looking at reaction 2.21, where deuterated ions, such as N_2D^+, DCO^+ and NH_3D^+ are formed. A subsequent dissociative recombination of NH_3D^+ leads to the high abundance of deuterated ammonia detected in space (Hatchell 2003, Roueff et al. 2005). H_2D^+ does not only influence the deuterium fractionation of molecules formed in gas-phase, but also the abundance of deuterated molecules, which originate from grain-surface-chemistry depend indirectly on the abundance of deuterated

H_3^+. As shown in section 2.2.2, reactions where atomic hydrogen is attached to existing molecules are important in grain-surface-chemistry. The amount of deuterium involved in these reactions depend on the atomic D/H ratio, but, in dark cloud cores, atomic hydrogen stems mostly from dissociative recombination reaction of hydrogen bearing ions. This way the H_2D^+ abundance determines the deuterium fractionation of species formed on grain surfaces. However, since these grain-surface species have to desorb from the dust before they can be observed, their measured deuterium fractionation may trace the H_2D^+ abundance from the past rather than the current one.

CH_2D^+ and C_2HD^+ play a similar role as H_2D^+, but, at least at low temperatures, these molecules are much less effective (Roberts & Millar 2000).

2.2.4 Molecular abundances in pre- and protostellar cores

Prestellar Cores

The prestellar phase is characterized by large core-edge abundance variations and a systematic molecular differentiation (Tafalla et al. 2002). These abundance variations are due to the freeze out of carbon bearing species, especially CO and CS, onto dust grains in cold ($\sim 10\ K$) and dense ($n_{H_2} \sim 10^5\ cm^{-3}$) molecular clouds (e.g., Bergin & Langer 1997, Caselli et al. 1999 , Kramer et al. 1999), following the mechanisms described in section 2.2.2. Nitrogen bearing species are less affected by depletion. Only some N_2H^+ depletion has been detected in a few objects (Bergin et al. 2002, Pagani et al. 2007). NH_3 stays in gas-phase even at temperatures of $\sim 7\ K$ (Crapsi et al. 2007). The reason, why nitrogen bearing molecules do not deplete that much is not completely understood so far, because the precursor molecule of these species, N_2, has approximately the same binding energy on various ices as CO (Bisschop et al. 2006), and should therefore deplete at approximately the same temperature. Recent theoretical studies suggest, that the robustness against depletion of these nitrogen bearing species is due to the fact, that a significant fraction of nitrogen is stored as atomic nitrogen, which suffers less from depletion (Flower et al. 2006a, Maret et al. 2006).

In order to study the abundance variations, Tafalla et al. (2002) observed transitions of CO, CS, NH_3 and N_2H^+ in five starless cores. In their work, they assumed an isothermal sphere and derived the density structure of the form

$$n(r) = \frac{n_0}{1+(r/r_0)^\alpha} \tag{2.22}$$

by fitting the dust continuum at $\lambda = 1.2\ mm$. The molecular abundance profiles were derived by applying a radiative transfer code. For CO and CS abundance profiles are of the form of

$$X(r) = X_0 \cdot exp(-n(r)/n_d) \tag{2.23}$$

with n_d in the order of a few times 10^4 cm^{-3}. The N_2H^+ abundance was found to be constant, i.e., no depletion of nitrogen bearing species was found. The Ammonia abundance rises approximately linearly with density ($X_{NH_3} = X_0(n/n_0)^\beta$ and $\beta \sim 1$).

The cold temperatures and the depletion of many molecules, especially the depletion of CO, leads also to a strongly enhanced abundance of deuterated molecules (see section 2.2.3). N_2D^+/N_2H^+ column density ratios up to 0.44 have been measured (Crapsi et al. 2005), which is about 4 orders of magnitudes above the elemental D/H ratio of $1.5 \cdot 10^{-5}$ (Oliveira et al. 2003). The local N_2D^+/N_2H^+ abundance ratio gets as high as 0.7 (Pagani et al. 2007). Enhanced abundances of deuterated ammonia (NH_2D/NH_3=0.5, Crapsi et al. (2007)) and DCO^+ ($DCO^+/HCO^+ \simeq 0.042$, Butner et al. (1995)) have been detected, too. Deuterated isotopologues of H_3^+, which play a crucial role in the deuteration of most molecules, have been also observed in prestellar cores (Caselli et al. 2003, Vastel et al. 2004, Vastel et al. 2006).

Protostellar Cores

During the subsequent protostellar phase not only densities and temperatures change but chemical evolution takes place, too. This chemical evolution during the protostellar collapse has been modeled recently by Lee et al. (2004). The dynamical model they used was an inside-out collapse model (Shu 1977), including dust continuum radiative transfer. Their chemical model includes gas-phase chemistry and freeze out onto, and desorption from grain surfaces. They followed a gas parcel through the entire phase of the collapse, including the *prestellar* phase to account for the depletion of molecules containing heavy elements during this phase, and calculated abundance profiles for the most important molecules. In Fig. 2.3 the abundance profile of six molecules are shown 10^5 years after the collapse has started.

From Fig. 2.3 one can see that the CO abundance plays a major role in the entire chemical network. Whereas CO is largely depleted at the center of prestellar cores, the embedded protostar has warmed up the envelope of the protostar already a little bit, and thus CO is desorbed from the grains again. The radius to which CO comes off of the grains depends on the temperature and increases with time. At this depletion radius, the CO abundance drops by a few orders of magnitude. Further outwards it increases slowly again.

It is not surprising that the HCO^+ abundance follows the abundance of CO, since HCO^+ is formed directly from CO. The only difference of the CO and the HCO^+ abundance is that HCO^+ gets less abundant towards the center. The N-bearing species N_2H^+ and, less pronounced, NH_3 are showing a kind of 'negative pattern' to the CO abundance. The central part is largely devoid of those molecules, but as soon as CO depletes the abundances of N-bearing species increases by 1-2 orders of magnitude. The reason for this behavior is that CO destroys N_2H^+ quite efficiently and hampers

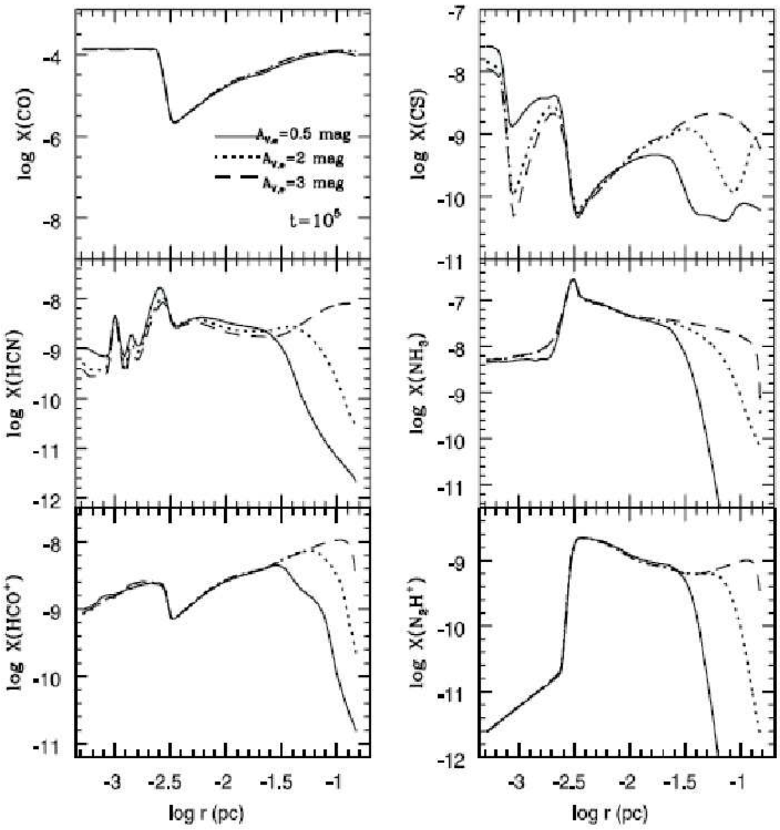

Fig. 2.3: *Abundance profiles of six molecules in a Class 0 protostar* 10^5 *years after the collapse has started. The Figure is taken from Lee et al. (2004).*

the formation of Ammonia. The abundance variations of CS and HCN are a more complex, since these species suffer from depletion as well.

The abundances of more complex molecules in protostars, such as CH_3OH and dimethyl ether, have been modeled by Aikawa et al. (2008). In their results, these complex molecules are frozen out in most part of the protostellar envelope. Only in the central part the complex molecules are in the gas phase, again due to the heating by the embedded protostellar core. Thus the results of Aikawa et al. (2008) and Lee et al. (2004) agree fairly well.

2.3 Massive star formation

2.3.1 The process of high mass star formation

For stars with final masses above about 8 $M_\odot$ the formation occurs in a different way than in low mass stars (Evans 1999). The first difference is that high mass stars reach the main sequence (MS) before their envelope has dissipated. This means, that the embedded star has already reached equilibrium, whereas the overall protostellar core is still in a stage equivalent to a Class I object in low mass star formation. Furthermore, the high luminosity of massive stars (the luminosity of a 10 $M_\odot$ star is about 3000 $L_\odot$) causes a considerable amount of radiation pressure, which counteracts accretion. The condition, which has to be fulfilled to allow accretion, is conveniently written as the ratio of inward and outward acceleration Γ (Wolfire & Cassinelli 1987).

$$\Gamma = \frac{\kappa_H L}{4\pi c G M(r)} \leq 1, \tag{2.24}$$

where κ_H is the radiation pressure coefficient per unit mass, M(r) the mass within the outer boundary of the flow R and L the total luminosity of the star. Hence Γ depends only on the dust properties and the L/M ratio. It should be noted that the L/M ratio is not the luminosity to mass ratio of the ZAMS, because additional luminosity from shocks and the mass of the envelope has to be included as well. Kahn (1974) calculated an upper mass limit of 40 $M_\odot$ of a star formed by accretion, but this result is very sensitive to the dust properties. Wolfire & Cassinelli (1987) recalculated the accretion onto a 60 $M_\odot$ star and found that the dust abundance has to be lower than 25% of the standard dust/gas ratio from Draine & Lee (1984). More recent two- and three-dimensional simulation of massive star formation showed that the mass limit, which can be gained by accretion, is higher, if the material is accrete through a disk. Yorke & Sonnhalter (2002) calculated an upper mass limit of 43 $M_\odot$, whereas Banerjee & Pudritz (2007) concluded, that even the most massive star (up to 100 $M_\odot$) can be formed by accretion.

An alternative theory of high mass star formation proposes that stars with mass $\geq$ 10 $M_\odot$ are formed by collisional coalescence of low and intermediate mass stars (e.g., Bonnell et al. 1998). This theory also explains why massive stars are hardly found to be isolated and predominately located in the center of stellar clusters (Zinnecker et al. 1993). High stellar densities of $\sim 10^4$ stars pc^{-3} are required for collisional coalescence to be effective. Such densities are typical for the central region of such clusters. Theoretical calculations of Bonnell et al. (1998) show that a 50 $M_\odot$ star can be built up in $5 \cdot 10^5$ years. The formation of a 50 $M_\odot$ star would require about 60-80 collisions of low and intermediate mass stars.

2.3.2 Interaction with surrounding material

Not only the way massive stars are formed differs from low mass stars, also their interaction with the environmental material is different. As we have seen above stars with masses above 8 $M_\odot$, i.e., O and B stars, reach the MS before the envelope has dissipated, and thus these stars are often deeply embedded in their parent cloud. In addition these stars are so hot, that they emit a significant amount of photons with energies above 13.6 eV (Lyα-photons). Furthermore most of the hydrogen in the stellar atmosphere is ionized and thus the Lyα-photons can escape, leading to the ionization of the surrounding material.

In the following I will not explain the physical processes leading to and occurring in HII-regions and photo dominated regions (PDRs), but I will only mention some of their physical properties. General references are e.g., Osterbrock & Ferland (2006) for HII regions and e.g., Hollenbach & Tielens (1997) for PDRs, respectively.

HII region

O and B stars, which are embedded into a gaseous cloud, are surrounded by an ionized region, a so-called HII region. Its size depends on the density structure of the environmental cloud as well as on the number of Lyman photons (photons with energies above 13.6 eV) emitted by the star(s). Density bounded HII region, i.e., HII regions whose size is limited by a decrease of the overall density shows rather fuzzy boundaries, whereas radiation bounded HII regions are confined by a sharp edge, the so-called Strömgren radius (Strömgren 1939). The electron temperature of most HII region is in the order of 5000 K and 15000 K. The electron temperature of an HII region is not controlled by the ionizing spectrum, but depends predominately on the abundance of heavy elements, especially oxygen (Shaver et al. 1983), since [OIII] lines at $\sim 5000\ \AA$ are strong cooling lines. The electron density of these HII regions is typically in the order of $10^2 - 10^3$ cm^{-3} (Odegard 1985).

Optically visible HII regions, e.g., M 42, are necessarily located at the nearside of the molecular cloud. Zuckerman (1973) argued, that the ionizing star of such a region causes an ionization front, which slowly expands into the molecular cloud. Due to the large pressure gradient at the HII region/molecular cloud interface (the particle density is increased by a factor ~ 4, the temperature rises by a factor of ~ 100), the ionized gas expands into the diffuse, low-density medium. Since the shape of the HII region reminds on a blister on the skin of a molecular cloud it is referred to as the "blister model" (Israel 1978). One prediction of the blister model is, that the lines of the HII region are at more negative velocities than the observed lines originating from the molecular cloud. Israel (1978) found indeed, that $\Delta v(\mathrm{HII}-\mathrm{CO}) = -3.4 \pm 0.4$ km/s for optically visible HII region, whereas for obscured HII region, no significant line shift could be found ($\Delta v(\mathrm{HII}-\mathrm{CO}) = -0.5 \pm 0.4$ km/s).

Photo Dominated Region

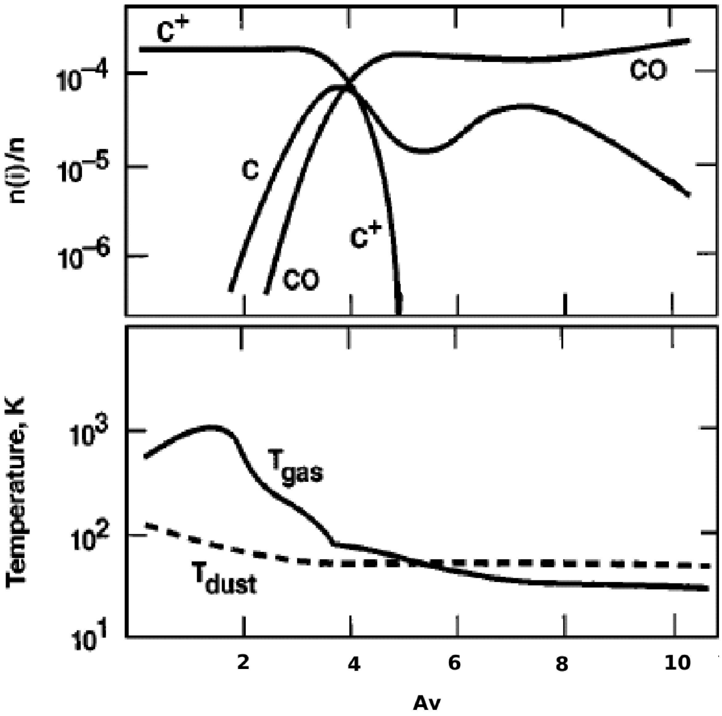

Fig. 2.4: *Structure of a PDR as a function of A_V from Tielens & Hollenbach (1985). The abundance of the most important carbon species (upper panel) and the dust and gas temperature (lower panel) are shown. This figure has been adapted from Hollenbach & Tielens (1997)*

Although almost all Lyman photons are absorbed within the Strömgren sphere, material beyond the Stömgren radius is still exposed to UV-photons with energies < 13.6 eV. The physical and chemical processes, which are going on in such regions are described by PDR models (Röllig et al. 2007, and references therein). The key parameter for the understanding of a PDR is the penetration of the UV radiation, which is determined by absorption and scattering at dust particles. The local dust and gas temperatures are calculated using a detailed heating and cooling balance. The amount of UV radiation determines also the abundances of the various molecular, atomic and ionic species, either immediately by radiative dissociation or indirectly via the temperature.

In Fig. 2.4 the abundances of C^+, C and CO, the dust temperature and the gas temperature as calculated by Tielens & Hollenbach (1985) are shown. At the surface of the PDR the gas can get as hot as 1000 K, but it declines with A_V. In this surface region, the biggest part of carbon in the gas-phase is stored in the form of C^+. After a transit region, at which atomic carbon becomes abundant, most carbon is store in CO, which becomes abundant at $A_V > 3$. At these A_V value the gas temperatures are about 250 K, but it is dropping quickly below 100 K.

3 The importance of THz lines in star forming regions

As already mentioned in chapter 1, observation in the THz regime are rare, because of a.) receivers for such frequency are very challenging to build and b.) the atmospheric transmission is very low. One receiver, which is built for observation from 1.2 to 1.5 THz, is CONDOR (Wieching 2006, see chapter1). Because the science, which can be done with CONDOR, was the starting point of this work, I will give a short introduction into the atmospheric transmission at frequencies around 1.4 THz, and the observable lines in this regime.

3.1 Atmospheric transmission

At frequencies above 1 THz, the terrestrial atmosphere is almost opaque. Only under excellent weather conditions and the best sites for sub-millimeter astronomy, ground based observations are, although still with very low transmission, possible. Two of these windows, which are centered at 1.3 THz and 1.5 THz, are in the range of the CONDOR receiver. To explain this low transmission several models, based on theoretical calculations and comparison with observations have been developed (e.g. Pardo et al. 2001, Pardo et al. 2004).

The most important parameter for determining the atmospheric transmission is the water content, measured as precipitable water vapor (pwv, given in mm). Water causes absorption in broad band (e.g., the absorption band centered at 1.4 THz in Fig. 3.1). O_3, which shows quite narrow features, because it exists predominantly in the high atmosphere, and O_2 and N_2, which are the main constituents of the atmosphere, have to be considered, too. However, contrary to the later species the pwv is highly time variable, and thus the crucial parameter for atmospheric calibration. The atmospheric transmission at frequencies below 1 THz can be explained sufficiently purely by the line absorption of these molecules, but at higher frequencies an additional, continuum like absorption is needed. The reason for this continuum like absorption is still under debate. It is believed to be caused by the H_2O pseudo-continuum, due to the far wings of water lines, but also collision induced absorption due to transient electric dipole moments generated during binary interaction of symmetric molecules and relaxation absorption of O_2 has been suggested (Pardo et al. 2001).

In Fig. 3.1 I show the atmospheric transmission from 1.2 THz to 1.6 THz for two different precipitable water vapor (pwv) values. The black line represents a 0.3 mm pwv atmosphere, which can be found only at high altitude and very try places, such as the Atacama Desert in Chile. The red spectrum shows the transmission for a 1 mm pwv atmosphere, which is generally considered as good weather conditions for sub-millimeter observations. Even under excellent weather conditions the atmospheric

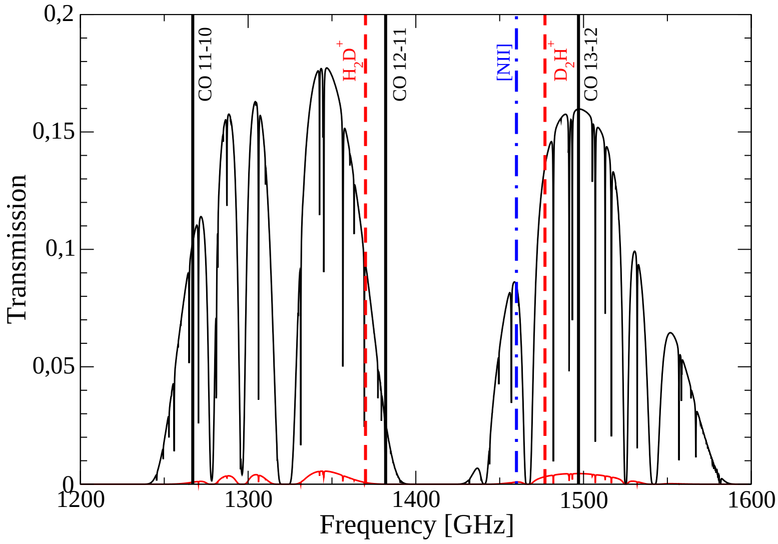

Fig. 3.1: *Atmospheric transmission versus frequency around 1.4 THz, obtained from the CSO Atmospheric Transmission Plotter*[3]*. The black spectrum represents an atmosphere with 0.3 mm pwv, the red spectrum represents an atmosphere with 1 mm pwv. The vertical lines indicate the frequencies of the most important lines in these atmospheric windows. Black (solid): high-J* ^{12}CO*, red (dashed): deuterated* H_3^+*, blue (dashed-dotted): [NII].*

transmission is ~ 15%. Therefore it is very hard to conduct ground-based observations in the THz regime. The vertical lines show the frequencies of astronomically interesting emission lines in this frequency regime (see below).

3.2 Important emission lines in the 1.3-1.5 THz window

The astrophysically interesting lines in the atmospheric windows, which are observable with the CO N^+ Deuterium Observation Receiver, are, as already indicated by the name of the receiver, rotational transitions of CO, fine structure lines of N^+ and ground state transitions of H_2D^+ and D_2H^+. In the following paragraphs I will give a short overview of these lines and the physical conditions, which are required to excite them. In Addition short analyses of a few observations are given.

3.2.1 High-J ^{12}CO lines

In the 1.3 THz and the 1.5 THz atmospheric windows, which both are observable with CONDOR, lie the three ^{12}CO lines with the rotational transitions: J=13-12, J=12-11, J=11-10. The J=12-11 line, however is at an unfavorable frequency, because of a water absorption band at 1.4 THz (see Fig. 3.1). The line parameters are listed in Tab 3.1.

Tab. 3.1: *Frequencies, energies of the upper levels, Einstein-A-coefficients, and critical densities for the three ^{12}CO lines observable with CONDOR.*

	ν [GHz]	E_{up} [K]	A [s^{-1}]	n_{crit} [cm^{-3}]
J=11-10	1267.014	364.97	$1.42 \cdot 10^{-4}$	$9.90 \cdot 10^{6}$
J=12-11	1381.994	431.20	$1.85 \cdot 10^{-4}$	$1.35 \cdot 10^{7}$
J=13-12	1496.923	503.13	$2.36 \cdot 10^{-4}$	$1.86 \cdot 10^{7}$

Because of the high energies of the J_{up} levels as well as the high critical densities (see section 4.3.1) high-J CO lines can be emitted only from hot ($T > 100$ K) and dense ($n \sim 10^{5.5}$ cm^{-3} or higher) molecular gas. The same is shown in more detail in Fig. 3.2, where the emissivity of the ^{12}CO 13-12, normalized to one, is displayed as a function of temperature and density. Only from gas with $T > 100$ K and $n > 10^{5.5}$ cm^{-3} a significant amount of ^{12}CO 13-12 emission originates. Therefore, the high-J CO lines are ideally suited to trace the hot dense gas without any contribution from cooler parts of the cloud. Gas, which emits high-J CO lines must be heated either by photons, e.g., in a PDR or an XDR, or by shocks, two phenomena, which take place in star forming region. Velocity resolved observations, which are possible with CONDOR, allow to distinguish between the two mechanisms. A narrow line width, for example, indicates that the emitting gas is heated by photons.

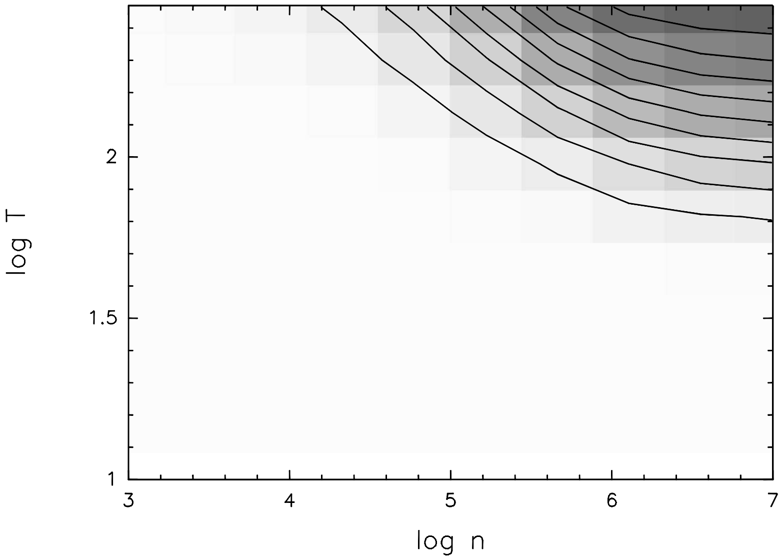

Fig. 3.2: *CO J=13-12 emissivity, normalized to one, as a function of temperature and H_2 density. The temperatures and densities plotted here are typical for molecular gas.*

Measurements of the integrated intensity of CO $J_{up} > 13$ with the Infrared Satellite Observatory (ISO), showed, that in low mass protostars the maximum line flux is emitted from CO lines in-between 1 and 2 THz (e.g., Giannini et al. 2001). Therefore the high-J CO lines are very important for the energy balance of protostellar cores as well.

For this thesis high-J CO lines were observed in several objects. In the following subsection I will summarize the ^{12}CO 13-12 observations in Orion FIR 4; in section 4 those of NGC 2024 are presented.

^{12}CO 13-12 observations of Orion FIR 4

Using the CONDOR receiver on the APEX telescope, we observed Orion FIR 4 ($RA_{J2000} = 5^h35^m13.41^s$, $Dec_{J2000} = -5°24'11.3''$). These observations were conducted on 2005 November 20, with the same setup as used for the observations in NGC 2024 (see section 4). Orion FIR 4 is suggested to be a high mass protostar as observations of far infrared fine-structure lines revealed a 300-500 K hot component with a density of $n(H_2) = 3 \cdot 10^5$ cm^{-3} (Herrmann et al. 1997) and broad line width have been observed (Mundy et al. 1986). Furthermore is Orion FIR 4 at the vertex of several outflows with velocity differences up to $\pm 15\ km/s$ (Schmid-Burgk et al. 1990).

The observed ^{12}CO 13-12 spectrum is shown in Fig. 3.3, left panel. For comparison the ^{12}CO 7-6 line, observed by Wilson et al. (2001) is displayed as well. A Gaussian fit to the ^{12}CO 13-12 line yield a peak T_{mb} of 210 K, a v_{LSR} of 9.0 ± 0.1 km/s and a Δv of 5.4 ± 0.3 km/s. For the conversion to T_{mb} we assumed a source coupling efficiency of 0.09, which has been measured on Mars. On the Moon, however, we measured a source coupling efficiency of 0.4. Therefore the coupling efficiency of Orion FIR 4 is uncertain and the given T_{mb} is an upper limit; the lower limit is $T_{mb} = 48$ K. A more detailed discussion of the source coupling efficiencies is given in section 4.2.1. The width of the ^{12}CO 13-12 line is narrower than the width of the ^{12}CO 7-6 line (5.4 km/s and 6.7 km/s, respectively), indicating that ^{12}CO 13-12 is emitted from a quiescent component. This narrow line width suggests that the gas is heated by photon rather than by shocks. Furthermore the ^{12}CO 7-6 line consists of two velocity components at 6 km/s and 9 km/s, respectively, whereas in the ^{12}CO 13-12 spectrum only the component at 9 km/s can be seen.

We modeled the physical properties of the hot gas in Orion FIR 4 using an escape probability code developed by Stutzki & Winnewisser (1985) (see section 4.3.1). This code calculates the optical depth at the line center, T_{mb} and the integrated intensity for a given line width, kinetic temperature, H_2 density and ^{12}CO column density. In this analysis we included next to the ^{12}CO 13-12 line also the integrated intensities of J=6-7 (Wilson et al. 2001), J=9-8 Kawamura et al. (2002), and integrated intensities of the transitions with J_{up} from 14 to 17, which have been observed at low spectral resolution with the ISO satellite (Sempere et al. 2000). According to our observations, we assumed a line width of 5 km/s and we used only the contribution of the 9 km/s component of the velocity resolved J=9-8 and J=7-6 transitions. The

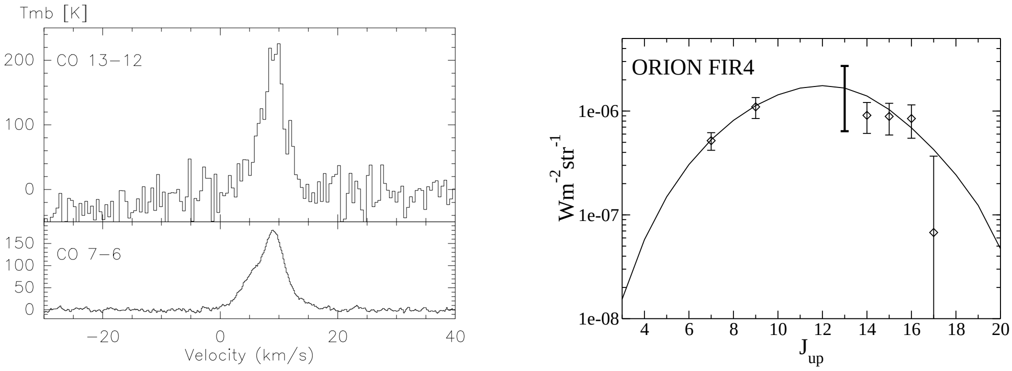

Fig. 3.3: **Left:** *Spectra of* ^{12}*CO* 13 – 12 *(with CONDOR) and* ^{12}*CO 7-6 (Wilson et al. 2001) of Orion FIR 4.* **Right:** *Fluxes of the mid-J and high-J CO transitions from Orion FIR 4. The solid line represents the best fit model. The thick bar shows the CONDOR observations.* ^{12}*CO 7-6 (Wilson et al. 2001),* ^{12}*CO 9-8 (Kawamura et al. 2002) and CO lines with* $J_{\rm up} > 13$ *(Sempere et al. 2000) are taken from literature.*

observed intensities and those of the best fit model are shown in Fig. 3.3, right panel. The best fit model corresponds to $T_{\rm kin} = 380 \pm 70$ K, $n(H_2) = 1.6 \pm 0.7 \cdot 10^5$ cm^{-3} and $N(CO) = 6.4 \pm 2.0 \cdot 10^{17}$ cm^{-2}. For this model, we assumed that the ISO beam is fully filled. If the filling factor of the ISO observations is lower, we calculated with values down to 0.1, the best fit density goes up to $5 \cdot 10^5$ cm^{-3}, but $T_{\rm kin}$ and N(CO) stay approximately constant. This result shows that the high-J CO lines are an excellent tool to study hot molecular gas.

3.2.2 Para-H_2D^+ and Ortho-D_2H^+ ground state transition

The two lines of deuterated H_3^+, which are observable with CONDOR, are H_2D^+ $1_{01} - 0_{00}$ and D_2H^+ $1_{11} - 0_{00}$. These lines are the ground state transitions of p–H_2D^+ and o-D_2H^+. The importance of H_2D^+ and D_2H^+ for deuterium chemistry has already been noted in section 2.2.3. Furthermore, these molecules are the only species that do not suffer from freeze-out, but are only abundant in regions were other tracers are depleted. Thus H_2D^+ as well as D_2H^+ are appropriate tracers for the deeply embedded parts of dark cloud cores. Furthermore the ortho/para ratio of H_2D^+ is a very interesting parameter, because it reflects the o/p ratio of H_2, and therefore traces indirectly the H_2 formation rate at low temperatures (Pagani et al. 1992, Le Bourlot 1991). Unfortunately, all energetically low lying transitions of these species are at frequencies where the Earth atmosphere has a poor transmission. The level diagram of the ortho- and para ground state transitions of $H_2D^+$and D_2H^+ (Fig 3.4) shows, that the frequencies of two lines (p-H_2D^+ and o-D_2H^+) are in the THz regime. But also the atmospheric transmission at 692 *GHz* (p-D_2H^+) and 372 *GHz* (o-H_2D^+), which is at the edge of an atmospheric water line, are unfavorable. Furthermore, because of the unknown ortho/para ratio of these species, a detection of both emission lines would be required for each molecule to be able to determine the abundances more reliably.

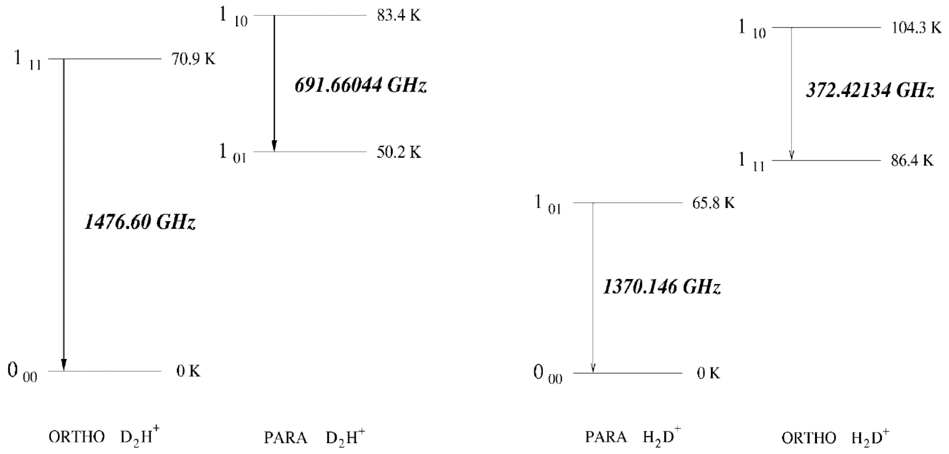

Fig. 3.4: *Level diagrams of the ground state transition of o-D_2H^+, p-D_2H^+, p-H_2D^+ and o-H_2D^+. This figure is taken from Vastel et al. (2004).*

The first detection of o-H_2D^+ in space was conducted by Stark et al. (1999). Since than (probable) detections of H_2D^+ has been reported in about a dozen other sources as well (e.g. Caselli et al. 2003, Hogerheijde et al. 2006, Cernicharo et al. 2007, Asensio Ramos et al. 2007). Emission of p-D_2H^+, however, has been detected only once so far (Vastel et al. 2004).

The difficulty of observing the THz lines of H_2D^+ and D_2H^+ is that deuterated H_3^+ exists only at temperatures $< 20\ K$, but the upper state is $\sim 70\ K$ above zero. Thus the upper state is poorly populated. Furthermore, the Einstein A coefficient is quite high ($A = 4 \cdot 10^{-3}\ s^{-1}$, for the p-$H_2D^+$ line), so that high densities are required to excite these lines, too. Assuming an optical depth of one and an excitation temperature of 20 K, which are already very favorable conditions, $T_B(H_2D^+) = 1.6$ K. The typical temperature for dark cloud cores, however, is rather 10 K, which would result in a T_B of 0.06 K. Therefore, detecting the p-H_2D^+ and o-D_2H^+ ground-state transition in emission is very challenging. Observations in absorption seem to be much more promising. However, one tentative detection of p-H_2D^+ in absorption towards the bright continuum source IRc2, is the only observation of the p-H_2D^+, reported so far (Boreiko & Betz 1993).

First attempts to constrain the ortho/para ratio of H_2D^+

A tentative detection of p-H_2D^+ at $\lambda = 1370\ GHz$ in absorption has been reported by Boreiko & Betz (1993) towards the infrared bright source Orion-IRc2. They see a $0.51 \pm 0.13\ K$ absorption feature in a 3.2 K continuum background ($T_{rec}\ scale$), leading to a minimum optical depth of 0.16. The integrated intensity is $1.8 \pm 0.4 \cdot 10^{-8}$ $Wm^{-2}sr^{-1}$, and thus Boreiko & Betz (1993) come up with a p-H_2D^+ column density in the ground-state of $4.4 \pm 0.9 \cdot 10^{13}$ cm^{-2}.

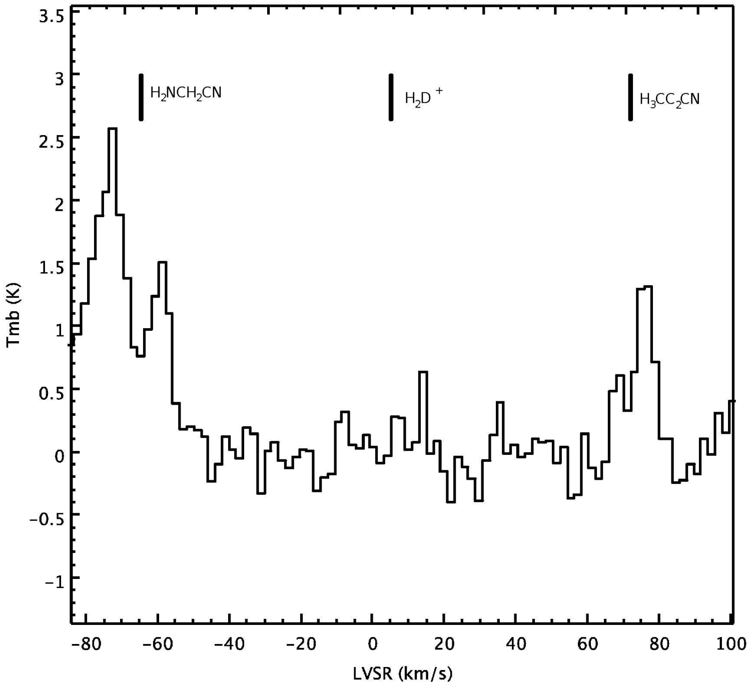

Fig. 3.5: *Spectrum of IRc2 at 372 GHz. The detected lines are most likely* H_2NCH_2CN *and* H_3CC_2CN*, both emitted from the hot core. The o-*H_2D^+ *ground-state transition has not been detected* ($\sigma = 0.16$ *K*)

I tried to observe the o-H_2D^+ ground-state at the same position using the James Clerk Maxwell Telescope (JCMT) on Mauna Kea, Hawaii. The observations were conducted in April 2007 with the HARP-B 16 pixel receiver array and the ACSIS autocorrelation spectrometer. The half power beam width (HPBW) at this frequency is 13.5″ and I used an aperture efficiency of 0.56 to correct for T_{MB}.

Unfortunately I did not detect any H_2D^+ line in IRc2. The spectrum is shown in (Fig. 3.5). The two lines at $v_{LSR} = -64$ km/s and $v_{LSR} = 72$ km/s are emitted by complex organic molecules, most likely H_2NCH_2CN and H_3CC_2CN, respectively. Both lines are expected to stem from IRc2 itself, indicating that the pointing was okay. The upper limit for the H_2D^+ $1_{10} - 1_{11}$ line, which is expected at a velocity of ~ 7 km/s, is 0.45 (3σ). The continuum background of IRc2 at $\lambda = 790$ μm, which is 379 GHz, is 2.2 K (White & Sandell 1995). The maximum optical depth of H_2D^+ can be determined by

$$\tau_{max} = -ln\left(1 - \frac{\Delta T_{mb}}{J(T) - J(T_{bg})}\right), \tag{3.25}$$

where ΔT_{mb} is the 3σ noise level of the observations, $J(T) = [h\nu/k]]/[exp(h\nu/kT) - 1]$ and T_{bg} is the background continuum. This results in an upper limit for the o-H_2D^+ column density of

$$N_{max} = \frac{8\pi^{3/2}\Delta\nu}{2\sqrt{ln\,2}\lambda^3 A} \cdot \frac{g_l}{g_u} \cdot \frac{\tau_{max}}{1 - exp(-h\nu/kT)} \cdot Q_{o-H_2D^+}. \tag{3.26}$$

$Q_{o-H_2D^+}$ is the partition function of ortho H_2D^+, and $\Delta\nu$ its line width. I assumed that $\Delta\nu$ of o-H_2D^+ is similar to the line width of p-H_2D^+. Using the column density of p-H_2D^+, given by Boreiko & Betz (1993), I calculated the upper limits for the ortho/para ratio of H_2D^+ as a function of the temperature (Fig 3.6).

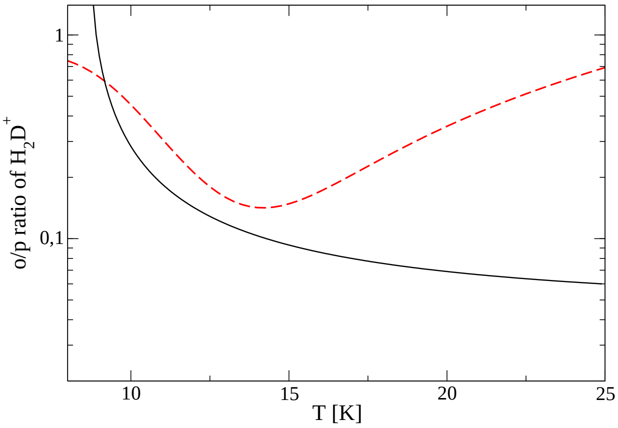

Fig. 3.6: *The upper limit of the o/p ratio of H_2D^+ as function of the temperature (black solid line). For comparison the modeled o/p ratio is plotted as well (red dashed line).*

At temperatures below 10 K no sensitive upper limit can be determined because of the strong background source. For temperatures above 10 K, the measured upper limit of the ortho/para ratio of H_2D^+ is clearly lower than the model prediction of Flower et al. (2004). However, this result is based on a tentative detection and a non-detection, and thus not very reliable.

3.2.3 [NII] Fine structure Line

In the ground-state the ^{3}P orbital contains two electrons, which have according to Hund's rule a total electron spin of one. Thus the ^{3}P orbital splits up into three individual states with total angular momentum (J) of 0, 1 and 2, which are separated by 6.0 meV (J=1 to J=0) and 10.2 meV (J=2 to J=1). The respective emission lines have wavelengths of $\lambda = 122\ \mu$m ($\nu = 2.46$ THz) and $\lambda = 205\ \mu$m ($\nu = 1460$ GHz, which is well observable with CONDOR).

Observations with the *COBE* satellite revealed that the 205 μm [NII] line is, next to the [CII] line at 158 μm and the [NII] line at 122 μm, the strongest emission line in our Galaxy (Fixsen et al. 1999). [NII] is observable over most of the sky. Towards the galactic center it reaches an intensity of 12 $nW\ m^{-2}\ sr^{-1}$ in a 10° beam. A comparison with the [NII] line at 122 μm ($\frac{I(122\ \mu m)}{I(205\ \mu m)} \sim 1$) suggests that most of the [NII] is emitted from low density material. However the *COBE* observations of [NII] at 122 μm suffer from a high noise level and thus do not allow a detailed comparison. Hence it is still under debate which fraction of the [NII] lines stems from warm ionized medium (WIM) at low densities and which fraction from classical HII regions.

As already mentioned above, the ratio $\frac{I([NII]\ 122\mu m)}{I([NII]\ 205\mu m)}$ can be used to derive the electron density of ionized gas (Rubin et al. 1994). The energy of the upper states differ by 118 K, which is small compared to the 10^4 K typical for ionized gas. Therefore the relative population of the upper energy states depends only marginally on the temperature. The Einstein A coefficient are $7.4 \cdot 10^{-6}\ s^{-1}$ and $2.1 \cdot 10^{-6}\ s^{-1}$ for the 122 μm line and the 205 μm line, respectively, and thus the critical densities differ by a factor of 3.5. This causes a strong dependency of the relative population of the upper state, and thus a strong dependency of the line ratio, on electron density. The results of a detailed calculation by Rubin et al. (1994) are shown in Fig. 3.7.

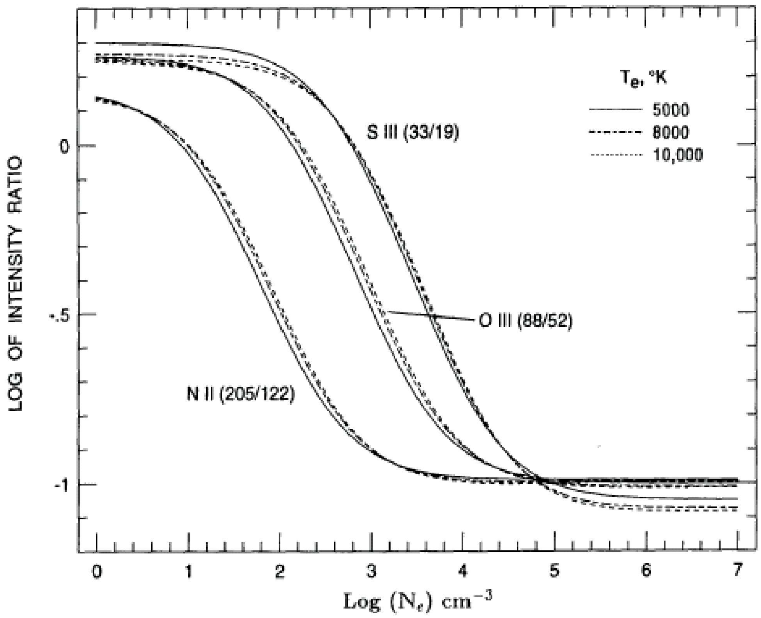

Fig. 3.7: *The intensity ratios of ^3P (J=2-1) to ^3P (J=1-0) is shown as a function of the electron density for temperatures of 5000 K, 8000 K and 10000 K. The intensity ratios of the electronically similar systems of [OIII] and [SIII] are also shown. This figure is taken from Rubin et al. (1994).*

The [NII] lines can be used to study ionized gas in the warm ionized medium (WIM) and in HII region, even if they are deeply embedded. Furthermore, the [NII] lines are an important complimentary observation to [CII] ($\lambda = 158\ \mu m$), a very important coolant in PDRs. Because nitrogen has an ionization potential of 14.5 eV (0.9 eV above the ionization potential of hydrogen) it traces only gas, which is ionized by soft UV radiation ($E_\nu < 29.6\ eV$). If hard UV radiation is present nitrogen gets multiply ionized. Ionized carbon ($E_{ion.} = 11.3\ eV$), however, is also present in warm neutral environments, such as PDRs. Observing both, [NII] and [CII] simultaneously allows to determine the fraction of the [CII] emission from the HII region, and thus its contribution to the energy balance of Photo Dominated Regions (PDR).

4 A line-of-sight model of the high mass star forming region NGC 2024

Parts of this chapter have been published in:

- Emprechtinger M., Wiedner, M. C., Simon, R., Wieching, G., et al.
  Warm molecular Gas in NGC 2024
  2008, A&A, submitted

4.1 Introduction

4.1.1 The complex structure of the molecular material in high-mass star-forming regions

High mass star formation occurs in clusters (see section 2.3.2), and thus a simple geometry of such regions is highly unlikely. Furthermore, UV radiation emitted from O and B stars ionizes the cloud partly, and outflows increase the complexity of such regions even more. At the Strömgren radius (Strömgren 1939) the hydrogen becomes neutral and later on molecular, forming a PDR. Because the massive star, which ionizes the hydrogen in the HII region, can be formed anywhere within the parent cloud molecular material can reside on any side of the HII region, but its excitation conditions may differ significantly due to different densities and different remaining UV radiation at the Strömgren radius. This makes interpretation of any observation of such regions challenging, because one has to deal with multiple velocity components and self-absorption.

Observations of CO lines in massive star forming region revealed complex line shapes (e.g., in M 17 Stutzki & Guesten 1990, W3 Kramer et al. 2004 and Mon R2 Giannakopoulou et al. 1997). These line profiles show double peaked structures, absorption notches and asymmetries like shoulders and large wings. In addition the line shape varies significantly with $J_{\rm up}$ and different isotopes, which trace different regimes of optical depth.

With this study we try to disentangle the physical structure of such a complex region and find a model, which explains the shapes and intensities of the observed CO lines consistently. For this we observed five ^{12}CO and two ^{13}CO transition ranging from $J_{\rm up}$ = 3 to 13 in NGC 2024, a massive star forming region in Orion. In Addition we included the integrated intensities of ^{12}CO $J_{\rm up}$ = 14 to ^{12}CO $J_{\rm up}$ = 17, observed with the ISO satellite (Giannini et al. 2000). The model, which we calculated, is based on the well established physical scenarios of the ”Blister model” and PDR models (see chapter 2). Using radiative transfer codes we tried to reproduce the observed CO lines.

4.1.2 NGC 2024

The massive star forming region NGC 2024 consists of an HII region and its associated molecular cloud, which is located at a distance of 415 pc (Anthony-Twarog 1982). It is part of Orion B, a very well studied Giant molecular cloud (e.g., Maddalena et al. 1986, Lada et al. 1991, Kramer et al. 1996, Mitchell et al. 2001).

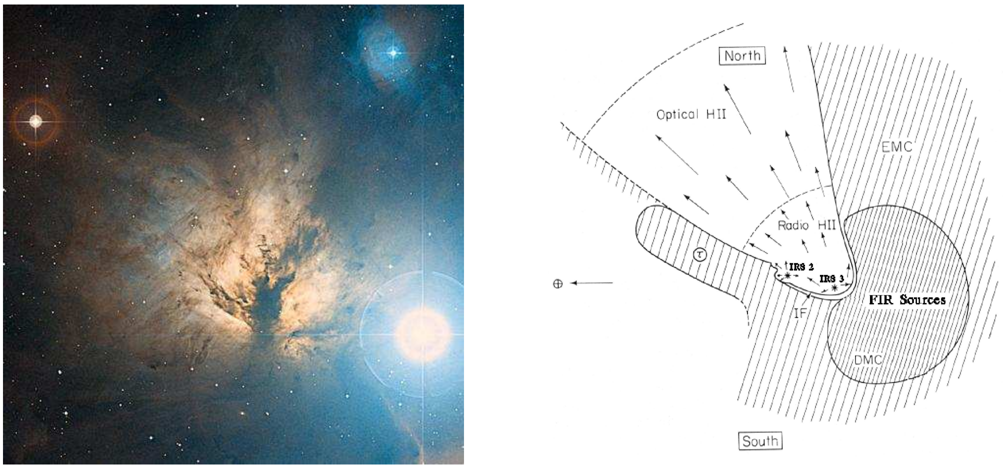

Fig. 4.1: **Left:** *Optical image of NGC 2024 from the Hubble Space Telescope. In contrast to the bright HII region the optical dust bar can be seen as dark ridge.* **Right:** *Schematic view of the geometry of NGC2024. Abbreviations are as follows: DMC = dense molecular cloud, EMC = extended molecular cloud, IF=ionization front and τ = high optical depth cloud (optical dust bar). Adapted from Barnes et al. (1989) by Giannini et al. (2000).*

A possible scenario for the three dimensional structure of the NGC 2024 region was proposed by Barnes et al. (1989), who combined observation from optical to radio wavelengths to construct a model of the cloud (Fig. 4.1). In their model, the HII region sits in front of the bulk of the cloud but is partly obscured in the optical by a very prominent ridge of high optical depth material. This intricate geometry provides an explanation for the complex line shapes, which may include contributions from fore- and background regions and are also subject to self-absorption. The ionizing sources of NGC 2024 are invisible at optical wavelengths because they are obscured by the dust ridge. IRS2 b, a late O or early B star, has been identified as the main ionizing source of NGC 2024 by observations in the near infrared (Bik et al. 2003). The optical depths through the dust ridge along lines-of-sight to stars inside the HII region in the range from 15 to 25 mag. Furthermore, the HII region is expected to expand into the molecular cloud and triggers star formation. Indeed some protostellar condensations (FIR 1 to 7) have been detected close to the HII region (Mezger et al. 1988, 1992). Their masses, derived from sub-millimeter continuum emission, range from 1.6 to 5.1 $M_\odot$ (Visser et al. 1998). These masses correspond to visual extinctions of 270 mag and 870 mag, and thus it is very likely that these condensations are located in the dense molecular cloud (DMC) behind the HII region. Furthermore massive outflows have been detected close to the source FIR 5 (e.g., Richer 1990, Sanders & Willner 1985) giving additional evidence for ongoing star formation.

The excitation conditions in the PDR, created by the UV radiation of the stellar cluster and located at the interface of the HII region and the dense molecular cloud (DMC), was studied using far infrared line emission observed with the ISO satellite (Giannini et al. 2000). In addition to observing [NII], [NIII] and [OIII] emission from the HII region, they also observed high-J CO lines, [CII], and [OI], which are expected to originate partly from the PDR. Comparison with the predictions of a PDR model (Burton et al. 1990) revealed a density of $\approx 10^6$ cm^{-3} and a UV field of $3 \cdot 10^4$ G$_0$ at the surface of the PDR.

Detailed investigations of the molecular cloud associated with NGC 2024 were performed by Graf et al. (1990, 1993), who did multi frequency studies of ^{12}CO (up to J=7-6) and its isotopologues. Temperatures of 23.5 K and 67.4 K for the foreground and the background component, as defined by Barnes et al. (1989), respectively, have been derived. The corresponding column densities are $5.4 \cdot 10^{22}$ cm^{-2} (A_v = 56 mag) and $2.0 \cdot 10^{23}$ cm^{-2} (A_v = 210 mag)). The peak velocities of the main component of the ^{12}CO lines v_{LSR} = 13 km/s differ significantly from those of the optical thin lines (e.g., of C^{18}O), which are at a velocity of 11 km/s. This discrepancy leads Graf et al. (1993) to suggest that the blue wings of the ^{12}CO lines are absorbed by the dust bar, which has a velocity of 9 km/s.

The ^{12}CO 7-6 integrated intensity map shows features similar to those seen in the 6 cm continuum map (Crutcher et al. 1986), which traces the ionized gas. This indicates that the ^{12}CO 7-6 mainly originates from the PDR at the surface of the molecular cloud and not from embedded protostellar objects. Contrary to ^{12}CO 7-6, the C^{18}O 2-1 and the C^{17}O 2-1 line, which originate both from regions deeper inside the cloud, peaks close to far infrared sources detected at 1.3 mm continuum (Mezger et al. 1988, 1992) In such a scenario, where the mid- and high-J CO lines stems from the PDR at the interface of the ionized gas ($T_e \sim 7500$ K, Churchwell et al. 1978) and the DMC (T_{kin} of a few tens of K) it is expected that a hot (several hundred K) and dense transient region exists. High-J CO lines trace only such regions, due to their high critical density ($\sim 10^7$ cm^{-2}) and their high energy of the upper level ($E_{up} \geq 250$ K).

4.2 Observation, Data-reduction and Results

4.2.1 Observed Lines

^{12}CO J = 13 – 12

The ^{12}CO 13-12 (ν = 1496.922909 GHz, Müller et al. 2001) observations were carried out on November 22, 2005 at the APEX 12 m telescope (Güsten et al. 2006), Tab. 4.1: *List of the observed CO transitions*

Line	Frequency [GHz]	Telescope	HPBW
^{12}CO 13-12	1497	APEX	4.3″ (80″)
^{12}CO 7-6	807	NANTEN2	23″
^{12}CO 6-5	692	KOSMA	50″
^{13}CO 6-5	661	KOSMA	50″
^{12}CO 4-3	461	NANTEN2	35″
^{12}CO 3-2	346	KOSMA	82″
^{13}CO 3-2	331	KOSMA	82″

located on Llano de Chajnantor, Chile. We used the CO N$^+$ Deuterium Observations Receiver (CONDOR, Wiedner et al. 2006), a heterodyne receivers, which operates at THz frequencies (1.25-1.53 THz). The typical double sideband (DSB) receiver noise temperature was between 1500 K and 1900 K. The mean atmospheric transmission at zenith during the observations was ~ 0.2. As backend, we used the APEX Fast Fourier Transform Spectrometer (FFTS), which has an intrinsic resolution of 60 kHz.

The expected diffraction limited main beam size of a 12 m telescope at 1.5 THz is 4.3″. The accuracy of the surface of the primary dish, derived from planet observations at frequencies between 350 GHz and 1500 GHz (with CONDOR), is 18 μm (Güsten et al. 2006). However, the primary dish of APEX consists of individual panels, which have a much higher surface accuracy of 8 μm, therefore we expect some of the power to be directed into an error beam. We assume that the error beam is approximately 80″, which corresponds to the size of the individual panel of the telescope (~ 70 cm). The source coupling efficiency is defined as

$$\eta_{c,source} = T_A^* \cdot F_{eff} / J(T_{source}) \tag{4.27}$$

where T_A^* is the measured antenna temperature, F_{eff} is the forward efficiency and $J(T_{source})$ is the Rayleigh-Jeans (RJ) temperature of the source, defined as

$$J(T) = \frac{h\nu}{k} \cdot 1/(exp(h\nu/kT) - 1). \tag{4.28}$$

The forward efficiency, determined by sky dips, is 0.8. The source coupling efficiency was determined on Mars ($J(T_{Mars})$ = 204 K) and Moon ($J(T_{Moon})$ = 325 K). The coupling efficiency of the moon was found to be 0.40. Since the Moon (θ_{source} = 0.5°) is bigger than the main beam and the expected error beam, the difference between the forward efficiency and the coupling efficiency cannot be explained by beam dilution. The CONDOR beam illuminates the secondary mirror of the APEX telescope with an edge taper of ~ 16.5 dB, resulting in a theoretical illumination efficiency of ~ 77%. Further losses are due to scattering on the surface. The average surface accuracy (ϵ)

of the individual panels of the APEX telescope is about 8 μm (Güsten et al. 2006). According to the Ruze formula (Ruze 1966)

$$\eta(\lambda) = \eta_0 \cdot exp\left(-\left(\frac{4\pi\epsilon}{\lambda}\right)^2\right) \tag{4.29}$$

this surface inaccuracy leads to losses of $\sim 23\%$. η_0, which includes losses such as the reflectivity, etc., was assumed to be one. These losses (forward efficiency, illumination efficiency of the secondary mirror and scattering on the surface) result in a coupling efficiency of the Moon of 0.47. Considering the simplicity of this estimation and the uncertainties of the individual losses, this agrees quite well to the measured $\eta_{c,Moon}$ of 0.40.

The coupling efficiency of Mars, which had a diameter of 18.2$''$ at this time, was only 0.09-0.12. From the different source coupling efficiencies and the assumptions of the beam sizes given above, we estimated that 80% of the flux of an extended source comes from the error beam, whereas only 20% are gathered from the main beam. In Fig 4.2, the assumed beam shape of CONDOR on APEX is displayed.

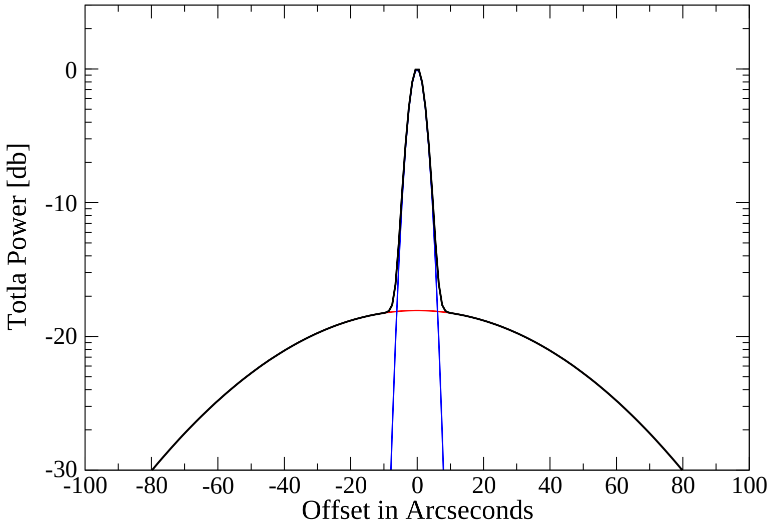

Fig. 4.2: *Assumed beam shape of the CONDOR receiver on APEX.*

Since NGC 2024 is an extended source, clearly larger than the error beam of our observations (Graf et al. 1993, Kramer et al. 1996), we use a coupling efficiency of 0.4.

Pointing and focusing were determined from observations of Mars, and we estimate a pointing accuracy better than 7$''$. We observed ^{12}CO J=13-12 towards five positions, along a cut from FIR 5 via IRS 3 to IRS 2. The coordinates of FIR 5 are $\alpha = 5^h\ 41^m\ 44.18^s$, $\delta = -1^\circ\ 55'\ 38.0''$ (J=2000, Mezger et al. 1988). The offsets of the other positions with respect to FIR 5 are listed in Tab. 4.2.

Tab. 4.2: *Positions of the* ^{12}*CO J=13-12 observations. The (0,0) position is* $\alpha = 5^{\mathrm{h}}\ 41^{\mathrm{m}}\ 44.18^{\mathrm{s}}$*,* $\delta = -1^\circ\ 55'\ 38.0''$ *(J=2000, Mezger et al. 1988).*

Position	$\Delta\alpha$ [$''$]	$\Delta\delta$ [$''$]
FIR 5	0.0	0.0
IRS 3	3.3	16.0
#1	8.8	28.6
#2	13.8	41.9
IRS 2	24.6	68.5

Observations of mid-J CO lines with NANTEN2

Simultaneous observations of ^{12}CO 7-6 ($\nu = 806.65$ GHz) and ^{12}CO 4-3 ($\nu = 461.04$ GHz) were carried out with the NANTEN2 4m telescope at Pampa La Bola, Chile. We obtained a $2' \times 2'$ map, which was centered on NGC 2024 IRS 3. The observations were carried out in December 2007, using the dual-channel 460/810 GHz test receiver, which had DSB receiver temperatures of $\sim$ 750 K and $\sim$ 250 K for the upper and the lower channel, respectively. Two AOS with bandwidths of 1 GHz and channel widths of $\sim$ 560 kHz were used as backends. The beam sizes (HPBW) of the observations were $25''$ and $37''$ for the ^{12}CO 7-6 and ^{12}CO 4-3 observations, respectively. The beam efficiencies are 0.5 and 0.45 for 460 and 810 GHz, respectively, and a forward efficiency of 0.86 was measured at both frequencies. The position of IRS 3 was taken to be $\alpha = 5^{\mathrm{h}}\ 41^{\mathrm{m}}\ 44.40^{\mathrm{s}}$, $\delta = -1^\circ\ 55'\ 22.8''$ (J=2000, Barnes et al. 1989). Pointing was checked on IRc2 in Orion A right before the observations and is expected to have an accuracy of $< 7''$.

Observations of mid-J CO lines with KOSMA

In addition to the ^{12}CO 13-12 transitions, we used archival, so far unpublished, maps of ^{12}CO 6-5 ($\nu = 691.5$ GHz), ^{12}CO 3-2 ($\nu = 345.7$ GHz), ^{13}CO 6-5 ($\nu = 661.1$ GHz) and ^{13}CO 3-2 ($\nu = 330.6$ GHz). The observations were conducted between January 27 and February 2 1998 at the Kölner Obervatorium für Submillimeter Astronomie (KOSMA), located on Gornergrat, Switzerland. The beam sizes (HPBW) of these observations are $\sim 50''$ and $82''$ at 690 GHz and 345 GHz, respectively. To map the central part of the molecular cloud associated with NGC 2024, we used a dual-channel SIS receiver (Graf et al. 1998) with typical DSB receiver noise temperatures of 100 and 400 K for the J=3-2 and J=6-5 lines, respectively. As backends, we used two acousto optical spectrometers (AOS). The Medium Resolution Spectrometer (MRS) has a bandwidth of 0.3 GHz and a resolution of 360 kHz. The Low Resolution Spectrometer (LRS) has a bandwidth of 1 GHz and a resolution of 1150 kHz. The forward efficiency, $F_{\mathrm{eff}} = 0.93$, was determined by skydips. For the J=3-2 observations, we used beam efficiencies (B_{eff}) of 0.59 and 0.62 for the ^{12}CO and the ^{13}CO line, respectively. For the J=6-5 observations, the beam efficiencies were 0.40 and 0.48, respectively.

4.2.2 Observed Spectra

To be able to compare the observed lines with each other, we convolved the maps observed with the KOSMA telescope and the NANTEN2 telescope to a spatial resolution of 80″, which is the spatial resolution of the J=3-2 spectra as well as the approximate size of the error beam of the ^{12}CO 13-12 observations. Since 70%-80% of the radiation is expected to come from the error beam at these high frequencies, we considered 80″ as the spatial resolution of the ^{12}CO 13-12 observations as well.

The spectra are shown in Fig. 4.3; the line parameters are listed in Tab. 4.3. While most of the lines have a Gaussian line profile (^{12}CO 13-12, ^{13}CO 6-5) or only relatively weak blue shifted shoulders (^{12}CO 7-6, ^{12}CO 6-5, ^{13}CO 3-2), the ^{12}CO 4-3 and 3-2 lines show complex line shapes with absorption notches, enhanced emission from the red shifted wing, and an additional bump at ~ 4.5 km/s.

The emission of the J=3-2 and J=6-5 transitions of ^{12}CO and ^{13}CO are fairly uniform in line intensity and shape at all five positions, and the integrated intensity of these lines drops towards IRS 2 only by ~ 30%. This uniformity is expected, since the separation between the positions of FIR 5 and IRS 2 is only 73″, which is on the order of the spatial resolution of the observations. The ^{12}CO 13-12 line peaks towards the southern three positions (FIR 5, IRS 3 and position #1) and declines noticeably towards the north, indicating that high-J CO emission stems from a rather compact region around IRS 3.

Because of the different and complex line shapes of the ^{12}CO and ^{13}CO lines, we give the centroid velocity of the spectra in the following. The velocities of the ^{13}CO lines are ~ 11 km/s, whereas the velocity of ^{12}CO 3-2 and ^{12}CO 6-5 is ~ 12 km/s. The J=13-12 line of ^{12}CO is found at a velocity of ~ 13 km/s, although there is a variation in the velocity of about 1 km/s with position. The velocity of the ^{13}CO lines is uniform throughout all five positions, whereas the velocity of ^{12}CO 3-2 and ^{12}CO 6-5 declines from south to north. This is due to a redshifted outflow detected in these two lines, which is strongest at the southern positions and reaches velocities up to ~ 20 km/s. This outflow was detected previously by Sanders & Willner (1985) and, in agreement with their observations, appears most prominent at southern positions. The lack of a blueshifted wing in our spectra is consistent with previous observations (e.g., Richer 1990 & Richer et al. 1992). One explanation given by Richer et al. (1989) is that the outflow exists in a very complex region close to the ionization front of the HII region. North of its origin lies very dense gas seen in 1.3 mm map (Mezger et al. 1992) and HCO^+ (Richer et al. 1989). Any material ejected by the protostar in this direction might be retarded by dense gas and/or destroyed by strong UV-radiation.

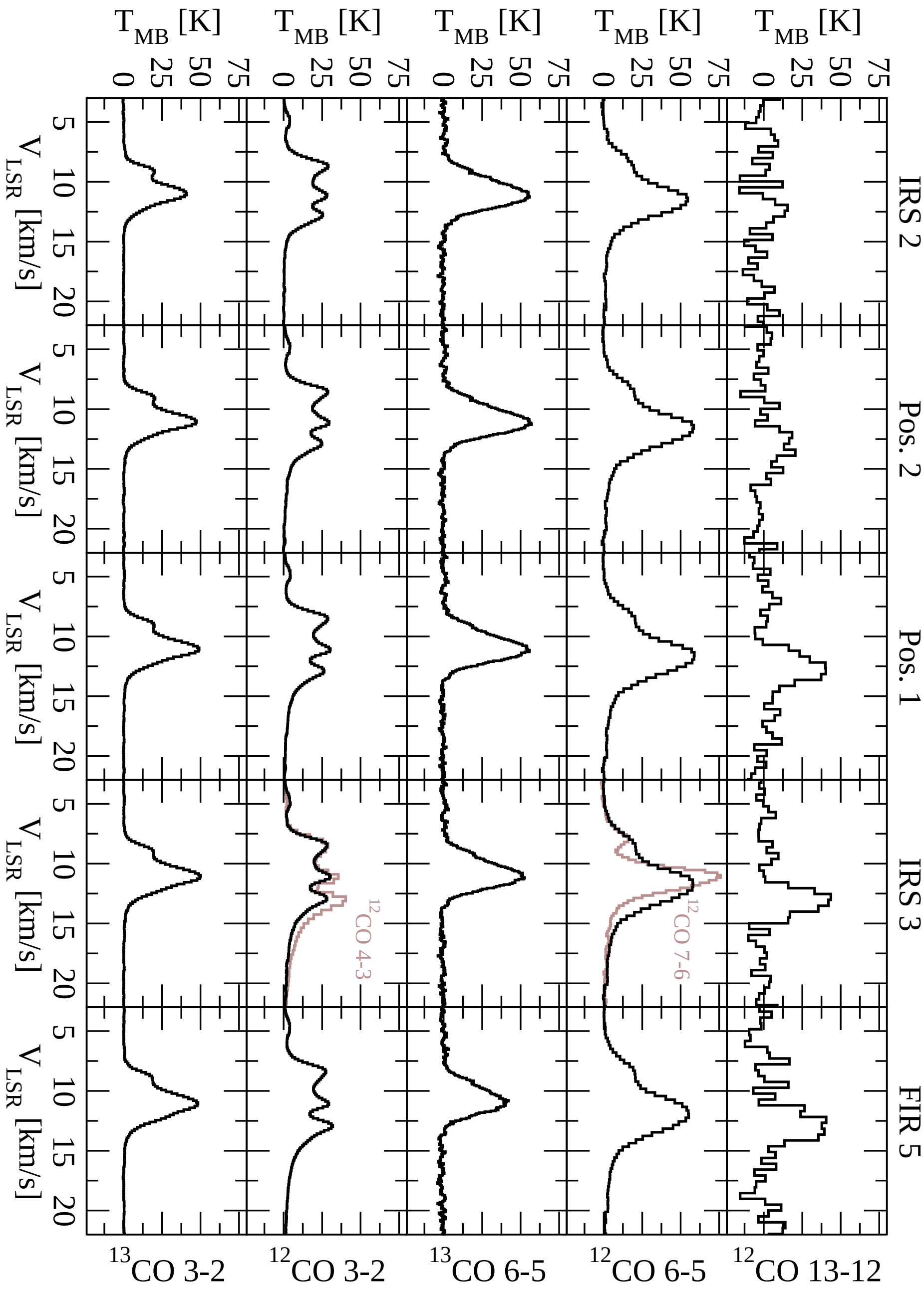

Fig. 4.3: *Spectra of CO emission from pointed observations in NGC 2024. The spectra are all convolved to a resolution of* 80″*, which is approximately the resolution of the observed* ^{12}*CO 3-2 and the* ^{13}*CO 3-2 spectra as well as the resolution of the error beam of the* ^{12}*CO 13-12 observations. The spectra are taken towards position north to south (left to right) as denoted in Tab. 4.2. The grey spectra, plotted together with* ^{12}*CO 6-5 and* ^{12}*CO 3-2 at ISR 3, are the* ^{12}*CO 7-6 and the* ^{12}*CO 4-3 spectra, respectively, and not by Gaussian fits.*

Tab. 4.3: *Here the integrated intensity,* v_{LSR} *and* Δv *of the lines shown in Fig. 4.3 are listed. Because of the complex line shapes, especially from the lower-J* ^{12}*CO lines, the* v_{LSR} *and* Δv *have been determined by using the first and second moment of the spectra, respectively.*

Position	Line	$\int \mathrm{T_{mb}}\,\mathrm{dv}$ [Kkm/s]	$\mathrm{V_{LSR}}$ [km/s]	Δv [km/s]
FIR 5	^{12}CO 13 – 12	120 ± 10	12.23 ± 0.3	3.34 ± 0.5
IRS 3	〃	109 ± 10	12.75 ± 0.3	3.92 ± 0.5
# 1	〃	127 ± 10	13.50 ± 0.3	4.51 ± 0.5
# 2	〃	57 ± 10	13.17 ± 0.3	3.54 ± 0.5
IRS 2	〃	< 30	–	–
IRS 3	^{12}CO 7 – 6	229 ± 10	11.5 ± 0.2	4.5 ± 0.5
FIR 5	^{12}CO 6 – 5	288 ± 10	12.0 ± 0.15	7.5 ± 0.5
IRS 3	〃	289 ± 10	11.9 ± 0.15	7.2 ± 0.5
# 1	〃	279 ± 10	11.9 ± 0.15	7.0 ± 0.5
# 2	〃	265 ± 10	11.9 ± 0.15	7.2 ± 0.5
IRS 2	〃	235 ± 10	11.8 ± 0.15	7.5 ± 0.5
FIR 5	^{13}CO 6 – 5	159 ± 5	10.9 ± 0.15	2.8 ± 0.5
IRS 3	〃	157 ± 5	10.9 ± 0.15	2.7 ± 0.5
# 1	〃	149 ± 5	10.8 ± 0.15	2.6 ± 0.5
# 2	〃	138 ± 5	10.7 ± 0.15	2.5 ± 0.5
IRS 2	〃	106 ± 5	10.5 ± 0.15	2.3 ± 0.5
IRS 3	^{12}CO 4 – 3	257.8 ± 10	11.5 ± 0.2	11.8 ± 0.3
FIR 5	^{12}CO 3 – 2	213 ± 10	11.9 ± 0.15	10.2 ± 0.2
IRS 3	〃	202 ± 10	11.9 ± 0.15	11.3 ± 0.2
# 1	〃	186 ± 10	11.6 ± 0.15	10.7 ± 0.2
# 2	〃	171 ± 10	11.0 ± 0.15	8.55 ± 0.2
IRS 2	〃	155 ± 10	10.7 ± 0.15	6.52 ± 0.2
FIR 5	^{13}CO 3 – 2	146 ± 5	10.9 ± 0.1	3.36 ± 0.2
IRS 3	〃	144 ± 5	10.8 ± 0.1	3.42 ± 0.2
# 1	〃	136 ± 5	10.8 ± 0.1	3.34 ± 0.2
# 2	〃	127 ± 5	10.8 ± 0.1	3.24 ± 0.2
IRS 2	〃	109 ± 5	10.7 ± 0.1	2.93 ± 0.2

The ^{12}CO 13-12 data displayed in Fig. 4.3 are binned to a resolution of 0.48 km/s, which is sufficiently high, because the line width of the J=13-12 line is on the order of 2.5 km/s. At this resolution we detected the line in four out of five positions with an S/N ratio $> 3\sigma$. At the position of IRS 2, we can claim only a tentative detection of 7.5 ± 3 K.

The ^{12}CO 6-5 line is not symmetric, but shows a shoulder at its lower velocity side. Its velocity of ~ 12 km/s is approximately 1 km/s redshifted with respect to the ^{13}CO 6-5 line. The difference in velocity can be explained by the two-component model, suggested by previous studies (Barnes et al. 1989, Graf et al. 1993). In this model, the foreground component (τ in Fig. 4.1) is assumed to be at a lower $v_{\rm LSR}$ than the background component (9.2 km/s and 11.1 km/s, respectively). Furthermore, the temperature of the foreground component (24 K) is lower than the temperature of 67 K of the background (Graf et al. 1993). Thus, the foreground component adds an absorption feature centered at 9.2 km/s to the ^{12}CO 6-5 line emitted from the background component. Therefore, the centroid velocity of the spectra appears redshifted with respect to the background component. In ^{13}CO 6-5, no signs of self-absorption appear, and thus its centroid velocity coincides with the $v_{\rm LSR}$ of the background component.

The profile of the ^{13}CO 3-2 line looks similar to the ^{12}CO 6-5 line, but it does not appear redshifted and lies at a velocity of ~ 11 km/s. The shape of the ^{12}CO 3-2 lines is dominated by deep absorption notches at velocities of 9.8 km/s and 11.9 km/s, which are caused by material located in front of the HII region. The alternative scenario, that the emission is composed of three individual, equally strong (~ 25 K), velocity shifted cloud components is unlikely, because these components are not seen in most of the other lines. A fourth, weaker peak (~ 3 K) can be seen at 4.6 km/s. ^{12}CO 2-1 observations (Kramer et al. 1996) revealed that this component extends further to the north-east and seems to be kinematically distinct from the main component.

The spectra of ^{12}CO 7-6 and ^{12}CO 4-3, convolved to a resolution of 80″, are superimposed on the ^{12}CO 6-5 and ^{12}CO 3-2 in Fig. 4.3, respectively. The ^{12}CO 4-3 spectrum looks very much like the one of ^{12}CO 3-2. The two absorption notches, the 4.6 km/s component, and the redshifted outflow can be seen in both spectra. Even the intensities are nearly identical. The only difference is that the emission from the outflow, i.e., at $v_{\rm LSR} > 12$ km/s, is slightly stronger in ^{12}CO 4-3.

The blueshifted shoulder of the ^{12}CO 6-5 spectrum, interpreted as self absorption, appears similar but more pronounced in ^{12}CO 7-6. However, the ^{12}CO 7-6 line is narrower, because the outflow signal is weaker than in ^{12}CO 6-5. ^{12}CO 7-6 seems to suffer much more from absorption and what is seen as a shoulder in ^{12}CO 6-5 appears as a second peak here. The different strengths of the absorption of ^{12}CO 7-6 and ^{12}CO 6-5 requires a strong gradient in the excitation of those lines. The velocity of the ^{12}CO 7-6 (11.5 km/s) line is in between the velocity of ^{12}CO 6-5 (~ 12 km/s) and ^{13}CO 6-5 (~ 11 km/s). If these velocity differences are indeed due to foreground absorption, the velocity dispersion of the ^{12}CO 7-6 absorbing material is significantly lower than the velocity dispersion of the material which absorbs ^{12}CO 6-5. The minimum, most likely caused by the foreground absorption, lies at 9.5 km/s, which is 0.3 km/s blue-shifted with respect to the absorption notches seen in ^{12}CO 4-3 and ^{12}CO 3-2.

Graf et al. (1993) observed NGC 2024 in ^{12}CO 7-6 as well, using the UKIRT telescope, which has a similar spatial resolution. Their spectrum at FIR 5, 16″ south of

IRS 3, shows a $\mathrm{v_{LSR}}$ of 12.8 km/s, clearly red shifted with respect to our observations. However the frequency stability of the Laser system that was used as local oscillator in these early measurements was about 1 MHz (~ 0.4 km/s). Furthermore, the UKIRT observations were made in a double beam switch mode with a chop throw of $3'$. Thus their off-position might have been not completely clean, leading to a different apparent line shape. Possible pointing errors cannot be the reason for different velocities reported in Graf et al. (1993)) and this work, because no big velocity gradients with position are seen in NGC 2024.

4.3 Modeling

The complex shape of the CO lines and especially the strong variation of the shape among those lines, are an evidence that NGC 2024 itself is a very complex region. It has a complex geometry including multiple components, turbulences, embedded protostars and kinematical activities, such as outflows. The aim of this investigation is to show that the major feature of the shapes and intensities of all observed ^{12}CO and ^{13}CO lines can be explained consistently with a physically reasonable model. To do so, we used two different radiative transfer codes. One uses the escape probability approximation, whereas the other solves the radiative transfer equation numerically (see below).

4.3.1 Radiative Transfer

The radiative transfer equation describes the change in intensity I_ν when radiation of the frequency ν passes through a medium with absorption coefficient κ_ν and emissivity ϵ_ν.

$$\frac{dI_\nu}{dx} = -\kappa_\nu I_\nu + \epsilon_\nu \tag{4.30}$$

Replacing $\kappa_\nu dx$ by $d\tau_\nu$ (τ is the optical depth) and ϵ_ν/κ_ν by the source function S_ν the solution of the radiative transfer equation is

$$I_\nu = I_{\nu,0} \cdot e^{-\tau} + \int_0^\tau S_\nu(\tau') \cdot e^{-\tau'} d\tau'. \tag{4.31}$$

It should be mentioned that both, I_ν and τ are functions of space, frequency and direction. $I_{\nu,0}$ is the background radiation. In many cases $I_{\nu,0}$ is only the cosmic micro-wave background, and thus isotropic. Since S_ν depends on I_ν (see below), it might become very complicated to solve equation 4.31, and thus either approximations (e.g., escape probability approximation) or numerical methods have to be used.

Escape probability approximation

The solution of the radiative transfer equation can be simplified by assuming constant excitation condition, i.e., a constant source function. Solving the integral in equation 4.31, leads to

$$I_\nu = I_{\nu,0} \cdot e^{-\tau} + S_\nu(1 - e^{-\tau}). \tag{4.32}$$

The term $e^{-\tau}$ is the escape probability of a photon along the line of sight. The frequency dependency of the optical depth is given by the normalized line profile ϕ_ν. The mean τ of a line is

$$\tau_{mean} = \frac{\int \tau_\nu d\nu}{\int \phi_\nu d\nu} \tag{4.33}$$

and thus the optical depth at the line center, $\tau_{\nu_0} = \tau_{mean} \cdot \Delta\nu$, where $\Delta\nu$ is the equivalent width of the line. The averaged escape probability of a photon emitted by a line transition from a cloud can be calculated averaging over the solid angel and the frequency ν, weighted by the line profile

$$\beta(\vec{r}) = \frac{1}{4\pi} \int \int e^{-\tau(\vec{r},\vec{n})} \phi_\nu d\nu d\Omega. \tag{4.34}$$

The averaged line intensity ($I(\vec{r})$) is therefore

$$I(\vec{r}) = (1 - \beta(\vec{r}))\, S + \beta(\vec{r}) \cdot I_{\nu,0}. \tag{4.35}$$

The averaged intensity given here depends on $\vec{r}$, because of the spatial variation of $\beta(\vec{r})$. Especially close to the edge of the cloud $\beta(\vec{r})$ increases. This is in contradiction to the adopted constant source function, which is related to the radiation field (see below). Thus this *escape probability approximation* is not self-consistent, and a mean source function has to be assumed.

Source function

The *source function*, which is the emissivity divided by the absorption coefficient, is determined only by the population of the specific quantum states. To assume *thermal equilibrium* is clearly not appropriate, because the conditions in space are clearly far from isothermal. Therefore the simplest way to derive the population of the quantum states is the assumption of *local thermal equilibrium* (LTE). LTE means, that the kinetic temperature (T_{kin}, which corresponds to the kinetic energy of the gas molecules), the radiation temperature (T_{rad}, i.e., the temperature of a *black-body*, which correspond to the local radiation field), and thus the excitation temperature (T_{ex}, i.e., temperature of the *Boltzmann distribution*, which corresponds to the population of the individual levels) are identical. But contrary the *thermal equilibrium* the temperature might vary with $\vec{r}$. In the case of LTE, the source function, in units of the $\mathrm{T_b}$, can be written as

$$S_\nu = h\nu/k \cdot 1/(exp(h\nu/kT) - 1) \tag{4.36}$$

These requirements are hardly met in the interstellar medium, because densities and optical depth are often too low, and thus the assumption of LTE is inappropriate. In astrophysics, however, the *terminus technicus* LTE is, although formally not correct, used if a *Boltzmann distribution* is assumed for the level population. But even this assumption is often over simplified (see below) and therefore a *statistical equilibrium* is more appropriate.

Statistical equilibrium assumes that the population of all quantum states of a molecule stays constant. Therefore, for each state x the equation

$$\sum_{i=1}^{\infty} n_i n_{H_2} \cdot C_{ix} + \sum_{i=1}^{\infty} n_i u_\nu \cdot B_{ix} + \sum_{i=x+1}^{\infty} n_i \cdot A_{ix} = \sum_{i=1}^{\infty} n_x n_{H_2} \cdot C_{xi} + \sum_{i=1}^{\infty} n_x u_\nu \cdot B_{xi} + \sum_{i=1}^{x-1} n_x \cdot A_{xi} \tag{4.37}$$

has to be fulfilled. In this equation C_{ab} are the rate coefficients of collisions with H_2, which changes the quantum state $a \rightarrow b$. A and B are the Einstein coefficients for spontaneous emission and stimulated emission/absorption, respectively. u_ν is the energy density of the radiation field with the line frequency ν and n_{H_2} the hydrogen density[4]. The assumption of statistical equilibrium is justified because the short time scales for emission, absorption and collisional relaxation (typically in the range of a few minutes to a few years), are much shorter than the time scales on which temperature and density vary. From equation 4.37, one can calculate the population of the individual quantum states and thus the excitation temperature for each transition. The source function is then determined by equation 4.36, using T_{ex}, which might differ for each transition, instead of T.

At high densities, the collision terms of equation 4.37, i.e., those terms containing C_{ab}'s, are much larger than all other terms. Thus the equation becomes simpler

$$\sum_{i=1}^{\infty} n_i n_{H_2} \cdot C_{ix} = \sum_{i=1}^{\infty} n_x n_{H_2} \cdot C_{xi} \tag{4.38}$$

The collision rate coefficients are related to each other by

$$\frac{C_{xi}}{C_{ix}} = g_i/g_x \cdot e^{-(E_i - E_x)/kT_{kin}}. \tag{4.39}$$

Therefore the population of the quantum states in this *collision dominated regime* follows the Boltzmann distribution with $T_{ex} = T_{kin}$.

---

[4] In equation 4.37 we assumed H_2 is the only collision partner, because it is by far the most abundant species in molecular clouds. However, as soon as a significant amount of the material is ionized, collisions with electrons become important, too. To include all possible collisional interactions additional terms for the possible collision partners have to be added, but the structure of equation 4.37 would still be the same.

At regimes, where the level population is determined by the radiation field, i.e., at low densities and sufficiently high radiation fields, equation 4.37 can be simplified as well

$$\sum_{i=1}^{\infty} n_i u_\nu \cdot B_{ix} + \sum_{i=x+1}^{\infty} n_i \cdot A_{ix} = \sum_{i=1}^{\infty} n_x u_\nu \cdot B_{xi} + \sum_{i=1}^{x-1} n_x \cdot A_{xi} \tag{4.40}$$

In such a regime, the level population follows a Boltzmann distribution as well and $T_{ex} = T_{rad}$. However, in general, the radiation field in molecular clouds can not be described by the *Planck function*, and thus no radiation temperature is defined. Furthermore, the radiation field decreases towards the edge of the cloud (see above). Therefore a full treatment of the radiation transfer equation (equation 4.31) is needed in the *radiation dominated regime*.

A measure for the densities at which collisions start to dominate the excitation and deexcitation processes is the *critical density*. It is defined as the density, where the collisional deexcitation rate overcomes the rate of spontaneous emission

$$n_{crit} = \frac{A_{ab}}{C_{ab}}. \tag{4.41}$$

Because the Einstein A coefficient increases with $\sim J^3$ and the collisional rate coefficient stay more or less constant, the critical density increases with J^3 as well. Typical value of the critical density for J=1-0 transition are in the range of $3 \cdot 10^3$ cm^{-3} (CO) and $3.6 \cdot 10^5$ cm^{-3} (N_2H^+).

The considerations above show that the assumption of a Boltzmann distribution is only valid for rather isothermal clouds with high densities, where $n_{H_2} >> n_{crit}$. The escape probability approximation can be used for a lager range of application, since in such codes the statistical equilibrium for the average cloud conditions is solved (Stutzki & Winnewisser 1985). Therefore deviations from the Boltzmann distribution, due to spontaneous emission are treated correctly. However, if large temperature and density gradients are present and/or the excitation is dominated by radiation, even escape probability approximation fails. In such cases equation 4.31 has to be solved numerically.

4.3.2 The Model of NGC 2024

The model of NGC 2024, which we propose is based on the geometry of the source as suggested by Barnes et al. (1989), i.e., we assume an HII region, which resides in front of a molecular cloud, but is obscured by some molecular material in the foreground. Furthermore, we rely on qualitative results of PDR models and ”Blister Models” to derive the temperature structure and the velocity structure, respectively.

For high densities and UV fields, which are expected to be present in NGC 2024 (e.g., Giannini et al. 2000), PDR-models predict that CO gets abundant at a temperature of a few hundred K. With increasing depth the temperature decreases approximately exponentially (e.g., Röllig et al. 2007[5]). In the so-called Blister Model (Israel 1978, Zuckerman 1973), an OB star is assumed to be located close to the surface of the molecular cloud forming an HII region. The ionization front of such an HII region moves slowly into this cloud establishing a high pressure gradient. Because of this pressure gradient the ionized gas moves away from the molecular cloud. Therefore hydrogen recombination lines appear at ~ 3 km/s more negative velocities than molecular lines, if the HII region is located at the near side of the molecular cloud (Israel 1978). In the case of NGC 2024 the ionized material cannot flow into space, but pushes on the foreground material. We therefore expect that the foreground component is seen at somewhat lower velocities as the bulk of the molecular material.

On the background of these well established physical principles, we try to find a temperature, density and velocity structure, which explain the line profiles of the observed ^{12}CO and ^{13}CO lines consistently. Since state-of-the-art PDR models do not deal with a complex velocity structure, these models are insufficient to explain the line profiles presented here. Therefore we used radiative transfer codes to reproduce the observed CO lines. Using an escape probability code, we derived an estimation of the temperature, density and column density of the hot, high-J CO emitting material. These results are later used as input for a full radiative transfer code.

4.3.3 Escape Probability Code Results

In addition to the new ^{12}CO 13-12 spectra of NGC 2024 presented in this work, the integrated CO intensities from J_{up}=14 to J_{up}=17 observed with the ISO satellite towards FIR 5 (Giannini et al. 2000) were taken from literature. The ^{12}CO 13-12 line does not show any sign of absorption or emission at ~ 9,5 km/s. Thus, we assume that the emission of ^{12}CO 13-12, as well as the other high-J CO lines (in this thesis I refer to all lines with frequencies > 1 THz as high-J CO lines), is purely determined by the material located behind the HII region. Therefore, we can use an escape probability code (Stutzki & Winnewisser 1985) to model the emission of ^{12}CO $J \geq 13$ and thus constrain the physical conditions required to excite the high-J CO lines. In this code, the emitting gas is treated as an isothermal cloud with homogeneous density. For a given set of kinetic temperatures (T_{kin}), H_2 densities ($n(H_2)$), and ^{12}CO column densities per velocity interval ($N(CO)/\Delta v$), the emitted line strengths (main beam temperatures and integrated intensities), as well as the optical depths (τ) at the line center are calculated.

To match the observed intensities of the high-J lines, a ^{12}CO column density of $9.5 \pm 0.7 \cdot 10^{16}$ cm^{-2} in a velocity interval $\Delta v = 4$ km/s, i.e., the width of the ^{12}CO 13-12 line, is required. Constraints on the gas temperature and density, however, are looser; many solutions are possible. Fig. 4.4 shows the observed high-J line intensities plotted

---

[5] All of their results are available under http://www.ph1.uni-koeln.de/pdr-comparison

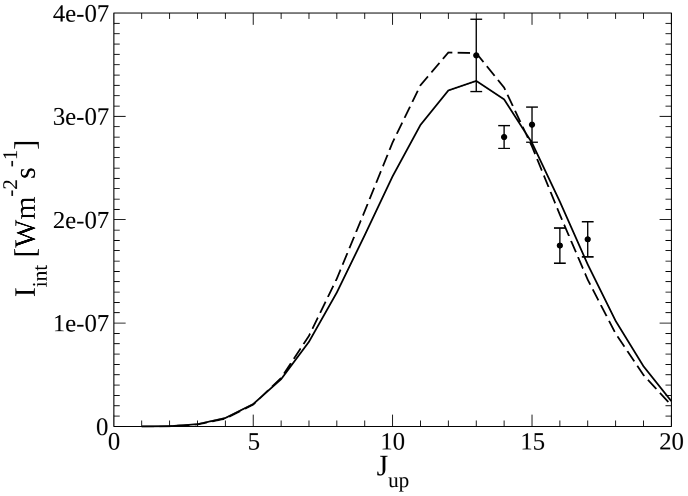

Fig. 4.4: *Observed line intensities and two possible solutions from the escape probability code for the high-J* ^{12}*CO lines. The models have been calculated for* $n_{H_2} = 1.3 \cdot 10^6$ cm^{-3} *and* $T_{gas} = 250$ K *(solid line) and* $n_{H_2} = 3 \cdot 10^5$ cm^{-3} *and* $T_{gas} = 410$ K *(dashed line).*

versus J$_{up}$. The solid and the dashed curves are two solutions from the escape probability code. The solid curve shows the result for a gas density of $1.3 \cdot 10^6$ cm^{-3} and a temperature of 250 K, whereas the dashed curve is the result for $n_{H_2} = 3 \cdot 10^5$ cm^{-3} and T=410 K. Both fits have a reduced χ^2 of 2.9. These are only two representative solutions among many more. All models with a χ^2 lower 10 have in common, that $T^3 \cdot n$ is approximately constant.

If we assume that the gas is distributed uniformly throughout the (80″) beam (and the area filling factor is one), then this layer of the PDR has a thickness of $5 \cdot 10^{14}$ to $1.5 \cdot 10^{15}$ cm (= 33-100 AU). At a distance of 415 pc, 100 AU corresponds to 0.25″, which indicates that this hot component is indeed a thin layer at the, possibly clumpy, surface of the molecular cloud.

4.3.4 Full Radiative Transfer Model

Using the escape probability code we had to restrict myself to the high-J CO lines. To include also the lower-J lines, and thus get a unified picture of the source, we have to use a full radiative transfer model, which includes multiple cloud components along the line of sight and therefore treats multiple emission components and self-absorption correctly. With such a model, we fitted the line shapes and intensities of all seven ^{12}CO and ^{13}CO lines observed at the position of IRS 3 and the integrated intensities of ^{12}CO with $J_{up} > 13$, simultaneously. The ^{12}CO line with $J_{up} > 13$ are the same data we used in the previous section. These data have been observed at the position of FIR 5, which lies 16″ south of IRS 3, a separation much lower than the spatial resolution of our observations. We used SimLine (Ossenkopf et al. 2001), a 1-dimensional, spherical radiative transfer code. By setting the inner radius of the model to a value, which is much larger than the beamsize times the distance of the observations, we used SimLine in a quasi plane-parallel way. Given density, temperature, and velocity profiles along the line of sight, the code computes the emitted line profiles.

Constraints on the models

A close look at the data in Fig. 4.3 and Table 4.3 reveals an apparent contradiction in the line strengths at v_{LSR} = 11 km/s. The strong (~ 50 K) ^{13}CO 6-5 emission, which indicates a large column density of hot molecular gas, belies the relatively weak (< 15 K) ^{12}CO 13-12 emission at the same velocity. The possibility that the ^{12}CO 13-12 line is absorbed by the foreground gas can be ruled out, since the estimated column density ($N_{H_2} = 2 \cdot 10^{22}$ cm^{-2}, which corresponds to A_v=20-25 mag, Bik et al. 2003) is orders of magnitudes too low for the derived temperatures (~ 25 K) to cause this absorption (Graf et al. 1993). Relatively strong ^{12}CO 13-12 emission at a v_{LSR} of ~ 13 km/s, where no other optically thin line shows an emission peak, suggests an error in the frequency calibration. The origin of such an error is puzzling, given that particular care was taken to check calibration during the observations. Immediately prior to observing NGC 2024, we observed Orion FIR 4 to check telescope pointing, and the ^{12}CO 13-12 emission had the expected velocity (Wiedner et al. 2006, Kawamura et al. 2002, Wilson et al. 2001). The uniformity of the v_{LSR} throughout the ^{13}CO 6-5 map also diminishes the likelihood that the anomalous ^{12}CO 13-12 velocity is due to a pointing error. Moreover, all software-set values (e.g., rest frequency and sky frequency of the line) were checked carefully, but no error was found. Despite this scrutiny to get a reasonable solution for our model, we are forced to assume that the v_{LSR} of ^{12}CO 13-12 and ^{13}CO 6-5 are both 10.9 km/s. This assumption is buttressed by unpublished high-J CO observations (Marrone, priv. comm.), which also indicate a v_{LSR} of ~ 11 km/s.

Previous investigations of NGC 2024 established a two-component model in which most of the molecular gas is behind the HII-region and a smaller amount is located in the foreground ridge that obscures the ionizing source in the optical. Most of the CO radiation is emitted by the background component and the foreground component complicates the line shapes of the lower-J lines (e.g., ^{12}CO 3-2). We adapted the existing models to get reasonable fits for all of the observed CO lines consistently. We additionally introduced a hot, dense, and thin gas component, located at the interface of the HII region and the DMC (Fig. 4.1), with physical conditions comparable to the results of the escape probability code. This hot material resides at the surface of the molecular cloud, which is illuminated by OB stars within the HII region. In the case of the foreground material, we have to assume several components as well. First, we have to adopt two components of cold gas at different velocities, as both the ^{12}CO 4-3 and the ^{12}CO 3-2 spectra show two absorption notches. In addition, it is reasonable that material located at the interface of the foreground component and the ionized gas is heated as well, and thus we introduced a layer of hot gas on this side of the HII region, too. Furthermore, the total column density of all components located in front of the HII region is restricted by the measurements of Av towards the obscured stars, which translates into a total H_2 column density of $2 \cdot 10^{22}$ cm^{-2}.

Solution of the Model

The result of the modeling is listed in Tab. 4.4. As mentioned above, five components (three foreground and two background components) were appropriate to get a reasonable solution for the observed spectra.

Tab. 4.4: *Physical properties of a 5-component radiative transfer model of NGC 2024. Properties with a range of values vary continuously with depth.*

Component	T [K]	n(H_2) [cm^{-3}]	r [cm]	N(H_2) [cm^{-2}]	v_{LSR} [km/s]	Δv_{turb} [km/s]
B1	75	$9 \cdot 10^5$	$8.0 \cdot 10^{16}$	$7.2 \cdot 10^{22}$	11.0	1.8
B2	75-330	$9 \cdot 10^5$-$2 \cdot 10^6$	$6.2 \cdot 10^{13}$	$8.9 \cdot 10^{19}$	11.0	1.8
F1	330-40	$1 \cdot 10^5$	$8.9 \cdot 10^{14}$	$8.9 \cdot 10^{19}$	9.3	1.3
F2	40-30	$1 \cdot 10^5 - 3 \cdot 10^4$	$1.7 \cdot 10^{17}$	$1.04 \cdot 10^{22}$	9.3-9.7	1.3-1.1
F3	30-15	$5 \cdot 10^4$	$5.9 \cdot 10^{15}$	$2.9 \cdot 10^{20}$	12.1	1.8

The background material was divided into two subcomponents, denoted by B1 and B2. B1 consists of warm (T= 75 K) and dense gas (n(H_2)= $9 \cdot 10^5$ cm^{-3}) with a high column density (N(H_2) = $7.2 \cdot 10^{22}$ cm^{-2}). B2 is a thin layer with a steep temperature and density gradient. At the surface of the cloud the temperature reaches 330 K and the density is as high as $2 \cdot 10^6$ cm^{-3}. B2 represents the hot interface between the HII region and the cooler molecular cloud. This is also the gas component that was specified in the solution of the escape probability code in the previous section. Both B1 and B2 have a velocity of v_{LSR} = 11 km/s and a FWHM of the turbulent velocity of Δv_{turb} = 1.8 km/s.

The foreground component was divided into three subcomponents, F1, F2, and F3, to explain the two absorption dips in the ^{12}CO 4-3 and ^{12}CO 3-2 spectra and for physical reasons, as mentioned above. The v_{LSR} of F2 shows a gradient from 9.3 km/s to 9.7 km/s towards the observer, and the v_{LSR} of F3 is 12 km/s. The total column density of the foreground component (F1+F2+F3; N(H_2)$_{tot}$ = $1.08 \cdot 10^{22}$ cm^{-2}) correspond to an optical extinction of $\sim 11^{mag}$, which is slightly lower than the 15 to 25^{mag} found by Bik et al. (2003). To convert the column density into A_v we used the relation

$N_{H_2}[cm^{-2}] = 0.94 \times 10^{21} A_v$ (mag). However, since the light of some of these stars might be extincted by dust in the vicinity of the star, the lower value of A_v is probably more appropriate.

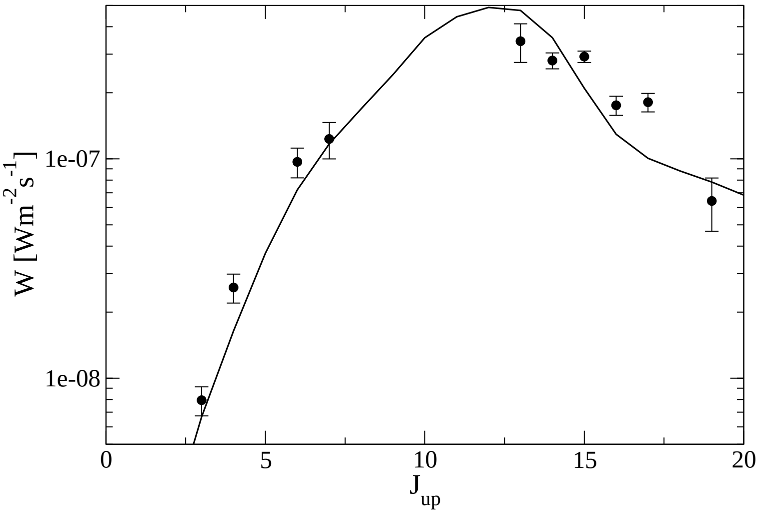

Fig. 4.5: *Integrated line intensity of ^{12}CO versus J_{up}. The observed data (full circles) include all ^{12}CO lines from this work and observations with the ISO satellite from Giannini et al. (2000). The solid line shows the results of the full radiative transfer code SimLine*

The complex shapes of the emission lines, especially the deep absorption notches in ^{12}CO 3-2, require depth-dependent gradients in the foreground subcomponents. F2 contains most of the foreground material (> 96 % of the mass). It consists of a $1.54 \cdot 10^{17}$ cm deep, 40 K warm gas layer, whose density decreases linearly from 10^5 cm^{-3} to $3 \cdot 10^4$ cm^{-3}. Subsequently the F2 gas density stays constant, but the temperature drops to 30 K within the next $1.4 \cdot 10^{16}$ cm. Simultaneously to the temperature decrease, the v_{LSR} shifts from 9.3 km/s to 9.7 km/s. F3 is a comparatively thin ($N_{H_2} = 2.9 \cdot 10^{20}$ cm^{-2}) component with a constant density of $5 \cdot 10^4$ cm^{-3}and a temperature that drops from 30 K to 15 K. The v_{LSR} of F3 is 12.2 km/s. F3 is responsible for one of the two absorption dips in ^{12}CO 3-2, as well as the absorption of the ^{12}CO 6-5 intensity.

From a physical point of view it is expected that the gas residing at the interface between molecular gas and the HII region is heated by the ionizing source of the HII region. Thus, we assume here that a hot component (F1) is located behind the bulk of the foreground material (i.e., F2). The density, v_{LSR}, and Δv are adopted to be the same as those found in F2 and only the temperature rises, like at the interface of the background material, to values of 330 K. Such an additional gas component does not change the modeled line emission as long as the H_2 column density is lower than $4.6 \cdot 10^{20}$ cm^{-2}. This upper limit is about five times larger than the H_2 column density of B2, which means that our data do not contradict the assumption of a hot interface layer, but we cannot constrain the physical properties of such a component either. The column density we give for F1 in Tab. 4.4 is selected to be the same as its counterpart at the backside of the HII region.

The F1 component represents the radiation heated counterpart of B2 on the nearside of the HII region. This additional gas component does not change the modeled line emission as long as the H_2 column density is lower than $4.6 \cdot 10^{20}$ cm^{-2}, i.e. as long as its column density is smaller than 5 times the column density of B2. Because the existence of such a component is physically reasonable, we assumed that the interface between the bulk of the foreground material (F2) and the HII region is heated similar to the interface at the background, i.e., column density and maximum temperature of F1 and B2 are similar. Density and velocity of F1 are the same as found for F2.

The geometric arrangement of the components B1, B2, F1, and F2 is well defined by our calculations and the temperature- and density trend of these components are shown in Fig. 4.7. However, the location of F3 is not clear, apart from residing in front of the HII region. The fact that this component is cold and not blueshifted with respect to the background component indicates that this component might be closest to the observer.

A comparison between the observed spectra and the model results is shown in Fig. 4.6. Given the known complexity of the source, and the limits of a five-component model, the model spectra fit the observations quite well. Two spectral features that were not included in the model fit are the redshifted outflow, which can be seen in ^{12}CO 6-5, ^{12}CO 4-3 and ^{12}CO 3-2, and the component at $v_{LSR} \sim 4.5$ km/s. Nevertheless, the main features of the five emission lines can be explained with our rather simple assumptions.

In Fig. 4.5 we show the integrated intensity of the ^{12}CO lines versus J_{up}. Especially for the low- and mid-J CO lines the model matches the observations quite well. At $J_{up} > 10$ the scatter of the observed data increases, possibly due to observational uncertainties.

Physical interpretation of the model results

The B1 component is equivalent to the DMC in Fig. 4.1. Because the properties of B1 are mostly based on the fits of ^{12}CO 13-12 and ^{13}CO 6-5, only the warm gas of the DMC is represented. Cold gas, which is deeper inside of the DMC, would have no effect on the modeled lines, either because the upper levels are not populated (^{12}CO 13-12, ^{13}CO 6-5), or the lines are already optically thick (^{12}CO 3-2 and ^{12}CO 6-5). Thus, the column density of B1 is just the lower limit for the DMC. Observations of C^{18}O 2-1 and C^{17}O 2-1 (Graf et al. 1993) revealed a three times lager H_2 column density than what we found here. The B2 component represents the thin, hot interface between the HII-region and the molecular gas. Due to the high UV radiation emitted by the ionizing source(s) of NGC 2024, the gas at the interface is strongly heated, which may result in temperatures up to 330 K. The B2 component is responsible for most of the high-J emission, and hence its properties are similar to those we found using the escape probability code.

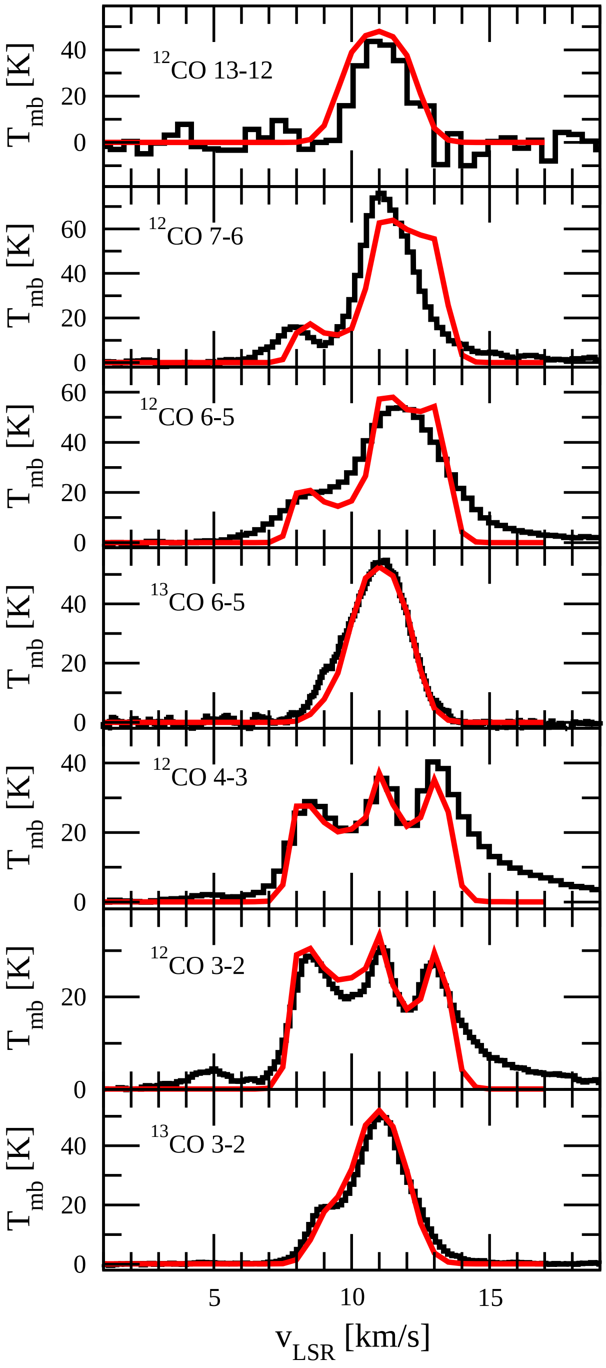

Fig. 4.6: *Observed (black) and model (red) spectra of ^{12}CO 13-12, ^{12}CO 6-5, ^{13}CO 6-5, ^{12}CO 3-2 and ^{13}CO 3-2. The observed spectrum of the ^{12}CO 13-12 line was shifted by -2.2 km/s (see text).*

The three subcomponents F1, F2, and F3 together represent the foreground material,

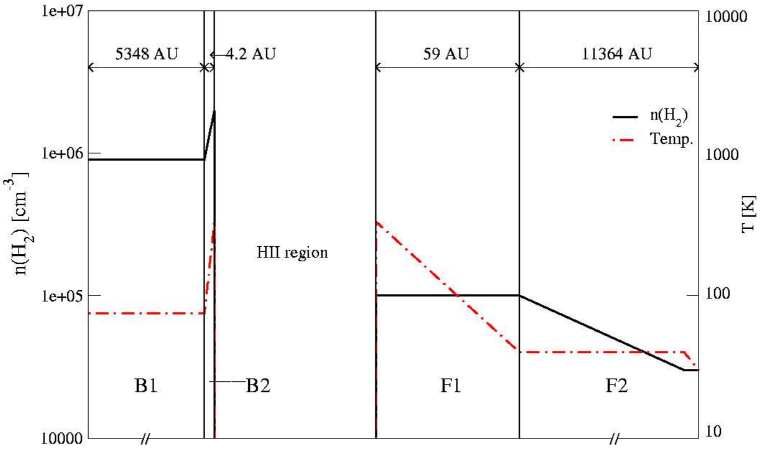

Fig. 4.7: *Temperature and density structure of NGC 2024. The observer is located to the right. Since it is not clear where the component F3 resides, we do not plot it here.*

τ in Fig. 4.1. The F1 subcomponent is, as mentioned above, not traced by the lines we observed here, but it represents the counterpart of B2 at the foreground component albeit at lower density. For the other two subcomponents located in front of the HII region, F2 and F3, we assume that matter is distributed uniformly across the area of the beam. One of the main difficulties in modeling the absorption features of the spectra is that the narrow absorption notches seen in the ^{12}CO 3-2 line suggest a velocity dispersion of Δv ~ 1.5 km/sof the foreground component, whereas the rather smooth line shape of ^{12}CO 6-5 indicates a much lager velocity dispersion (> 3 km/s). The little peaks and edges, appearing in the ^{12}CO 6-5 and ^{12}CO 7-6 modeled spectrum (Fig. 4.6) occur because of this discrepancy. A further complication is that the intensity differences in the absorption features of ^{12}CO 6-5 and ^{12}CO 3-2 and the requirement that the total N_{H_2} column density is ~ 10^{22} cm^{-2} (i.e., the lines are optically thick) make it necessary to include a temperature gradient. Furthermore, interstellar matter shows clumpy structure on all scales. In NGC 2024, substructures on scales down to the resolution of previous observations were detected (Kramer et al. 1996, Lada et al. 1991, see Section 4.1.2). Therefore, we expect a clumpy structure within the beam as well, which would cause a much more complex structure of the foreground. Such small scale structures must be taken into account for more detailed modeling. For example, dense, cold clumps, smaller than the FWHM of the beam, which mainly affect the ^{12}CO 3-2 line, but due to their low temperature leave the ^{12}CO 6-5 line rather unaffected, are a possible explanation for the narrow absorption notches observed in ^{12}CO 3-2 and 4-3, whereas the line shape of ^{12}CO 6-5 is much smoother. However, observations at higher spatial resolution would be necessary to verify this hypothesis.

The velocity difference between the background gas and the bulk of the foreground material is 1.5 km/s. Assuming that the velocity difference is caused by the pressure of the ionized gas, according to the ”Blister model” this velocity shift corresponds to a total momentum per unit area of 5.67 kg cm^{-1} s^{-1}, which has to be transferred to the F2 component. We calculated the internal pressure of the ionized gas, which pushes the foreground component, using measured electron temperature (8160 K) and electron density of $\sim 10^3$ cm^{-3} (Odegard 1985). Such a pressure has to act for approximately 200 000 years to accelerate the foreground component to its current velocity. However, the mass of the F1 component is highly unknown, and T_e and n_e may have changed in the past, so that this simple calculation may be somewhat debatable, but it shows, that the observed velocity structure can be indeed explained by a blister model.

Comparison with other models

The properties of the background components agree fairly well with the results obtained by Graf et al. (1993). The main difference between their model and the present one is that Graf et al. (1993) assumed LTE conditions, whereas in the SimLine code, the balance equations for all level populations and energy densities are solved self-consistently (Ossenkopf et al. 2001). In the previous study, an H_2 column density of the background component of $2.0 \cdot 10^{23}$ cm^{-3} was found, which is three times more than what we found here. This difference arises because they included rarer isotopes, e.g., $C^{18}O$ and $C^{17}O$, which are optically thin and trace material located deep inside the cloud. Most of this material is hidden due to the high optical depths in the ^{12}CO and ^{13}CO lines we observed. The temperature determined by Graf et al. (1993), 67.4 K, is in good agreement with the 75 K determined in our work. Also the kinematic parameters Graf et al. (1993) report (v_{LSR} = 11.1 km/s and Δv = 1.8 km/s) match our results. Since they do not observe high rotational transitions of CO (no lines with $J_{up} > 7$), they have no information about the hot interface region.

Giannini et al. (2000) give a CO column density of $2 - 5 \cdot 10^{18}$ cm^{-2}, which corresponds to an H_2 column density of $2.1 - 5.3 \cdot 10^{22}$ cm^{-2}. This column density, which is about 50% lower than the total column density we found ($N_{H_2,total} = 8.3 \cdot 10^{22}$ cm^{-2}), was derived using an escape probability code. The fact that Giannini et al. fitted only a single, isothermal gas component, might explain the different results. In particular the background material will be underestimated in such an approach due to self absorption effects. The kinetic temperature they give (110-130 K) is in the range of the values we found, but because of their isothermal approach hard to compare with our results.

For the foreground components, we found a total H_2 column density of $1.07 \cdot 10^{22}$ cm^{-2}, which corresponds to an A_v of 11.4. This is lower than the visual extinction of 15 to 25 found towards several stellar objects inside the HII region (Bik et al. 2003). However, due to the low spatial resolution of our observations, the beam-averaged column density might be well lower than the values obtained from individual stars. The H_2 column density of the foreground component given by Graf et al. (1993) is a factor of two larger than our value. They also found a temperature of 23.5 K, i.e., slightly lower than our results (30-40 K), which might be caused by the fact that they assumed LTE conditions.

4.4 Chapter summary

In this chapter we showed seven ^{12}CO and ^{13}CO lines from $J_{up} = 3$ to $J_{up} = 13$ towards the massive star forming region NGC 2024. The lines profile differ a lot and range from almost Gaussian (^{12}CO 13-12, ^{13}CO 6-5) to highly complex and multiply peaked (^{12}CO 3-2, ^{12}CO 4-3), which indicates a complex internal structure of NGC 2024.

In addition to the lines we present here, the integrated ^{12}CO lines with from $J_{up} = 14$ to $J_{up} = 17$ has been observed with the ISO satellite (Giannini et al. 2000). Since the ^{12}CO 13-12 does not show any sign of self absorption, the assumption that lines observed with ISO don't suffer from self absorption either is justified. Hence we could use an escape probability code (Stutzki & Winnewisser 1985) to model the physical conditions of the region where these high-J CO lines originate from. We found, that these lines are emitted from a hot (> 250 K), dense ($> 3 \cdot 10^5$ cm^{-3}), and thin (∼ 100 AU) layer, which is most likely located at the interface of the HII region and the molecular cloud.

Based on the principles of the Blister model and the PDR scenario, we constructed a model for NGC 2024 using 1D radiative transfer code SimLine (Ossenkopf et al. 2001). This model explains the profiles of the observed ^{12}CO and ^{13}CO lines quite well. In our model, the bulk of the molecular gas resides at the back of the HII region and consists of warm (75 K) and dense ($9 \cdot 10^5$ cm^{-3}) material. We also find evidence for a hot (up to 330 K) and thin (400 AU) layer located at the surface of the molecular cloud, from which most high-J CO emission originates. The molecular ridge in front of the HII region consists of molecular material at lower densities ($3 \cdot 10^4$ cm^{-3} – 10^5 cm^{-3}). The column density is of the order of 10^{22} cm^{-2}, which correspond to an A_v of 11 mag. This value is in good agreement with measurements of the optical extinction towards stars within the HII region (Bik et al. 2003).

Overall, this study shows that for the example of NGC 2024, emission lines with complex and varying line shapes, as often observed in massive star forming regions, can be explained consistently with a rather simple, yet physically reasonable model. To explain the twelve emission lines consistently, including the detailed complex line shapes of seven lines, five components with different physical parameters and thus 15 free parameter are required. Five of these 15 free parameters determine the temperature structures, which are constrained by the additional condition that the resulting temperature structures should be similar to temperature structures obtained by PDR models. The different velocities of the individual components can be well explained with a Blister Model of H II regions. Both the relatively large number of included lines and the fact that our results can be explained by physical models, lead us to the conclusion that we found a plausible scenario for the warm molecular gas in NGC 2024.

Complex line profiles of low-J CO lines are commonly observed in massive star forming regions and with modern observatories (e.g., SOFIA, APEX and Herschel), more and more mid- and high-J CO observations will be available. This case study of NGC 2024 shows that with physical insight into these complex regions and careful modeling, the complex line-shapes and multi-line observations can be used to derive valuable information on the physical conditions in massive star forming regions.

5 Comparison of a pre- and a protostellar core in IC 5146

In chapter 2 the predicted differences of the various abundance profiles of molecules in prestellar and protostellar cores are shown. The chemistry in the center of prestellar cores is dominated by the depletion of many molecules, including CO, due to freeze out onto dust grains. In protostellar cores this CO depleted region moves outwards, because the inner parts of the cloud core gets heated by the evolving protostellar core. Both, the change of the abundances as well as the increase of the temperature, leads to variation in the observed line emission. The eastern part of the cloud filament associated with the cluster IC 5146, which contains a starless and a protostellar core, is a good candidate to investigate these differences. Observations of $C^{18}O$, N_2H^+ and NH_3, as well as measurement of A_V were analyzed to show the different abundance profiles in the two classes of objects more clearly. Pointed observations of $H^{13}CO^+$ 3-2 and DCO^+ 3-2, tracing the deuterium fractionation (see chapter 2), were included in this analysis, too.

5.1 The cloud filament associated with IC 5146 and its eastern core

The molecular cloud associated with the stellar cluster IC 5146, is a dark cloud filament which lies at 460 pc distance (Lada et al. 1999). In their work, Lada et al. (1999) developed a new method to map optical extinction using Infra-red colors (H & K) of background stars. Fig 5.1 shows the A_V map of the Northern Streamer of IC 5146.

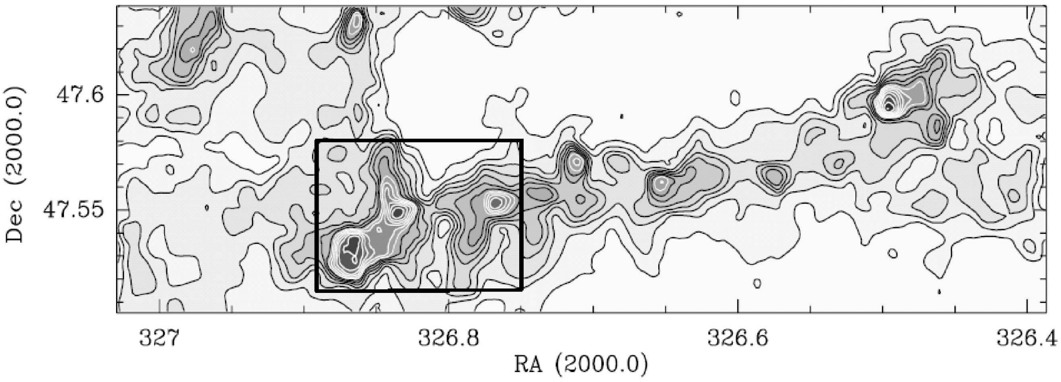

Fig. 5.1: *A_V map of the Northern Streamer of IC 5146 at a resolution of 30″. The black box indicates the region, which we investigated. This figure has been adapted from Lada et al. (1999)*

This map of optical extinction (constructed from NIR photometry towards background stars) was compared with $C^{18}O$ and $C^{17}O$ IRAM data near one starless core, revealing a significant amount of CO depletion (Kramer et al. 1998, 1999). Bergin et al. (2001) studied the depletion of $C^{18}O$, N_2H^+ and CS using the same Av data, but the observations were done with the FCRAO, which has a resolution of $\sim 50''$ at these frequencies. They found that the abundance of CS and CO is reduced at $A_v > 10-15^{\rm mag}$, whereas the N_2H^+ abundance is low and constant at optical extinctions $< 15^{mag}$ and rises at higher A_v values. In addition, these A_v data were combined with SCUBA 450/850 μm images of the filament (Kramer et al. 2003). They found changes of dust emissivity in half a dozen of the embedded cores. These changes are consistent with theoretical models of ice agglomeration on dust grains.

While most of the cloud is largely devoid of star formation activity (Dobashi et al. 1993), the FU Orionis star Elias 1-12 (Elias 1978), which lies within the eastern core of IC5146, is an exception. ISO LWS observations of Elias 1-12 (V1735 Cyg) show [OI], [CII] and probable [NII] emission (Lorenzetti et al. 2000), which indicates that it is surrounded by an UCHII region and warm molecular gas, most likely originating from a Photo-Dominated-Region (PDR). PDR models lead to an estimated UV field of 316 G_0 and a density of 3150 cm^{-3}.

5.2 Observation

In this chapter we present a number of tracers, which have been observed in the eastern part of IC 5146 with many different telescopes, and thus different spatial resolutions. A summary of the tracers is given in Tab. 5.1.

Tab. 5.1: *Observational data of the observed tracers.*

Tracer	Resolution	Telescope	Remarks
$C^{18}O$ 2-1	11″	IRAM-30m	
N_2H^+ 1-0	25″	IRAM-30m	
NH_3 (1,1)	40″	Effelsberg	
NH_3 (2,2)	40″	Effelsberg	
A_v	30″	MMT	
450 μm	8″	JCMT	western part only
850 μm	14″	JCMT	western part only
$H^{13}CO^+$ 3-2	18.5″	JCMT	pointed observations
DCO^+ 3-2	22.5″	JCMT	pointed observations

5.2.1 Ammonia

The NH_3 (1,1) and NH_3 (2,2) observations were carried out between the 19th and the 22nd of April 2006 at the 100m telescope in Effelsberg. We used the 1.3 cm (23 GHz) receiver located in the primary focus, which has a bandwidth of 2.7 GHz. The main beam efficiency is $\approx 52\%$ and the half power beam width is $39''$. The elevation dependence of the sensitivity was corrected by using the normalized Gain curve[6]. For pointing, focusing and flux calibration we used the planetary nebula NGC 7027, which has a continuum flux of 5.39 Jy at 23.9 GHz (Ott et al. 1994). Pointing was checked approximately every 3 hours, and pointing was expected to be better than $7''$. Mapping was done by raster mapping with a spacing of $20''$. The NH_3(1,1) line was clearly detected throughout the core (Fig. 5.3), but NH_3(2,2) was only marginally detected above the noise level (0.16 K).

To detect the NH_3 (2,2) line at more positions and with a higher signal to noise ratio, we re-observed the parts of the core, which show the highest NH_3 (1,1) emission in April 2007, using the same setup as described above. For calibration, pointing and focusing NGC 7027 was used again. With this additional observation, we were able to detect NH_3 (2,2) in all three cores with an $S/N > 3$. The noise level in these observations was reduced from 0.16 K to 0.04 K (T_{MB}).

5.2.2 $H^{13}CO^+$ and DCO^+

We observed the eastern core of IC 5146 towards two selected positions ($506''/-110''$ and $335''/-50''$, with respect to the central position of our maps at $\alpha = 21:46:32.5$, $\delta = +47:33:55.0$ (J 2000)) in $H^{13}CO^+$ 3-2 and DCO^+ 3-2, using the JCMT. The observations were carried out at the end of June 2005 using the A3 receiver. The rest frequencies of these lines are 260.225 GHz and 216.110 GHz, respectively. We observed these lines using the frequency switching mode with a frequency offset of 8.2 MHz and an integration time of 12 minutes. System temperatures were between 426 and 522 K, which results in noise levels between 50 to 70 mK on 0.25 kms^{-1} channels. DCO^+ was detected at both positions with a S/N ratio above 5, but we failed to detect $H^{13}CO^+$ 3-2 at the position $335''/-50''$, whereas it was clearly detected at $506''/-110''$ (see sect. 5.3.2).

5.2.3 $C^{18}O$ 2-1 and N_2H^+ 1-0

The $C^{18}O$ 2-1 integrated intensities and N_2H^+ 1-0 spectra are so far unpublished data, and have been observed in 2004 and 2001, respectively. Both lines were observed with the IRAM 30m telescope. The $C^{18}O$ 2-1 ($\nu = 219.560$ GHz) observations have

---

[6] www.mpifr-bonn.mpg.de/div/effelsberg/calibration/1.3cmpf.html

been conducted with HERA, a 3×3 pixel array receiver, which was tilted by 18.5°. As backend the VESPA autocorrelator was used. The data were taken with the OTF-mode and frequency switching. At the observing frequency of $\sim$ 220 GHz the beam width (HPBW) is 11″ and the main beam efficiency is 0.55.
For the N_2H^+ 1-0 ($\nu = 93.173$ GHz) observations, conducted in September 2001, the single pixel receiver was used. These data were taken in OTF-mode and frequency switching, too. The HPBW at 93 GHz is 25″.

5.2.4 Optical Extinction

This map is based on merged NIR data obtained at the 4m Kitt Peak telescope with the FLAMINGOS detector and the Multiple Mirror Telescope (MMT), which improves on the previous NIR data (Lada, priv. comm.).

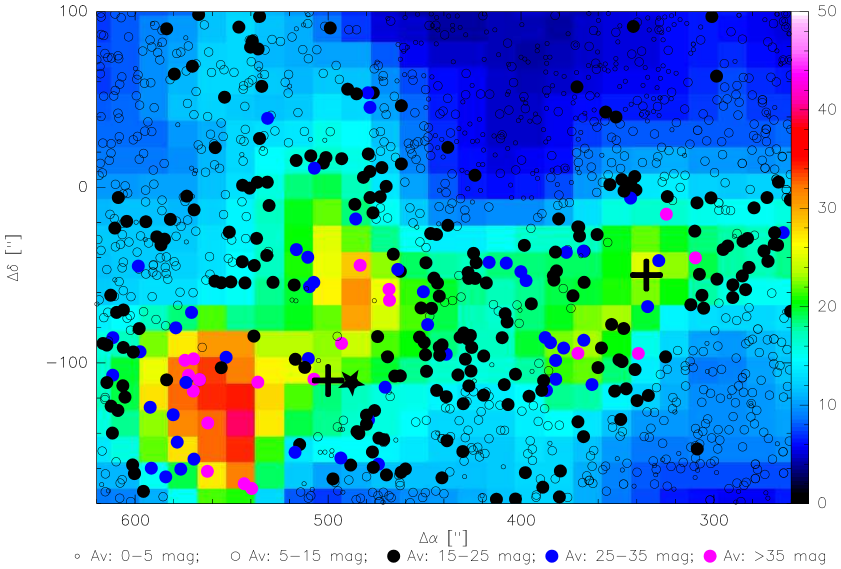
100
0
−100
Δδ ['']
600
500
400
300
Δα ['']
50
40
30
20
10
0
∘ Av: 0−5 mag; ○ Av: 5−15 mag; ● Av: 15−25 mag; ● Av: 25−35 mag; ● Av: >35 mag

Fig. 5.2: *A_V map of the eastern core of IC 5146 (colors). On top of the A_V map are the individual stars are plotted. The 0/0 position of the map is at* $\alpha = 21:46:32.5$, $\delta = +47:33:55.0$ *(J 2000). The star marks the position of the FU-Orionis star Elias 1-12, whereas the crosses are the positions of the NH_3 peak (Position 1 & 2).*

Lada et al. (1999) developed a new method to map optical extinctions. Instead of counting stars they derived the optical extinctions towards background stars using their H-K colors. To derive a homogeneously sampled map, they convolved the extinctions of the individual stars with a Gaussian. The final resolution of the A_V map is given by the width of the Gaussian and is determined by a minimum number of background stars per resolution element, which is chosen by compromising between resolution and error of the A_V measurement. Observing a nearby, extinction free reference field allows to correct for the intrinsic stellar color.

The derived extinction in the region immediately around Elias 1-12 has to be treated with caution, since this source is very bright and there is a fair amount of nebulosity. Thus within 60″ around Elias 1-12 the extinction measurements are doubtful.

In Addition 850 μm and 450 μm continuum data, obtained with SCUBA at the JCMT, are available for the western part of the observed region (Kramer et al. 2003).

5.3 Results

5.3.1 Maps

The maps of the observed molecular lines (Tab. 5.1) are shown in Fig. 5.3. The 0/0 position of these maps is at α=21:46:32.5, δ=+47:33:55.0 (J=2000). All four tracers, in which we mapped the eastern cores, look very similar. In the region, which we have mapped, three cores can be seen in optical extinction (Fig. 5.2), but since the determination of A_V is doubtful in the vicinity of Elias 1-12 (marked with a star in Fig. 5.2) the two eastern cores might be in fact one elongated core. The A_V of the individual core is always above 25 magnitudes and reaches values of $\approx$ 45 at its maximum.

The nitrogen bearing species NH_3 and N_2H^+ show a quite similar morphology (Fig. 5.3) and in general the integrated intensities of these transitions follow A_V quite well. Even the material, which connects the cores, can be seen in both emission lines. The shape of the cores as seen in N_2H^+ and NH_3 strengthen the suspicion, that the two cores shown in A_V are indeed one. Furthermore an additional core shows up at $\Delta\alpha = 500''$, $\Delta\delta = -20''$. In the A_V map this feature appears just as an appendage. The western core, which is core #2 in Kramer et al. (2003), located at $\Delta\alpha = 335''$, $\Delta\delta = -45''$ seems to be elongated in the north-west direction in A_V, whereas it appears rather roundish in the N-bearing species. A secondary peak of core #2 at $\Delta\alpha = 390''$, $\Delta\delta = -80''$ shows up only in N_2H^+, but not in NH_3.

At low A_V (< 15 mag) the $C^{18}O$ 2-1 map matches the optical extinction best. The northern core, shown in NH_3 and N_2H^+, cannot be seen as an individual core in $C^{18}O$ but looks rather like A_V. Core #2 shows an elongated shape in $C^{18}O$ as well. Even gas with low column density, which shows up south of the material bridge seen in N-bearing species, is traced by $C^{18}O$ as well as by A_V. But at higher optical extinction (A_V > 20 mag) this correlation gets weaker and weaker. The western core looks rather like a plateau than a peaked structure and the integrated $C^{18}O$ intensity even seems to have a dip at the position of the A_V maximum. The correlation between A_V and $C^{18}O$ 2-1 gets weaker towards the center of the main core too. But due to the ambiguity of the determination of A_V around Elias 1-12 this weakening might be due to observational effects.

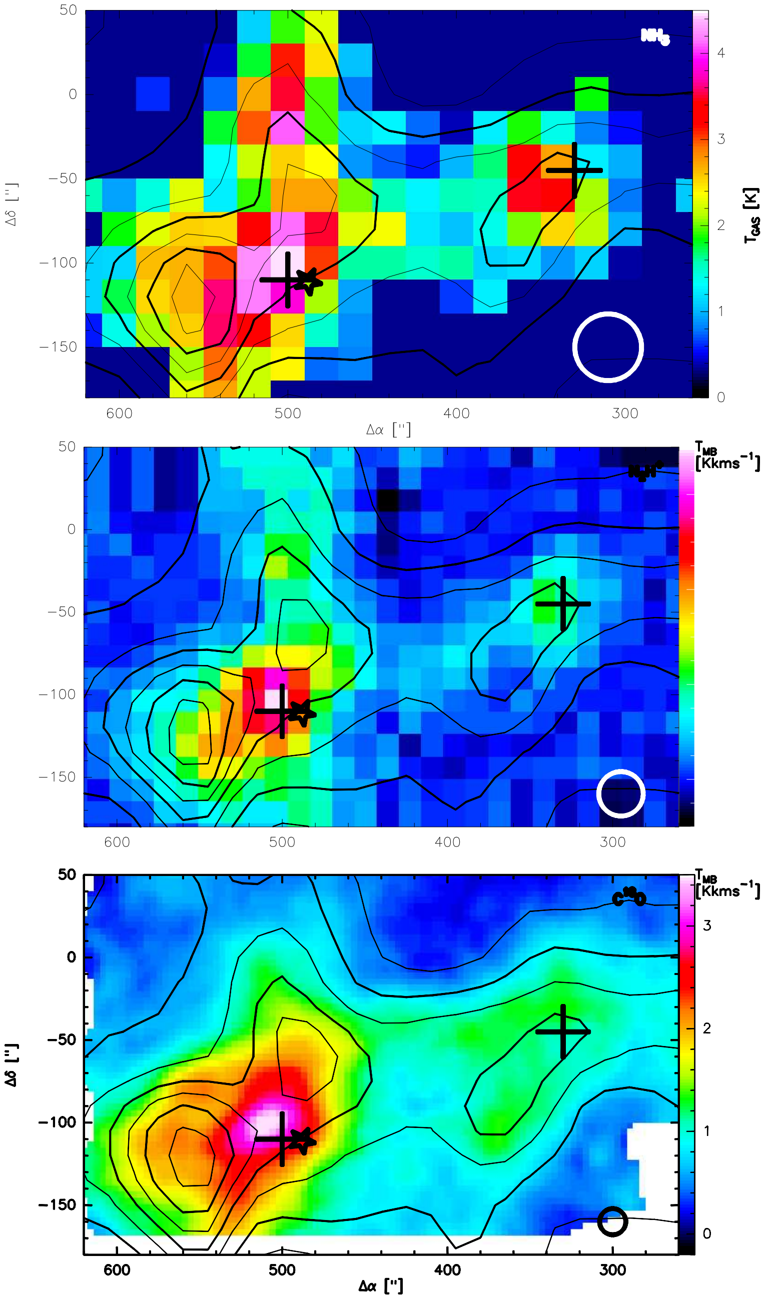

Fig. 5.3: *The integrated intensity of* NH_3 *(1,1) (upper panel),* N_2H^+ *1-0 (middle panel) and* $C^{18}O$ *2-1 (lower panel) of the eastern core of IC 5146 (color). The contours are in all three maps the optical extinction* A_V*. The stars mark the position of Elias 1-12 and the crosses Position 1 and Position 2, respectively. The circle at the lower right corner of each map indicates the HPBW of the respective observations.*

Correlation between molecular line intensities and optical extinction

In Fig. 5.4 the correlation between the integrated line intensity of the various lines and the optical extinction are shown. As already seen in the maps $C^{18}O$ 2-1 correlates

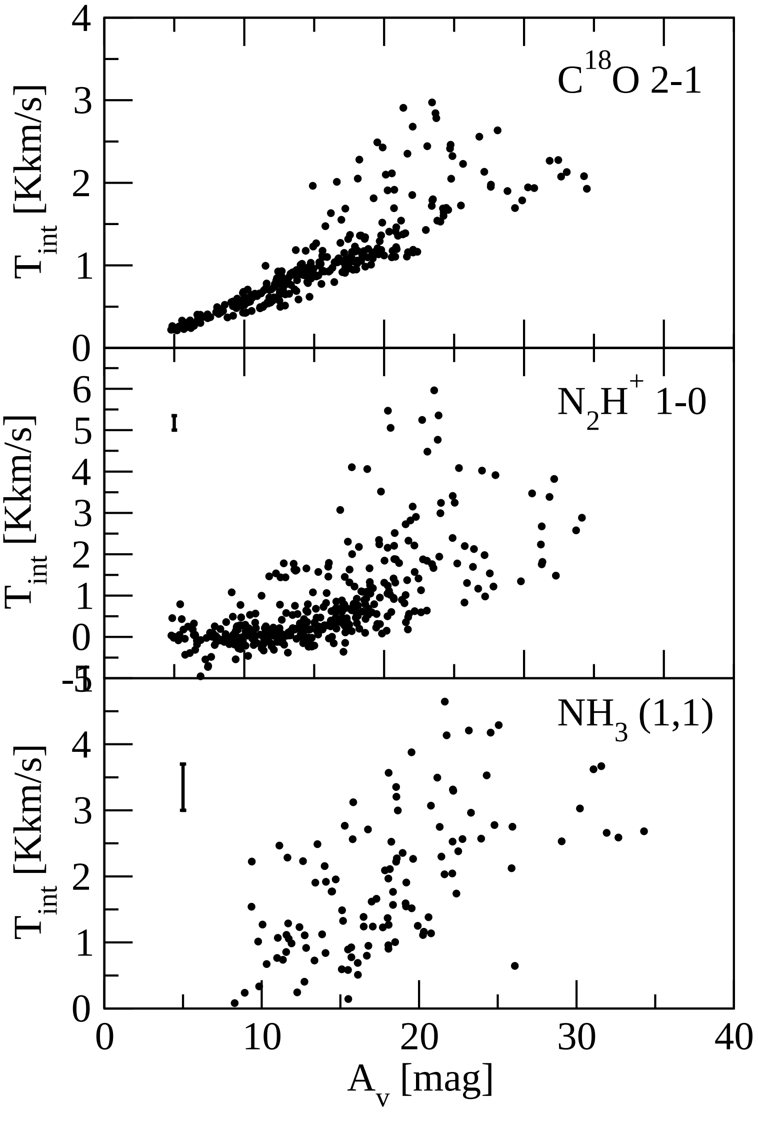

Fig. 5.4: *Scatter plot of the integrated line intensity of the three molecules versus the optical extinction* A_v*. At the upper left corner the error bars are plotted*

very well with Av up to 15 magnitudes, but above this value the correlation is weaker. The same is true for N_2H^+, however, below an extinction of 15 mag hardly any N_2H^+ emission is detected. At high extinctions the N_2H^+ emission rises quite fast compared to the increase of the $C^{18}O$ intensity. A correlation, similar to the one of N_2H^+, can be found between the NH_3 integrated intensity and optical extinction as well, although it shows a large scatter. This scatter is partly due to a larger error of the obtained integrated intensity of NH_3, but temperature difference and optical depth effects might play a role, too.

Line Width

In Fig. 5.5 the FWHM of the N_2H^+ line is shown. The line width is rather narrow throughout the cloud ($\Delta v \leq 0.8$ km/s). Only a narrow strip from north-east to south-west right through the geometric center of the main core shows somewhat lager line widths (> 1 km/s). Towards the western core and the north of the region the line gets as narrow as 0.5 km/s, indicating that these cores are still quiescent. In general the N_2H^+ 1-0 line width we found is somewhat larger than the line width found in starless cores (< 0.5 km/s, Crapsi et al. 2005), but they lie well in the range of line widths of protostars (Mardones et al. (1997) found line widths between 0.29 km/s and 1.84 km/s in protostars).

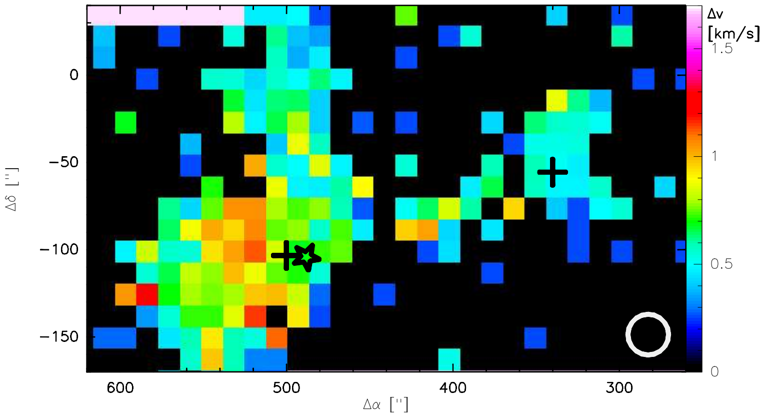

Fig. 5.5: *Line width of the N_2H^+ 1-0 line. The markers indicate the same positions as in Fig. 5.2.*

5.3.2 Spectra

In the following section we show some spectra towards selected positions. The first position is at 500″/-110″ (hereafter Position 1), which is close to the absolute maximum of the integrated intensities of all three molecular tracers. Furthermore it is quite close to the position of Elias 1-12 ($\Delta\alpha = 488''$, $\Delta\delta = -111''$). The second position is at the peak of the western core ($\Delta\alpha = 335''$, $\Delta\delta = -50''$ hereafter Position 2), which does not show any sign of star formation (Dobashi et al. 1993). The individual spectra are shown in Fig. 5.6 & 5.7.

Whereas at Position 1 all lines have been detected, at Position 2 just an upper limit for the $H^{13}CO^+$ line of 0.16 K is available. Most lines show as narrow line widths as the N_2H^+ line (see above). The only exception is the $H^{13}CO^+$ line at Position 1. The line width determined by a single Gaussian fit ($\Delta v = 1.41$ km/s see Tab. 5.2) is already significantly larger than the one of N_2H^+. Furthermore it seems to be the case

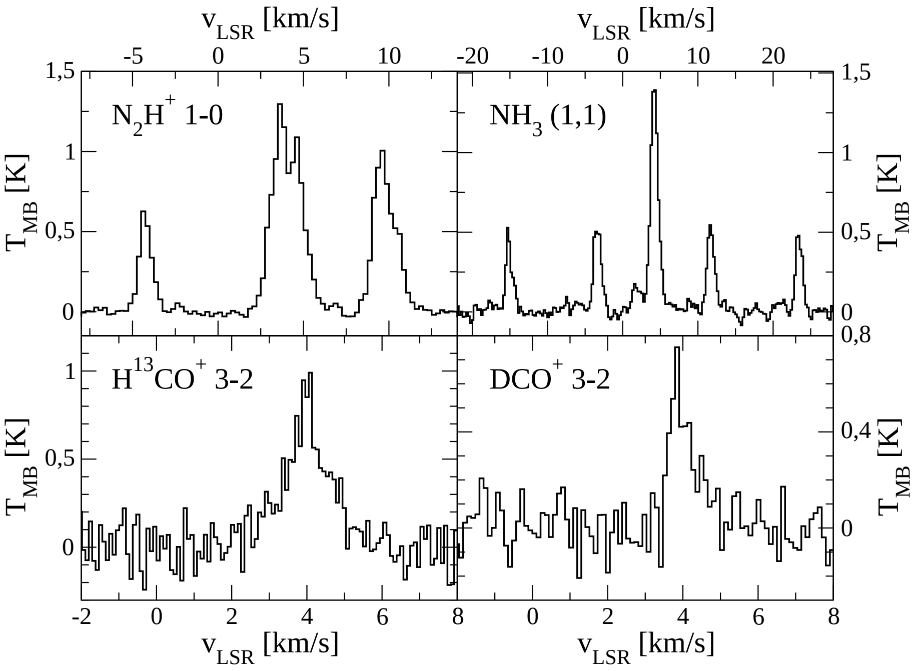

Fig. 5.6: *Spectra towards position 1 ($\Delta\alpha = 500''$, $\Delta\delta = -110''$).*

Tab. 5.2: *Observational data of the observed transitions. The data are obtained by Gaussian fit. In the cases of NH_3 (1,1) and N_2H^+ 1-0, all hyperfine components were fitted by a Gauss*

Tracer	T_{mb} [K]	v_{LSR} [kms^{-1}]	Δv [kms^{-1}]
		Pos.1	
N_2H^+ 1-0	1.30 ± 0.07	4.01 ± 0.1	0.87 ± 0.03
NH_3 (1,1)	1.39 ± 0.04	4.13 ± 0.1	0.93 ± 0.03
NH_3 (2,2)	0.32 ± 0.03	4.00 ± 0.1	1.00 ± 0.08
$H^{13}CO^+$ 3-2	0.91 ± 0.20	4.04 ± 0.1	1.41 ± 0.1
DCO^+ 3-2	0.69 ± 0.10	4.00 ± 0.1	0.81 ± 0.1
		Pos.2	
N_2H^+ 1-0	0.52 ± 0.07	4.21 ± 0.1	0.53 ± 0.02
NH_3 (1,1)	1.36 ± 0.03	4.38 ± 0.1	0.60 ± 0.10
NH_3 (2,2)	0.22 ± 0.03	4.36 ± 0.1	0.66 ± 0.12
$H^{13}CO^+$ 3-2	< 0.16	-	-
DCO^+ 3-2	0.34 ± 0.07	4.19 ± 0.1	0.61 ± 0.09

that the line consists of two velocity components. A narrow one, with an FWHM of 0.4 km/s, and a broader one with a line width of 1.74 km/s. The v_{LSR} is 4.0 kms^{-1} and ~ 4.2 kms^{-1} at position 1 and position 2, respectively. At position 1 the velocities of the individual lines agree fairly well, even the somewhat high v_{LSR} NH3 (1,1) is still within the range of error. The isotopologues of HCO^+ show a slight asymmetry in line shape at position 1. A similar asymmetry is found in ^{12}CO 1-0 towards Elias 1-12 (Dobashi et al. 1993) and is most likely an indication of an outflow. Towards position 2 the velocity of the NH_3 lines is ~ 0.15 kms^{-1} higher than the velocity of the other lines. This might be caused by the lower spatial resolution and lower critical density of the ammonia transition. The data of the observed lines are listed in Tab. 5.2.

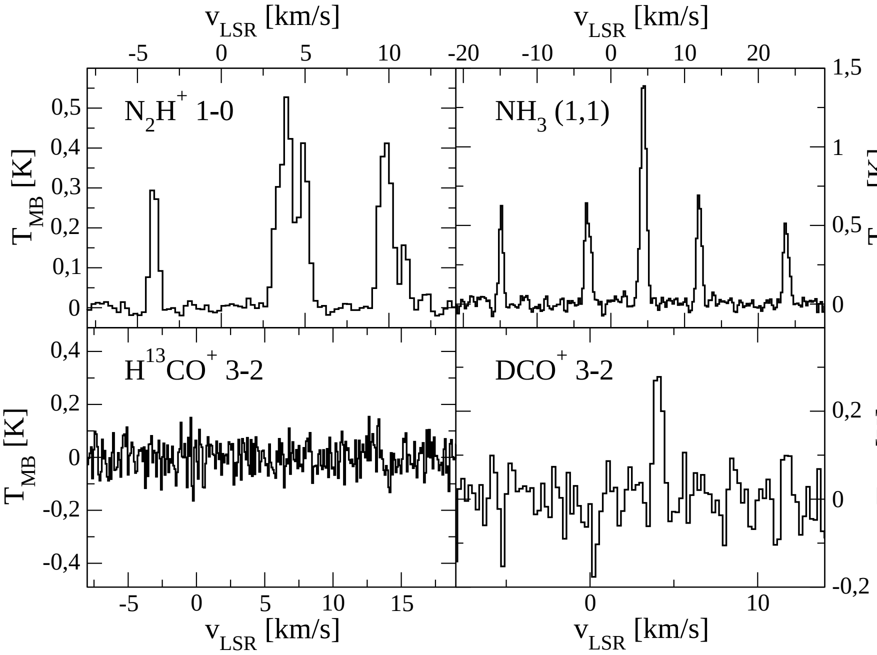

Fig. 5.7: *Spectra towards position 2 ($\Delta\alpha = 335''$, $\Delta\delta = -50''$).*

The most noticeable difference between the two sets of spectra is the non detection of $H^{13}CO^+$ 3-2 at Position 2, whereas DCO^+ is detected in both cores. This indicates that the physical conditions, especially the temperature, at the two positions are different. This suspicion is strengthened by the fact that the other lines are stronger towards Position 1 as well. Together with the slightly different line width and the asymmetry of the HCO^+ isotopologues these differences indicate, that the gas at Position 1 is warmer and less quiescent than the gas at Position 2. Therefore the gas at Position 1 might be influenced by embedded protostars.

5.3.3 Gas temperature

For the positions at which NH_3 (2,2) is detected, the gas temperature can be determined straight forward following Ho & Townes (1983)

$$\mathrm{T_R} = -41.5/\ln\left[\frac{-0.282}{\tau_\mathrm{m}(1,1)}\ln\left\{1 - \frac{\Delta\mathrm{T^*_a}(2,2,\mathrm{m})}{\Delta\mathrm{T^*_a}(1,1,\mathrm{m})}\cdot(1-\mathrm{e}^{-\tau_\mathrm{m}(1,1)})\right\}\right] \tag{5.42}$$

where ΔT_a^* is the observed brightness temperature, τ the optical depth and $\mathrm{T_R}$ the rotational temperature of ammonia. For all other positions we determined an upper limit for T_R using the 3σ level of the NH_3 (2,2) spectrum as upper limits for $T_a^*(2,2,m)$.

In the case of optically thin NH_3 (1,1) lines, i.e., in cases where τ of the NH_3 (1,1) line could not be determined, we calculated the temperature using

$$\mathrm{T_R} = -41.5/\ln\left[\frac{-0.282\cdot\Delta\mathrm{T^*_a}(2,2,\mathrm{m})}{\Delta\mathrm{T^*_a}(1,1,\mathrm{m})}\right] \tag{5.43}$$

which is the equation quoted above in the optical thin limit. In general, the rotational temperature of ammonia is somewhat lower than the kinetic temperature of the gas, but at temperatures below 20 K this difference is not significant (Ho & Townes 1983).

The resulting temperature map is shown in Fig 5.8. It can be seen that the temperature inside the cores is $\approx$ 10 K. Just towards the center of the main core the temperature is enhanced and reaches values of 17 K. The position of enhanced gas temperature coincides with the position of wider line width as mentioned in Section. 5.3.1. Both the enhanced temperature as well as the increased line width are a clear indication for ongoing star formation. The increase of temperature towards the edges of the cloud has to be treated with caution, since these temperatures are just upper limits.

Kramer et al. (2003) investigated the dust temperature towards the western core of our sample. The temperature they found is slightly higher than the gas temperature found here. Whereas the gas temperature is about 10 K, dust temperatures are 15 K at the central part of the core and it is rising quickly towards the cores' outskirts. However, this can be possibly explained by observational effects.

5.4 Abundance profiles of pre- and protostellar cores

In this section we want to point out the chemical differences of starless cores and cores with embedded protostars. At first we have to proof that core at Position 2 is indeed a prestellar core, whereas the main core is a good candidate for a protostellar environment, since Elias 1-12 is embedded in it.

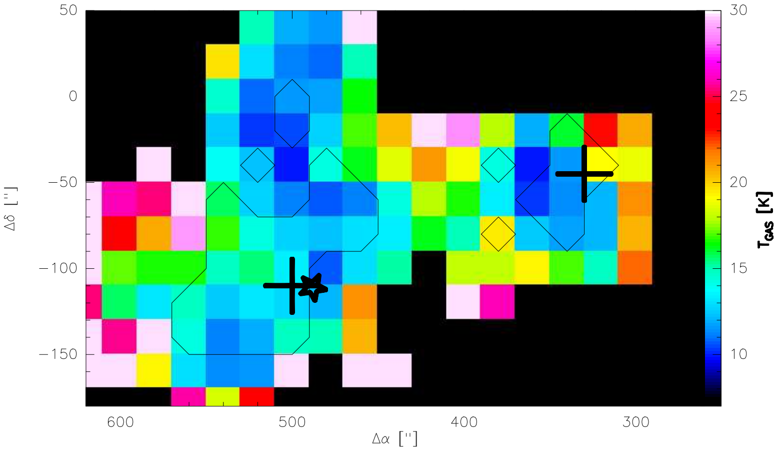

Fig. 5.8: *Map of the gas temperature determined from the* NH_3 (2,2)/NH_3 (1,1) *ratio. The black line is surrounding the area in which* NH_3 *(2,2) is detected with an S/N ratio larger than 3. Outside the contour a* 3σ *upper limit for* NH_3 *(2,2) is used. The markers indicate the same positions as in Fig. 5.2.*

5.4.1 The Core at Position 2 - A prestellar core?

Since the NH_3 (2,2) line has been detected towards Position 2, gas temperatures could be determined to be 10 K throughout the core. This is a typical temperature for dark cores devoid of IRAS sources (Jijina et al. 1999), but as mentioned above lower than the dust temperature.

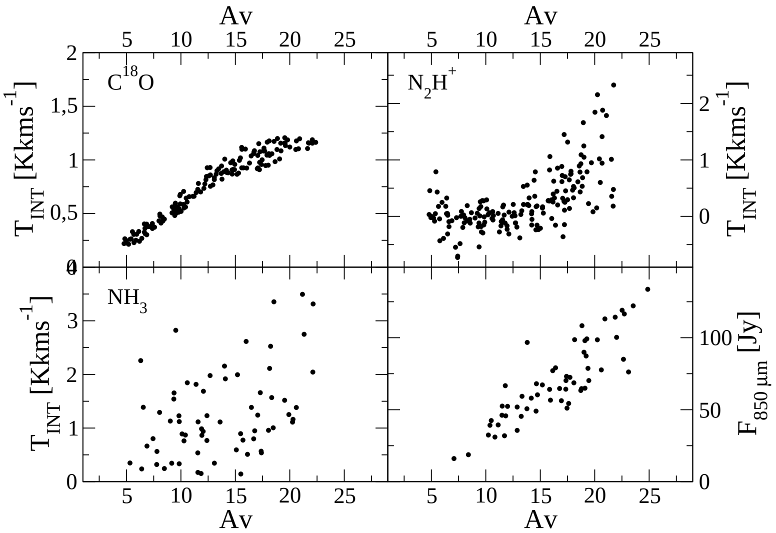

Fig. 5.9: *Scatter plot of the integrated intensities of* $C^{18}O$ *2-1,* N_2H^+ *1-0,* NH_3 *(1,1) and the* 850 μm *continuum versus* A_V.

In Fig. 5.9 the scatter plots of the integrated intensities of $C^{18}O$ 2-1, N_2H^+ 1-0, NH_3 (1,1) and the 850 μm continuum versus A_v of the western core are shown. In general the correlations of these intensities are much better than the one for the entire region, which indicates that the physical conditions in the western core are rather homogeneous. $C^{18}O$ 2-1 increases linearly with A_v up to $\approx$ 15 mag and seems to be constant above, indicating that CO freezes out onto dust grains at higher optical extinction. Contrary to $C^{18}O$, the integrated intensities of N_2H^+ and NH_3 stay low until A_v = 15 mag and subsequently rises quickly with A_v. The steep increase in N_2H^+ and NH_3 intensity is most likely due to depletion of CO, which destroys N_2H^+ and hampers the formation of NH_3. Because of the similarity of the trends of NH_3 and N_2H^+, it seems to be the case that NH_3 (1,1) and N_2H^+ 1-0 emission trace the same kind of gas. The main difference of the trends is that the scatter in the NH_3 vs. A_v correlation is much larger.

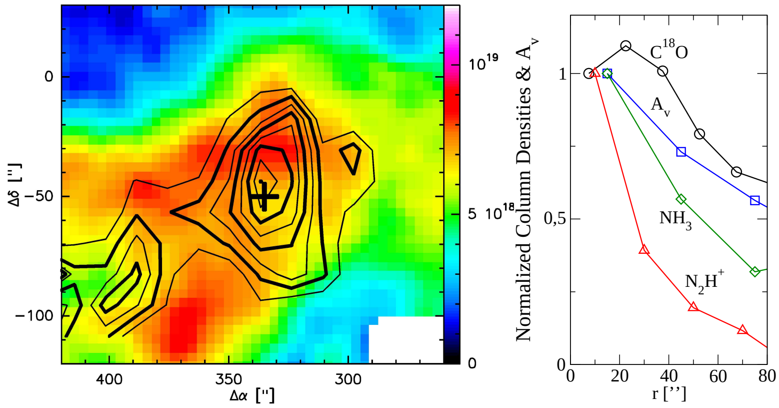

Fig. 5.10: **Left:***Map of the core at Position 2. The colors are N($C^{18}O$). Contours show N(N_2H^+). The cross marks the central position for the radial averaging.* **Right:** *The normalized radial averaged N($C^{18}O$) (○),* N(N_2H^+) (△), *N(NH_3) (◇) and A_v (□). The central column densities are* $6.9 \cdot 10^{14}$ cm^{-3}, $4.1 \cdot 10^{12}$ cm^{-3}and$4.3 \cdot 10^{14}$ cm^{-3} *for $C^{18}O$, N_2H^+ and NH_3, respectively. The optical extinction at the center is 21 magnitudes.*

Column densities and optical extinction in core #2

In Fig. 5.10 a map and normalized radial profiles of A_v and column densities of NH_3, $C^{18}O$ and N_2H^+ are shown. For the averaged radial profile of all data, a central position of the core of $\Delta\alpha = 335''$, $\Delta\delta = -50''$, i.e., position 2, was used. Column densities were calculated assuming LTE and a constant excitation temperature of 10 K, using the formula

$$N_{tot} = \frac{8\pi^{3/2}\Delta v}{2\sqrt{ln2}\lambda^3 A} \frac{g_l}{g_u} \frac{\tau}{1-\exp(-h\nu/kT_{ex})} \frac{Q_{rot}}{g_l \cdot \exp(-E_l/kT_{ex})} \tag{5.44}$$

or

$$N_{tot} = \frac{8\pi \cdot W}{\lambda^3 A} \frac{g_l}{g_u} \frac{1}{J_\nu(T_{ex}) - J_\nu(T_{bg})} \frac{1}{1 - \exp(-h\nu/kT_{ex})} \frac{Q_{rot}}{g_l \cdot \exp(-E_l/kT_{ex})} \tag{5.45}$$

for optically thick and optically thin emission, respectively (see appendix of Caselli et al. (2002b)). For NH_3 and N_2H^+ the optical depth τ was determined by fitting the hyperfine structure (see chapter 6), whereas $C^{18}O$, as well as $H^{13}CO^+$ and DCO^+, were assumed to be optical thin. The H_2 column density was calculated form the A_v data by using the relation given by Frerking et al. (1982):

$$N_{H_2} = 9.4 \cdot 10^{20} A_v \text{ (mag)} \quad [\text{cm}^{-2}] \tag{5.46}$$

The derived column densities are listed in Tab. 5.3. Since at the center of the western core hardly any background stars are detected, the determination of the central A_v fails. The given value is derived by a convolution of the detected stars with a Gaussian, and thus has to be considered as a lower limit.

Tab. 5.3: *Column densities at Position 2 and the relative abundances of the molecules investigated*

Molecule	Column Density [cm^{-2}]	Relative Abundances
H_2 (from A_v)	$2 \cdot 10^{22}$	1
$C^{18}O$	$6.9 \cdot 10^{14}$	$3.45 \cdot 10^{-8}$
N_2H^+	$4.1 \cdot 10^{12}$	$2.05 \cdot 10^{-10}$
NH_3	$1.47 \cdot 10^{14}$	$7.35 \cdot 10^{-9}$
$H^{13}CO^+$	$< 6.35 \cdot 10^{10}$	$< 3.18 \cdot 10^{-12}$
DCO^+	$1.65 \cdot 10^{11}$	$8.25 \cdot 10^{-12}$

From the averaged profile (Fig. 5.10) one can see that the nitrogen bearing species follow the trend, which can be seen in continuum and extinction data quite well, whereas the $C^{18}O$ abundance profile shows clearly a central dip. Furthermore the $C^{18}O$ column density falls off less steep than the column densities of the other molecules. In the map of Fig. 5.10 it can be seen that $C^{18}O$ and N_2H^+ appear to be complementary. Assuming a $^{12}C^{16}O/^{12}C^{18}O$ ratio of 500 (Wilson & Rood 1994), we derived a CO/H_2 ratio of $1.2 \cdot 10^{-5}$. Assuming a canonic abundance ratio of CO/H_2 of $9 \cdot 10^{-5}$ this leads to a depletion factor f_D (= $x_{can.}/x_{obs.}$) of 5.2, when compared with $N(H_2)$ derived from A_V.

The high deuterium fractionation at Position 2 should be noticed as well. Since $H^{13}CO^+$ 3-2 has not been detected (see Fig. 5.7) we can give a lower limit of the DCO^+/HCO+ ratio only. The integrated intensity of DCO^+ 3-2 is 0.13 Kkms^{-1}, as upper limit for the $H^{13}CO^+$ line we used 0.047 Kkms^{-1} (3σ). With $^{12}CO/^{13}CO$ ratios of 65 (Frerking et al. 1982) this lead to a lower limit of the DCO^+/HCO+ ratio of 0.04.

All results mentioned above indicate that this core is indeed a prestellar core. Both, the low temperatures as well as the large CO depletion factor, which is most likely due to the freeze out of CO onto dust grains, are typical for this kind of objects (see e.g., Tafalla et al. 2002). The radial abundance profiles are very similar to those of L 1544 (Caselli et al. 2002b), which is one of the best studied prestellar cores. Even the lower limit (0.04) of the DCO^+/HCO^+ ratio is consistent with the ratios of other prestellar cores. For example, a ratio of 0.06 has been observed in L 1544 (Caselli et al. 2002b), whereas Jørgensen et al. (2004) found DCO^+/HCO^+ ratio < 0.02 in a sample of protostellar cores. However it should be mentioned that L 1544 as well as the objects observed by Jørgensen et al. (2004) exhibit larger column densities than the core investigated here.

Modeling the internal structure of core #2

To derive the physical conditions inside the core we calculated a model, assuming a density profile of a Bonnor-Ebert Sphere, which is embedded into molecular material of a density of $5 \cdot 10^3$ cm^{-3}. This low density material represents the cloud filament, in which the core is embedded. To match the observed A_V in the vicinity of the core, the thickness of the cloud filament was adopted to be 0.487 pc. Furthermore we assumed that the dust temperature is low at the inner part of the core, whereas it is warmer towards the outskirts, as suggested by the projected dust temperature profile given by Kramer et al. (2003). CO is adopted to be completely depleted in the innermost part of the core. Further outwards its relative abundance is assumed to rise until the canonical value for the $C^{18}O/H_2$ ratio is reached. For the conversion of the angular scales into physical sizes a distance of 460 pc was used (Lada et al. 1999). The central position of the core was set to $\Delta\alpha = 335''$, $\Delta\delta = -50''$.

We compared the model results with the observed optical extinction and the apparent dust temperature, which is the dust temperature calculated from the ratio of the 450 μm and the 850 μm continuum flux, using the following equation:

$$\frac{S_{450}}{S_{850}} = \left(\frac{850}{450}\right)^5 \frac{\exp(17\ \mathrm{K}/T_{\mathrm{dust}}) - 1}{\exp(32\ \mathrm{K}/T_{\mathrm{dust}}) - 1} \tag{5.47}$$

The modeled dust continuum was derived by integrating along the line of sight over the dust emissivity, which we calculated via

$$\frac{S_\lambda}{A_V} = B_\lambda(T_{\mathrm{dust}})\Omega_\lambda \frac{1}{1.086}\frac{\kappa_\lambda}{\kappa_V} \tag{5.48}$$

where $B_\lambda(T_{\mathrm{dust}})$ is the Planck function, Ω_λ the main beam solid angle and κ_λ the extinction coefficient. For this analysis a $\frac{\kappa_\lambda}{\kappa_V}$ of $2.1 \cdot 10^{-5}$ and a spectral index β of 2 were assumed. To avoid the problem of the difficult determination of A_V at the center of the core, we fitted our model to the optical extinction of the individual stars instead

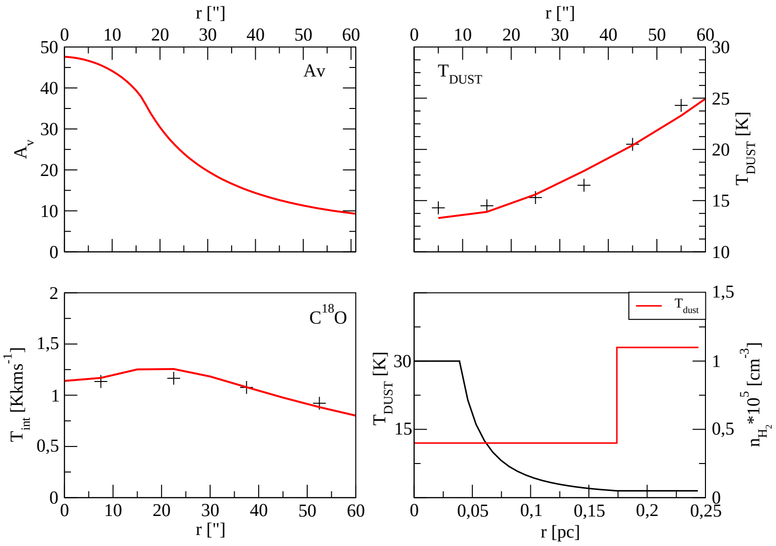

Fig. 5.11: *In the first three plots comparisons of radial averaged quantities, such as Av, apparent* $T_{\rm Dust}$ *and the integrated intensity of* $C^{18}O$ *(crosses) with the model results (red solid line) are shown. The central position of the core was set to the peak of the optical extinction, which is at* $\Delta\alpha = 335\,''$; $\Delta\delta = -50\,''$. *The fourth plot shows the* H_2 *density and the local dust temperature as function of the radius.*

of using the convolved A_V map. Therefore we reached much larger optical extinctions towards the core center (47 mag instead of the lower limit of 21 mag).

In Fig. 5.11 the results of the modeling are shown. The radius of the central density plateau of the Bonnor-Ebert Sphere, at which an H_2 density of $5 \cdot 10^5$ cm^{-3} is reached, is 0.0174 pc. From this point outwards the density drops $\propto r^{-2}$ until a density of $5 \cdot 10^3$ cm^{-3}, which is reached at a radius of 0.174 pc. The dust temperature in the interior of the core (12 K) is approximately a factor two lower than the one in the low density, surrounding material (33 K).

The profile of the gas temperature was derived from the Ammonia observations. We calculated radial averages of the NH_3 (1,1) and (2,2) spectra with a spacing of 20$''$ and reproduced these lines using the 1-dimensional radiative transfer code SimLine (Ossenkopf et al. 2001). Since the density profile was already fixed by the extinction measurements and the continuum observations, the gas temperature and the abundance of NH_3 were the only free parameter. A comparison between observed and modeled spectra is shown in Fig. 5.12. As results we got a relative NH_3 abundance of $2.5{\cdot}10^{-9}$, which is constant throughout the entire core. The gas temperature, we derived is 10 K in the dense part of the core and increases to 15 K in the low density ($n = 5 \cdot 10^3$ cm^{-3}) environmental material.

The $C^{18}O$ intensity was modeled using SimLine again. According to our model CO is frozen out completely within the inner 0.04 pc. Further outwards the relative $C^{18}O$

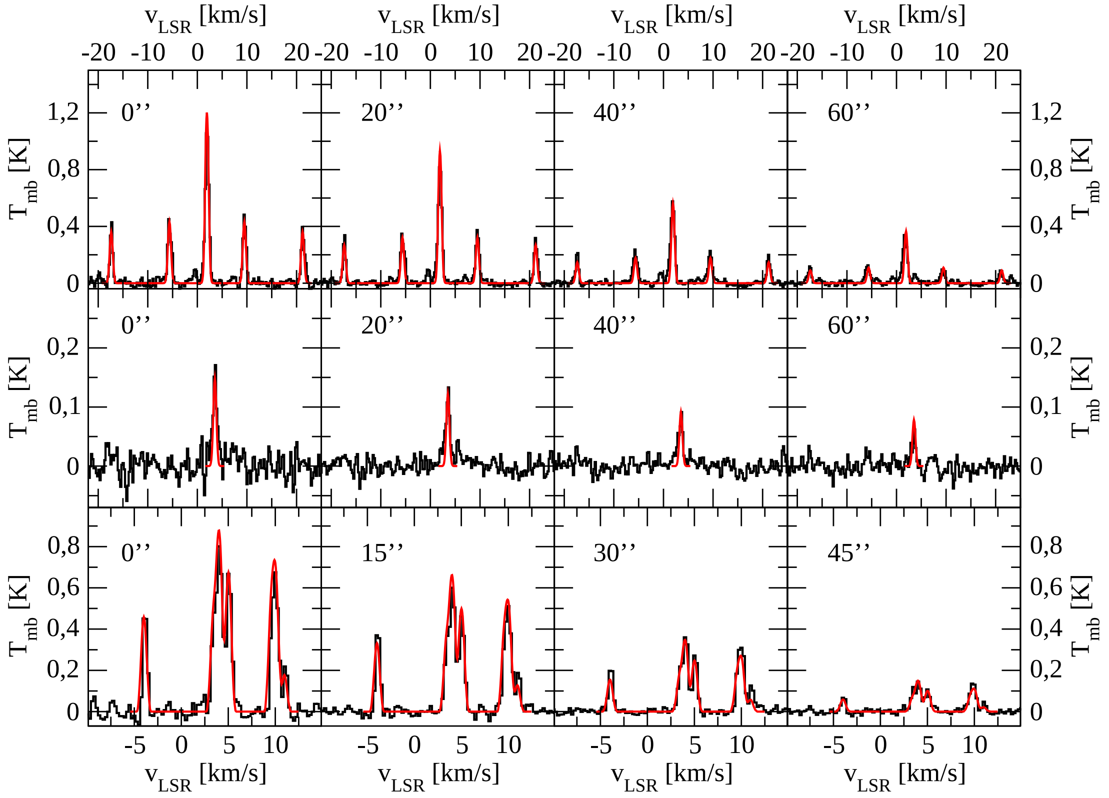

Fig. 5.12: *Observed (black) and modeled (red) spectra of NH_3 (1,1) (upper row), NH_3 (2,2) (middle row) and N_2H^+ 1-0 (lower row) of core #2. The observed spectra are radial averages at* 0″, *20″, 40″ and* 60″ *(NH_3) and* 0″, *15″, 30″ and* 45″ *(N_2H^+), respectively.*

abundance increases until it reaches its canonical value ($\frac{[C^{18}O]}{[H_2]} = 1.696 \cdot 10^{-7}$) at 0.174 pc (Fig. 5.13). Using a step function for the CO abundance, i.e., assuming that the CO abundance is zero below a certain radius and using the canonical value above, does not match with the rather smooth dip, which is seen in the integrated intensity map. Therefore some kind of moderately increasing CO abundance has to be adopted. This is actually in good agreement with theoretical models (e.g., Lee et al. 2004). A decrease of the gas temperature towards the center of the core, which would cause the dip of the $C^{18}O$ intensity, too, can be ruled out by the NH_3 data. However, even at a gas temperature of 5 K in the inner part of the core a CO depletion factor of at least 15 is needed to match the observations.

For modeling the N_2H^+ emission, we used a non-LTE Monte-Carlo code developed by Pagani et al. (2007). This code, which is developed from the Bernes code ((Bernes 1979)), is calculating the 1D radiative transfer of both N_2H^+ and N_2D^+ and includes, contrary to SimLine, a correct treatment of the line overlap of the individual hyperfine transitions. Furthermore the code makes use of recently published collisional coeffi-

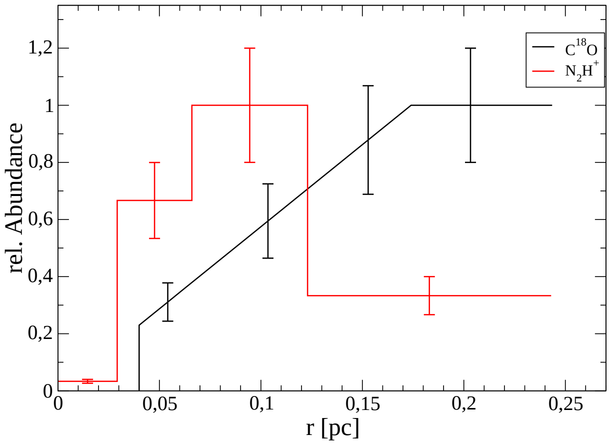

Fig. 5.13: **Left:** *Local density of* $C^{18}O\times10^3$ *(black) and* $N_2H^+\times10^5$ *(red).* **Right:** *Relative abundances of* N_2H^+ *(red) and* $C^{18}O$ *(black). The abundances are normalized to the abundance at the outskirts of the core, which is* $5.25\cdot10^{-10}$ *and* $1.676\cdot10^{-7}$ *for* N_2H^+ *and* $C^{18}O$*, respectively.*

cients between individual hyperfine levels (Daniel et al. 2005). As input parameter, we used the density and the temperature-profile derived from the A_v data and the NH_3 observations, respectively. Thus, the local N_2H^+ abundance is the only free parameter. We compared the modeled line profiles with radial averages of the observed line spectra at radii of 0″, 15″, 30″ and 45″ from the center ($\Delta\alpha = 335''$, $\Delta\delta = -50''$). The best-fit results are shown in Fig. 5.12, lower row. The best fit result gives an abundance of N_2H^+ relative to H_2 of $1.0\cdot10^{-10}$ for the outer parts of the cloud. Towards smaller radii the N_2H^+ abundance increases, most likely because CO, which destroys N_2H^+, starts to deplete. At a radius of 0.1 pc, an N_2H^+ abundance of $3.0\cdot10^{-10}$, which is the maximum, is reached. Further inwards the N_2H^+ abundance drops again, possibly due to the freeze out of N_2, the parent species of N_2H^+. At the core's center an abundance of $1.0\cdot10^{-11}$ is reached. The abundance profile of N_2H^+ and $C^{18}O$ are shown in Fig. 5.13.

Comparison with other prestellar cores

Comparing the results we found for core #2 with results from the literature, it seems to be an ordinary prestellar core. The central density of this core ($n_{cen.} = 5\cdot10^5$ cm^{-3}) is approximately the same as in B 68 (Alves et al. 2001, Bergin et al. 2006) and the difference in the modeled central opacity is due to the fact that core #2 is embedded into a cloud filament. Thus, core #2 has a rather low central density. Many other prestellar cores, e.g. L 1544 and L 183, show central densities, which are a factor 10 higher (Crapsi et al. 2007, Pagani et al. 2007).

For the core itself, we found a constant gas temperature of 10 K and only in the low density ($n = 5 \cdot 10^3$ cm^{-3}) environment the temperature increases to 15 K. A constant temperature throughout the prestellar core has been assumed by Tafalla et al. (2002), too. In some prestellar cores a temperature decrease towards the center has been found (e.g., L 1544, Crapsi et al. (2007) and B68, Bergin et al. 2006), which might be present here as well, but resolved out due to the larger distance of this object.

The $C^{18}O$ abundance profile agrees very well with the abundance profile of other prestellar cores (Tafalla et al. 2002, Bergin et al. 2006). In all analyses CO is almost completely depleted at the center of the core and increases outwards until the canonical value is reached. Such an abundance profile is also confirmed by theoretical models (Lee et al. 2004). The N_2H^+ abundance, which we found in this work, is very similar to the one found in L 183 (Pagani et al. 2007). In both cases the N_2H^+ abundance increases with increasing density, but is strongly depleted in the innermost regions of the core. The N_2H^+ abundance profile found in B68 (Maret et al. 2007) looks qualitatively similar, but is an order of magnitude lower than the abundances found here. However, in their paper Maret et al. (2007) state, that the predicted optical depth for N_2H^+ is lower than the observed one. For ammonia, we found a constant abundance throughout the entire core. In many other prestellar cores the abundance of NH_3 increases towards the center (Tafalla et al. 2002, Crapsi et al. 2007). Only in L 1400K Tafalla et al. (2002) found a constant NH_3 abundance, too.

5.4.2 The structure of the protostellar core

In this section we want to point out the different physical and chemical conditions in prestellar and protostellar cores by comparing the molecular abundances in the main core and core #2 (see Fig. 5.6 & 5.7).

On the 40″ resolution of our NH_3 data the gas temperatures of Position 1 (15 K) is considerably higher than the one of Position 2 (10 K). Additionally $H^{13}CO$ 3-2 is very strong at Position 1, also indicating that gas temperatures at the cores center might be warmed up by the embedded protostar. At Position 1 we calculated a DCO^+/HCO^+ ratio of 0.0098, assuming again LTE (15 K) and an $H^{12}CO^+/H^{13}CO^+$ ratio of 56. The DCO^+/HCO^+ ratio is rather insensitive to the adopted temperature. An assumed gas temperature of 50 K, for example, leads to a ratio of 0.0102, only 4 % higher than the one at 10 K. Both values are smaller than the one expected for starless cores and even smaller than the one found in Class 0 protostars by Jørgensen et al. (2004). Furthermore, the detection of emission lines of atoms and atomic ions (Lorenzetti et al. 2000) towards Elias 1-12 indicates that the chemistry is influenced by the protostar.

The scatter plots of the integrated intensities of $C^{18}O$ 2-1, N_2H^+ 1-0 and NH_3 (1,1) versus A_V in the environment of Elias 1-12 are shown in Fig. 5.14. Contrary to the scatter plots of Position 2 all three correlation show a quite linear, indicating, that the

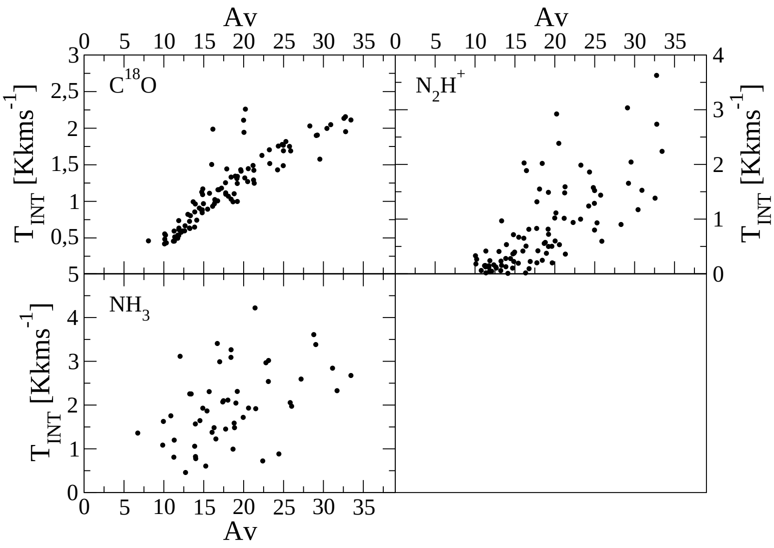

Fig. 5.14: *Scatter plots of $C^{18}O$ 2-1, N_2H^+ 1-0 and NH_3 (1,1) integrated intensity versus optical extinction around Elias 1-12. Data points in the close vicinity of Elias 1-12 (r< 50″) are excluded, because of the difficulties in determining A_V.*

chemistry does not change a lot with optical extinction. This is expected, because the embedded protostar heats the material, and thus significant changes in the chemistry, such as the freeze out of CO, should be less important than in prestellar cores. The slope of the correlation between $C^{18}O$ and A_V (0.0745 Kkm/s per mag) corresponds very well to the slope of the same correlation in core #2 at $A_V < 15$ mag. The slopes of the nitrogen bearing species (0.095 for N_2H^+ and 0.068 for NH_3) are in between the slopes of the corresponding species below $A_V = 15$ mag and above $A_V = 15$ mag in core #2.

Contrary to the prestellar core, this core shows a clearly elongated shape. Especially in N_2H^+, which traces the dense gas, due to its high critical density, the elliptical shape can be clearly seen (Fig. 5.3). To take this elongated shape into account, we averaged all quantities (A_V and integrated intensities) along ellipses rather than use the radial average to characterize the density- and temperature profile of the core. The ratio of the major to the minor axes of this ellipses are, derived from the N_2H^+ data, 1.75 and its orientations is 45° with respect to the north-south direction. For the following calculations we use the parameter *A* to describe the ellipses. *A* is:

$$A = \mathrm{r}/\sqrt{(1.75^2 \cdot \cos^2\Phi + \sin^2\Phi)} \tag{5.49}$$

where r is the distance from the center and Φ is the angle from the major axis. Thus *A* corresponds to the minor axis of the ellipse. The center of the ellipses was set to the peak position of the N_2H^+ at $\Delta\alpha = 508''$ and $\Delta\delta = -102''$, which is close to the position of Elias 1-12 (22″).

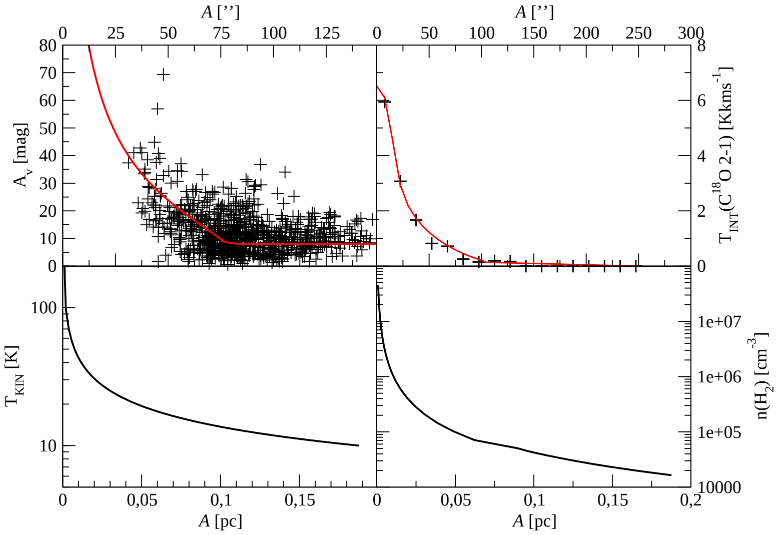

Fig. 5.15: *A_v versus A. The crosses indicate the positions and extinctions for the individual background stars. No stars closer than 50" to Elias 1-12 are taken into account. The red line is the result from the model fit (upper left panel). Averaged $C^{18}O$ emission (crosses) versus model result (upper right panel).The two lower panels display the kinetic temperature (left) and the H_2 density (right) as function of A.*

In order to disentangle the physical structure of the protostellar core we fitted a density profile $n(A) \propto A^{-\alpha}$, which is again embedded in a low density, ambient material. Since the optical extinctions derived from background stars closer than 50″ to Elias 1-12 are not reliable, we could only derive the density profile of outskirts of the protostellar envelope. However, as a final result we obtained a density of $n(H_2)=3.5 \cdot 10^4$ cm^{-3} at $A = 50''$, an exponent $\alpha = 1.5$, and an H_2 column density of $7.5 \cdot 10^{21}$ of the lower density, ambient material. The fit result is shown in Fig. 5.15.

The NH_3 (1,1) and (2,2) lines were used again to derive the temperature profile in the protostellar core as well, and SimLine was used for the modeling. The temperature profile, which explains the ammonia lines best, can be described by a power law with an index of -0.4. As a lower limit for the temperature we inferred 10 K, which is reached at a radius of 0.188 pc. In the inner 0.03 pc NH_3 is not abundant at all. Most likely, the ammonia is destroyed by the radiation from the embedded protostar. Between $A = 0.03$ pc and $A = 0.188$ pc region the NH_3 abundance is $1.7 \cdot 10^{-9}$, which is 68% of the value found in the core #2. However, further outwards the abundance is increasing by a factor of two.

N_2H^+ was modeled using the Monte-Carlo code, mentioned in section 5.4.1. As with core #2, we used in this case the temperature and density profile derived by fitting Av and NH_3 data, and therefore the relative abundance of N_2H^+ was the only free parameter again. The observed and modeled spectra of N_2H^+ 1-0 are shown in Fig. 5.16.

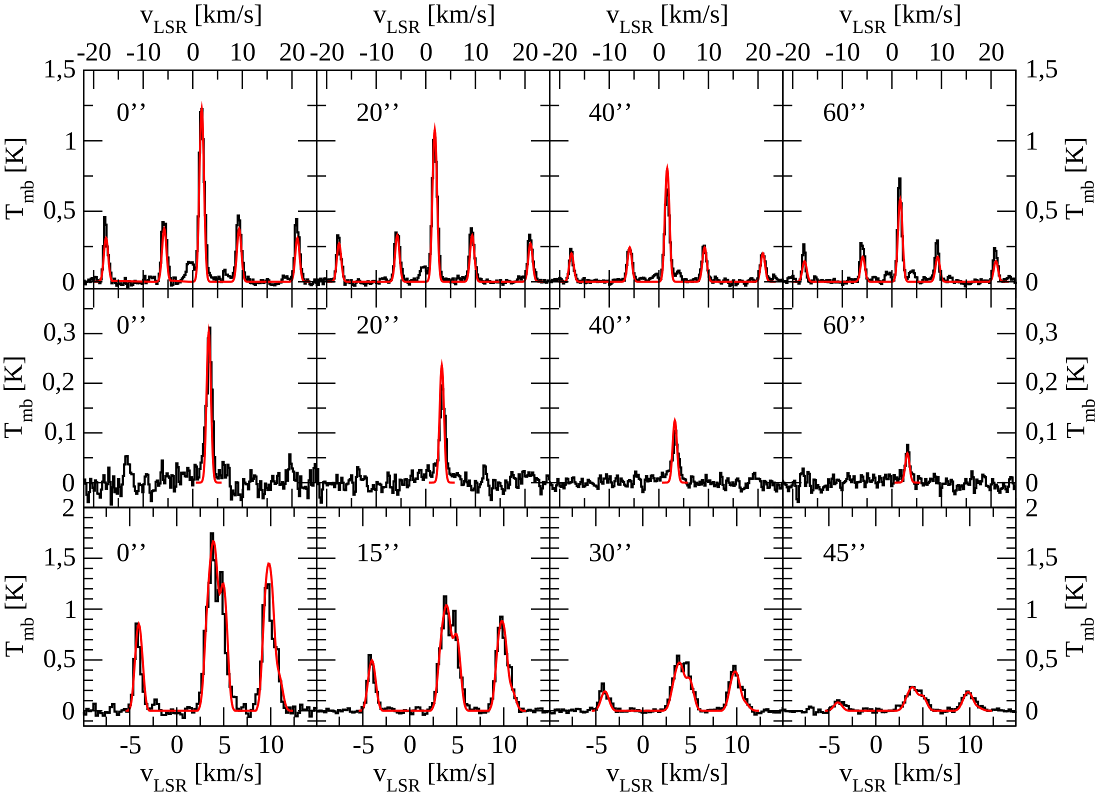

Fig. 5.16: *Observed (black) and modeled (red) spectra of NH_3 (1,1) (upper row), NH_3 (2,2) (middle row) and N_2H^+ 1-0 (lower row) of the main core. The observed spectra are radial averages at* 0″, *20″, 40″ and* 60″ *(NH_3) and* 0″, *15″, 30″ and* 45″ *(N_2H^+), respectively.*

Overall the model matches the observations quite well. N_2H^+ is, like NH_3, not present in the inner 0.03 pc of the core. When moving away from the center the abundance rises until a maximum of $3 \cdot 10^{-10}$ at a radius of 0.075 pc is reached, and decreases further outwards again. Thus, at its maximum the N_2H^+ abundance in the protostar is comparable to the maximum abundance in the prestellar core.

For the modeling of the $C^{18}O$ abundance we used SimLine again. Like for N_2H^+, the relative abundance is the only free parameter. The inner region, which is lacking $C^{18}O$ is only 0.023 pc, and thus slightly smaller than the central ”hole” of N_2H^+ and NH_3. From r=0.023 pc to r=0.03 pc, i.e., at temperatures above 20 K, the $C^{18}O$ abundance is $1.607 \cdot 10^{-7}$, which is the canonical value (Frerking et al. 1982). Further outwards, the abundance is lower by a factor of 0.18 (x(CO)=$3.0 \cdot 10^{-8}$. The best fit of the $C^{18}O$ model is shown in Fig. 5.15, upper right panel. The radial abundance profiles of all three molecules are displayed in Fig. 5.17.

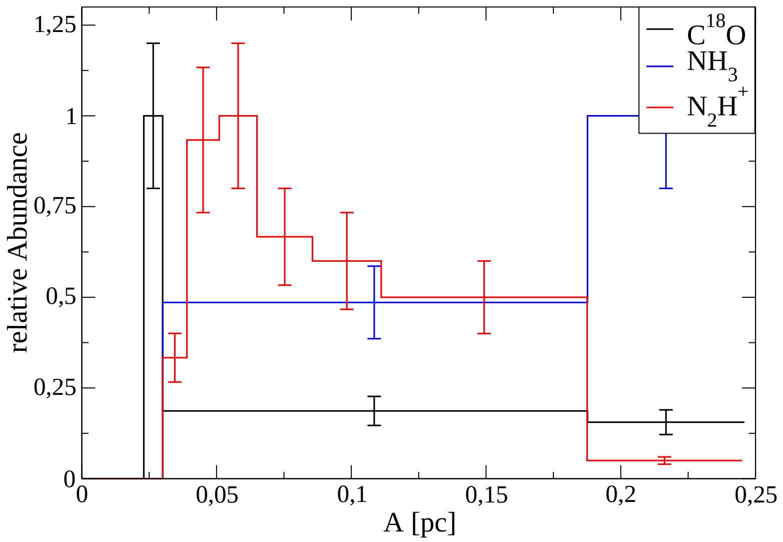

Fig. 5.17: *Normalized abundance profiles of $C^{18}O$, NH_3 and N_2H^+ at Position 2. The inner 0.023 pc seems to be void any molecular gas, probably due to the radiation of the embedded protostar.*

5.4.3 Comparison with other protostellar cores

The density law we found for the eastern core of IC 5146 ($n \propto r^{-1.5}$) is in good agreement with the prediction of models of star formation (e.g., Shu 1977, Hunter 1977). However, Looney et al. (2003) found indication that the power-law index might be as high as 2. They derived also a power-law index for the temperature profile, which coincides with our result, -0.4, as well. Deviations from the power-law occur only at radii < 200 AU, which correspond to 0.5″ at 460 pc distance.

$C^{18}O$ reaches its canonical value only in regions with temperatures above 20 K, i.e., where CO desorbs form the dust again. Similar results has been predicted by theoretical studies (e.g., Lee et al. 2004), but in their models the CO abundance increases with decreasing density again. They also show that N_2H^+ and ammonia are only abundant in regions, where CO is depleted, which we found in the protostar studied in this work as well.

5.5 Summary

In this chapter, we tried to reveal the different physical and chemical structure of starless cores and protostars. For this we combined observations of $C^{18}O$, N_2H^+ and ammonia with A_V data derived from infrared observations of background stars. The density structure of the starless core can be described by a Bonnor-Ebert-sphere, with a central plateau of an H_2 density of $5 \cdot 10^5$ cm^{-3} and a radius of 0.0174 pc. The gas temperature of this core is 10 K, and thus its matches the one of many other prestellar cores. In the protostellar core both, the density structure and the temperature structure follow a power-law with power-law-indices of -1.5 and -0.4, respectively. Both values agree fairly well with theoretical predictions (e.g., Hunter 1977).

The abundance profiles in prestellar cores of various molecules differ significantly from those in protostars. In prestellar cores CO and N_2H^+ are depleted in the central region due to the freeze out of CO and N_2, a parent species of N_2H^+. At larger radii the N_2H^+ abundance rises quickly until it maximum is reached at 0.1 pc, whereas the CO abundance increases just moderately. At even larger distances from the center the N_2H^+ abundance decreases again due to its destruction by CO. The abundance profiles in the protostellar core are determined by the additional energy input from the embedded star. Therefore no freeze out of CO and N_2H^+ can be seen in the center of the core. The fact that the inner 0.02 pc seems to be devoid of any of the observed molecules is more likely due to destruction of these molecules by UV radiation of Elias 1-12. This hypothesis is also confirmed by the detection of [NII] (Lorenzetti et al. 2000), which traces ionized gas only. In the neighboring region, CO is at its canonical abundance and frozen out at larger radii, where the temperature is below 20 K. The nitrogen bearing species show again their maximum abundance in places, where CO is largely depleted.

6 Deuterium fractionation as evolutionary tracer in Class 0 protostars

Parts of this chapter have been published in:

- Emprechtinger, M., Caselli, P., Volgenau, N. H., Stutzki, J. & Wiedner, M. C.
  The N_2D^+/N_2H^+ ratio as an evolutionary tracer of Class 0 protostars
  2008, A&A, accepted

6.1 Introduction

In this chapter we demonstrate that the abundance of deuterated ions trace low mass protostellar evolution. Most evolutionary tracers established so far, are based on the continuum emission of protostars, and are thus insensitive to the earliest phases of protostellar evolution, where most parts of the envelope are still cold and not affected by the embedded protostellar core.

6.1.1 Evolutionary tracer based on continuum observations

Since no single, optically thick, photosphere exits in protostellar cores T_{eff} cannot be determined, and thus protostars, unlike the later stages of stellar evolution, cannot be placed in the Hertzsprung-Russell diagram (Hertzsprung 1905, Russell 1914). Hence alternative indicators for the evolutionary stage of protostars are required. The most obvious variation throughout the star forming process is the increase of the average dust temperature. Therefore changes in the SED of the protostellar core are well suited to identify its evolutionary stage. In this section we will discuss four tracers, which are based on the increase of the temperature during star formation.

L-A_v diagram

Adams (1990) introduced the L_Bol-A_v diagram to trace the stage of the early phases of stellar evolution. With increasing temperature, i.e. with increasing evolutionary stage, the bolometric luminosity of the protostellar core increases as well, whereas A_v decreases slightly due to accretion onto the embedded protostar and the dissipation of the surrounding envelope. Adams (1990) calculated theoretical evolutionary tracks based on star forming models. A comparison with observations showed that disk accretion has to be included, but even then the observed dispersion is higher than predicted. Furthermore some under-luminous objects are among their sample. Therefore a more detailed theory of star formation is needed. Additionally the visual extinction is not easy to determine. Thus the utility of the L-A_v diagram as a diagnostic tool is limited.

$\mathbf{L_{BOL}/L_{smm}}$

A more empirically based, and thus model independent measure is the L_{smm}/L_{bol} ratio (André et al. 1993). They defined L_{smm} as the luminosity emitted longwards of 350 μm. With increasing temperature of the protostellar envelope the peak of the SED shifts bluewards and thus the L_{smm}/L_{bol} ratio decreases. For objects with $M_{env} \sim M_\star$, i.e., Class 0/I borderline objects, a typical value for the L_{smm}/L_{bol} ratio is $5 \cdot 10^{-3}$.

Bolometric Temperature ($\mathrm{T_{BOL}}$)

To use $\mathrm{T_{BOL}}$ as an evolutionary tracer for young stellar objects (YSO) was proposed by Myers & Ladd (1993). The bolometric temperature of a spectrum is the temperature of a blackbody with the same mean frequency ν_{mean}. It can be written as:

$$T_{Bol} = [\zeta(4)/4\zeta(5)]h\nu_{mean}/k = 1.25 \cdot 10^{-11}\nu_{mean}\ \mathrm{K\ Hz^{-1}} \tag{6.50}$$

where $\zeta(n)$ is the Riemann ζ function and

$$(n-1)! \cdot \zeta(n) = \int_0^\infty \frac{x^{n-1}}{e^x - 1} dx. \tag{6.51}$$

The bolometric temperature should be used instead of T_{eff}, which is used to classify main sequence stars. In a sample of 129 YSO in Taurus-Auriga, the bolometric temperature ranges from 60 K to 5250 K. The protostars evolve from low to high T_{bol} and the sequence terminates at the main sequence in the L_{BOL} versus T_{BOL} diagram.

$\mathbf{L_{Bol}}$ vs. $\mathbf{F^{D_0}_{1.3\ mm}}$ diagram

Saraceno et al. (1996) introduce the $\mathrm{L_{Bol}}$ vs. $\mathrm{F^{D}_{1.3\ mm}}$ diagram as evolutionary diagram for YSO's, where $\mathrm{L_{Bol}}$ is the bolometric luminosity and $\mathrm{F^{D_0}_{1.3\ mm}}$ is the distance normalized flux at $\lambda = 1.3\ mm$. The distance is normalized following Terebey et al. (1993) by using a power law:

$$F^{D_0}_{1.3\ mm} = F^{obs}_{1.3\ mm} \cdot \left(\frac{D}{D_0}\right)^\gamma \tag{6.52}$$

and $\gamma = 0.7$. $F^{obs}_{1.3\ mm}$ is the observed 1.3 mm flux, D the distance to the object. In Fig. 6.1 the $\mathrm{L_{Bol}}$ vs. $\mathrm{F^{D_0}_{1.3\ mm}}$ diagram for Class 0 and Class I protostars is shown.

During the Class 0 phase, $\mathrm{F^{D_0}_{1.3\ mm}}$ stays more or less constant and L_{Bol} is increasing. This is due to the massive envelope, which is responsible for most of the millimeter emission still present in this early evolutionary stage. Later on the envelope dissipates and thus $\mathrm{F^{D_0}_{1.3\ mm}}$ decreases, whereas L_{Bol} stay constant due to the increasing luminosity of the embedded protostar. This is what one would expect, because the $\mathrm{F^{D_0}_{1.3\ mm}/L_{Bol}}$ ratio is very similar to the $\mathrm{L_{smm}/L_{bol}}$ ratio.

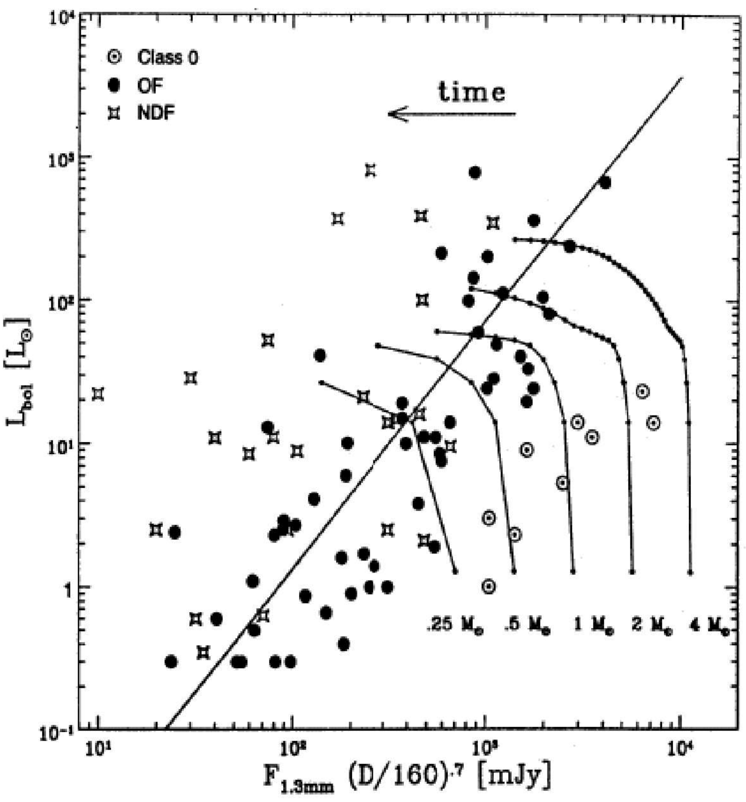

Fig. 6.1: L_{Bol} vs. $F^{D_0}_{1.3\ mm}$ *diagram. The objects shown in this diagram are Class 0 sources (Class 0), Class I sources with detected outflow (OF) and Class I sources without detected outflows (NDF). The solid line shows the best fit correlation of the OF sources. The dashed lines display evolutionary tracks for several initial envelope masses. The Figure is taken from Saraceno et al. (1996).*

6.1.2 Principle Ideas

The idea of using the deuterium fractionation, i.e. the enhanced abundance of deuterated species compared to the abundance of their protonated counterparts, as an evolutionary tracer of the early protostellar stages is based on the knowledge of the chemical network of deuterated species. In section 2.2.3 we showed, that deuterated isotopologues of H_3^+, which are the key molecules for the entire deuterium chemistry are abundant only in cold, dense environments, in which CO and other heavy species are largely depleted from gas phase.

During the prestellar phase (left side in Fig. 6.2) the central region of the cores are largely depleted from almost every heavy element, including CO, and thus the H_2D^+/H_3^+ ratio, and subsequently the deuterium fractionation of many other molecules, can exceed the cosmic D/H ratio by 5 orders of magnitude. For example N_2D^+/N_2H^+ ratios

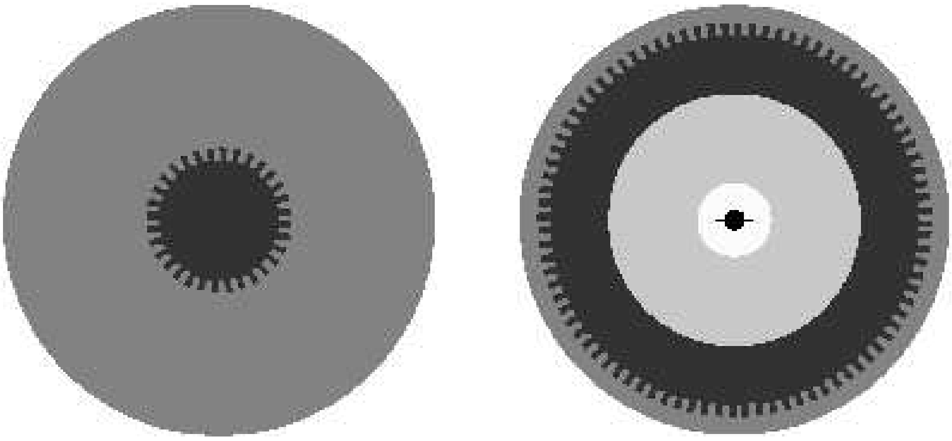

Fig. 6.2: *Scratch of a prestellar (left) and a protostellar envelope (right), taken from Jørgensen et al. (2005). The black color indicates regions, at which CO is depleted, whereas in the dark grey parts of the envelope it is still in gas-phase. The light grey color in the right image marks regions, at which CO is reevaporated into the gas-phase again due to the heating of the embedded protostar.*

up to 0.44 have been measured in such objects (Crapsi et al. (2005)). However, as soon as the collapse starts and a protostar forms, the cold gas, now called protostellar envelope warms up. Therefore more and more CO is expected to desorb from the grains and to destroy H_2D^+ and multiple deuterated isotopologues. Furthermore the reaction

$$H_2D^+ + H_2 \rightarrow H_3^+ + HD, \qquad (6.53)$$

which is endothermic by 230 K, becomes more and more likely. Therefore the deuterium fractionation of H_3^+ decreases again, and, because these species are the key molecules for deuterium chemistry, other deuterated molecules are expected to follow this trend as well. An exception are deuterated molecules, which are formed on dust grains (e.g. H_2CO and CH_3OH). These molecules desorb with increasing temperature and thus such species are abundant in the warmed up parts of the protostellar envelope. Measurements of several transitions of HDCO and D_2CO revealed excitation temperatures of 33 K and 26 K, respectively (Loinard et al. 2000), which is significantly warmer than temperatures at which H_2D^+ is expected to be abundant (< 20 K).

Although the deuterated species of H_3^+ trigger the deuterium chemistry of dense cores, the deuteration of H_3^+ is, unfortunately, very difficult to determine. First, H_3^+ is a symmetric molecule and thus lacks a dipole moment. Hence its rotational transitions are all forbidden, H_3^+ is hard to observe and thus the deuterium fractionation is difficult to determine. Furthermore multiply deuterated species of H_3^+ exist as well, and have to be taken into account. Moreover the fact that H_2D^+ and D_2H^+ exists in an ortho and a para from, which are far from thermal equilibrium, complicates the determination as well. And last but not least H_2D^+ and D_2H^+ are challenging to observe themselves, due to low atmospheric transmission. For all these reasons we used the N_2D^+/N_2H^+ ratio rather than the deuterium fractionation of H_3^+. It is formed via the reaction

$$N_2 + H_2D^+ \rightarrow N_2D^+ + H_2 \tag{6.54}$$

which is, since it is an ion neutral reaction, quite fast. In addition it is destroyed by CO (forming DCO^+) and electrons quite efficiently, and thus vanishes from the gas phase at the same time as H_2D^+. Nitrogen bearing species, especially N_2H^+ and NH_3, also seem to be very robust against depletion as well (Tafalla et al. 2002, Crapsi et al. 2007). Only in very cold prestellar cores indications of N_2H^+ freeze out can be found (Bergin et al. 2002, Pagani et al. 2007). Hence we choose the deuterium fractionation of N_2H^+ for this investigation, but other ratios might be considered, too.

6.1.3 Previous Studies of the N_2D^+/N_2H^+ Ratio in Star Forming Regions

The deuterium fractionation of N_2H^+ in prestellar (starless) cores has been studied recently (Crapsi et al. (2005)). In this work 31 of these objects have been observed and N_2H^+/N_2D^+ ratios in the range of < 0.03 and 0.44 have been reached. However, most (77 %) of the prestellar cores show an abundance ratio lower than 0.1. A tight correlation between the deuterium fractionation and the CO depletion factor (f_D(CO)), i.e., the degree of CO depletion from the gas phase could be found (see Fig. 6.3). The N_2D^+/N_2H^+ ratio increases moderately, until f_D(CO)=15. When even more CO is depleted from gas phase the N_2D^+/N_2H^+ ratio increases extremely fast, until the maximum of the deuterium fractionation is reached.

Crapsi et al. (2005) found, that in prestellar cores the CO depletion factor seems to increases with time, i.e. the CO abundance seems to decrease during the prestellar evolution. Thus the CO depletion factor can be used as an evolutionary tracer for these objects. One reason for the progressing CO depletion is that the time scales for the freeze out of CO onto dust at a density of a few times 10^4 cm^{-2} is approximately the live time of the starless cores, another one is that the density of the core increases on its way to the collapse.

Further evidences for an increasing N_2H^+ deuterium fractionation where found by comparing the N_2D^+/N_2H^+ ratio with dynamical evolutionary tracers, such as the H_2 density n(H_2) and the skewness of the N_2H^+ 1-0 line, which both are expected to increase with time. Although no clear correlation can be found for the individual parameters, they are all consistent with the assumption that the N_2D^+/N_2H^+ ratio increases towards the begin of the collapse.

Roberts & Millar (2007) determined the N_2D^+/N_2H^+ ratio in five low mass protostellar cores, using the UofA 12m telescope (HPBW of 70″ for N_2H^+ 1-0). Furthermore, they measured the D_2CO/H_2CO- and the $HDCO/H_2CO$ ratio in these cores. The $HDCO/H_2CO$ ratio is similar in most cores (~ 0.06), only in the one with highest

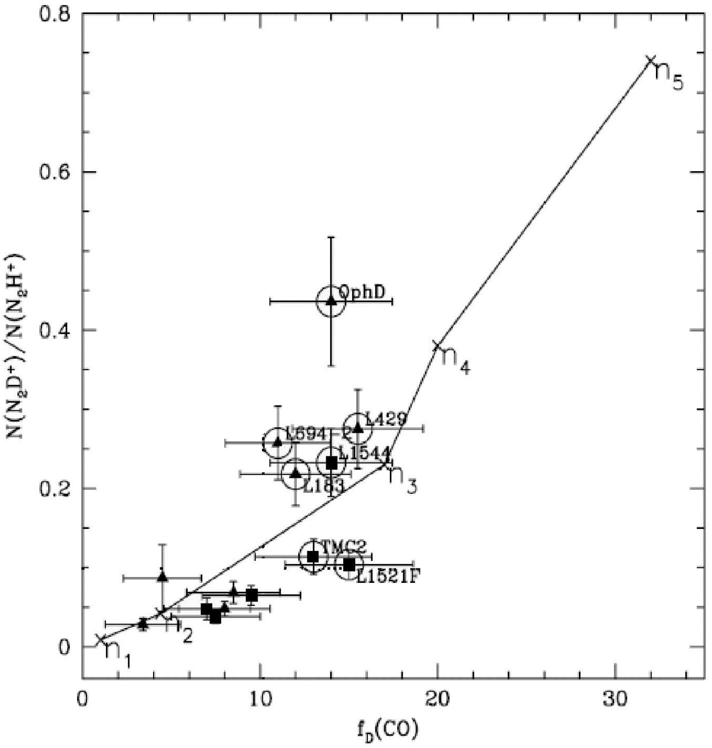

Fig. 6.3: *N_2D^+/N_2H^+ ratio as function of the CO depletion factor. The solid line is the result of a time dependent model. This figure is taken from Crapsi et al. (2005)*

N_2D^+/N_2H^+ ratio, HDCO/H_2CO is lower (0.02). For four sources it seems that the N_2D^+/N_2H^+ ratio is anti-correlated with the D_2CO/H_2CO ratio. Only in one source, L 1527, both N_2D^+ and D_2CO abundances are anomalously low. Overall, they did not find a correlation between deuterium fractionation and the bolometric temperature.

The N_2D^+/N_2H^+ ratio has also been studied in high mass star forming regions (Fontani et al. 2006). The deuterium fractionation in these regions is always smaller than 0.02, i.e. a factor ten lower than in low mass star forming region. This might be due to the larger distance to high mass star forming region, which are typically a few kpc away, whereas the observed low mass star forming regions are ten times closer. Therefore warm non-depleted and thus non-deuterated material within the beam might affect the results of the high mass star forming regions. Interferometric observations of one massive star forming region revealed an N_2D^+/N_2H^+ ratio as high as in low mass star forming regions (Fontani et al. 2008).

6.2 Observations

6.2.1 Source sample

Tab. 6.1: *Source Sample. References:* [1]*Černis (1990),* [2]*Jijina et al. (1999),* [3]*Froebrich (2005),* [4]*Gueth et al. (2003).*

Source	RA (J2000.0)	DE (J2000.0)	Distance [pc]
L 1448 IRS 2	03:25:22.42	30:45:12.2	220[1]
L 1448 IRS 3	03:25:36.45	30:45:20.3	220[1]
L 1448 C	03:25:38.82	30:44:05.3	220[1]
L 1455 A1	03:27:42.19	30:12:43.2	220[1]
L 1455 A2	03:27:49.88	30:11:42.8	220[1]
Per 4 S	03:29:17.93	31:27:30.8	220[1]
Per 4 N	03:29:22.76	31:33:30.5	220[1]
Per 5	03:29:51.63	31:39:03.9	220[1]
Per 6	03:30:14.88	30:23:48.5	220[1]
IRAS 03282+3035	03:31:21.00	30:45:30.7	220[1]
Barnard 1-b	03:33:21.34	31:07:35.2	220[1]
HH 211	03:43:56.80	32:00:50.2	220[1]
Barnard 5 IRS1	03:47:41.64	32:51:42.7	220[1]
L 1527	04:39:53.59	26:03:05.5	140[2]
L 483	18:17:29.83	-04:39:38.3	200[2]
SMM 5	18:29:51.22	01:16:40.7	310[3]
L 723	19:17:53.16	19:12:16.6	300[2]
L 673 A	19:20:25.84	11:19:51.7	300[2]
B 335	19:37:01.43	07:34:06.9	250[2]
L 1157	20:39:06.54	68:02:13.4	440[4]

The source sample contains 20 protostellar sources of the type Class 0, but some of them are known to be at the borderline to Class I (e.g. L 1455 A1, L 1527 (Froebrich 2005) and Barnard 5 IRS 1, which already shows a disk like structure (Velusamy & Langer 1998)). Most of the objects are located in the Perseus molecular cloud and all of them are at a distance closer than 500 pc. For the sources located in Perseus we assumed a distances of 220 pc (Černis 1990), which is a close estimate. Other authors (e.g., Herbig & Jones 1983) give distances larger than 300 pc. 11 objects belong to a sample of sources cataloged by Froebrich (2005), and for 17 source kinetic gas temperatures are known from Ammonia observations (Jijina et al. 1999). In Tab. 6.1 the objects, their coordinates and their estimated distances are listed. The sources were selected in terms of being a.) well known (e.g., most of them are listed by Jijina et al.

(1999)) and b.) representing a range of stages of Class 0 sources, from very young objects (e.g., HH 211, which is one of the youngest protostars according to Froebrich (2005)) to borderline objects (Class 0/1) as mentioned above.

6.2.2 Observations

The observations have been carried out in January 2006 using the IRAM-30m telescope. In Tab. 6.2 the molecular line transitions, their frequencies, and their corresponding beam widths are given.

Tab. 6.2: *Observed emission lines*

Line	Frequency [GHz]	HPBW [$''$]
N_2D^+ 1-0	77.109	32
N_2H^+ 1-0	93.173	27
$C^{18}O$ 1-0	109.782	22
N_2D^+ 2-1	154.217	16
N_2D^+ 3-2	231.322	10.5
HCO^+ 3-2	267.558	9.5

To observe all the lines listed in Tab. 6.2 two different receiver set-ups were used. The first set-up uses frequency switching to observe $C^{18}O$ 1-0, N_2D^+ 2-1, N_2D^+ 3-2 and HCO^+ 3-2 simultaneously with the receivers A and D. The offsets were 10 ($C^{18}O$ 1-0), 15 (N_2D^+ 2-1), 25 (N_2D^+ 3-2) and 28 (HCO^+ 3-2) MHz, respectively.

To observe the N_2D^+ 1-0 line an external local oscillator together with the B 100 receiver has to be used. In this mode frequency switching is not available, therefore the second set-up uses position switching. Simultaneously with the N_2D^+ 1-0 line, N_2H^+ 1-0 and N_2D^+ 3-2 have been observed with the A 100 and A 230 receiver, respectively. As back end the autocorrelator VESPA was used, which was adjusted to a resolution of about 0.05 km/s at each frequency.

During the observation the τ of the atmosphere at 225 GHz was about 0.25, which are average weather conditions in winter and thus system temperatures between 150 K (N_2H^+ 1-0) and 800 K (HCO^+ 3-2) were reached. Pointing was checked every two hours and the pointing accuracy was better than $7''$. Antenna temperatures and main beam temperatures are related by the main beam efficiency η_{MB}, which is between 0.8 and 0.42[7], depending on the observing frequency.

Tab. 6.3: *Observational parameters of the* $C^{18}O$ *and* HCO^+ *lines. The sources, whose integrated* HCO^+ *intensities are indicated with an* ** *show double peaked spectra, those, which are indicated with a* * *not. The kinetic temperatures marked with an* ^{H} *are taken from Hatchell (2003) all other* T_{kin} *are listed in Jijina et al. (1999).*

Source	IRAS	F(60μm) [Jy]	F(100μm) [Jy]	$T_{\rm Kin}$ [K]	W [Kkm/s] ($C^{18}O$)	Δv [km/s] ($C^{18}O$)	W [Kkm/s] HCO^+))
L 1448 IRS 2	03222+3034	14.3	<169	-	3.23	0.77	13.0**
L 1448 IRS 3	03225+3034	25.1	169	12.0	5.75	1.22	29.0*
L 1448 C	F03226+3033	53.4	355	13.7^{H}	3.36	1.11	20.6**
L 1455 A1	03245+3002	47.1	93.6	15.0	1.65	1.03	8.82*
L 1455 A2	F03247+3001	66.4	206	11.0	0.90	0.80	6.59*
Per 4 S	-	-	-	9.0	2.84	0.81	8.76*
Per 4 N	03262+3123	1.07	<12.4	10.0	1.30	0.44	5.36*
Per 5	03267+3128	1.88	<10.4	11.0	1.79	0.69	15.0*
Per 6	03271+3013	7.53	8.19	11.0	1.52	0.74	6.06**
IRAS 03282	03282+3035	2.33	13.9	11.3^{H}	1.95	1.47	12.8**
Barnard 1-B	03301+3057	<6.18	35.5	12.0	8.09	1.59	14.0**
HH 211	03407+3152	<2.06	<30.8	12.8^{H}	5.19	0.81	17.4**
Barnard 5 IRS 1	03445+3242	15.5	15.4	10.8^{H}	3.99	1.00	9.36**
L 1527	04368+2557	17.8	73.3	10.8^{H}	4.12	0.65	13.0**
L 483	18148-0440	89.1	166	10.0	5.12	0.81	22.8**
SMM 5	-	-	-	12.0	8.66	1.57	10.7*
L 723	19156+1906	6.93	20.7	11.0	2.45	1.29	12.2**
L 673 A	19180+1114	2.55	10.6	12.0u	2.31	0.92	12.8*
B 335	19345+0727	8.3	42	9.9	2.34	0.44	3.62**
L 1157	20386+6751	10.9	43.5	-	1.57	0.61	13.4**

Tab. 6.4: *Line parameters of the N_2H^+ and N_2D^+ lines.*

	N_2H^+ (1-0)			N_2D^+				
Source	$\int T_{MB}dv$ [Kkm/s]	τ	T_{ex} [K]	$\int T_{MB,J=1-0}dv$ [Kkm/s]	$\int T_{MB,J=2-1}dv$ [Kkm/s]	$\int T_{MB,J=3-2}dv$ [Kkm/s]	τ J=2-1	Δv_{2-1} [km/s]
L 1448 IRS 2	12.93	11.6	6.8	1.7	1.10	0.73	< 0.1	0.53
L 1448 IRS 3	24.65	4.1	11.4	4.02	5.05	3.22	2.6	0.59
L 1448 C	12.477	5.3	7.29	< 1	2.32	1.38	< 0.1	0.72
L 1455 A1	7.20	1.4	9.18	< 1	0.68	< 0.74	< 0.1	0.42
L 1455 A2	8.60	3.0	9.06	< 1	1.03	< 0.73	< 0.1	0.33
Per 4 S	5.08	3.5	8.53	1.3	1.43	0.98	< 0.1	0.32
Per 4 N	4.62	3.6	7.57	1.3	0.75	< 0.68	< 0.1	0.31
Per 5	7.53	3.8	8.70	< 1	1.07	1.08	< 0.1	0.36
Per 6	4.64	< 0.1	-	< 1	< 0.18	< 0.69	-	-
IRAS 03282	9.53	5.3	8.62	< 1	3.58	1.47	3.9	0.34
Barnard 1-B	19.05	8.6	7.62	5.92	7.48	4.82	4.9	0.78
HH 211	9.18	6.23	7.6	2.31	5.24	2.08	4.9	0.39
Barnard 5 IRS 1	8.59	6.4	7.18	< 1	0.50	0.65	< 0.1	0.50
L 1527	3.91	5.6	5.74	< 1	< 0.18	< 0.59	-	-
L 483	14.05	12.1	7.26	2.06	1.75	1.13	2.8	0.37
SMM 5	15.39	4.9	8.89	< 1	2.46	1.43	< 0.1	0.58
L 723	5.70	2.4	6.63	< 1	0.34	1.29	< 0.1	0.32
L 673 A	7.34	2.9	8.64	< 1	0.45	0.63	< 0.1	0.34
B 335	6.05	9.0	5.65	< 1	0.42	0.42	< 0.1	0.46
L 1157	8.38	2.09	8.92	< 1	0.53	1.00	< 0.1	0.56

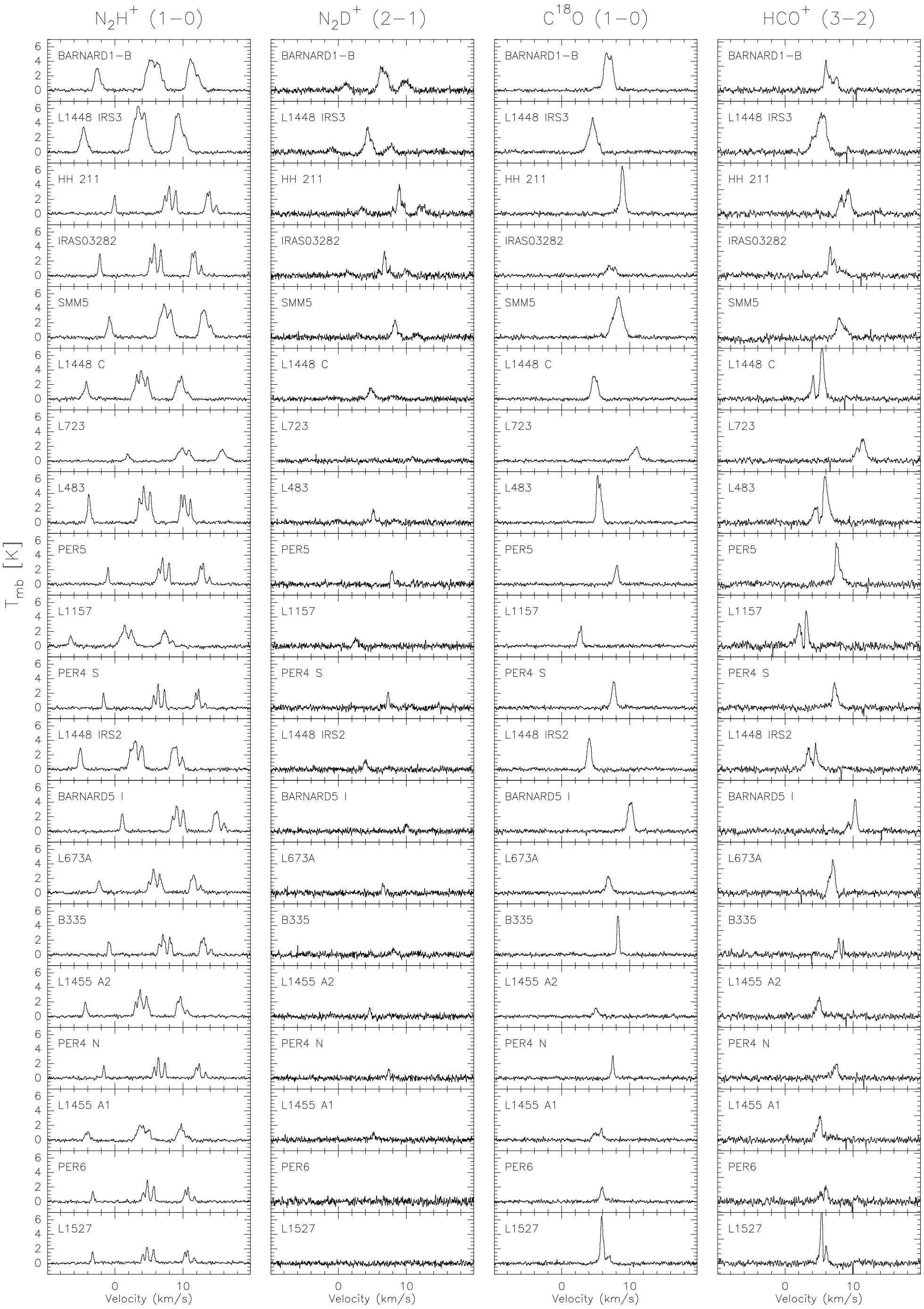

Fig. 6.4: *Spectra of N_2H^+ 1-0, N_2D^+ 2-1, $C^{18}O$ 1-0 and HCO^+ 3-2 (from left to right) of all 20 protostars of our sample. To be able to plot all spectra on the same scale we divided the intensities of HCO^+ by four.*

6.3 Results

6.3.1 N_2H^+ & N_2D^+

The results of the N_2H^+ and N_2D^+ observations are summarized in Tab. 6.4 and spectra are shown in Fig. 6.4. The N_2H^+ 1-0 line was detected in all sources of our sample, and the integrated intensities range from 3.91 Kkm/s to 24.65 Kkm/s, which is comparable to the results of the observations in prestellar cores (Crapsi et al. 2005).

N_2D^+ was observed in three different transitions (J=1-0, J=2-1 & J=3-2). All three lines were detected in six objects. The ground-state transition, N_2D^+ 1-0, was detected in only seven sources at an S/N ratio of ~ 5. The reason for the rarity of N_2D^+ 1-0 detections is that the Einstein-A coefficient, i.e. the transition probability, increases with ~ J^3, and thus the A-coefficient for the J=1-0 line is approximately ten times lower than the A-coefficient of the J=2-1 line. Furthermore, the relatively low energies ($E = J(J+1)\cdot 1.85\ K$) and the higher degeneracies of higher rotational states lead to an efficient population of those states under conditions present in protostellar cores (n> 10^5 cm^{-3}, T=10-20 K). The 2-1 line is the most frequently detected N_2D^+ line, with typical integrated intensities of 0.34-7.48 Kkm/s. Only two objects, Per 6 and L 1527, do not show emission in J=2-1. These two objects also show no emission in the other N_2D^+ lines. The N_2D^+ 3-2 line is detected in 15 out of the 20 cores ($T_{int} = 0.42 - 4.82$ Kkm/s).

Due to the nuclear spin of the nitrogen atom (I=1) each rotational transition of N_2H^+ and N_2D^+ splits into several hyperfine components, which can be used to derive the optical depths (τ) for the transitions. τ was determined by fitting these individual hyperfine components using the "METHOD HFS" of the CLASS program[8]. This routine fits the spectra with

$$\mathrm{T_b(v)} = \frac{\mathrm{p_1}}{\mathrm{p_4}}(1 - \exp(-\tau_\mathrm{v})) \tag{6.55}$$

and

$$\tau_\mathrm{v} = \mathrm{p_4} \cdot \sum_\mathrm{i} \mathrm{r_i} \cdot \exp\left(\frac{\mathrm{v - v_i - p_2}}{\alpha \mathrm{p_3}}\right)^2 \tag{6.56}$$

$\alpha = \frac{1}{2\sqrt{ln2}}$, which is the normalization factor for the Gaussian profile. r_i and v_i are the relative intensities and the velocity offsets of the individual hyperfine components. Those values were taken from Womack et al. (1992). p_1-p_4 are the parameters, which are fitted. p_1 is $T_{mb}\cdot\tau$, p_2 the source velocity, p_3 the line width (FWHM) and p_4 the optical depth τ.

The N_2H^+ 1-0 line widths found in our protostellar sample are significantly larger than the ones in prestellar cores. The average line width for our sample is 0.61 kms^{-1},

---

[7] http://www.iram.fr/

[8] http://www.iram.fr/IRAMFR/GILDAS/

whereas Crapsi et al. (2005) found an average line width of 0.26 kms^{-1}. The line widths reported by (Roberts & Millar 2007) are slightly higher than ours (0.85 kms^{-1}), but this difference might be due to the lower spatial resolution of their observations. This suggests that non-thermal motions are not only concentrated nearby the protostar, but that they pervade the whole associated core. The optical depths in the protostellar cores are typically lower by a factor of three, which might be due to the higher temperatures expected in protostars.

Assuming a beam filling factor of one and a constant excitation temperature, one can subsequently derive the column densities for the respective molecule. T_{ex} was determined using the solution of the radiative transfer equation

$$T_b = (J(T_{ex}) - J(T_{bg})) \cdot (1 - e^{-\tau}) \tag{6.57}$$

where J(T) is

$$J(T) = \frac{h\nu}{n} \cdot \frac{1}{\exp(\frac{h\nu}{kT} - 1)} \tag{6.58}$$

Since both, the brightness temperature (T_b) and the optical depth (τ) are known, T($_{ex}$) is the only unknown variable which is left.

In the case of optically thin emission τ the excitation temperature can not be determined. But for the N_2H^+ 1-0 line this was the case in only one object (Per 6). For Per 6 we assumed an average T_{ex}. The N_2H^+ excitation temperature found in our sample of Class 0 protostars (listed in Tab. 6.4) range from 6.8 K to 11.4 K, which is lower than the kinetic temperature, but typically 2-3 K higher than the excitation temperature in prestellar cores (Crapsi et al. (2005)). The enhanced T_{ex} is due to heating of the embedded protostellar core.

The column density was derived with the formula

$$N_{tot} = \frac{8\pi^{3/2}\Delta v}{2\sqrt{ln2}\lambda^3 A} \frac{g_l}{g_u} \frac{\tau}{1 - \exp(-h\nu/kT_{ex})} \frac{Q_{rot}}{g_l \cdot \exp(-E_l/kT_{ex})} \tag{6.59}$$

were τ could be determined and

$$N_{tot} = \frac{8\pi \cdot W}{\lambda^3 A} \frac{g_l}{g_u} \frac{1}{J_\nu(T_{ex}) - J_\nu(T_{bg})} \frac{1}{1 - \exp(-h\nu/kT_{ex})} \frac{Q_{rot}}{g_l \cdot \exp(-E_l/kT_{ex})} \tag{6.60}$$

in the optically thin case (see appendix of Caselli et al. (2002b)).

To determine the column densities we used the N_2H^+ 1-0 and the N_2D^+ 2-1 line. We did so for three reasons. First N_2D^+ 2-1 is observed in most of the sources. Second, the 2-1 transition of N_2D^+ is observed with the highest S/N ratio. The S/N ratio of four of the six N_2D^+ 1-0 lines, for example, is too low to obtain a reliable τ from hyperfine component fitting. Third, the ratio of the N_2D^+ 2-1/N_2H^+ 1-0 lines permits a direct comparison with previous studies (Crapsi et al. (2005), Fontani et al. (2006)).

In most cases, the J=2-1 lines are optically thin, so that τ, and thus T_{ex} can be determined by fitting the hyperfine components in only five cases. In these five sources the excitation temperatures of the two molecules are quite similar, and thus we assumed a similar excitation temperature of N_2H^+ and N_2D^+ for the other protostars, too.

Tab. 6.5: *N_2H^+ and N_2D^+ column densities.*

Source	$N(N_2H^+)$ [cm^{-2}]	$N(N_2D^+)$ [cm^{-2}]	$N(N_2D^+)/N(N_2H^+)$
L 1448 IRS 2	$3.1 \cdot 10^{13}$	$1.3 \cdot 10^{12}$	0.042±0.014
L 1448 IRS 3	$4.8 \cdot 10^{13}$	$3.9 \cdot 10^{12}$	0.081±0.010
L 1448 C	$2.4 \cdot 10^{13}$	$2.5 \cdot 10^{12}$	0.104±0.017
L 1455 A1	$9.2 \cdot 10^{12}$	$6.3 \cdot 10^{11}$	0.068±0.043
L 1455 A2	$1.4 \cdot 10^{13}$	$9.6 \cdot 10^{11}$	0.069±0.029
Per 4 S	$7.9 \cdot 10^{12}$	$1.4 \cdot 10^{12}$	0.177±0.032
Per 4 N	$7.1 \cdot 10^{12}$	$7.8 \cdot 10^{11}$	0.110±0.057
Per 5	$1.2 \cdot 10^{13}$	$1.0 \cdot 10^{12}$	0.083±0.033
Per 6	$6.1 \cdot 10^{12}$	$<1.8 \cdot 10^{11}$	< 0.029
IRAS 03282	$1.6 \cdot 10^{13}$	$3.5 \cdot 10^{12}$	0.219±0.026
Barnard 1-B	$4.5 \cdot 10^{13}$	$8.1 \cdot 10^{12}$	0.180±0.009
HH 211	$1.7 \cdot 10^{13}$	$4.6 \cdot 10^{12}$	0.271±0.024
Barnard 5 IRS 1	$1.6 \cdot 10^{13}$	$5.4 \cdot 10^{11}$	0.034±0.025
L 1527	$7.2 \cdot 10^{12}$	$< 2.5 \cdot 10^{11}$	<0.034
L 483	$3.3 \cdot 10^{13}$	$1.9 \cdot 10^{12}$	0.057±0.012
SMM 5	$2.9 \cdot 10^{13}$	$2.3 \cdot 10^{12}$	0.079±0.019
L 723	$8.8 \cdot 10^{12}$	$4.0 \cdot 10^{11}$	0.045±0.040
L 673 A	$1.3 \cdot 10^{13}$	$4.3 \cdot 10^{11}$	0.033±0.031
B 335	$1.4 \cdot 10^{13}$	$6.0 \cdot 10^{11}$	0.043±0.029
L 1157	$1.1 \cdot 10^{13}$	$5.0 \cdot 10^{11}$	0.045±0.036

The resulting N_2D^+ and N_2H^+ column densities are listed in Tab. 6.5. The estimated errors on the column densities are of the order of $2 \cdot 10^{12}$ cm^{-2} and $4 \cdot 10^{11}$ cm^{-2} for N_2H^+ and the N_2D^+, respectively. As expected, the N_2D^+/N_2H^+ ratios vary significantly from object to object (Tab. 6.5). It has values between < 0.029 (Per 6) and 0.27 (HH 211), but for most objects it is below 0.1.

By determining T_{ex} and the column densities as described above, we assume implicitly that the beam filling factors of the N_2H^+ and N_2D^+ observations are one. Because dark cloud cores are typically larger than the beam size of our observations (e.g. Caselli et al. 2002a) and the fact that the kinetic temperature of these cores is only ~ 1.5 times the excitation temperature of N_2H^+ indicates that the filling factor is indeed close to one, and certainly > 0.67. Using the lower limit for the filling factor would lower the N_2H^+ column density by 40% and the N_2D^+ column density by 55%. Therefore, the derived N_2D^+/N_2H^+ ratios could be up to 25% lower. The general trend, however, which we will discuss in the next section, remains.

The N_2D^+ column density has been also calculated using the (3–2) line, when detected, and following the same procedure as described above. In 13 out of 15 objects the two values for the column density agree within the range of error. In L 1448 IRS3 and L 1157, the column densities determined using N_2D^+ 3-2 are a factor two higher than the one determined using the 2-1 line. However, because the satellite lines get weaker with increasing J, and due to the higher noise-level of most of these data, the column densities derived from the J=2-1 transition are more reliable.

The N_2H^+ and N_2D^+ column densities derived here are of the same order as those found by Crapsi et al. (2005) for prestellar cores (10^{13} cm^{-2} and 10^{12} cm^{-2} for N_2H^+ and N_2D^+, respectively). Also the range of values for the N_2D^+/N_2H^+ ratio is very similar to the one found in low mass prestellar cores (Crapsi et al. (2005)). The average N_2D^+/N_2H^+ ratio in Class 0 protostars is 0.097, in which 20% of the objects show an N_2D^+/N_2H^+ ratio larger than 0.15. For starless cores the average ratio is 0.106 and 18% of the sources show ratios larger than 0.15. However, the N_2D^+/N_2H^+ ratio in low mass protostars (and prestellar cores) is significantly larger than the one in high mass star forming regions (Fontani et al. (2006)), where the ratio is always smaller than 0.02 (but see Fontani et al. (2008), who measured deuterium fractionations of ~0.1 toward a high mass star forming region, using interferometric observations).

For three objects in our sample, L 1448 C, HH 211 and L 1527, the N_2D^+/N_2H^+ ratio has been determined by Roberts & Millar (2007) as well. In general they found somewhat higher N_2D^+/N_2H^+ ratio than we did. In L 1448 C their ratio is 1.63±0.4 times larger than the one found by us and in HH 211 1.14±0.18 times larger. For L 1527, we report an upper limit of 0.034 only, whereas Roberts & Millar found a ratio of 0.06. The fact that Roberts & Millar (2007) found a similar N_2D^+/N_2H^+ ratios at much lower spatial resolution indicates that the deuterium fractionation occurs, as expected, in the cold, extended envelope of the protostellar core. If deuterium fractionation would occur only in the central region, one would expect to find lower N_2D^+/N_2H^+ ratios at lower resolution, because of beam dilution.

We also estimated the volume density of the cores, using the integrated intensity ratios of the three N_2D^+ lines. We assumed an isothermal cloud with a kinetic temperature determined from NH_3 observations (Tab. 6.3). The volume density was estimated by fitting the N_2D^+ J=3-2/J=2-1 ratio, using a radiative transfer code (Pagani et al. (2007), see section 6.6.2). We derived values between $5 \cdot 10^6$ cm^{-3} and 10^7 cm^{-3}. Only IRAS 03282 shows a lower density ($6 \cdot 10^5$ cm^{-3}). However, because temperature and density are expected to decline with radius and the observations taken with a lower spatial resolution thus trace lower average temperature, densities and, since protostars are assumed to be spherical, lower column densities. Therefore the N_2D^+ 3-2 intensity is very likely overestimated with respect to the N_2D^+ 2-1 line strength and the obtained densities are upper limits. For six sources we could also determine the density using the N_2D^+ J=2-1/J=1-0 ratio. We were not able to find a density, with which we could reproduce all three lines simultaneously. The density values derived from the J=2-1/J=1-0 line ratio are about a factor 10 lower than those determined from the J=3-2/J=2-1 ratio. This is again most likely due to the lower spatial resolution of the observation at lower frequencies.

6.3.2 $C^{18}O$ & HCO^+

$C^{18}O$ 1-0 and HCO^+ 3-2 lines were detected in all 20 sources of our sample. The results are listed in Tab. 6.3. The line profile of $C^{18}O$, which is assumed to be optically thin, looks roughly Gaussian. The only two exceptions are L 1455 A1 and IRAS 03282, which show a much more complex line shape. The $C^{18}O$ line width (FWHM) is quite narrow, typically below 1 km/s. This indicates that the bulk of the molecular gas is cold and turbulence is low. The $C^{18}O$ 1-0 and HCO^+ 3-2 spectra are displayed in Fig. 6.4.

Contrary to $C^{18}O$, HCO^+ 3-2 is clearly optically thick. Large deviations from a Gaussian line profile can be seen, and in 12 objects double-peaked profiles appear, a clear indication for self-absorption. Asymmetries in the line shape indicate large scale velocity pattern, which are probably caused by infall motions.

Gregersen et al. (2000) observed several young protostars in HCO^+ 3-2 using the CSO. They found line shapes, which show similar asymmetries to those we observed (see section 6.4.4), but the intensities of the lines they observed are significantly lower, which is most likely due to the larger beam size at the CSO (9.5″ and 32.5″, respectively). For three sources, in which HCO^+ 3-2 has been observed by Gregersen et al. (2000) and by us, we determined beam filling factors. Assuming a beam efficiency of 69.8% for the CSO at 269 GHz to convert the T_A^* they give into T_{MB}, we derived filling factors between 0.26 and 0.36 for the CSO beam. These filling factors indicated that HCO^+ 3-2 might be emitted from a compact, warm nucleus at the center of the core. Such a nucleus would have a diameter of approximately 17″.

6.4 Correlating the Deuterium fractionation with other physical properties

In this section we correlate the obtained values for the N_2D^+/N_2H^+ ratio with several physical parameters of the protostar, which might have an influence on the deuterium fractionation. Some of these parameters, such as dust temperature and bolometric luminosity have been used to quantify the evolutionary stage of the protostar (see section 6.1.1). The individual parameters will be discussed in the respective subsections.

6.4.1 Dust Temperature

At first we will compare the deuterium fractionation of N_2H^+ with the dust temperature. In general it is expected that T_{Dust} rises as the protostar evolves, but the exact relation between time end dust temperature is ambiguous. Different theoretical models yield very different ages for the same protostar (Froebrich (2005) and references therein).

Following equation (1) in Kramer et al. (2003) the dust emission can be written as

$$F_\nu \propto \nu^{3+\beta} \cdot \frac{1}{e^{h\nu/kT_{Dust}} - 1} \tag{6.61}$$

where F_ν is the emitted continuum flux at frequency ν, β the emissivity index and T the dust temperature. For all of our sources, with the exception of Per 4 S and SMM 5, counterparts can be found in the IRAS point source or faint source catalog. Additional millimeter and submillimeter continuum data are available for many of the sources (see Tab. 6.6). We fitted these data to derive best values for T_{Dust} and β using the equation above. The fits represent the continuum observations in general quite well. However, in some objects we see a significant enhancement of the observed flux at the longer wavelengths (see for example the SED of L 1157 in Fig. 6.5), which indicates that a component of cold dust might be present in these sources.

For 15 out of 16 sources, for which more than two data points are available, β=1 has been found to be the best value. Only for Barnard 5 IRS1, β=0 (i.e. black-body radiation) gives better results. In the three case where only two data points could be found in the literature, we assumed β=1. The derived emissivity index is lower than the typical value of $\beta = 2$ for molecular clouds (e.g. Ward-Thompson et al. (2002), Visser et al. (1998)). It is very likely that the low emissivity index found here is caused by the strong temperature gradient in protostars, and not due to different dust grain emissivities itself. In fact, the cold envelope is still bright at a wavelength of about 1 mm, whereas practically all radiation emitted at $\lambda < 100\mu$m stems from the hot core. Therefore, the dust mass radiating at longer wavelengths is much larger than the dust mass radiating at shorter wavelengths, and thus the combined spectrum gets flattened. We modeled the continuum emission using a local emissivity index of two (see section 6.6), but got as index for the whole modeled cloud a β-value of one.

The resulting dust temperatures ranges from approximately 20 K up to 50 K (see Tab. 6.6), are clearly above the excitation temperature of N_2H^+, as well as the kinetic gas temperature (Tab. 6.4). This might be due to the fact that dust traces the warm embedded protostellar core, which is the main source of heat, rather than the cooler envelope, which is traced by N_2H^+.

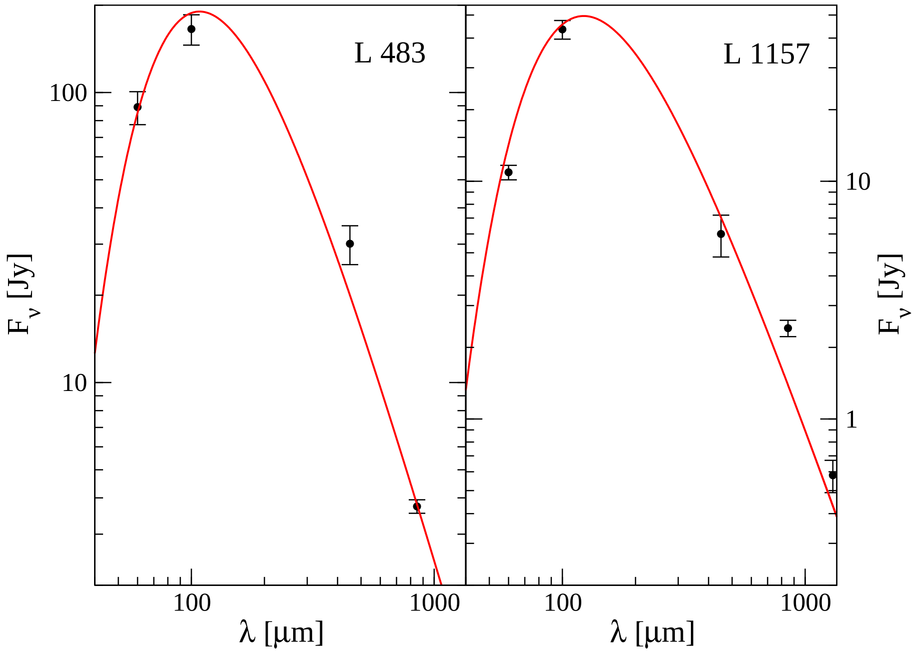

Fig. 6.5: *Two examples for the fitting results* T_{Dust}. *The enhanced flux at* $\lambda = 850\ \mu m$ *in L 1157 might be explained be the presence of cold dust.*

In Fig. 6.6 the N_2D^+/N_2H^+ ratio versus dust temperature is plotted. All objects with N_2D^+/N_2H^+ ratio above 0.15 turned out to be at the cold end of the sample with T_{Dust} of about 20 K. As the dust temperature increases, the deuterium fractionation drops off and reaches a value of approximately 0.05 at 30 K.

6.4.2 CO Depletion Factor

The relative CO abundance is a very crucial parameter for the deuterium fractionation since CO is one of the main destroyers of H_2D^+, the progenitor of N_2D^+ (see chapter 2). Theoretically, the N_2D^+/N_2H^+ ratio should be very sensitive to CO depletion (e.g. Roberts & Millar (2000)).

The CO depletion factor f_D is defined as

$$f_D = x_{can}/x_{obs} \tag{6.62}$$

where x_{can} is the canonical ISM abundance ratio of $[C^{18}O]/[H_2] = 1.7 \cdot 10^{-7}$ (Frerking et al. (1982)).

The total number of hydrogen molecules within the beam is determined by the continuum emission around 1 mm (1.3 mm, 1.1 mm or 850 μm), using the equation

$$n_{H_2} = \frac{F_\nu \cdot d^2}{\kappa_\nu \cdot B_\nu(T_{Dust})} \cdot \frac{1}{\mu} \tag{6.63}$$

Tab. 6.6: *The (sub)millimeter continuum data available in the literature, the dust temperatures, the $C^{18}O$ column densities and the CO depletion factors of the protostars.*

Source	Wavelength of additional data [μm]	Ref.	T_{Dust} [K]	$N(C^{18}O)$ [cm^{-2}]	$f_D(CO)$
L 1448 IRS 2	450,850,1100	1,3	27	$5.24\cdot10^{15}$	3.0 ± 0.6
L 1448 IRS 3	1100	3	27	$9.33\cdot10^{15}$	5.1 ± 1.0
L 1448 C	450,850,1100	2,3	32	$6.19\cdot10^{15}$	3.2 ± 0.6
L 1455 A1	450,850,1100	3,5	37	$3.04\cdot10^{15}$	1.7 ± 0.4
L 1455 A2	-	-	30	$1.58\cdot10^{15}$	-
Per 4 S	1100	3	-	-	-
Per 4 N	1100	3	23	$1.88\cdot10^{15}$	2.8 ± 0.11
Per 5	1100	3	26	$2.83\cdot10^{15}$	1.9 ± 0.4
Per 6	-	-	45	$3.69\cdot10^{15}$	-
IRAS 03282	450,850,1100	2,3	23	$2.83\cdot10^{15}$	4.5 ± 0.9
Barnard 1-B	1100,850	3,4	18	$1.00\cdot10^{16}$	3.4 ± 0.7
HH 211	1100,450,850	3,5	< 21	$<7.08\cdot10^{15}$	3.4 ± 0.7
Barnard 5 IRS 1	1100	3	50	$1.06\cdot10^{16}$	0.4 ± 0.09
L 1527	450,850,1300	2	27	$6.68\cdot10^{15}$	2.7 ± 0.5
L 483	450,850	2	34	$9.89\cdot10^{15}$	2.4 ± 0.5
SMM 5	-	-	-	-	-
L 723	450,850	2	25	$3.76\cdot10^{15}$	3.4 ± 0.7
L 673 A	-	-	28	$3.85\cdot10^{15}$	-
B 335	450,850,1100	2	27	$3.80\cdot10^{15}$	3.8 ± 0.8
L 1157	1300,450,850	2,5	30	$2.75\cdot10^{15}$	4.9 ± 1.0

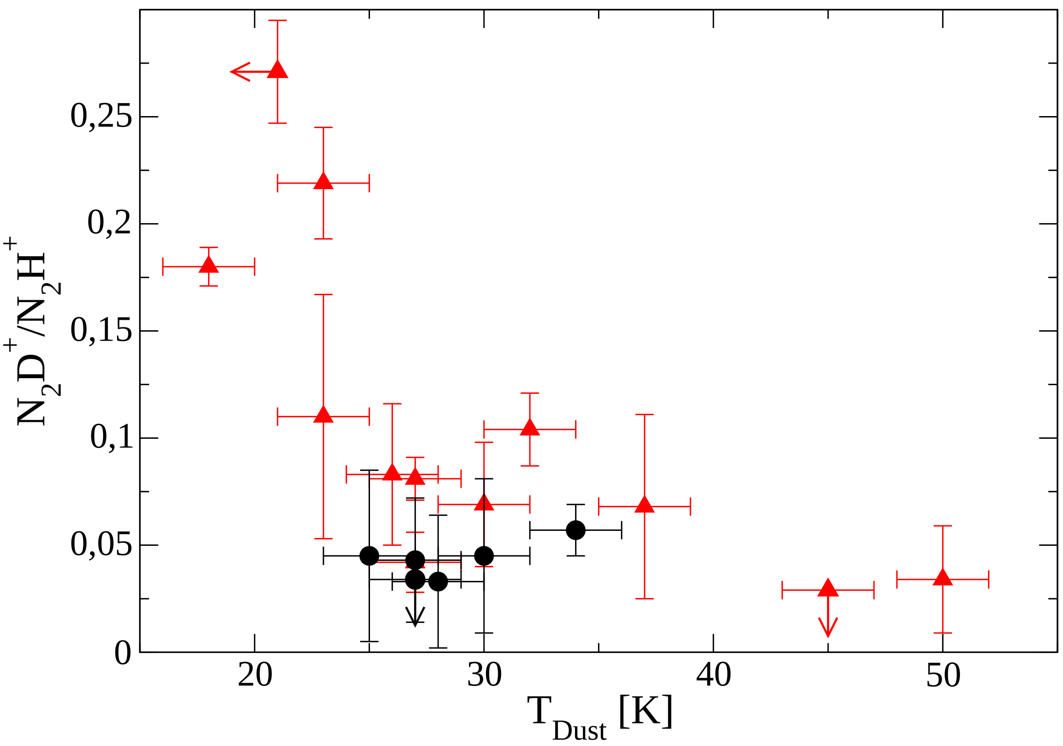

Fig. 6.6: *Dust temperature versus deuterium fractionation. At low temperatures the largest* N_2D^+/N_2H^+ *ratios can be seen. With increasing* T_{Dust} *the deuterium fractionation sinks. The objects marked with a triangle are the ones located in the Perseus cloud.*

(Terebey et al. 1993) where F_ν is the continuum flux, d is the distance to the object, $B_\nu(T_{Dust})$ is the Planck function, T_{Dust} is the dust temperature, as determined in the previous subsection, and μ is the mass of one H_2 molecule. For the conversion factor, κ_ν, we used a value of 0.005 cm^2/g at a wavelength of 1.2 mm (André et al. (1996)). To calculate the conversion factor at other wavelengths, we express the relation between opacity and wavelength as a power law

$$\kappa_\lambda = \kappa_0 \left(\frac{\lambda_0}{\lambda}\right)^\beta \tag{6.64}$$

We used a β-value of one (zero for Barnard 5 IRS1), as suggested by the fits of the continuum data. The biggest uncertainty in the determination of the H_2 column densities is κ, because it is not well determined and some authors use values twice as high as we do (e.g. Froebrich (2005)).

To be able to compare the ~ 1 mm continuum data with our $C^{18}O$ 1-0 observations, we have to estimate the continuum flux density within a 22″ beam, the spatial resolution of the $C^{18}O$ 1-0 observations. The fact that the angular diameters of the protostellar envelopes are always larger than the beam is an important issue in this conversion.

To compare the data taken with different beam sizes, we follow Terebey et al. (1993). They showed that the flux of a dark cloud with $\rho = r^{-p}$ and $T = r^{-q}$ as density and temperature distribution, respectively, can be written as:

$$F_\nu \propto d^{1-(p+q)} \cdot \theta^{3-(p+q)} \tag{6.65}$$

where d is the distance and θ is the beam size. In their sample of protostars, most of them being Class 0, they found that 1.7 is an appropriate value for (p+q). With these formulae the canonical CO abundance, x_{can}, was calculated.

We determined the actual $C^{18}O$ column density assumed that $C^{18}O$ is optically thin and used the formula:

$$N_{tot} = \frac{8\pi \cdot W}{\lambda^3 A} \frac{g_l}{g_u} \frac{1}{J_\nu(T_{ex}) - J_\nu(T_{bg})} \frac{1}{1 - \exp(-h\nu/kT_{ex})} \frac{Q_{rot}}{g_l \cdot \exp(-E_l/kT_{ex})} \tag{6.66}$$

again.

Furthermore we adopted again a constant excitation temperature, but since the critical density of $C^{18}O$ is considerably lower than that for N_2H^+ we expect that $T_{ex}(C^{18}O) > T_{ex}(N_2H^+)$ and comparable to the kinetic gas temperatures. However, since the beam sizes of the Ammonia observation, which have been used to derive T_{kin}, vary between 40″ and 88″ from object to object, we used a constant excitation temperature of 15 K for all sources. This assumption might introduce some error (< 15%) in the estimation of the depletion factor. Especially in the more evolved objects, where the envelope might have been already warmed up, the depletion factor is underestimated. The total number of $C^{18}O$ atoms can be calculated by

$$n_{C^{18}O} = N_{C^{18}O} \cdot d^2 \cdot \Omega \tag{6.67}$$

where $n_{C^{18}O}$ is the total number of $C^{18}O$ molecules within the beam, $N_{C^{18}O}$ the $C^{18}O$ column density, d the distance to the protostar and Ω the solid angle of the beam.

The derived depletion factors are in the order of 1 to 4.5 (Tab. 6.6 Colum 4). In Fig. 6.7 (middle panel), we show the correlation between CO depletion and deuterium fractionation in our sample of protostars. In addition we show the same correlation found in low-mass prestellar cores (Crapsi et al. (2005) and massive prestellar cores (Fontani et al. 2006). The correlation we found for protostars looks very similar to the correlation found in low mass prestellar cores. At low values of $f_D(CO)$ (< 3) the deuterium fractionation is low as well (< 0.1). At depletion factors above three, the N_2D^+ /N_2H^+ ratio rises quickly with CO depletion until it reaches 0.25. The only difference between the correlation found here and the correlation found in low mass prestellar cores is that in prestellar cores the deuterium fractionation stays low until a depletion factor of ~ 10 is reached. Contrary to low mass pre- and protostars, in high mass prestellar cores no dependency of the deuterium fractionation on $f_D(CO)$ can be found. Since those high mass prestellar cores are at lager distances (a few kpc), these observations might be

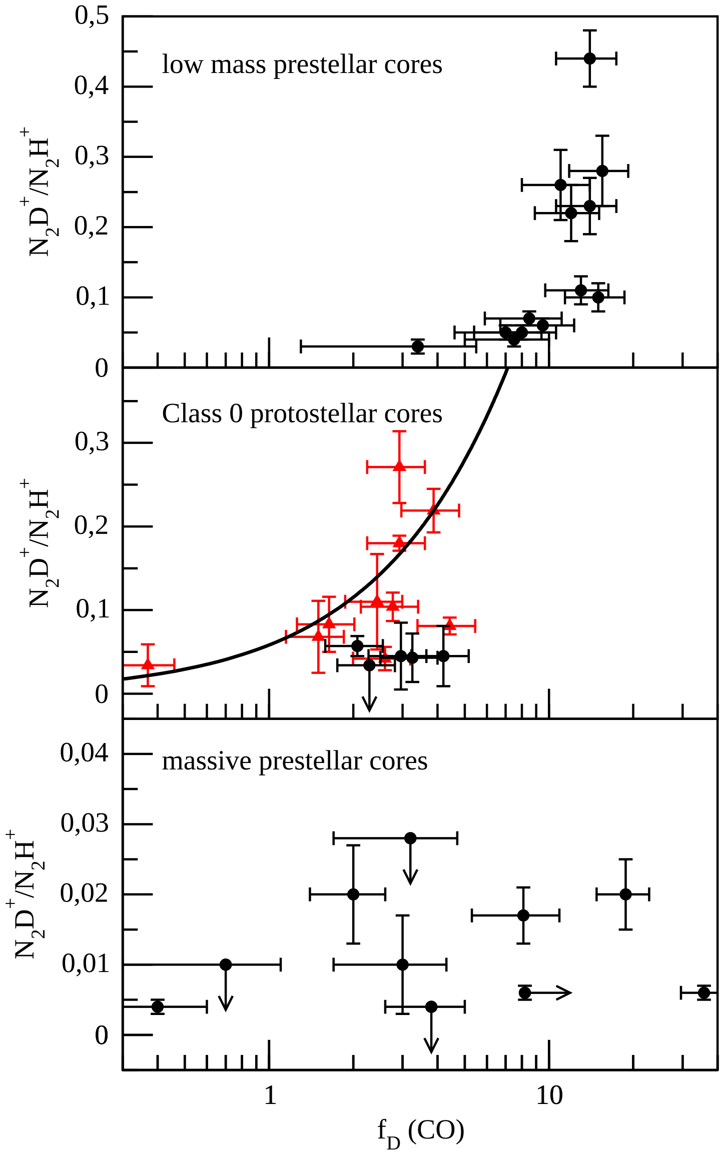

Fig. 6.7: *CO depletion factor versus N_2D^+/N_2H^+ ratio of prestellar cores (upper panel, Crapsi et al. (2005)), Class 0 protostars (middle panel, this work) and massive prestellar cores (lower panel, Fontani et al. (2006)). The protostellar objects marked with a triangle are located in the Perseus cloud. Between the Perseus objects a good correlation between f_D(CO) and deuterium fraction is seen. We fitted the sub-sample of the sources located in Perseus with a formula adopted from Caselli et al. (1998)(see text). The fit result is displayed in the middle panel. The N_2D^+/N_2H^+ ratio of the sources not located in Perseus lie below the fit to the Perseus sources.*

more affected by non-depleted, non-deuterated gas along the line of sight (see Fontani et al. 2006).

The sources, which are not located in the Perseus cloud show lower deuterium fractionation than sources located in Perseus with the same CO depletion factor. The main difference of the Perseus sources and the others is that the spatial resolution of the continuum observations at ~ 1 mm is 31″ for the Perseus sources, whereas it is 40″ for the other objects. Hence systematic errors in the beam correction cloud explain the too high CO depletion factor of the non-Perseus sources. The only source located in Perseus, which does not fit the correlation is L 1448 IRS 3. This source is known to be a source with high internal activities (e.g. Volgenau et al. (2006), Looney et al. (2000)), which might affect both deuterium fractionation and CO depletion. Furthermore it can be seen that the correlation among the sub-sample of the sources located in Perseus is much better than the correlation of the whole sample. We applied a least square fit to this sub-sample using the formula

$$\mathrm{N_2D^+/N_2H^+} = \frac{\mathrm{c_1}}{(\mathrm{c_2} + \mathrm{k_{CO}} \cdot \mathrm{x_{can}(CO)/f_D(CO)})} \tag{6.68}$$

which we adopted from expression (1) in Caselli et al. (1998). Thus the constant c_1 is $1/3 \cdot k_f \cdot x(HD)$, ($k_f$ is the formation rate of H_2D^+ and x(HD) the HD abundance), c_2 is the electron abundance (x(e)) times the dissociative recombination rate of H_2D^+, k_{co} is the destruction rate of H_2D^+ by CO, and $x_{can}(CO)$ is the canonical CO abundance. The fit result is shown in Fig. 6.7. The correlation coefficient we found is 0.719, indicating that the observed data agrees fairly well with the expected theoretical fit. Taking the reaction rates listed in Caselli et al. (1998) and assuming a temperature of 10 K, we derived an HD abundance of $3 \cdot 10^{-5}$, which is quite close to the cosmic D/H ratio. The electron abundance we found is $\sim 7 \cdot 10^{-9}$, which is at the low end of the values found for dense cloud cores. However, due to the uncertainties of temperature, density and the determination of $f_D(CO)$ (see below), the fitted values have to be taken with caution and errors can be as large as one order of magnitude.

The good correlation of the Perseus sources might be due to the fact that all Perseus sources lie approximately at the same distance. Furthermore, the continuum observations used for the determination of f_D have been done at the same wavelength (1100 μm), with the same beam width ($\theta = 31''$). Hence, possible systematic errors, introduced by uncertainties in the correction for the beam width are the same and cause just a constant scaling error of the CO depletion factor, but the correlation holds. The non–Perseus sources have been observed with different setups, and this causes some scatter in the N_2D^+/N_2H^+ versus f_D diagram.

The errors of the depletion factor are of the order of 20 %. This error does not include the uncertainty of the excitation temperature, dust temperature and κ, which are the main sources of systematic errors in this analysis. A wrong κ value, however, would just scale f_D differently, but it would not change the correlation itself. This applies to the dust temperature, too, because we used continuum measurement around 1 mm to determine $f_D(CO)$, which is clearly in the Rayleigh-Jeans regime. If the assumption of a constant average excitation temperature in all objects is incorrect, this would also change the correlation significantly. But, if we assume that $T_{ex}(C^{18}O)$ is somehow related to the dust temperature, i.e. objects with higher T_{Dust} have also higher $C^{18}O$ excitation temperature, the depletion factor of cooler objects (i.e. with high deuterium fractionation) would be underestimated, whereas $f_D(CO)$ of warmer objects would be overestimated. Such effects would strengthen the correlation we found.

6.4.3 Bolometric Luminosity

Due to the increase of the dust temperature during protostellar evolution, the SED changes with the evolutionary stage. Several measures have been developed to determine the evolutionary stage of a protostar (see section6.1.1). For example, Saraceno et al. (1996) suggest that the ratio of $L_{BOL}/F_{1.3}^{D_0}$ determines the evolutionary stage of protostars, where $F_{1.3}^{D_0}$ is the distance normalized flux at 1.3 mm. As the protostar warms up, L_{BOL} should rise quickly, whereas $F_{1.3}^{D_0}$, which is a measure for the envelope mass and which is less dependent on the temperature, is expected to stay constant or decrease slightly. Hence the $L_{BOL}/F_{1.3}^{D_0}$ ratio increases as the protostar evolves. We choose this method, because it is a sensible measure for the evolution of the protostar and because the required data were available in the literature for a significant fraction of our source sample.

Tab. 6.7: *Bolometric luminosity and distance normalized flux of some protostars. References:* [1]*Froebrich (2005),* [2]*Shirley et al. (2000)*

Source	L_{BOL} [$L_\odot$]	$F_{1.3}^{220\ pc}$	$L_{BOL}/F_{1.3}^{220\ pc}$
L 1448 IRS 2	6.0[1]	0.80	7.5
L 1448 C	8.3[1]	0.53	15.6
L 1455 A1	9.7[1]	0.19	50.2
IRAS 03282	1.2[2]	0.32	3.8
Barnard 1-B	2.8	0.74	3.8
HH 211	3.6[1]	0.61	5.9
L 1527	1.9[1]	0.38	5.0
L 483	13.0[2]	0.70	18.5
SMM 5	3.6[1]	-	-
L 723	3.3[2]	0.45	7.4
B 335	3.1[2]	0.45	6.9
L 1157	5.8[2]	0.68	8.6

Bolometric luminosities as well as the millimeter continuum data of several sources of our sample can be found in the literature. For this analyses only fluxes at λ = 1.3 mm (5 sources), 1.1 mm (4 sources) and 850 μm (2 sources) were taken. The continuum fluxes at 1.1 mm and 850 μm were corrected using, again, a β of one and, in the case of Barnard 5 IRS 1, zero, respectively. For the distance normalization and the correction of the different beam sizes of the continuum observations we followed again Terebey et al. (1993) i.e.

$$\mathrm{F}_{1.3}^{220\ \mathrm{pc}} = \mathrm{F}_{1.3}^{\mathrm{obs.}} \cdot (\mathrm{D}/220\ \mathrm{pc})^{0.7} \cdot (\theta/31'')^{-1.3}, \tag{6.69}$$

where $\mathrm{F}_{1.3}^{\mathrm{obs.}}$ is the observed continuum flux, D is the actual distance of the object and θ is the beam size. In this work we normalized all observations to a distance of 220 pc and a beam size (FWHM) of 31″. From the errors given for the continuum fluxes and the bolometric temperatures we estimated an error of 30 % for the $\mathrm{L_{BOL}}/\mathrm{F}_{1.3}^{\mathrm{D_0}}$ ratio. The resulting normalized fluxes and the bolometric luminosities for the cores, where available, are listed in Tab. 6.7.

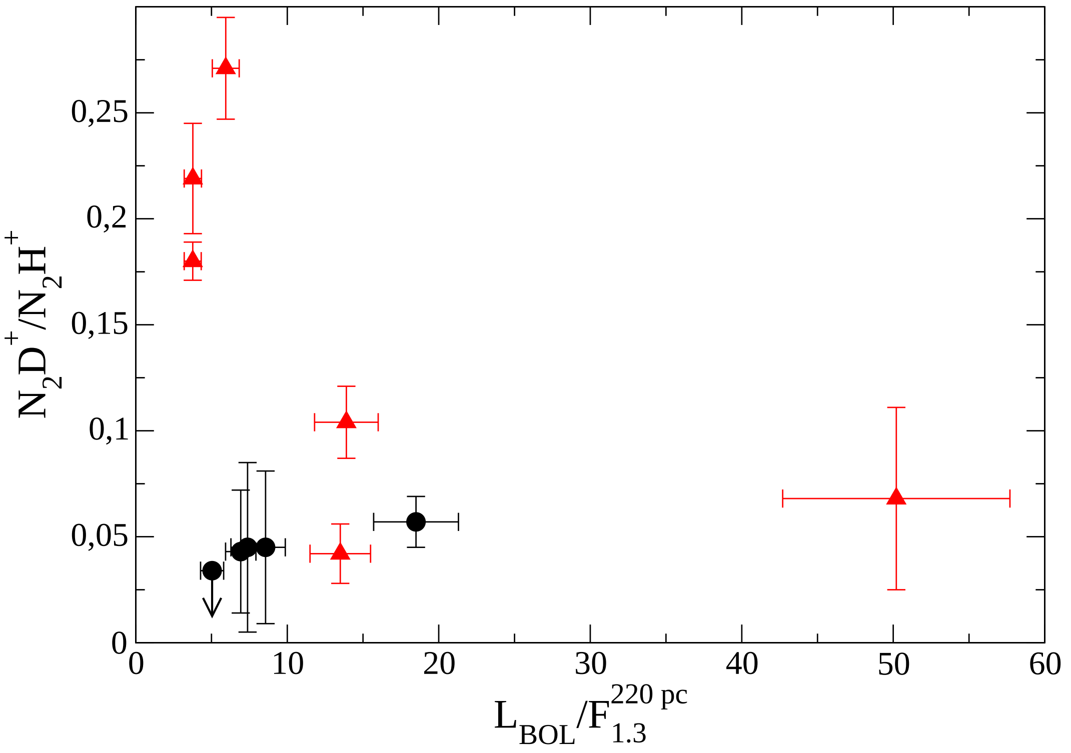

Fig. 6.8: *N_2D^+/N_2H^+ versus $\mathrm{L_{BOL}}/\mathrm{F}_{1.3}^{\mathrm{D_0}}$. All objects with high deuterium fractionation are at low $\mathrm{L_{BOL}}$, i.e. at early evolutionary stages. The red triangles represent the objects located in Perseus.*

The correlation between $\mathrm{L_{BOL}}/\mathrm{F}_{1.3}^{\mathrm{D_0}}$ and N_2D^+/N_2H^+ is shown in Fig. 6.8. The objects with the highest deuterium fractionation (> 0.15) (IRAS 03282, Barnard 1-B and HH 211) are among those with the lowest $\mathrm{L_{BOL}}/\mathrm{F}_{1.3}^{\mathrm{D_0}}$ ratios, i.e. these are the protostars in the least evolved stages. With increasing $\mathrm{L_{BOL}}/\mathrm{F}_{1.3}^{\mathrm{D_0}}$ ratio the deuterium fractionation drops quickly. However, if one just considers the cores located in Perseus, this fall-off is less steep. This might be due to an overestimation of the continuum flux of the non Perseus sources due to systematic errors in the normalization. L 1455 A1 has by far the highest $L_{BOL}/F_{1.3}^{D_0}$ ratio, and thus is expected to be the most evolved protostar in this plot. This is also confirmed by the relatively low CO depletion factor and high dust temperature. L 1527 is a notable outlier in the sample. Its $L_{BOL}/F_{1.3}^{D_0}$ ratio is one of the lowest in our sample (5.0), but it has an N_2D^+/N_2H^+ ratio < 0.034 (more discussion on this source is presented in chapter 6.5).

6.4.4 Kinematic of the Gas

So far, we correlated the N_2D^+/N_2H^+ ratio with physical parameters, which all are related to temperature, and thus to the evolutionary stage of the protostar. In this section we will investigate the relation of deuterium fractionation with the kinematics of the gas. Infall, for example, heats up the gas and thus is expected to influence the gas-phase chemistry.

First we compare the N_2D^+/N_2H^+ ratio with the N_2D^+ 2-1 line width (Tab. 6.4). All kinds of processes, such as thermal broadening, turbulent motions or systematic motions, e.g. infall, contribute to the full width at half maximum (FWHM) of an optically thin line. Thermal broadening, however, plays a minor role, since the thermal line width (FWHM) of N_2D^+ at 10 K is only 0.12 km/s (0.17 km/s at 20 K). In Fig. 6.9, the FWHM of N_2D^+ 2-1 is plotted versus the N_2D^+/N_2H^+ ratio. Most of the protostars with high N_2D^+/N_2H^+ ratios have narrow N_2D^+ lines. The two exceptions are Barnard 1-B ($\Delta v = 0.78$ km/s) and L 1448 C ($\Delta v = 0.72$ km/s), which show the broadest N_2D^+ lines of all objects. However, all Perseus sources with a $\Delta v > 0.5$ km/s, including Barnard 1-B and L 1448 C, show multiple embedded sources (Volgenau 2004, Matthews & Wilson 2002). Therefore, relative velocity differences between the individual cores cause an additional broadening of the line, which might explain our observational results.

To be able to trace only the systematic motion of the gas, e.g. infall motion, we used the asymmetry parameter δv, which was introduced by Mardones et al. (1997) as

$$\delta v = \frac{v_{thick} - v_{thin}}{\Delta v_{thin}} \tag{6.70}$$

v_{thick} is the velocity of an optical thick line, v_{thin} is the velocity of an optical thin line and Δv_{thin} is its line width. As shown by Mardones et al., a negative value of δv can arise from infall. If infall dominates the kinematics of the protostar, a foreground component, which is expected to be cooler and thus causes absorption, is redshifted with respect to the warmer core. Thus an optically thick line appears blueshifted. We used HCO^+ 3-2 as the optically thick line and $C^{18}O$ 1-0 as the optically thin line. The velocity of the optically thin $C^{18}O$ line was derived by a Gauss fit, except for L 1455 A1 and IRAS 03282, whose line shapes largely deviate from a Gaussian. In these two

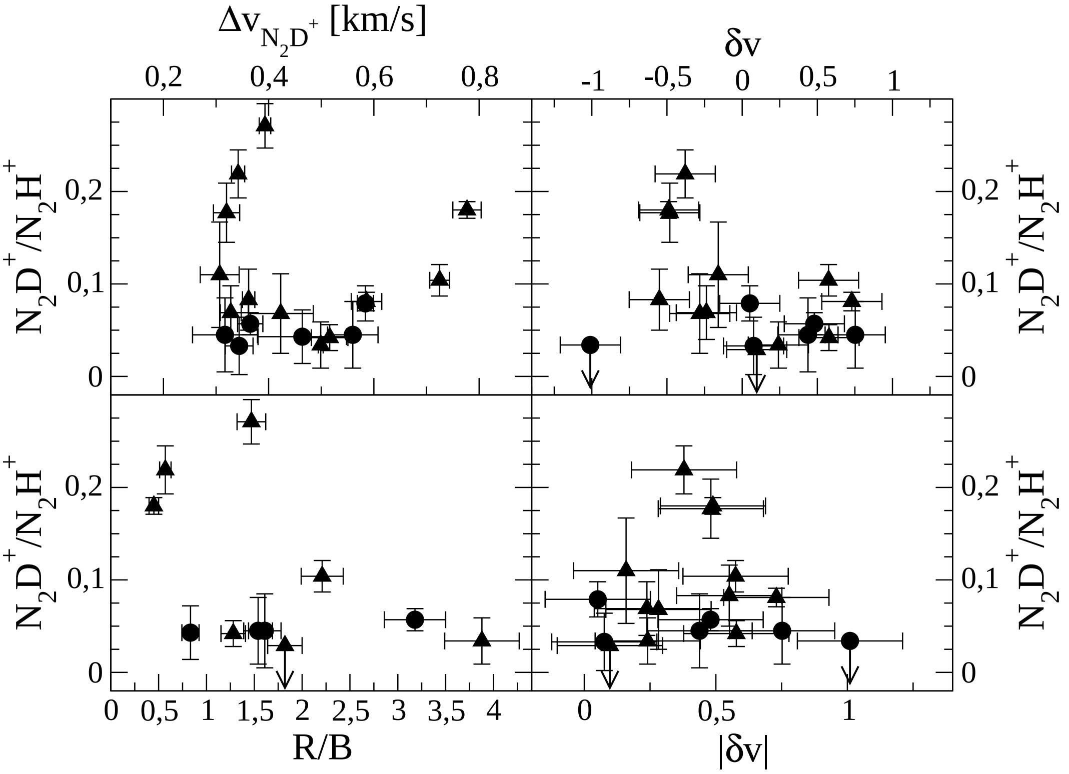

Fig. 6.9: *N_2D^+/N_2H^+ ratio versus $\Delta v_{N_2D^+}$ (upper left), R/B (lower left). δv (upper right) and $|\delta v|$ (lower right). The sources marked with a triangle are again those located in the Perseus cloud.*

cases we used the peak velocity. As v_{thick} we used the peak velocity of the HCO^+ 3-2 line. In the case of double peaked HCO^+ lines we used, following Mardones et al. (1997), the peak velocities of the stronger of the two peaks, which might cause some ambiguity for double peaked lines with nearly equal peak intensities. Alternatively, the intensity ratio of the red to the blue peak (R/B) of optical thick, double peaked lines can be used as an asymmetry parameter. In this case R/B < 1 indicates infall. Since more than 50 % of HCO^+ we observed show a double peaked line shape we calculated this ratio as well. The results for δv and the R/B ratio are listed in Tab. 6.8.

In our sample, we found seven sources with a clear indication of an infall (i.e. $\delta v < -0.25$) and sources showing redshifted, optically thick lines (i.e. $\delta v > 0.25$). Six sources do not show any clear indication ($-0.25 < \delta v < 0.25$). Contrary to Mardones et al. (1997) and Gregersen et al. (2000), we do not find more blueshifted that redshifted objects. The blue excess, which is defined by Mardones et al. (1997) as

$$\text{blue excess} = \frac{N_{\text{blue}} - N_{\text{red}}}{N_{\text{total}}} \tag{6.71}$$

in our sample is 0 ± 0.19. If we exclude the objects with an ambiguous δv due to nearly equal peak intensities of the double peaked HCO^+ line, we derive a blue excess of 0.06 ± 0.2. Both values are smaller than 0.28 and 0.25, the values found by Gregersen et al. (2000) and Mardones et al. (1997), respectively. This is possibly due to the relatively small number of objects in our sample.

Tab. 6.8: *Velocities of $C^{18}O$ and HCO^+ lines and asymmetry parameter. The δv marked with an * are ambiguous due to nearly equal peak intensities of the double peaked HCO^+ line, i.e. the R/B ratio is close to one.*

Source	v [km/s] $C^{18}O$	v [km/s] HCO^+)	δv	R/B
L 1448 IRS 2	4.08	4.53	0.58^*	1.28
L 1448 IRS 3	4.51	5.40	0.73	-
L 1448 C	4.81	5.45	0.57	2.21
L 1455 A1	5.41	5.12	-0.28	-
L 1455 A2	5.13	4.94	-0.24	-
Per 4 S	7.64	7.25	-0.48	-
Per 4 N	7.51	7.44	-0.16	-
Per 5	8.03	7.65	-0.55	-
Per 6	5.95	6.02	0.1	1.82
IRAS 03282	7.18	6.62	-0.38	0.57
Barnard 1-B	6.79	6.01	-0.49	0.45
HH 211	8.92	9.27	0.43^*	1.47
Barnard 5 IRS 1	10.05	10.29	0.24	3.88
L 1527	6.04	5.38	-1.01	
L 483	5.48	5.87	0.48	3.18
SMM 5	8.26	8.18	0.05	-
L 723	10.86	11.43	0.44	1.61
L 673 A	6.90	6.97	0.08	-
B 335	8.31	7.90	-0.94^*	0.833
L 1157	2.70	3.16	0.75	1.54

The deuterium fractionation of N_2H^+ is plotted against the kinematical parameter Δv, δv, R/B and $|\delta v|$ in Fig. 6.9. δv and, less clearly, R/B are correlated with the deuterium fractionation, and only L 1527, which is a peculiar source (see section 6.5), does not follow the general trend and indicate strong infall motion. The higher the N_2D^+/N_2H^+ ratio, the more blueshifted the optically thick emission lines. Such a result was somehow expected, since outflow activity rises with the evolution of the protostar (Richer et al. 2000). The results are also in good agreement with the results of Mardones et al. (1997). Using observations of CS, $C^{34}S$ and H_2CO lines, they found that the blue excess of Class 0 protostars is clearly enhanced compared to Class I objects. However, using observations of HCO^+, $H^{13}CO^+$ and N_2H^+ lines, Gregersen et al. (2000) did not find such trend. They speculate that infall asymmetry disappears later in HCO^+. Because our sample contains no true Class I objects, we cannot directly compare their results with ours.

6.5 Evolutionary Sequence of the Sample

According to the dust temperature, the CO depletion and $L_{BOL}/F_{1.3}^{220pc}$ we can determine an evolutionary sequence of the protostars in our sample and compare the evolutionary stage with the deuterium fractionation.

The youngest objects in our sample are Barnard 1-B, IRAS 03282 and HH 211. All three evolutionary tracers indicate those sources are among the youngest. The depletion factor, f_D(CO), indicates that L1448 IRS3 and L 1157 are young objects, too, but their T_{DUST} suggest that these sources are, instead, more evolved. A possible solution to this discrepancy lies in acknowledging several assumptions we made in determining the CO depletion factor (e.g. in converting the beam sizes of the continuum and the $C^{18}O$ observations). Although, overall, these assumptions seem to be justified, they might not be valid for all sources, and thus the f_D (CO) values may be less accurate. The three protostars we identified as the youngest also have the highest N_2D^+/N_2H^+ ratios (0.18, 0.22, and 0.27 in Barnard 1-B, IRAS 03282, and HH 211, respectively). By this measure, Per 4 S, with a deuterium fractionation of 0.177, should also be very young, but no complementary data are available to confirm this.

The objects at a moderate evolutionary stage are those with a deuterium fractionation around 0.1 (L 1448 IRS 3, PER 4 N, PER 5). The exception is L 1448 C ($N_2D^+/N_2H^+ = 0.10$), which seems to be more evolved than the others. However, among these intermediately-evolved sources, there are also some with deuterium fractionations of ~ 0.05 (L 723, B 335, L 1448 IRS 2). For SMM 5 ($N_2D^+/N_2H^+ = 0.079$), we are unable to determine the evolutionary stage independently, but, because of its N_2D^+/N_2H^+ ratio, we think that it belongs to the group of intermediately-evolved objects. The N_2D^+/N_2H^+ ratios of the most evolved protostars are, with the exception of L 1448 C (0.10), ~ 0.05.

L 1527 is a special case. The T_{Dust} (27 K) and especially the $L_{BOL}/F_{1.3}^{D_0}$ ratio (5.0) suggest that it is a younger object, but its low N_2D^+/N_2H^+ ratio and the fact that an embedded source is detected at wavelengths $< 5\mu m$ indicates that this source is more evolved (Froebrich 2005). Chemical models, which reproduce the observed abundance of long-chain unsaturated hydrocarbons and cyanopolyynes, indicate a more evolved evolutionary stage of L 1527 as well (Hassel et al. 2008)). From infrared observations, Tobin et al. (2008) conclude that L 1527 contains a massive protostellar disc, which is seen edge-on. Therefore L 1527 might be a more evolved object than indicated by continuum observations, due to the large obscuration of the central object. Hence, the N_2D^+/N_2H^+ ratio seems to be even more reliable than continuum measurements at identifying the youngest protostellar objects.

In conclusion, the N_2D^+/N_2H^+ ratio can be used to clearly identify the youngest objects among the Class 0 sources. For more evolved objects, the correlation of evolutionary stage and N_2D^+/N_2H^+ ratio is not so clear, but an overall decrease in deuteration with evolutionary stage can be seen.

6.6 Comparison with chemical- and radiative transfer model

To explain the results discussed in the previous section, we examined a model of a ”typical” Class 0 object rather than a specific source. First, we describe the physical properties, e.g. the temperature and density profiles, of the model. Subsequently, we calculate the abundances of the important species and apply a radiative transfer code to simulate the observations.

6.6.1 Cloud structure

The density structure of the model is that of a singular isothermal sphere (Shu 1977)):

$$n(r) \propto r^{-2}. \tag{6.72}$$

Such density profiles have been found for Class 0 protostars, too (Looney et al. 2003). The inner boundary of the protostellar envelope is set to 100 AU. This limit is arbitrarily chosen, but at a distance of 220 pc, which is the distance of the Perseus molecular cloud, 100 AU corresponds to an angle of $0.46''$, which is much smaller than the angular resolution of our observations. Therefore, the model results are not sensitive to the chosen inner boundary. The outer boundary is defined by the radius where the density is 10^4 cm^{-3}. Kirk et al. (2006) estimated the external pressure on cores in the Perseus region and found values of $\log_{10}(P_{ext}/k)$ between 5.5 and 6.0. Assuming a temperature between 15 and 30 K, this leads to a gas density between $\sim 10^4$ cm^{-3} and $\sim 5 \cdot 10^4$ cm^{-3}. Around L 1448 IRS 3, Kwon et al. (2006) find a density of $6-9 \cdot 10^3$ cm^{-3}. Thus, 10^4 cm^{-3} can be considered an average value for the gas number density surrounding Perseus cores.

The total envelope mass is assumed to be of the order of one to a few solar masses. However, since the model results depend strongly on the density, the total mass varies for different models (see below). For the temperature profile, we use a power law with an index of -0.4, which is the exponent for optically thin emission from protostellar envelopes, as found by Looney et al. (2003). They also showed that, with a density power-law index of 2, the radial temperature distribution can significantly deviate from the power-law at radii smaller than 100-200 AU. However, given that we used an inner boundary of 100 AU for the envelope, such deviations do not noticeably influence the model. To avoid very low temperatures in the outskirts of the envelope, we assumed a temperature profile like that found in prestellar cores (Crapsi et al. 2007), as soon as the power-law drops below this value:

$$T(r) = T_{out} - \frac{T_{out} - T_{in}}{1 + (r/r_0)^{1.5}} \tag{6.73}$$

i.e. the temperature slowly rises again. In this equation, we assumed T_{out} = 15 K, T_{in}=7 K, and r_0=3633 AU. This radius corresponds to an angle of 26″ at a distance of 220 pc, as found in L 1544. However, since we used this temperature profile only for the outer, low-density part of the envelope, the influence of these parameters on the model results is negligible. Density and temperature profiles are shown in Fig. 6.10.

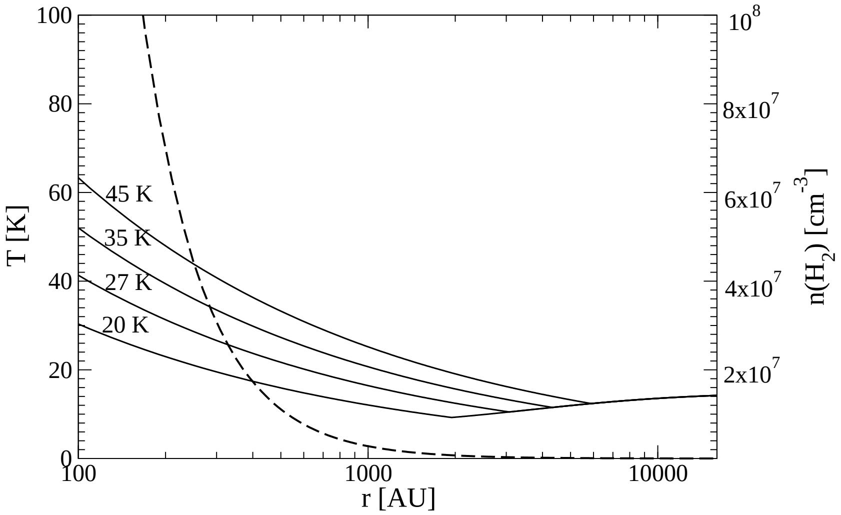

Fig. 6.10: *Density (dashed line) and temperature (solid lines) profiles of the protostellar core models. The four temperature profiles represent models that yield values for T_{Dust} of 20 K, 27 K, 35 K and 45 K, respectively.*

Using this cloud structure, we calculate the continuum flux at 60 μm, 100 μm, 850 μm and 1.2 mm from the formula:

$$F_\nu = \int n(r) \cdot B_\nu(T(r)) \cdot \kappa_\nu \cdot \mu \, dr \tag{6.74}$$

where n is the density, B(T) is the Planck function, and μ is the mass of the gas molecules. For the opacity per unit mass, κ_ν, we use again 0.005 g/cm^2 at 1.2 mm, which assumes optically thin continuum emission. Furthermore, we assumed an emissivity index of $\beta = 2$, which is a typical value for molecular clouds (Ward-Thompson et al. 2002) and not the $\beta = 1$ shown by previous fits. We used $\beta = 2$, because the cold (~ 10 K) outskirts of the envelope still emit a significant amount of radiation at mm wavelengths, but much less at 60 μm. The strong temperature gradient in protostellar cores causes the spectrum integrated over the entire core to be flattened. Thus, the emissivity index derived from a single temperature fit is underestimated. The values for the continuum emission obtained by this method are then fitted, following the procedure described in section 6.4.1, and the absolute temperature scale is varied to obtain models with dust temperatures of 20 K, 27 K, 35 K and 45 K, respectively, which covers the whole range of observed values.

6.6.2 Chemical- and radiative transfer model

The chemical code we used here is described in Caselli et al. (2002b), but has been recently updated (Caselli et al. 2008). We assumed a radial symmetric cloud with the density- and temperature profile mentioned above. We followed the time dependent freeze-out of CO and N_2, assuming binding energies of 1100 K and 982.3 K, following the prescription of Öberg et al. (2005) and Schnee et al. (2007). Furthermore thermal as well as non-thermal desorption due to cosmic-ray impulsive heating were included, but dynamical effects were neglected. As initial abundances of CO and N_2 we assumed $9.5 \cdot 10^{-5}$ and $4.0 \cdot 10^{-5}$, respectively. We did not include atomic oxygen in the model, because of the large uncertainty in its abundance in cold cloud cores (e.g. Bergin & Snell 2002, Caselli et al. 2002b). All deuterated versions of H_3^+ are included. The abundances of the ionic species (HCO^+, N_2H^+ and their deuterated counterparts) are given by a steady state equation of the chemical network, using instantaneous abundances for the neutral species. The reaction rates have been taken from the UMIST database for astrochemistry[9]. For the proton-deuteron exchange reaction (e.g. $H_3^+ + HD \rightarrow H_2D^+ + H_2$), we used both ”standard” rates (e.g. as used by Roberts et al. 2004 and Ceccarelli & Dominik 2005) and reaction rates more recently measured by Gerlich et al. (2002), which seems to better fit the data. The cosmic-ray ionization rate has been fixed at ζ=3×10^{-17} s^{-1}, the average value measured toward high-mass star forming regions by van der Tak & van Dishoeck (2000). The model ran for an evolution time of 10^6 years, which is expected to be a typical age of these objects. After 10^6 years, the abundances of the various molecules have nearly reached chemical equilibrium, and thus the exact evolution time is not a critical parameter (see section 6.6.5 for discussion).

The results from the chemical model were used as input parameters for a radiative transfer model. We used a non-LTE Monte-Carlo code developed by Pagani et al. (2007). This code, which is developed from the Bernes code (Bernes 1979), calculates the 1D radiative transfer of both N_2H^+ and N_2D^+ and includes line overlap of the hyperfine transitions. Furthermore, recently published collisional coefficients between individual hyperfine levels have been implemented (Daniel et al. 2005). For the convolution with the beam, we assumed a Gaussian beam shape with HPBW as listed in Tab. 6.2. The distance to the cloud was set to 220 pc, i.e. the distance of the Perseus cloud. From the spectra that we obtained from the Monte-Carlo-code, we determined the N_2D^+/N_2H^+ ratio using the CTEX procedure, just as we did for the observed spectra (see section 6.3.1). Hence, the comparison between the model and the observations is consistent, because possible systematic errors, introduced by the assumption of a constant excitation temperature, are taken into account.

---

[9] www.udfa.net

6.6.3 Comparison between models and observations

We computed the N_2D^+/N_2H^+ ratios for four models with fitted dust temperatures of 20 K, 27 K, 35 K and 45 K, respectively. The deuterium fractionation in these models ranges from 0.23 at 20 K to 0.03 at 45 K. These values fit the observations very well (see Fig. 6.11). We derived an H_2 density at a radius of 100 AU of $2.77 \cdot 10^8$ cm^{-3}, which corresponds to a total envelope mass of 4.6 $M_\odot$. The modeled correlation between the deuterium fractionation and the CO depletion factor (f_D (CO)) fits the observations quite well, too, but in the cooler objects ($T_{Dust} \sim 20$ K) the modeled CO freeze-out is very sensitive to the temperature. Thus a marginal temperature variation leads to a significant change of the CO depletion factor, and therefore the quality of the fit depends strongly on the used model. In Fig. 6.11, a comparison of the models with the observations of the Perseus sources is shown. Results from the models are also listed in Table 6.9. We obtained the most reasonable results using the reaction rates measured by Gerlich et al. (2002) for the proton-deuteron exchange reaction. Using the ”standard rates”, we could only fit the observed N_2D^+/N_2H^+ ratios by increasing the total envelope mass to 25 $M_\odot$, a value that is clearly larger than expected for low mass protostars.

To check that the assumption of a constant excitation temperature does not give a significantly different result from the $T^{-0.4}$ profile, we calculated beam averaged column densities from the model abundance profiles as well. The N_2D^+/N_2H^+ ratios determined from the beam averaged column densities are the same as before, to within 20%. The estimated error of the observed N_2D^+/N_2H^+ ratio is also approximately 20%, so the fit is good, independent of the method used. The trend of a decreasing deuterium fraction with increasing T_{Dust} is true for both the ratio determined by the CTEX method and the ratio of the beam averaged column density.

Tab. 6.9: *Model results*

T_{Dust}	N_2D^+/N_2H^+ (CTEX)	HCO^+/DCO^+	f_D(CO)
20 K	0.23	0.09	4.73
27 K	0.14	0.05	2.55
35 K	0.07	0.03	1.97
45 K	0.03	0.02	1.67

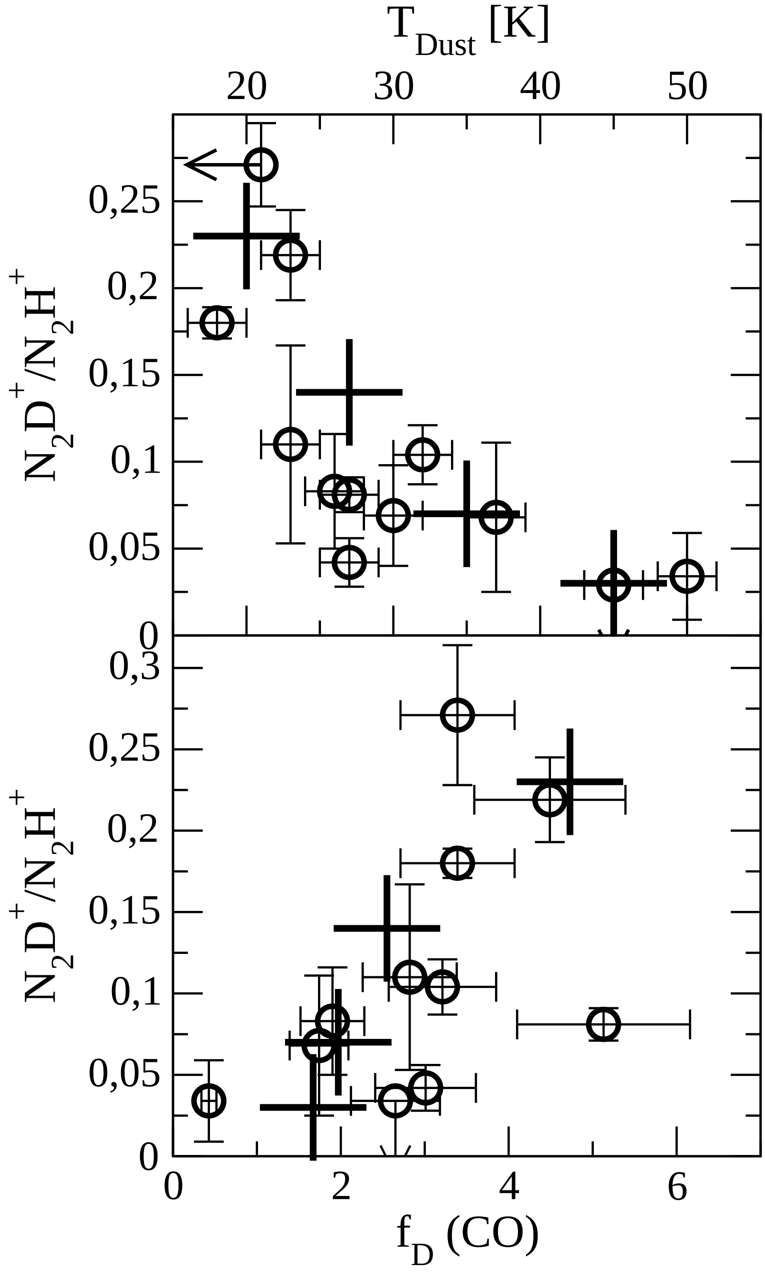

Fig. 6.11: **Upper panel:** *N_2D^+/N_2H^+ ratio versus dust temperature.* **Lower panel:** *N_2D^+/N_2H^+ ratio and the CO depletion factor F_D (CO). The open circles are the observed values for the sub-sample of cores in the Perseus cloud; the crosses are the model results. The N_2D^+/N_2H^+ ratio of the models was determined using the CTEX method.*

The N_2D^+ J=3-2/J=2-1 intensity ratios of the models range from 0.44 to 1.10, which is comparable to the observed ratios. For the J=2-1/J=1-0 ratios, the models give values a factor of two higher than what is observed. However, these ratios are very sensitive to temperature, density and abundance variations. Taking the simplicity of the model into account, we consider these values in agreement with the observations.

Besides N_2D^+ and N_2H^+, the abundances of HCO^+ and DCO^+ are also calculated by the chemical model. The DCO^+/HCO^+ ratio is significantly lower than the N_2D^+/N_2H^+ ratio and ranges from 0.02 to 0.08 in the models with dust temperatures of 45 K and 21 K, respectively. The HCO^+ and DCO^+ column densities are averaged over a $21''$ beam, and thus comparable to the observations conducted by Jørgensen et al. (2005). The values for the DCO^+/HCO^+ ratio reported by them are between 0.004 and 0.048 and thus a little lower than the modeled ratios (see Tab. 6.9 & 6.10).

6.6.4 Chemical stratification within the core

The temperature gradient, caused by the heating of the central object, leads to strong variations of the abundances of many molecules and molecular ions. The more immediate cause for these variations is the freeze-out of CO, which occurs at a temperature of ~ 20 K. The absence of CO in the gas phase has a big influence on the abundance of many other species, since many molecular ions, e.g. N_2H^+, are destroyed by reactions with CO. In addition, the deuterium fractionation is enhanced in regions where CO is depleted (see section 2.2.2). Therefore, the protostellar envelope can be roughly divided into three zones (Fig. 6.12 & r̃efmolec). In the inner zone, the temperature has increased above ~ 20 K, and thus CO is evaporated from the grains again. Therefore the abundance of N_2H^+ and the deuterium fractionation is relatively low in this region. As soon as the temperature drops below the critical temperature of ~ 20 K, the CO abundance drops drastically. At the same time, the N_2H^+ abundance rises by 1-2 orders of magnitude. The N_2D^+/N_2H^+ ratio rises as well, but its maximum is at a larger radius than the CO abundance minimum. This is because the temperature at the minimum of the CO abundance is ~ 20 K, where the destruction of H_2D^+ via the reaction $H_2D^+ + H_2 \rightarrow H_3^+ + HD$ is not negligible. At even larger radii, the degree of CO depletion decreases as the gas density decreases, which causes the N_2H^+ abundance to stay more or less constant, and the deuterium fractionation to drop again.

During the Class 0 phase the temperature of the central object increases, and so does the temperature of the envelope. Consequently, the radius at which CO freezes out onto dust grains shifts further outwards, and the fraction of the cloud in which the abundance of deuterated molecules is enhanced gets smaller with time. Furthermore, the mean density of the gas at which the deuteration occurs decreases, and thus the mean local N_2D^+/N_2H^+ ratio declines as well. This leads to the decrease of the N_2D^+/N_2H^+ column density ratio, which we observed in the cores in our sample.

The reason for the different ratios of the deuterated and non-deuterated forms of HCO^+ and N_2H^+ is that the deuterium fractionation is strongest in places where CO, a progenitor of HCO^+ & DCO^+, is mostly depleted. Furthermore, N_2H^+ is destroyed by

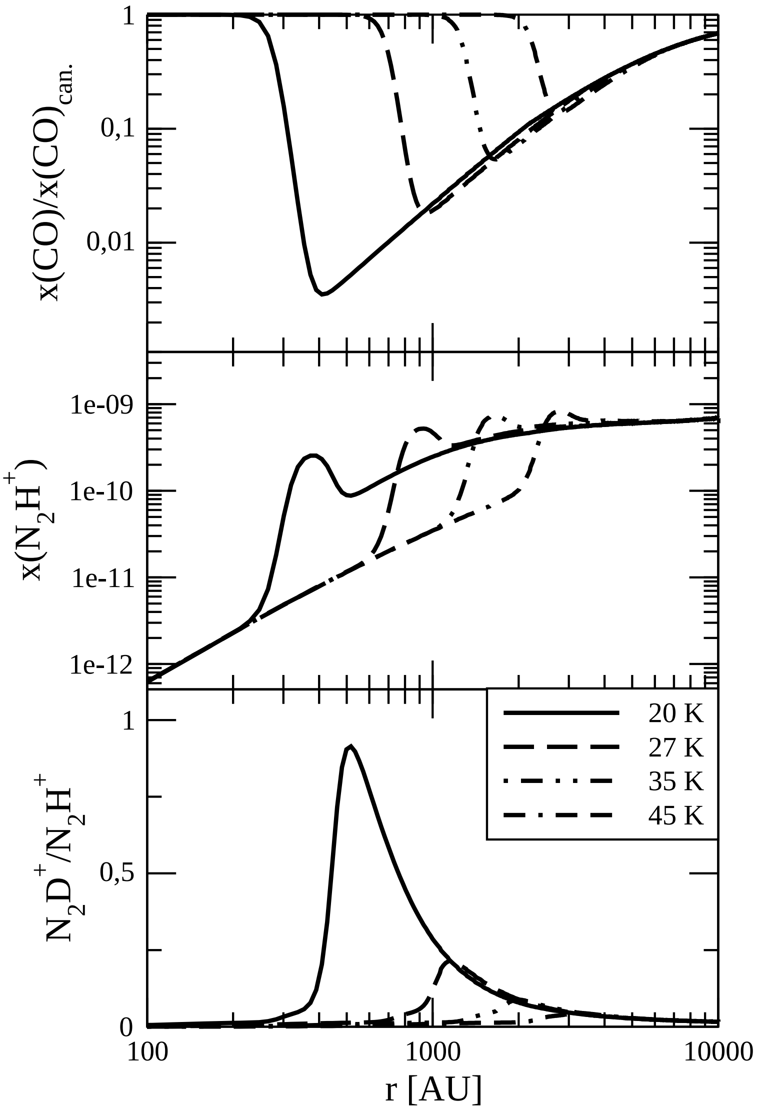

Fig. 6.12: *The relative abundance of CO (upper panel) and* N_2H^+ *(middle panel) and the* N_2D^+/N_2H^+ *ratio are shown as a function of radius. It can be clearly seen that the radius at which CO starts to deplete, as well as the peak of deuterium fractionation, shifts outwards and diminishes with increasing temperature.*

CO forming HCO^+. Thus, contrary to N_2H^+, HCO^+ is also relatively strong in the warm and dense inner part of the envelope, and the ratio of the column densities of DCO^+ and HCO^+ is significantly lower than the N_2D^+/N_2H^+ ratio. This can be seen in Fig. 6.13, in which the abundance of the molecules and molecular ions are shown as a function of radius.

The radial abundance profiles we found with our static model are in good agreement with the results of Lee et al. (2004), who calculated a self-consistent dynamical and

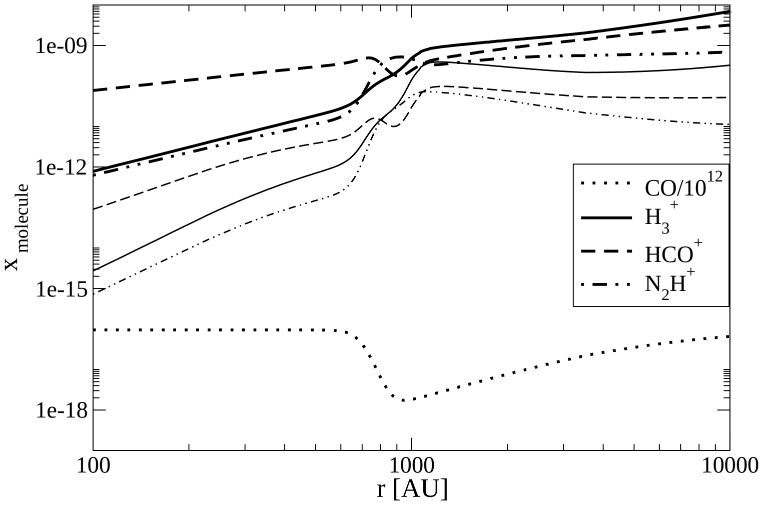

Fig. 6.13: *The abundances of CO, H_3^+, H_2D^+, HCO^+, DCO^+, N_2H^+, and N_2D^+ relative to H_2 are shown as a function of radius. The thick lines show the abundance profile of the protonated species. The thin lines show their singly-deuterated counterparts. These profiles apply to the model with* T_{Dust} = 27 K.

chemical model of the entire star forming process. In their model, the deuterated species are not calculated, but the abundance profiles of CO, N_2H^+ and HCO^+ at a time ~ 10^5 yr after the collapse starts are similar to the profiles we found (see their Fig. 11). This similarity indicates that the assumption of a chemical equilibrium is valid at least for the simple species. In a more recent paper, Aikawa et al. (2008) get somewhat shorter timescales for the protostellar evolution; $9.3 \cdot 10^4$ years after the beginning of the collapse, the CO desorption radius is ~ 2000 AU, which is comparable to the results of our 45 K model. But even for these shorter time scales, the assumption of chemical equilibrium is still valid (see next section).

6.6.5 Sensitivity of the Model

In this section we discuss how variations of the parameter which were fixed in our model, such as the cosmic-ray ionization rate and binding energies of CO on dust, influence the out-coming N_2D^+/N_2H^+ ratio.

At first we discuss the influence of the different run-times of the models, because this is the least known value. The estimated ages of Class 0 protostars ranges from ~ 10^4 to a few times 10^5 years after the collapse has started (Froebrich 2005). But the time estimates vary by a factor of 10 depending which model is used. However, the crucial time for the deuterium chemistry is anyhow, the time passed since CO started to freeze out, because the CO depletion is the slowest reaction in the chemical network. Thus, the entire prestellar phase, has to be taken into account, too. After a time of

10^6 years, the abundances have already reached equilibrium. Reducing the time to 10^5 years changes the N_2D^+/N_2H^+ ratio only marginally. The difference between the ratios after 10^6 years and 10^5 years is less than 0.01. In models with a run-time of 10^4 years the abundances aren't in equilibrium anymore. In the coldest protostar (20 K) the deuterium fractionation is already high (0.26), but for the warmer objects the N_2D^+/N_2H^+ ratio is a factor ~ 2 lower than in chemical equilibrium. Although already quite low, these values would still agree with the observations. Run-times longer than 10^7 years do not change the results, because equilibrium is already reached.

Another important parameter is the cosmic-ray ionization rate. In our model we used $\zeta = 3 \cdot 10^{17}$ s^{-1} (van der Tak & van Dishoeck 2000). A ζ of $6 \cdot 10^{17}$ s^{-1} increases the N_2H^+ abundance by a factor of 1.5 but the deuterium fractionation is lowered by 40%. A cosmic-ray ionization rate of $1.5 \cdot 10^{17}$ s^{-1} increases the N_2D^+/N_2H^+ ratio by 30%.

A similar effect on the deuterium fractionation as ζ has the central density, and subsequently the envelope mass. In our models the density was varied to match the observed N_2D^+/N_2H^+ ratio best. The only constrain we put on the central density was, that the resulting envelope mass should be on the order of a few solar masses. For the best fit model we derived an envelope mass of 4.6 $M_\odot$. Decreasing the density by a factor of 0.5 has a similar effect on the N_2D^+/N_2H^+ ratio as doubling the cosmic-ray ionization rate, i.e. the deuterium fractionation decreases by 40%. With a density twice as high as the best fit model, the N_2D^+/N_2H^+ increases by a factor of 1.2.

The last crucial parameter, we investigated here, is the binding energy of CO and N_2 on dust grains. In our model we used binding energies of 1100 K and 982.3 K for CO and N_2, respectively, which are the binding energies on mixed CO-H_2O ice. We also calculated the models using the values for E_b on pure CO ice (855 and 790 for CO and N_2, respectively, (Öberg et al. 2005). With these values, the resulting N_2D^+/N_2H^+ ratios drop to < 0.04 for all four temperatures.

6.7 Deuterium fractionation of other molecules

The deuterium fractionation of N_2H^+ reflects the present time temperature and density better than most other molecules, since it does not significantly deplete (see e.g. Caselli et al. 2002a, Bergin & Snell 2002, Schnee et al. 2007) and the chemical reaction for N_2D^+ formation and destruction are quite fast and simple. Memories of cold phases in the past of the dark cloud core are therefore not expected to be seen in the observed N_2D^+/N_2H^+ ratio. A comparison of the deuterium fractionation of N_2H^+ with the deuterium fractionation of other molecules is interesting, because the qualititative and quantitative differences with evolution of the D/H ratios reflects the different chemical processes. Thus, the physics of star formation might be revealed in more detail. The deuterium fractionation of the individual molecules is listed in Tab. 6.10. The reason for the significantly lower deuterium fractionation of HCO^+ has been discussed in the previous section, and is due to the freeze-out of CO, which is a progenitor of HCO^+.

Tab. 6.10: *Deuterium fractionation of several molecular species.*

Source	$\frac{N_2D^+}{N_2H^+}$ 1	$\frac{NH_2D}{NH_3}$ 2	$\frac{DCO^+}{HCO^+}$ 3	$\frac{D_2CO}{H_2CO}$ 4
L1448 IRS 3	0.081	0.17	-	-
L1448 C	0.104	0.20	0.011	0.24
IRAS 03282	0.219	0.22	-	-
HH 211	0.271	0.33	-	-
Barnard 5	0.034	0.18	-	-
L 1527	< 0.034	-	0.048	0.44
L 483	0.057	-	0.006	-
L 723	0.045	-	0.004	-
L 1157	0.045	-	0.016	≤ 0.08

[1]This work, [2]Hatchell (2003), [3]Jørgensen et al. (2004), [4]Parise et al. (2006).

H_2CO and CH_3OH

Deuterated formaldehydes (HDCO and D_2CO) are very abundant, too. The HDCO/H_2CO ratios as well as the D_2CO/H_2CO ratios are in the order of 0.1 (Parise et al. 2006). In their work, Parise et al. determined also the deuterium fractionation of methanol, which exceeds even the deuterium fractionation of formaldehyde (e.g. $CH_2DOH/CH_3OH \sim 0.5$). For both molecules no obvious correlation between deuterium fractionation and the evolutionary stage could be found. Because grain surface chemistry, and thus freeze-out and desorption mechanisms, are involved in the deuteration of methanol and formaldehyde, the observed deuterium fractionation is likely a memory of the previous, prestellar phase (Ceccarelli et al. 2001).

NH_3

The deuterium fractionation of NH_3 has been studied by Hatchell (2003). Like N_2H^+, NH_3 is formed from N_2 and does not seem to freeze out (Tafalla et al. 2002). Thus, N_2D^+ and NH_2D emission should originate from the same region. As a consequence, the deuterium fractionation of N_2H^+ and NH_3 should be comparable. For the coldest T_{Dust} objects (IRAS 03282 & HH 211), i.e. the youngest objects in our sample (HH 211 & IRAS 03282), the deuterium fractionation of NH_3 is indeed comparable to the fractionation of N_2H^+. But the warmer the dust gets, the more the ratios diverge. In Barnard 5, which is the most evolved object, the NH_2D/NH_3 ratio increases up to a factor of five higher than the N_2D^+/ N_2H^+ ratio. The differing trends in the two ratios can be explained as follows. Both N_2D^+ and NH_2D are formed directly or indirectly via H_2D^+ or its multiply deuterated forms, i.e. the formation mechanism is only effective in cold, CO-depleted environments. In regions were CO desorbs from the dust due to the warming up of the protostar, N_2D^+ disappears faster than NH_2D not only because the H_2D^+/H_3^+ ratio decreases (this affects the formation of both species), but also because N_2D^+ reacts directly with CO to form DCO^+.

6.7.1 Preliminary analyzed NH_2D and NH_3 observations

To investigated the differences in the trend of the deuterium fractionation of N_2H^+ and NH_3, we observed the 15 protostars of our sample, which are not studied by Hatchell (2003), in NH_3 (1,1) and (2,2) and NH_2D 1_{11}-1_{01}. The final goal of this investigation will be to derive an absolute time scale for the protostellar evolution. Due to the fast reactions of ionic molecules with neutrals, the deuterium fractionation of N_2H^+ is approximately at equilibrium at all times, and the decline of the N_2D^+/N_2H^+ ratio is due to the smaller and smaller fraction of CO depleted material in the protostellar envelope (see section 6.6.4). The decline of the deuterium fractionation of NH_3 seems to be slower, because the neutral species do not react that fast. Measuring the different decline rates for the NH_2D/NH_3 ratio and the N_2D^+/N_2H^+ ratio, together with time dependent chemical models, would thus allow us to derive absolute time scales.

The ammonia observations have been conducted at the Effelsberg 100m telescope in December 2007. The same setup as for the NH_3 observations in IC 5146 (see chapter 5), was used. The deuterated Ammonia 1_{11}-1_{01} line at a frequency of 85.9 GHz was observed with the IRAM 30m telescope in June 2007, using frequency switching ($\Delta\nu = 7.9$ MHz). The beam width (HPBW) of the IRAM observations is 29″, which is comparable to the 40″ resolution of our ammonia observations. For the conversion to T_{mb} a beam efficiency of 0.78 was used. The focus and pointing were checked every two hours and pointing was better than 3″. The lines are displayed in Fig. 6.14 and their parameters are listed in Tab. 6.11.

Column Densities

Like N_2H^+, the NH_3 and NH_2D line split up into several hyperfine components due to the nuclear spin $I = 1$ of the nitrogen atom. Hence the optical depth of these two species can be determined as well. However, the excitation temperature was not determined by the detection equation (equation 6.57), but following the procedure described in chapter 5 (equation 5.42). For T_{ex} of NH_2D we assumed the same excitation temperature as for NH_3. Because the excitation temperature was determined independent from the line intensity, we could determine the beam filling factor (ff) of the sources using the equation

$$ff = \frac{T_b}{(J_{T_{ex}} - J_{BG}) \cdot (1 - e^{-\tau})}. \tag{6.75}$$

The filling factor of NH_3 and NH_2D are listed in Tab. 6.11.

Tab. 6.11: *Parameters of the observed NH_3 and NH_2D lines.*

Source	NH_3 (1,1)			NH_3 (2,2)	T_{rot}	NH_2D		
	$\int T_{MB}dv$ [Kkm/s]	τ	ff	$\int T_{MB}dv$ [Kkm/s]	[K]	$\int T_{MB}dv$ [Kkm/s]	τ	ff
L 1448 IRS 2	12.9 ± 0.3	2.46 ± 0.12	0.64 ± 0.03	0.66 ± 0.07	12.7 ± 0.3	1.91 ± 0.05	2.47 ± 0.20	0.19 ± 0.05
L 1455 A1	9.1 ± 0.3	1.76 ± 0.14	0.45 ± 0.03	0.51 ± 0.07	12.3 ± 0.3	0.92 ± 0.05	< 0.1	-
L 1455 A2	9.4 ± 0.3	1.95 ± 0.12	0.56 ± 0.03	0.41 ± 0.07	11.2 ± 0.3	0.96 ± 0.05	1.02 ± 0.10	0.24 ± 0.05
Per 4 S	3.7 ± 0.3	1.14 ± 0.19	0.40 ± 0.03	0.25 ± 0.07	11.7 ± 0.3	1.80 ± 0.05	1.97 ± 0.21	0.29 ± 0.05
Per 4 N	4.2 ± 0.3	1.29 ± 0.10	0.40 ± 0.03	0.21 ± 0.07	12.6 ± 0.3	1.34 ± 0.05	1.78 ± 0.28	0.20 ± 0.05
Per 5	6.7 ± 0.3	1.46 ± 0.16	0.57 ± 0.03	0.27 ± 0.07	11.8 ± 0.3	2.42 ± 0.05	1.81 ± 0.18	0.36 ± 0.05
Per 6	4.2 ± 0.3	1.48 ± 0.18	0.29 ± 0.03	0.39 ± 0.07	13.0 ± 0.3	< 0.15	-	-
Barnard 1-B	18.3 ± 0.3	3.15 ± 0.17	0.54 ± 0.03	1.04 ± 0.07	12.0 ± 0.3	7.95 ± 0.05	5.19 ± 0.10	0.34 ± 0.05
L 1527	4.5 ± 0.3	0.81 ± 0.12	0.65 ± 0.03	0.27 ± 0.07	11.7 ± 0.3	< 0.15	-	-
L 483	18.3 ± 0.3	6.28 ± 0.03	0.57 ± 0.03	1.05 ± 0.07	11.8 ± 0.3	2.57 ± 0.05	5.15 ± 0.21	0.19 ± 0.05
SMM 5	13.2 ± 0.3	2.26 ± 0.15	0.49 ± 0.03	0.94 ± 0.07	12.1 ± 0.3	3.33 ± 0.05	2.04 ± 0.15	0.30 ± 0.05
L 723	3.50 ± 0.3	0.92 ± 0.15	0.23 ± 0.03	0.15 ± 0.07	13.4 ± 0.3	0.68 ± 0.05	< 0.1	-
L 673 A	11.7 ± 0.3	1.70 ± 0.15	0.71 ± 0.03	0.77 ± 0.07	13.0 ± 0.3	1.84 ± 0.05	1.96 ± 0.19	0.21 ± 0.05
B 335	7.0 ± 0.3	1.98 ± 0.16	0.47 ± 0.03	0.31 ± 0.07	11.6 ± 0.3	1.21 ± 0.05	1.50 ± 0.35	0.20 ± 0.05
L 1157	4.73 ± 0.3	1.83 ± 0.13	0.29 ± 0.03	0.37 ± 0.07	11.8 ± 0.3	1.57 ± 0.05	1.11 ± 0.26	0.28 ± 0.05

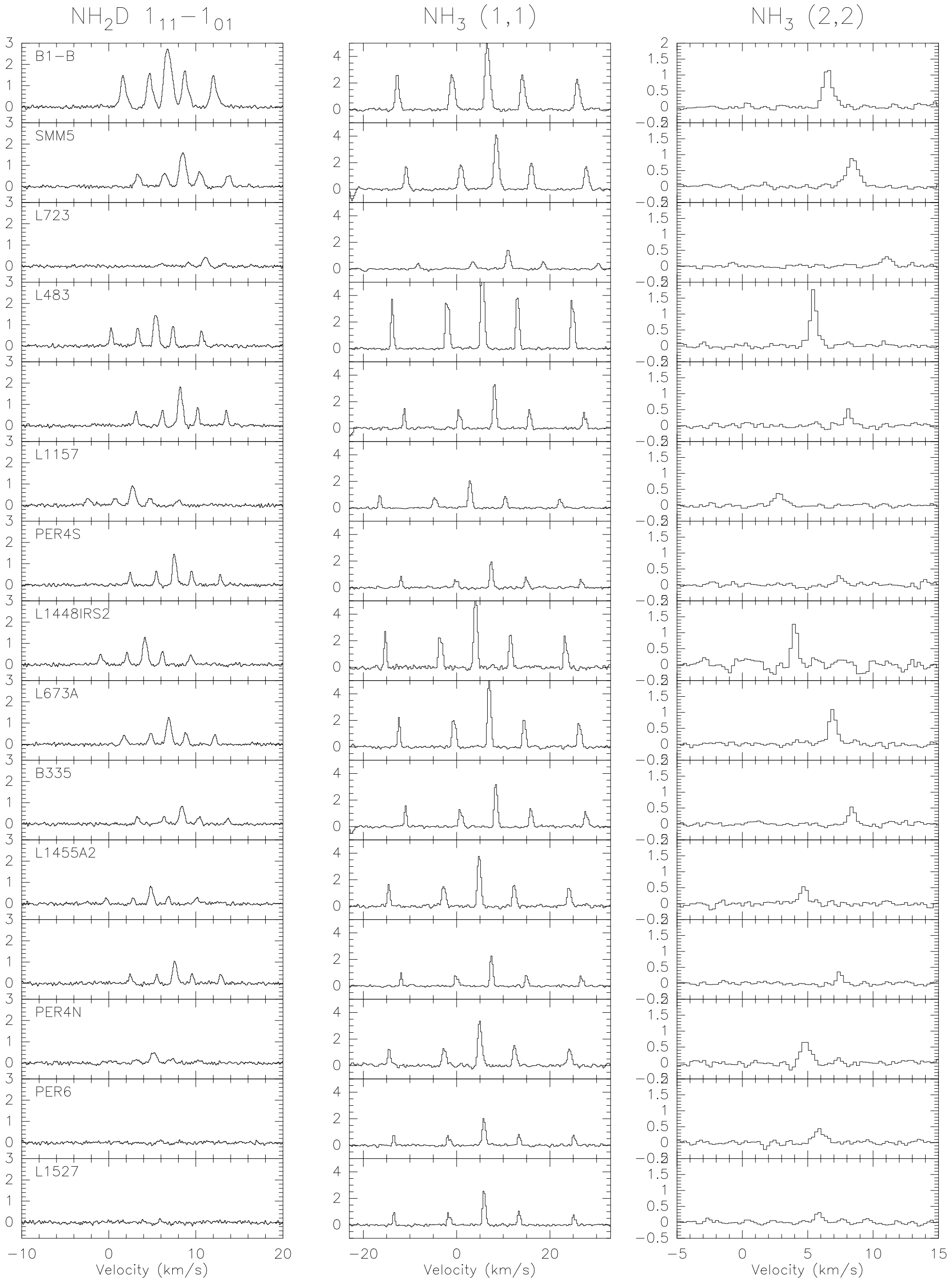

Fig. 6.14: *Spectra of NH_2D and NH_3 in 15 protostellar cores. The temperature scale is given in T_{MB}.*

The column densities were then determined using equation 6.59 and 6.60 for optically thick and optically thin lines, respectively, but multiplied with the filling factor to correct for the beam filling. The column densities are listed in Tab. 6.12.

Tab. 6.12: *Column densities of NH_3 and NH_2D*

Source	$N(NH_3)$ [cm^{-2}]	$N(NH_2D)$ [cm^{-2}]	$\frac{N(NH_2D)}{NH_3}$
L 1448 IRS 2	$5.72 \pm 0.39 \cdot 10^{14}$	$3.21 \pm 0.88 \cdot 10^{13}$	0.056 ± 0.015
L 1455 A1	$3.65 \pm 0.38 \cdot 10^{14}$	$1.17 \pm 0.20 \cdot 10^{13}$	0.032 ± 0.006
L 1455 A2	$4.26 \pm 0.35 \cdot 10^{14}$	$1.03 \pm 0.24 \cdot 10^{13}$	0.024 ± 0.006
Per 4 S	$1.49 \pm 0.27 \cdot 10^{14}$	$2.67 \pm 0.54 \cdot 10^{13}$	0.179 ± 0.049
Per 4 N	$1.60 \pm 0.17 \cdot 10^{14}$	$2.16 \pm 0.63 \cdot 10^{13}$	0.135 ± 0.041
Per 5	$2.75 \pm 0.33 \cdot 10^{14}$	$3.58 \pm 0.61 \cdot 10^{13}$	0.130 ± 0.027
Per 6	$1.49 \pm 0.24 \cdot 10^{14}$	$< 2.05 \cdot 10^{12}$	< 0.014
Barnard 1-B	$9.23 \pm 0.72 \cdot 10^{14}$	$1.56 \pm 0.23 \cdot 10^{14}$	0.169 ± 0.028
L 1527	$1.72 \pm 0.28 \cdot 10^{14}$	$< 1.79 \cdot 10^{12}$	< 0.010
L 483	$1.19 \pm 0.07 \cdot 10^{15}$	$4.82 \pm 1.28 \cdot 10^{13}$	0.041 ± 0.011
SMM 5	$5.83 \pm 0.53 \cdot 10^{14}$	$5.34 \pm 0.97 \cdot 10^{13}$	0.092 ± 0.019
L 723	$1.12 \pm 0.23 \cdot 10^{14}$	$9.67 \pm 0.20 \cdot 10^{12}$	0.086 ± 0.018
L 673 A	$4.50 \pm 0.43 \cdot 10^{14}$	$3.26 \pm 0.83 \cdot 10^{13}$	0.072 ± 0.020
B 335	$3.16 \pm 0.33 \cdot 10^{14}$	$1.77 \pm 0.60 \cdot 10^{13}$	0.056 ± 0.020
L 1157	$2.02 \pm 0.25 \cdot 10^{14}$	$2.25 \pm 0.66 \cdot 10^{13}$	0.111 ± 0.035

In Fig. 6.15 the NH_2D/NH_3 ratio as function of T_{Dust} is shown (blue circles). In addition we plotted also the N_2D^+/N_2H^+ ratio (red triangles) and the NH_2D/NH_3 determined by Hatchell (2003) (green diamonds). The deuterium fractionation of NH_3 from this work follows the N_2D^+/N_2H^+ ratio quite well, but the NH_2D/NH_3 ratio determined by Hatchell (2003) stays at much higher values. Both data sets have been observed with the same telescopes, and therefore different spatial resolutions cannot be the reason for these differences. The main difference in calculating the deuterium fractionation of NH_3 is that Hatchell (2003) assumed a filling factor of one. Therefore the column densities determined by her work are those towards column density peaks, which might be not the same position for NH_3 and NH_2D, whereas the column densities we derived are the beam averaged values. Because the N_2D^+/N_2H^+ ratios are beam averaged values as well, the NH_2D/NH_3 ratios determined in this work have to be used for comparison.

The fact, that the deuterium fractionation of N_2H^+ and NH_3 shows a similar trend can be explained by the similar gas phase chemistry of both species. NH_2D and N_2D+ are formed by reaction of a parent molecule (NH_3 and N_2, respectively) with deuterated H_3^+, and, in the case of NH_2D, by a dissociative recombination of NH_3D^+. Therefore the deuterium fractionation of these molecules reflects the abundance of H_2D^+ and higher deuterated isotopologues. However, NH_3, and thus NH_2D are formed on dust grains, too (Boogert et al. 2008), and thus one would expect, that the deuterium fractionation of NH_3 stays at a higher level than the deuterium fractionation of N_2H^+. But,

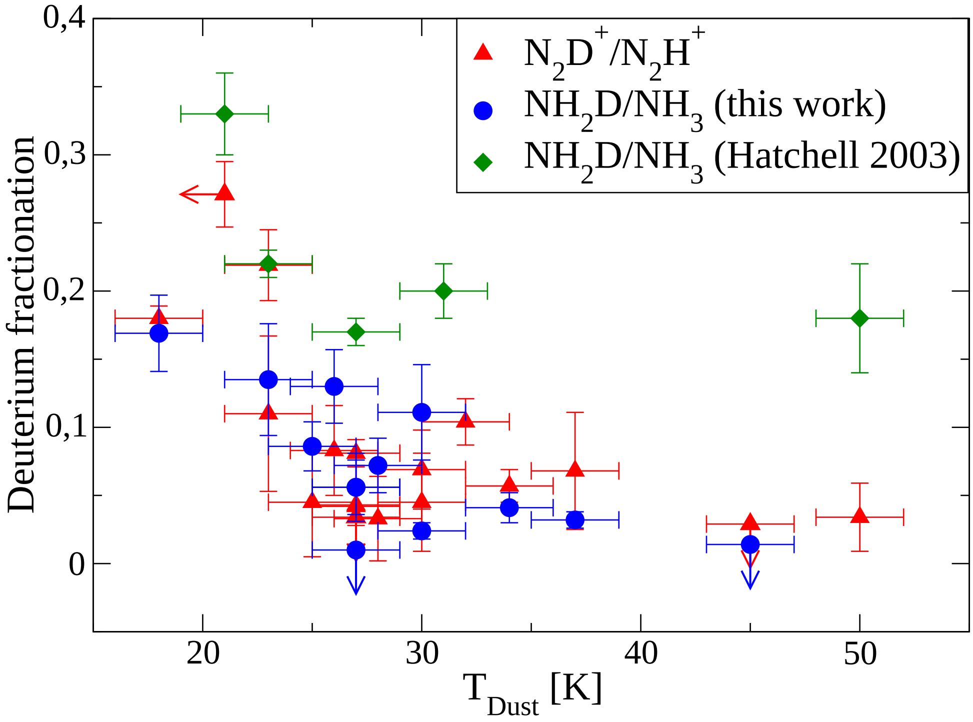

Fig. 6.15: *Correlation of the deuterium fractionation of NH_3 and N_2H^+ as function of the dust temperature. The NH_2D/NH_3 ratios are plotted as blue circles. For comparison we plotted also the N_2D^+/N_2H^+ ratios (red triangles) and the deuterium fractionation of NH_3 determined by Hatchell (2003) (green diamonds).*

the fact, that NH_3 is not destroyed by CO and thus abundant in the inner, warmer part of the protostellar core, where N_2H^+ is destroyed, lowers the deuterium fractionation of NH_3 again, and seems to balance the enhancement due to grain surface chemistry.

To evaluate the results of the NH_2D/NH_3 observations more carefully, a more sophisticated model than in this work has to be used. Such a model has to include a larger set of chemical reactions (NH_3 chemistry), as well as a time-dependent treatment of the gas phase reaction and grain surface chemistry. Further theoretical studies are needed to get a deeper insight into the deuteration processes of molecules involved in a more complex chemistry.

6.8 Chapter summary

We observed 20 Class 0 protostars in N_2H^+ 1-0, N_2D^+ 1-0, 2-1 and 3-2, $C^{18}O$ 1-0 and HCO^+ 3-2. The integrated intensities of the N_2H^+ 1-0 lines in our sample are comparable to those found in prestellar cores (Crapsi et al. 2005). The optical depths are typically 67% lower in the Class 0 sources, but because the excitation temperature is 2-3 K higher and the line width is about 2.5 time lager, the N_2H^+ column densities ($\sim 10^{13}$ cm^{-2}) are also comparable. The presence of a protostar also affects the kinematics of the cores. N_2H^+ lines are significantly wider in Class 0 sources than in prestellar cores (on average, 0.61 km/s and 0.26 km/s, respectively). A comparison of our HCO^+ observations with observations conducted with a ~three times larger beam (Gregersen et al. 2000) leads us to the conclusion that HCO^+ 3-2 stems mainly from a compact region of about 4000 AU in size.

The dependence of the N_2D^+/N_2H^+ ratio on dust temperature, CO depletion factor, and the $L_{BOL}/F_{1.3}^{220\ pc}$ ratio clearly indicates a close relation between deuterium fractionation and evolutionary stage of a Class 0 protostar. For the sub-sample of sources in the Perseus cloud, the correlation is striking. This might be an indication for the influence of the environment on the deuterium fractionation.

The correlation of the deuterium fractionation and the CO depletion factor looks qualitatively like the one found in prestellar cores (Crapsi et al. 2005). However, whereas in prestellar cores, the N_2D^+/N_2H^+ ratio stays low until $f_D(CO) \sim 10$, in protostars, the ratio starts to rise at $f_D(CO) \sim 3$. This difference occurs because CO is highly depleted at the center of prestellar cores, but not at the center of protostellar cores.

There is a weak correlation of N_2D^+ line width with N_2D^+/N_2H^+ ratio, but line broadening by multiple sources makes this conclusion suspect. A clear correlation with other kinematical tracers, especially with δv, is found. Sources with a high N_2D^+/N_2H^+ ratio clearly show infall motion ($\delta v \sim -0.4$). The lower the deuterium fractionation gets, the more δv increases. This might reflect the fact that outflow activity increases with evolutionary stage (Richer et al. 2000).

A model with a power law density and temperature profile reproduces the correlation between the N_2D^+/N_2H^+ ratio and both T_{Dust} and the CO depletion factor very well. In these models, the protostellar envelopes are chemically stratified. The inner part is too warm for CO to freeze out, so that the N_2H^+ abundance and the deuterium fractionation are low. At radii where the temperature drops below ~ 20 K, CO is mostly depleted and the N_2D^+/N_2H^+ ratio increases by several orders of magnitude. At even larger radii, the lower density decreases the degree of CO depletion, and thus the N_2D^+/N_2H^+ ratio also decreases.

The results of this work, in combination with the results of Crapsi et al. (2005) show that the deuterium fractionation is highest at the moment of collapse. The primary use of the deuterium fractionation of N_2H^+ is to identify very young protostellar objects, because the decline of the N_2D^+/N_2H^+ ratio is rather steep.

Comparisons of N_2H^+ fractionation with the deuterium fractionation of HCO^+ show clear differences, which are either due to the influence of freeze-out on dust grains or due to different destruction mechanisms. HCO^+ is, unlike N_2H^+, not destroyed in the inner, already warmed up part of the protostellar core where the deuterium fractionation is quite low. Therefore the DCO^+/HCO^+ ratio is expected to be lower than the N_2D^+/N_2H^+ ratio. The DCO^+/HCO^+ ratios were observed by Jørgensen et al. (2004). These ratios agree within a few percent to the ones predicted by our model. The NH_2D/NH_3 ratio is very similar to the deuterium fractionation of N_2H^+, which is somehow expected, because both species are formed by N_2 and H_3^+ and its deuterated forms. However, ammonia chemistry includes also grain surface reactions and gas-phase reactions, which require a time dependent treatment. Therefore, more sophisticated model has to be used to interpret these observations.

7 Summary and Outlook

Molecular gas, which is located in the environment of protostars and/or newly formed stars, exists under various physical conditions. Whereas cold and dense gas can be found in prestellar cores and early protostellar environments, it can be as warm as several hundred Kelvin next to OB stars. For each environment different tracers have to be found to determine the exact parameters.

As I pointed out in chapter 3 and showed by the investigation of the high mass star forming region NGC 2024 (chapter 4), high-J ^{12}CO lines only trace hot (several hundred K) and dense ($> 5 \cdot 10^5$ cm^{-3}) gas. Furthermore, the narrow line profiles found in NGC 2024 and ORION-S FIR 4 indicates that the gas is heated by radiation rather than by shocks. Based on the physical scenarios of the ”Blister model” and PDR models, I developed a model of NGC 2024, which explains the emission of twelve ^{12}CO and ^{13}CO lines consistently. This model, which I computed by using the radiation transfer code SimLine, describe the temperature, density and velocity structure along the line-of sight. However, so far such an investigation has been conducted only in NGC 2024. Similar studies in sample of several massive star forming regions would be required to ascertain, whether the results found in NGC 2024, can be applied to such objects in general. Furthermore, a higher spatial resolution and at least small scale mapping of one high-J CO line is absolutely necessary to get an idea of the 3 dimensional structure of the hot gas. In addition to using the high-J CO lines as tracers for the hottest parts of the molecular material, they are also the strongest lines (in energy units) in massive star forming regions (see for example Fig. 4.5). Hence those lines are very crucial for the cooling of photo dominated regions, and thus a comparison of the high-J CO lines with other important coolants, such as the [CII] fine structure transition ($\lambda = 157.7\,\mu$m) and several H_2O lines would provide detailed insights into the cooling balance of PDRs.

Deuterated molecules trace a completely different physical regime. Because these species are destroyed at temperatures above ~ 20 K, deuterated molecules are abundant predominately in cold and dense regions. Their volatileness at higher temperatures makes the abundance of some of these molecules, as shown in chapter 6 to a very accurate indicator of the evolutionary stage of very young pre- and protostellar cores. Especially the nitrogen bearing molecules N_2H^+ and NH_3 show a clear correlation between their deuterium fractionation and the dust temperature, whereas the DCO^+/HCO^+ ratio seems to stay low at all times. However, the deuterium fractionation of other molecules has to be studied in more detail in a sample of pre- and protostellar cores. Such an investigation would provide a deeper understanding of the deuterium chemistry. Furthermore, regions at which most other tracers are frozen out onto dust grains can be studied with the help of deuterated ions, especially H_2D^+ and D_2H^+, as well. The deuterium fractionation of molecules, which are assumed to be mainly formed on grains, such as H_2CO and CH_3OH, and its trend with the evolutionary stage, would be interesting to study, too. The differences between the deuterium fractionation of gas phase produced molecules and molecules formed on dust grains would give a better insight into the importance of the different chemical mechanisms in cold environments. Observations of H_2D^+ and D_2H^+ in both, their ortho and para forms, are also still missing. Due to the uncertainty of the o/p ratio, especially in the case of H_2D^+, such measurements would provide the first determination of the total H_2D^+ and D_2H^+ column densities. Since these two species are the key to the understanding of deuterium chemistry in these cold regions, such observations are thought after. In addition the o/p ratio of H_2D^+ allows also conclusions on the o/p ratio, and thus to the formation rate, of H_2, which implies that these observations give deeper insights into the overall molecule formation at low temperatures.

All these observations, the one of [CII], H_2O, high-J CO (with higher spatial resolution) and para-H_2D^+, are not/or just with great difficulties possible with present day telescopes. However, within the next few years, several new ground-base, airborne and satellite borne telescopes for radiation at submillimeter wavelengths will start operation.

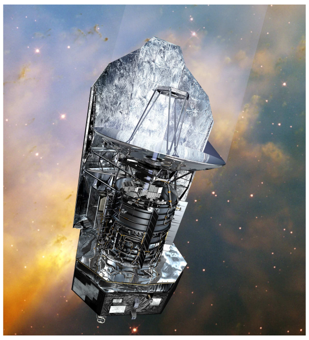

Fig. 7.1: *The Herschel Space Telescope*

One of these new telescopes is the *Herschel Space Observatory (HSO)*, which is a satellite borne telescope with a diameter of the primary mirror of 3.5 meter (i.e., a spatial resolution of $15''$ at 1.5 THz). The HSO is designed for imaging photometry and spectroscopy from 670-60 μm. One of the on-board instruments, the Heterodyne Instrument for the Far-Infrared (HIFI), is designed to conduct spectrally highly resolved observations of submillimeter lines, such as emission lines of H_2O, $H_2^{18}O$, CO, and [CII]. Therefore this telescope will be perfectly suited for observation of massive star forming regions and PDRs. Unfortunately only the o-D_2H^+ and not the p-H_2D^+ ground state transition are observable with the HSO.

Fig. 7.2: *SOFIA*

Another possibility to overcome the earth atmosphere, which causes sever absorption (see chapter 3), is to use airborne observatories. In 2009, the Stratospheric Observatory For Infrared Astronomy (SOFIA), will conduct its first light observations. SOFIA is a modified Boeing 747SP, which carries a 2.5m reflecting telescope. At an operating altitude of ~14 km, most of the atmosphere is below SOFIA, but molecules, which are very abundant in the earth atmosphere, such as O_2 and $H_2^{16}O$, are not observable even from SOFIA. However, heterodyne spectroscopy of high-J CO lines, [CII] and $H_2^{18}O$, but also the p-H_2D^+ and o-D_2H^+ ground state transition will be feasible with SOFIA, and thus our understanding of molecular gas, especially in star forming regions, will greatly benefit form this new observatory. The advantage of SOFIA over satellite borne observatories is, that it allows to us upgraded and in the future developed instruments. Thus, yet unexplored FIR regions might be observed at high resolution with SOFIA with in planned operating time (20 years).

But not only satellite- and airborne observatories will be available in the near future, also new ground based observatories will be provided. A very ambitious project is the Atacama Large Millimetre Array (ALMA). ALMA will consist of 64 antennas with 12 and 7 meter diameter, and will operate at wavelengths between 9.6 and 0.3 mm. At its highest frequencies it is expected to reach a spatial resolution of $0.005''$, which is about ten times better than the resolution of the Hubble space telescope. Although ALMA will not be able to observe at THz frequencies, it provides the possibility to study the chemistry in star forming regions with a tremendously high resolution.

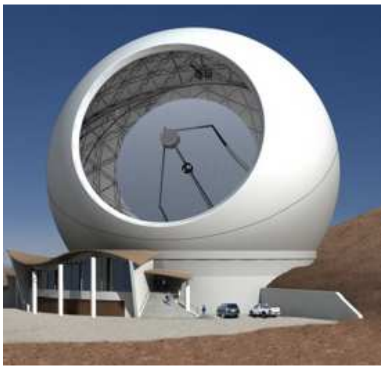

Fig. 7.3: *Artistic picture of CCAT*

Another ground based telescope for submillimeter observations, which is in its planning stage, is the Cornell Caltech Atacama Telescope (CCAT). CCAT will be located on Cerro Chajnantor, Chile, at an altitude of 5612 meter above sea level, which will allow observations of frequencies up to 1.5 THz. CCAT is planned to be a 25m telescope with a surface accuracy of $\sim 10\,\mu$m rms. Thus CCAT will be the ideal telescope for spectroscopic observations of the lines in the 1.3-1.6 THz window.

In general the upcoming times will be very exciting for submillimeter astronomy. New telescopes, but also newly developed receiver technology will provide a completely new view of the interstellar material. Thus data in a hitherto not reached quality and quantity will be available soon, which will increase our knowledge of the processes of star formation tremendously.

References

Adams, F. C. 1990, ApJ, 363, 578

Aikawa, Y., Wakelam, V., Garrod, R. T., & Herbst, E. 2008, ApJ, 674, 984

Alves, J. F., Lada, C. J., & Lada, E. A. 2001, Nature, 409, 159

André, P., Ward-Thompson, D., & Barsony, M. 1993, ApJ, 406, 122

André, P., Ward-Thompson, D., & Barsony, M. 2000, Protostars and Planets IV, 59

André, P., Ward-Thompson, D., & Motte, F. 1996, A&A, 314, 625

Anthony-Twarog, B. J. 1982, AJ, 87, 1213

Asensio Ramos, A., Ceccarelli, C., & Elitzur, M. 2007, A&A, 471, 187

Balbus, S. A. & Hawley, J. F. 1998, Reviews of Modern Physics, 70, 1

Banerjee, R. & Pudritz, R. E. 2007, ApJ, 660, 479

Bardsley, J. N. 1968a, J. Phys. B (*Proc. Phys. Soc.*), [II], 1, 349

Bardsley, J. N. 1968b, J. Phys. B (*Proc. Phys. Soc.*), [II], 1, 365

Barnes, P. J., Crutcher, R. M., Bieging, J. H., Storey, J. W. V., & Willner, S. P. 1989, ApJ, 342, 883

Bergin, E. A., Alves, J., Huard, T., & Lada, C. J. 2002, ApJ, 570, L101

Bergin, E. A., Ciardi, D. R., Lada, C. J., Alves, J., & Lada, E. A. 2001, ApJ, 557, 209

Bergin, E. A. & Langer, W. D. 1997, ApJ, 486, 316

Bergin, E. A., Maret, S., van der Tak, F. F. S., et al. 2006, ApJ, 645, 369

Bergin, E. A. & Snell, R. L. 2002, ApJ, 581, L105

Bernes, C. 1979, A&A, 73, 67

Bik, A., Lenorzer, A., Kaper, L., et al. 2003, A&A, 404, 249

Bisschop, S. E., Fraser, H. J., Öberg, K. I., van Dishoeck, E. F., & Schlemmer, S. 2006, A&A, 449, 1297

Bodenheimer, P. & Sweigart, A. 1968, ApJ, 152, 515

Bonnell, I. A., Bate, M. R., & Zinnecker, H. 1998, MNRAS, 298, 93

Bonnor, W. B. 1956, MNRAS, 116, 351

Boogert, A. C. A., Pontoppidan, K. M., Knez, C., et al. 2008, ApJ, 678, 985

Boreiko, R. T. & Betz, A. L. 1993, ApJ, 405, L39

Burton, M. G., Hollenbach, D. J., & Tielens, A. G. G. M. 1990, ApJ, 365, 620

Butner, H. M., Lada, E. A., & Loren, R. B. 1995, ApJ, 448, 207

Caselli, P. 2005, in Cores to Clusters: Star Formation with Next Generation Telescopes, ed. M. S. N. Kumar, M. Tafalla, & P. Caselli, 47

Caselli, P., Benson, P. J., Myers, P. C., & Tafalla, M. 2002a, ApJ, 572, 238

Caselli, P., van der Tak, F. F. S., Ceccarelli, C., & Bacmann, A. 2003, A&A, 403, L37

Caselli, P., Vastel, V., van der Tak, F. F. S., Ceccarelli, C., & Bacmann, A. 2008, A&A, subm.

Caselli, P., Walmsley, C. M., Tafalla, M., Dore, L., & Myers, P. C. 1999, ApJ, 523, L165

Caselli, P., Walmsley, C. M., Terzieva, R., & Herbst, E. 1998, ApJ, 499, 234

Caselli, P., Walmsley, C. M., Zucconi, A., et al. 2002b, ApJ, 565, 344

Ceccarelli, C. & Dominik, C. 2005, A&A, 440, 583

Ceccarelli, C., Loinard, L., Castets, A., et al. 2001, A&A, 372, 998

Cernicharo, J., Polehampton, E., & Goicoechea, J. R. 2007, ApJ, 657, L21

Černis, K. 1990, Ap&SS, 166, 315

Churchwell, E., Smith, L. F., Mathis, J., Mezger, P. G., & Huchtmeier, W. 1978, A&A, 70, 719

Crapsi, A., Caselli, P., Walmsley, C. M., et al. 2005, ApJ, 619, 379

Crapsi, A., Caselli, P., Walmsley, M. C., & Tafalla, M. 2007, A&A, 470, 221

Crutcher, R. M., Henkel, C., Wilson, T. L., Johnston, K. J., & Bieging, J. H. 1986, ApJ, 307, 302

Daniel, F., Dubernet, M.-L., Meuwly, M., Cernicharo, J., & Pagani, L. 2005, MNRAS, 363, 1083

Dobashi, K., Onishi, T., Iwata, T., et al. 1993, AJ, 105, 1487

Draine, B. T. & Lee, H. M. 1984, ApJ, 285, 89

Ebert, R. 1955, Z. Astrophys., 37, 217

Eddington, A. S. 1926, The Internal Constitution of Stars, Cambridge University Press

Elias, J. H. 1978, ApJ, 223, 859

Evans, II, N. J. 1999, ARA&A, 37, 311

Evans, II, N. J., Rawlings, J. M. C., Shirley, Y. L., & Mundy, L. G. 2001, ApJ, 557, 193

Fixsen, D. J., Bennett, C. L., & Mather, J. C. 1999, ApJ, 526, 207

Flower, D. R., Pineau des Forêts, G., & Walmsley, C. M. 2004, A&A, 427, 887

Flower, D. R., Pineau Des Forêts, G., & Walmsley, C. M. 2006a, A&A, 456, 215

Flower, D. R., Pineau Des Forêts, G., & Walmsley, C. M. 2006b, A&A, 449, 621

Fontani, F., Caselli, P., Bourke, T. L., Cesaroni, R., & Brand, J. 2008, A&A, 477, L45

Fontani, F., Caselli, P., Crapsi, A., et al. 2006, A&A, 460, 709

Fraser, H. J., Collings, M. P., McCoustra, M. R. S., & Williams, D. A. 2001, MNRAS, 327, 1165

Frerking, M. A., Langer, W. D., & Wilson, R. W. 1982, ApJ, 262, 590

Froebrich, D. 2005, ApJS, 156, 169

Gammie, C. F. 2001, ApJ, 553, 174

Gerlich, D., Herbst, E., & Roueff, E. 2002, Planet. Space Sci., 50, 1275

Giannakopoulou, J., Mitchell, G. F., Hasegawa, T. I., Matthews, H. E., & Maillard, J.-P. 1997, ApJ, 487, 346

Giannini, T., Nisini, B., & Lorenzetti, D. 2001, ApJ, 555, 40

Giannini, T., Nisini, B., Lorenzetti, D., et al. 2000, A&A, 358, 310

Graf, U. U., Eckart, A., Genzel, R., et al. 1993, ApJ, 405, 249

Graf, U. U., Genzel, R., Harris, A. I., et al. 1990, ApJ, 358, L49

Graf, U. U., Haas, S., Honingh, C. E., et al. 1998, in Presented at the Society of Photo-Optical Instrumentation Engineers (SPIE) Conference, Vol. 3357, Proc. SPIE Vol. 3357, p. 159-166, Advanced Technology MMW, Radio, and Terahertz Telescopes, Thomas G. Phillips; Ed., ed. T. G. Phillips, 159–166

Gregersen, E. M., Evans, II, N. J., Mardones, D., & Myers, P. C. 2000, ApJ, 533, 440

Gueth, F., Bachiller, R., & Tafalla, M. 2003, A&A, 401, L5

Güsten, R., Nyman, L. Å., Schilke, P., et al. 2006, A&A, 454, L13

Hasegawa, T. I. & Herbst, E. 1993, MNRAS, 261, 83

Hassel, G. E., Herbst, E., & Garrod, R. T. 2008, ApJ, 681, 1385

Hatchell, J. 2003, A&A, 403, L25

Hayashi, C., Hōshi, R., & Sugimoto, D. 1962, Progress of Theoretical Physics Supplement, 22, 1

Herbig, G. H. & Jones, B. F. 1983, AJ, 88, 1040

Herbst, E. & Klemperer, W. 1973, ApJ, 185, 505

Herrmann, F., Madden, S. C., Nikola, T., et al. 1997, ApJ, 481, 343

Hertzsprung, E. 1905, Zur Strahlung der Sterne (Z. Wiss. Photog. 3)

Ho, P. T. P. & Townes, C. H. 1983, ARA&A, 21, 239

Hogerheijde, M. R., Caselli, P., Emprechtinger, M., et al. 2006, A&A, 454, L59

Hollenbach, D. J. & Tielens, A. G. G. M. 1997, ARA&A, 35, 179

Hunter, C. 1977, ApJ, 218, 834

Israel, F. P. 1978, A&A, 70, 769

Jeans, J. H. 1902, Philosophical Transactions of the Royal Society of London. Series A, Containing Papers of a Mathematical or Physical Character, 199, 1

Jijina, J., Myers, P. C., & Adams, F. C. 1999, ApJS, 125, 161

Jørgensen, J. K., Schöier, F. L., & van Dishoeck, E. F. 2004, A&A, 416, 603

Jørgensen, J. K., Schöier, F. L., & van Dishoeck, E. F. 2005, A&A, 435, 177

Kahn, F. D. 1974, A&A, 37, 149

Kawamura, J., Hunter, T. R., Tong, C.-Y. E., et al. 2002, A&A, 394, 271

Kepler, F. J. 1618, Harmonices Mundi libri V

Kirk, H., Johnstone, D., & Di Francesco, J. 2006, ApJ, 646, 1009

Kramer, C., Alves, J., Lada, C., et al. 1998, A&A, 329, L33

Kramer, C., Alves, J., Lada, C. J., et al. 1999, A&A, 342, 257

Kramer, C., Jakob, H., Mookerjea, B., et al. 2004, A&A, 424, 887

Kramer, C., Richer, J., Mookerjea, B., Alves, J., & Lada, C. 2003, A&A, 399, 1073

Kramer, C., Stutzki, J., & Winnewisser, G. 1996, A&A, 307, 915

Kroupa, P. 2002, Science, 295, 82

Kwon, W., Looney, L. W., Crutcher, R. M., & Kirk, J. M. 2006, ApJ, 653, 1358

Lada, C. J. 1987, in IAU Symposium, Vol. 115, Star Forming Regions, ed. M. Peimbert & J. Jugaku, 1–17

Lada, C. J., Alves, J., & Lada, E. A. 1999, ApJ, 512, 250

Lada, C. J. & Wilking, B. A. 1984, ApJ, 287, 610

Lada, E. A., Bally, J., & Stark, A. A. 1991, ApJ, 368, 432

Larson, R. B. 1969, MNRAS, 145, 271

Larson, R. B. 2003, Reports of Progress in Physics, 66, 1651

Le Bourlot, J. 1991, A&A, 242, 235

Lee, J.-E., Bergin, E. A., & Evans, II, N. J. 2004, ApJ, 617, 360

Loinard, L., Castets, A., Ceccarelli, C., et al. 2000, A&A, 359, 1169

Looney, L. W., Mundy, L. G., & Welch, W. J. 2000, ApJ, 529, 477

Looney, L. W., Mundy, L. G., & Welch, W. J. 2003, ApJ, 592, 255

Lorenzetti, D., Giannini, T., Nisini, B., et al. 2000, A&A, 357, 1035

Mac Low, M.-M. & Klessen, R. S. 2004, Reviews of Modern Physics, 76, 125

Maddalena, R. J., Morris, M., Moscowitz, J., & Thaddeus, P. 1986, ApJ, 303, 375

Mardones, D., Myers, P. C., Tafalla, M., et al. 1997, ApJ, 489, 719

Maret, S., Bergin, E. A., & Lada, C. J. 2006, Nature, 442, 425

Maret, S., Bergin, E. A., & Lada, C. J. 2007, ApJ, 670, L25

Marrone, D. P., Battat, J., Bensch, F., et al. 2004, ApJ, 612, 940

Matthews, B. C. & Wilson, C. D. 2002, ApJ, 574, 822

Mezger, P. G., Chini, R., Kreysa, E., Wink, J. E., & Salter, C. J. 1988, A&A, 191, 44

Mezger, P. G., Sievers, A. W., Haslam, C. G. T., et al. 1992, A&A, 256, 631

Millar, T. J., Roberts, H., Markwick, A. J., & Charnley, S. B. 2000, in Royal Society of London Philosophical Transactions Series A, Vol. 358, Astronomy, physics and chemistry of H_3^+, 2535–+

Mitchell, G. F., Johnstone, D., Moriarty-Schieven, G., Fich, M., & Tothill, N. F. H. 2001, ApJ, 556, 215

Müller, H. S. P., Thorwirth, S., Roth, D. A., & Winnewisser, G. 2001, A&A, 370, L49

Mundy, L. G., Scoville, N. Z., Baath, L. B., Masson, C. R., & Woody, D. P. 1986, ApJ, 304, L51

Myers, P. C., Adams, F. C., Chen, H., & Schaff, E. 1998, ApJ, 492, 703

Myers, P. C., Fuller, G. A., Goodman, A. A., & Benson, P. J. 1991, ApJ, 376, 561

Myers, P. C. & Ladd, E. F. 1993, ApJ, 413, L47

Öberg, K. I., van Broekhuizen, F., Fraser, H. J., et al. 2005, ApJ, 621, L33

Oberst, T. E., Parshley, S. C., Stacey, G. J., et al. 2006, ApJ, 652, L125

Odegard, N. 1985, ApJS, 57, 571

Oliveira, C. M., Hébrard, G., Howk, J. C., et al. 2003, ApJ, 587, 235

Ossenkopf, V., Trojan, C., & Stutzki, J. 2001, A&A, 378, 608

Osterbrock, D. E. & Ferland, G. J. 2006, Astrophysics of Gaseous Nebulae and Active Galactic Nuclei, Univ. Sci. Books

Ott, M., Witzel, A., Quirrenbach, A., et al. 1994, A&A, 284, 331

Pagani, L., Bacmann, A., Cabrit, S., & Vastel, C. 2007, A&A, 467, 179

Pagani, L., Salez, M., & Wannier, P. G. 1992, A&A, 258, 479

Pardo, J. R., Cernicharo, J., & Serabyn, E. 2001, IEEE Trans. on Antennas and Propagation

Pardo, J. R., Wiedner, M. C., Serabyn, E., et al. 2004, ApJS, 153, 363

Parise, B., Ceccarelli, C., Tielens, A. G. G. M., et al. 2006, A&A, 453, 949

Penston, M. V. 1969, MNRAS, 145, 457

Richer, J. S. 1990, MNRAS, 245, 24P

Richer, J. S., Hills, R. E., & Padman, R. 1992, MNRAS, 254, 525

Richer, J. S., Hills, R. E., Padman, R., & Russell, A. P. G. 1989, MNRAS, 241, 231

Richer, J. S., Shepherd, D. S., Cabrit, S., Bachiller, R., & Churchwell, E. 2000, Protostars and Planets IV, 867

Roberts, H., Herbst, E., & Millar, T. J. 2004, A&A, 424, 905

Roberts, H. & Millar, T. J. 2000, A&A, 364, 780

Roberts, H. & Millar, T. J. 2007, A&A, 471, 849

Röllig, M., Abel, N. P., Bell, T., et al. 2007, A&A, 467, 187

Roueff, E., Lis, D. C., van der Tak, F. F. S., Gerin, M., & Goldsmith, P. F. 2005, A&A, 438, 585

Rubin, R. H., Simpson, J. P., Lord, S. D., et al. 1994, ApJ, 420, 772

Russell, H. N. 1914, Pop. Astron.

Ruze, R. 1966, Proc. IEEE, 54, 4, 633

Salpeter, E. E. 1955, ApJ, 121, 161

Sanders, D. B. & Willner, S. P. 1985, ApJ, 293, L39

Saraceno, P., André, P., Ceccarelli, C., Griffin, M., & Molinari, S. 1996, A&A, 309, 827

Schmid-Burgk, J., Guesten, R., Mauersberger, R., Schulz, A., & Wilson, T. L. 1990, ApJ, 362, L25

Schnee, S., Caselli, P., Goodman, A., et al. 2007, ApJ, 671, 1839

Sempere, M. J., Cernicharo, J., Lefloch, B., González-Alfonso, E., & Leeks, S. 2000, ApJ, 530, L123

Shaver, P. A., McGee, R. X., Newton, L. M., Danks, A. C., & Pottasch, S. R. 1983, MNRAS, 204, 53

Shen, C. J., Greenberg, J. M., Schutte, W. A., & van Dishoeck, E. F. 2004, A&A, 415, 203

Shirley, Y. L., Evans, II, N. J., Rawlings, J. M. C., & Gregersen, E. M. 2000, ApJS, 131, 249

Shu, F. H. 1977, ApJ, 214, 488

Shu, F. H., Adams, F. C., & Lizano, S. 1987, ARA&A, 25, 23

Smith, M. D. 1998, Ap&SS, 261, 169

Stark, R., van der Tak, F. F. S., & van Dishoeck, E. F. 1999, ApJ, 521, L67

Strömgren, B. 1939, ApJ, 89, 526

Stutzki, J., Genzel, R., Graf, U. U., et al. 1991, IAUS, 147, 235

Stutzki, J. & Guesten, R. 1990, ApJ, 356, 513

Stutzki, J. & Winnewisser, G. 1985, A&A, 144, 13

Sun, K., Ossenkopf, V., Kramer, C., et al. 2008, ArXiv e-prints, 807

Tafalla, M., Myers, P. C., Caselli, P., Walmsley, C. M., & Comito, C. 2002, ApJ, 569, 815

Terebey, S., Chandler, C. J., & André, P. 1993, ApJ, 414, 759

Tielens, A. G. G. M. & Hollenbach, D. 1985, ApJ, 291, 747

Tobin, J. J., Hartmann, L., Calvet, N., & D'Alessio, P. 2008, ApJ, 679, 1364

van der Tak, F. F. S. & van Dishoeck, E. F. 2000, A&A, 358, L79

van Dishoeck, E. F. 2004, ARA&A, 42, 119

Vastel, C., Caselli, P., Ceccarelli, C., et al. 2006, ApJ, 645, 1198

Vastel, C., Phillips, T. G., & Yoshida, H. 2004, ApJ, 606, L127

Velusamy, T. & Langer, W. D. 1998, Nature, 392, 685

Visser, A. E., Richer, J. S., Chandler, C. J., & Padman, R. 1998, MNRAS, 301, 585

Volgenau, N. H. 2004, Ph.D. Thesis, University of Maryland

Volgenau, N. H., Mundy, L. G., Looney, L. W., & Welch, W. J. 2006, ApJ, 651, 301

Walmsley, C. M., Flower, D. R., & Pineau des Forêts, G. 2004, A&A, 418, 1035

Ward-Thompson, D., André, P., & Kirk, J. M. 2002, MNRAS, 329, 257

White, G. J. & Sandell, G. 1995, A&A, 299, 179

Wieching, G. 2006, Ph.D. Thesis, Universität zu Köln

Wiedner, M. C., Wieching, G., Bielau, F., et al. 2006, A&A, 454, L33

Wilson, R. W., Jefferts, K. B., & Penzias, A. A. 1970, ApJ, 161, L43+

Wilson, T. L., Muders, D., Kramer, C., & Henkel, C. 2001, ApJ, 557, 240

Wilson, T. L. & Rood, R. 1994, ARA&A, 32, 191

Wolfire, M. G. & Cassinelli, J. P. 1987, ApJ, 319, 850

Womack, M., Ziurys, L. M., & Wyckoff, S. 1992, ApJ, 387, 417

Woodall, J., Agúndez, M., Markwick-Kemper, A. J., & Millar, T. J. 2007, A&A, 466, 1197

Yorke, H. W. & Sonnhalter, C. 2002, ApJ, 569, 846

Zinnecker, H., McCaughrean, M. J., & Wilking, B. A. 1993, in Protostars and Planets III, ed. E. H. Levy & J. I. Lunine, 429–495

Zuckerman, B. 1973, ApJ, 183, 863

List of Figures

2.1 Relative gas-phase abundance as function of T_{Dust} 14

2.2 Abundance of H_2D^+ 16

2.3 Abundance profile in a Class 0 protostar 19

2.4 Abundances and Temperatures in a PDR 22

3.1 Atmospheric transmission around 1.4 THz 24

3.2 CO J=13-12 emissivity 25

3.3 Orion FIR 4 results 27

3.4 Level diagram of the ground state transition of deuterated H_3^+ 28

3.5 Spectrum of IRc2 at 372 GHz 29

3.6 Upper limits of the o/p ratio of H_2D^+. 30

3.7 NII intensity ratios as function of n_e 31

4.1 Structure of NGC 2024 34

4.2 Beam shape of CONDOR on APEX 37

4.3 Spectra of CO emission from pointed observations in NGC 2024. . . . 40

4.4 Escape probability solutions of NGC 2024 48

4.5 Integrated line intensity of ^{12}CO versus J_{up} 51

4.6 Observed and model spectra of CO 53

4.7 Temperature and density structure of NGC 2024 54

5.1 A_v map of the Northern Streamer of IC 5146. 59

5.2 A_v map of the eastern cores of IC 5146 (colors). 62

5.3 Maps of the eastern part of IC 5146. 64

5.4 Integrated line intensity versus the optical extinction A_v 65

5.5 Line width of the N_2H^+ 1-0 line 66

5.6 Spectra towards position 1 ($\Delta\alpha = 500''$, $\Delta\delta = -110''$). 67

5.7 Spectra towards position 2 ($\Delta\alpha = 335''$, $\Delta\delta = -50''$). 68

5.8 Map of the gas temperature determined from the NH_3 70

5.9 Scatter plot of the integrated intensities versus A_v 70

5.10 Map and abundance profiles at Position 2 71

5.11 Model results of core #2 74

5.12 Observed and modeled spectra of core #2 75

5.13 Modeled abundance profiles of core #2 76

5.14 Scatter plots of integrated intensities versus optical extinction 78

5.15 A_v versus A 79

5.16 Observed and modeled spectra of Position 1 80

5.17 Normalized abundance profiles of $C^{18}O$, NH_3 and N_2H^+ at Position 2 81

6.1 L_{Bol} vs. $F^{D_0}_{1.3\ mm}$ diagram 85

6.2 Scratch of a prestellar and a protostellar envelope 86

6.3 N_2D^+/N_2H^+ ratio as function of the CO depletion factor. 88

6.4 Spectra of N_2H^+ 1-0, N_2D^+ 2-1, $C^{18}O$ 1-0 and HCO^+ 3-2 93

6.5 Two examples for the fitting results T_{Dust}. The enhanced flux at λ = 850 μm in L 1157 might be explained be the presence of cold dust. . . 100

6.6 Dust temperature versus deuterium fractionation. 102

6.7 CO depletion factor versus N_2D^+/N_2H^+ ratio 104

6.8 N_2D^+/N_2H^+ versus $L_{BOL}/F^{D_0}_{1.3}$. 107

6.9 N_2D^+/N_2H^+ versus kinematical parameter. 109

6.10 Density and temperature profiles of protostellar cores 113

6.11 Comparison between observations and the model 116

6.12 Chemical stratification in protostellar cores 118

6.13 Abundance profiles in protostellar cores 119

6.14 Spectra of NH_2D and NH_3 in 15 protostellar cores. 124

6.15 NH_2D/NH_3 vs. T_{Dust} 126

7.1 The Herschel Space Telescope 130

7.2 SOFIA 130

7.3 Artistic picture of CCAT 131

List of Tables

3.1 High-J CO lines 25

4.1 List of the observed CO transitions 36

4.2 Positions of the ^{12}CO J=13-12 observations. 38

4.3 Integrated intensities, v_{LSR} and Δv of the observed lines 41

4.4 Physical properties of the radiative transfer model of NGC 2024. . . . 50

5.1 Observational data of the observed tracers. 60

5.2 Observational data of the observed transitions. 67

5.3 Column densities at Position 2 and the relative abundances of the molecules investigated 72

6.1 Source Sample 89

6.2 Observed emission lines 90

6.3 Observational parameters of the C^{18}O and HCO^{+} lines. 91

6.4 Line parameters of the N$_2$H$^+$ and N$_2$D$^+$ lines. 92

6.5 N$_2$H$^+$ and N$_2$D$^+$ column densities. 96

6.6 Dust temperature, C^{18}O column density and f_D(CO) 101

6.7 Bolometric luminosity and distance normalized flux of some protostars. 106

6.8 Velocities of C^{18}O and HCO$^+$ lines and asymmetry parameter. 110

6.9 Model results 115

6.10 Deuterium fractionation of several molecular species. 121

6.11 NH$_3$ and NH$_2$D line data 123

6.12 Column densities of NH$_3$ and NH$_2$D 125

Publikationen

1. Emprechtinger M., Wiedner, M. C., Simon, R., Wieching, G., et al.
   Warm molecular Gas in NGC 2024
   2008, A&A, submitted

2. Emprechtinger, M., Caselli, P., Volgenau, N. H., Stutzki, J. & Wiedner, M. C.
   The N_2D^+/N_2H^+ ratio as an evolutionary tracer of Class 0 protostars
   2008, A&A, accepted

3. Hogerheijde, M. R., Caselli, P., Emprechtinger, M., van der Tak, F. F. S., et al.
   Probable detection of H_2D^+ in the starless core Barnard 68
   2006, A&A, 454, 59

4. Wiedner, M. C., Wieching, G., Bielau, F., Rettenbacher, K., Volgenau, N. H., Emprechtinger, M., et al.
   First observations with CONDOR, a 1.5 THz heterodyne receiver
   2006, A&A, 454, 33

5. Emprechtinger, M., Wiedner, M. C., Simon, R., Wieching, G., et al.
   Hot Molecular Gas in NGC2024
   2008, EAS Publications Series, 31, 173

6. Wiedner, M. C., Bielau, F., Emprechtinger, M., Ricken, O., Volgenau, N., et al.
   Far-Infrared Astronomy with the CO N^+ Deuterium Observations Receiver (CONDOR) 2008, EAS Publications Series, 31, 215

7. Emprechtinger, M., Volgenau, N. H. & Wiedner, M. C.
   Deuterated Molecules as Evolutionary Indicators of Class 0 Protostars 2007, Molecules in Space and Laboratory, 21

8. Wiedner, M. C., Bielau, F., Emprechtinger, M., Rettenbacher, K., et al.
   Observations at THz frequencies with CONDOR
   2007, Molecules in Space and Laboratory, 16

9. Wiedner, M. C., Wieching, G., Bielau, F., Emprechtinger, M., et al.
   CONDOR - A heterodyne receiver at 1.25-1.5 THz
   2007, IAUS, 237, 495

10. Volgenau, N. H., Wiedner, M. C., Wieching, G., Emprechtinger, M., et al.
    CONDOR observations of high mass star formation in Orion
    2007, IAUS, 237, 492

11. Emprechtinger, M., Simon, R., Wiedner & M. C.
    N_2D^+ abundance in high mass star forming regions
    2005, AN, 326, 649

12. Bielau, F., Emprechtinger, M., Graf, U. U., Honingh, C. E., et al.
    CONDOR - 1.4 THz hetrodyne receiver for APEX and for GREAT on SOFIA
    2005, AN, 326, 575

13. Emprechtinger, M. & Wiedner, M. C.
    Deuterium Chemistry in star forming regions
    2005, IAUS, 235, 248

Danksagung

Ohne den Rat und die Unterstützung vieler Menschen wäre die Fertigstellung dieser Arbeit nicht möglich gewesen. Ganz besonders möchte ich mich bei den folgenden Personen bedanken:

- Bei Prof. Dr. Jürgen Stutzki für die Möglichkeit am I. Physikalischen Institut diese Dissertation anzufertigen. Für die exzellente Beratung und für die Möglichkeit an internationalen Projekten mitzuarbeiten.
- Bei Prof. Dr. Thomas Michely und Prof. Dr. Axel Klein, dass Sie sich bereit erklärt haben als zweiter Referent bzw. als Vorsitzender der Prüfungskommission bei meinem Promotionsverfahren zu fungieren.
- Bei Dr. Martina Wiedner für die Betreuung in den letzten Jahren, für die Anregungen und Diskussionen und nicht zuletzt auch für die Freiräume, die mir bei meiner Arbeit gelassen wurden. Außerdem möchte ich Ihr für das Korrekturlesen dieser Arbeit danken.
- Bei Dr. Nikolaus Volgenau für die gemeinsame Arbeit und die tolle Stimmung im Zimmer und während diverser Beobachtungskampagnen. Die kritischen und anregenden Diskussionen mit ihm haben viel zum gelingen dieser Arbeit beigetragen. Außerdem möchte ich mich bei Gundolf Wieching und dem gesamten CONDOR-Team für die gute Zusammenarbeit, vor allem während der Beobachtungen in Chile, bedanken
- Bei Dr. Paola Caselli für die die Unterstützung bei der Analyse und der Interpretation der N_2D^+ Daten.
- Bei Dr. C. Kramer, Dr. R. Simon, Dr. M. Röllig, Dr. V. Ossenkopf und Dr. M. Miller für die fachliche und anderweitige Unterstützung, deren kritische Fragen und den gemeinsamen Diskussionen. Außerdem möchte ich mich für angenehme Atmosphäre in der Gruppe bedanken.
- Oliver Ricken, Kefeng Sun, Markus Cubik, Michael Masur, Pablo Garcia Fuentes, Martin Phillip und Marc Hitschfeld für die vielen fachlichen, aber im besonderen auch für die den Alltag auflockernden nicht-physikalischen Gespräche. Vor allem bei Marc möchte ich mich für die allmorgendliche gemeinsame Tasse Kaffee bedanken, die den Start in den Tag entscheidend erleichtert hat.
- Bei meinen Wohungskollegen Connie und Sergio für die schöne Zeit, das gute Essen und dafür, dass nach Feierabend auch über Themen fernab der Physik gesprochen wurde.
- Bei meinen Eltern, ohne deren langjährige moralische und finanzielle Unterstützung ich nie die Möglichkeit gehabt hätte diese Dissertation anzufertigen.

Finanzielle Förderung

- Diese Arbeit wurde Großteils im Rahmen des SFB 494[10] durch die Deutsche Forschungsgemeinschaft (DFG) finanziert.
- Während der Jahre 2006 und 2007 wurde ich durch die Studienstiftung des Deutschen Volkes im Rahmen der Promotionsförderung unterstützt.
- IRAM danke ich für die finanzielle Unterstützung der Beobachtungen am 30m Teleskop in Granada.
- RadioNet bin ich für die Übernahme der Kosten der Beobachtungsreise ans JCMT zu Dank verpflichtet.

---

[10] Sonderforschungsbereich 494: Die Entwicklung der Interstellaren Materie - Terahertz-Spektroskopie im Weltall und Labor

Erklärung

Ich versichere, dass ich die von mir vorgelegte Dissertation selbständig angefertigt, die benutzten Quellen und Hilfsmittel vollständig angegeben und die Stellen der Arbeit – einschließlich Tabellen, Karten und Abbildungen –, die anderen Werken im Wortlaut oder dem Sinn nach entnommen sind, in jedem Einzelfall als Entlehnung kenntlich gemacht habe; daß diese Dissertation noch keiner anderen Fakultät oder Universität zur Prüfung vorgelegen hat; dass sie – abgesehen von unten angegebenen Teilpublikationen – noch nicht veröffentlicht worden ist sowie, daß ich eine solche Veröffentlichung vor Abschluss des Promotionsverfahrens nicht vornehmen werde.

Die Bestimmungen dieser Promotionsordnung sind mir bekannt. Die von mir vorgelegte Dissertation ist von Prof. Dr. Stutzki betreut worden.

Köln, den 3. November 2008

Lebenslauf

Name:	Martin Emprechtinger
Geboren:	am 1. Februar 1978, in Ried im Innkreis
Staatsbürgerschaft:	Österreich

Schulausbildung

Sep. 1984-Jul. 1988:
Voksschule in Neuhofen im Innkreis, Österreich

Sep. 1988-Jul. 1992:
Hauptschule I in Ried im Innkreis, Österreich

Sep. 1992-Jul. 1997:
Höhere Technische Bundeslehranstallt in Wels, Österreich
Fachrichtung: Chemische Betriebstechnik
Matura abgelegt am 23. Jun. 1997

Okt. 1998-Sep. 1999:
Ableistung des Zivildienstes im Allgemeinen Krankenhaus der Stadt Linz, Österreich

Universitätsausbildung

Okt. 1999-Jan. 2002:
1. Studienabschnitt in Physik und Astronomie an der Universität Innsbruck, Österreich
1. Diplomprüfung abgelegt am 22. Jan. 2002

Jan. 2002-Okt. 2004:
2. Studienabschnitt in Physik an der Universität Innsbruck, Österreich
2. Diplomprüfung abgelegt am 13. Okt. 2004
Titel der Diplomarbeit: ”Photo-ionization models of Planetary Nebulae”
Betreut durch Prof. Kimeswenger

Seit Dez. 2004
Promotionsstudium Physik an der Universität zu Köln
Titel der Dissertation: ”Physical and Chemical Properties of Molecular Gas in Star Forming Regions”
Betreut durch Prof. Stutzki